

UNCLASSIFIED

AD NUMBER

AD339910

CLASSIFICATION CHANGES

TO: **unclassified**

FROM: **secret**

LIMITATION CHANGES

TO:
Approved for public release, distribution unlimited

FROM:
Distribution: DoD only: others to Director, Defense Nuclear Agency, Attn: STTI. Washington, DC 20305.

AUTHORITY

Defense Threat Reduction Agency ltr., dtd October 11, 2000.; Same.

THIS PAGE IS UNCLASSIFIED

SECRET
FORMERLY RESTRICTED DATA

AD 339910L

*Reproduced
by the*

DEFENSE DOCUMENTATION CENTER

FOR

SCIENTIFIC AND TECHNICAL INFORMATION

CAMERON STATION, ALEXANDRIA, VIRGINIA



FORMERLY RESTRICTED DATA
SECRET

NOTICE: When government or other drawings, specifications or other data are used for any purpose other than in connection with a definitely related government procurement operation, the U. S. Government thereby incurs no responsibility, nor any obligation whatsoever; and the fact that the Government may have formulated, furnished, or in any way supplied the said drawings, specifications, or other data is not to be regarded by implication or otherwise as in any manner licensing the holder or any other person or corporation, or conveying any rights or permission to manufacture, use or sell any patented invention that may in any way be related thereto.

NOTICE:

THIS DOCUMENT CONTAINS INFORMATION
AFFECTING THE NATIONAL DEFENSE OF
THE UNITED STATES WITHIN THE MEAN-
ING OF THE ESPIONAGE LAWS, TITLE 18,
U.S.C., SECTIONS 793 and 794. THE
TRANSMISSION OR THE REVELATION OF
ITS CONTENTS IN ANY MANNER TO AN
UNAUTHORIZED PERSON IS PROHIBITED
BY LAW.

339910L

AIR FORCE
BALLISTIC MISSILE DIVISION

TECHNICAL LIBRARY

Document No. K-507

Copy No. 1

SECRET

RESTRICTED DATA

WT-1334

OPERATION REDWING — PROJECT 5.8

Report

EVALUATION OF THE A3D-1 AIRCRAFT
FOR SPECIAL WEAPONS DELIVERY
CAPABILITY (U), - 8

"This document contains information affecting the National Defense of the United States within the meaning of the Espionage Laws, Title 18, U. S. C., Section 793 and 794. Its transmission or the revelation of its contents in any manner to an unauthorized person is prohibited by law."

Airframe Design Division
Bureau of Aeronautics
Department of the Navy
and

Advanced Design Section
El Segundo Division
Douglas Aircraft Company, Inc.
El Segundo, California

⑦ NA

⑩ 27 Sep 50

⑫ 148 JP

⑬ NA

⑭ NA

⑮ NA

⑯ NA

⑰ NA

⑱ S-RD

FORMERLY RESTRICTED DATA

Handle as Restricted Data in foreign dissemination. Section 144b, Atomic Energy Act of 1954.

This material contains information affecting the national defense of the United States within the meaning of the espionage laws, Title 18, U.S.C., Secs. 793 and 794, the transmission or revelation of which in any manner to an unauthorized person is prohibited by law.

3

SECRET

RESTRICTED DATA



A3D-1 airplane instrumented for Operation Redwing.

RESTRICTED DATA
SECRET

FOREWORD

This report presents the preliminary results of one of the projects participating in the military-effect programs of Operation Redwing. Over-all information about this and the other military-effect projects can be obtained from WT-1344, the "Summary Report of the Commander, Task Unit 3." This technical summary includes: (1) tables listing each detonation with its yield, type, environment, meteorological conditions, etc.; (2) maps showing shot locations; (3) discussions of results by programs; (4) summaries of objectives, procedures, results, etc., for all projects; and (5) a listing of project reports for the military-effect programs.

RESTRICTED DATA
5-6

SECRET

ABSTRACT

This report presents the results of the participation of the A3D airplane in Project 5.8 of Operation Redwing.

Primary objective of this project was to determine the response of the structure of the A3D-1 aircraft to the thermal effects of a thermonuclear explosion, primarily for the purpose of establishing critical thermal envelopes for the aircraft when utilized for the delivery of large yield devices.

The A3D is a twin-engine, swept-wing, carrier-based jet airplane which is intended for use as a high-altitude bomber having relatively long range and high performance.

On the basis of existing structural strength it was determined that actual delivery capability limitations of the A3D as a high altitude bomber would be caused by thermal response rather than response to gust inputs. Therefore, participation in Operation Redwing was limited to shots for which thermal response would be the limiting factor.

In Project 5.8, the A3D airplane participated in seven shots: Cherokee (3.8 Mt), Zuni (3.5 Mt), Flathead (380 kt), Apache (1.9 Mt), Navajo (4.8 Mt), Tewa (5.0 Mt), and Huron (270 kt).

Since thermal effects were critical for A3D high-altitude delivery, the emphasis of the instrumentation was on measuring the thermal energy received at the airplane and its effect on the temperature response in the thin skin panels on the lower surface of the airplane.

Additional instrumentation was installed to measure overpressure, effect of shock wave on engine performance, and aircraft response to shock wave gust loadings. Originally the gust instrumentation consisted of accelerometers at the airplane center of gravity, but during the test operation additional accelerometers and some strain gages were added in the wing.

Results of the tests are presented as direct and indirect irradiance and radiant exposure versus time, temperature in thin skin areas versus time, maximum temperature rise at each thermocouple locations, peak overpressure, time of shock arrival, and limited data on structural loads and accelerations caused by the shock wave gust. Calculated weapon effects and aircraft response are compared with the measured results to show the adequacy of prediction methods.

Prediction methods presented in this report for the thermal effects gave good agreement with the measured results for thermal fields, temperature time history, and maximum temperature rise. Although agreement was good, results indicate a need for additional information and understanding of the atmospheric attenuation and the heat transfer properties of the air flowing over the airplane surfaces.

Excellent agreement was obtained between the measured and calculated peak overpressure and time of shock arrival.

No undesirable engine response was observed at shock arrival. Observed changes in engine performance were no larger than possible variations caused by accuracy of the measuring and recording equipment.

As previously stated, the emphasis of the instrumentation was on thermal effects. Structural load instrumentation was limited to a few strain gages installed at the EPG during the test program. Despite the questionable accuracy and meagerness of the wing response data, fuselage accelerometer data confirmed the original estimates that gust response would not be criti-

cal for the mission being considered. In general, the gust response instrumentation was not complete enough to permit improvements in the structural response prediction methods.

Maximum temperature rise experienced during the tests was 370°F. Therefore, although it is not possible to define an absolute upper limit, it can be stated that the airplane safely withstood this temperature rise without any damage.

With regard to the delivery capability of the A3D airplane, it can be stated that all the test positions, with the exception of Shot Cherokee, were closer to the explosion than if the airplane had dropped the device and executed a horizontal turn escape maneuver.

In view of the good agreement of the weapons effects prediction methods with the experimental values, delivery capability studies based on these methods may be considered valid.

CONTENTS

FOREWORD	5
ABSTRACT	7
CHAPTER 1 INTRODUCTION	17
1.1 Objectives	17
1.2 Background	17
1.3 Theory	18
1.3.1 Thermal Energy Input	18
1.3.2 Thermal Response	21
1.3.3 Gamma Radiation	22
1.3.4 Shock Wave Effects	22
1.3.5 Gust Loads	22
CHAPTER 2 PROCEDURE	23
2.1 Operation	23
2.1.1 Description of the A3D-1 Airplane	23
2.1.2 Shot Participation	24
2.1.3 Criteria for Selecting Desired Aircraft Positions	24
2.1.4 Positioning of Aircraft for Test	24
2.1.5 Systems for Positioning Aircraft	24
2.2 Instrumentation	24
2.2.1 Scope of Instrumentation	24
2.2.2 Oscillograph Recorded Data	26
2.2.3 Data Recorded on Photo Recorder	27
2.2.4 Method of Instrumentation Operation	27
CHAPTER 3 RESULTS AND DISCUSSION OF SHOT PARTICIPATION, AIRCRAFT POSITIONS, AND FLIGHT ENVIRONMENTAL DATA	28
3.1 Shot Participation	28
3.2 Aircraft Positions and Flight Environmental Data	28
3.2.1 Accuracy of Aircraft Position	29
3.2.2 Comments on Positioning Methods	29
CHAPTER 4 RESULTS AND DISCUSSION OF THERMAL INPUT DATA	32
4.1 Scattered Radiation	32
4.2 Reflected Energy from Terrain Surface	33
4.3 Discussion of Radiometer and Calorimeter Measurements	37
4.3.1 Shot Flathead	39

4.3.2	Shot Zuni	39
4.3.3	Shot Tewa	39
4.3.4	Shots Navajo, Apache, Cherokee, and Huron	48
4.4	Correlation of Measured and Computed Thermal Field	48
CHAPTER 5 RESULTS AND DISCUSSION OF STRUCTURAL TEMPERATURE MEASUREMENTS		
5.1	Quartz Covered Thermocouple for Aerodynamic Cooling	51
5.2	Temperature Time History	51
CHAPTER 6 RESULTS AND DISCUSSION OF TEMPERATURE RISE CALCULATED FROM MEASURED THERMAL INPUT		
6.1	Calculation of Temperature Time History	72
6.2	Simplified Calculation of Maximum Temperature Rise	82
CHAPTER 7 RESULTS AND DISCUSSION, GAMMA RADIATION		
CHAPTER 8 RESULTS AND DISCUSSION, SHOCK WAVE EFFECTS		
8.1	Overpressure	85
8.2	Time of Shock Arrival	85
8.3	Engine Operation	87
8.4	Airplane Response to Gust Loading	88
8.4.1	Center of Gravity Acceleration	88
8.4.2	Wing Bending Moment	92
8.4.3	Pitching Velocity	93
CHAPTER 9 DELIVERY CAPABILITY OF THE A3D AIRPLANE		
CHAPTER 10 CONCLUSIONS		
CHAPTER 11 RECOMMENDATIONS		
APPENDIX A METHOD OF SCALING SHOCK WAVE EFFECTS		
APPENDIX B DETERMINATION OF HEAT TRANSFER COEFFICIENT		
APPENDIX C INSTRUMENTATION		
C.1	Recording Instrumentation	102
C.2	Instrumentation for Thermal Measurements	102
C.3	Special Instrumentation for Thermal Effects Data	102
C.4	Measurement of Thermal Radiation Received by Aircraft	102
C.5	Camera Installations	105
C.6	Overpressure Measurements	105
C.7	Engine Instrumentation	105
C.8	Miscellaneous Instrumentation	105
C.9	Measurement of Load Factor Increment Due to Gust	110
APPENDIX D ADDITIONAL TEST DATA		
REFERENCES		

FIGURES

1.1	Normalized pulse of thermal irradiance	18
2.1	Instrumentation locations	25
4.1	Fireball and reflection area at various times, Shot Tewa	34
4.2	Fireball and reflection area at various times, Shot Flathead	35
4.3	Fireball and reflection area at various times, Shot Apache	36
4.4	Field of view of direct thermal instruments, Shot Flathead	38
4.5	Field of view of 90 degree indirect thermal instruments, Shot Flathead	38
4.6	Thermal irradiance as a function of time, Shot Flathead	40
4.7	Radiant exposure of direct thermal instruments, Shot Flathead	40
4.8	Radiant exposure of indirect thermal instruments, Shot Flathead	41
4.9	Field of view of direct thermal instruments, Shot Zuni	41
4.10	Field of view of 90 degree indirect thermal instruments, Shot Zuni	42
4.11	Thermal irradiance as a function of time, Shot Zuni	42
4.12	Radiant exposure of direct thermal instruments, Shot Zuni	43
4.13	Radiant exposure of indirect thermal instruments, Shot Zuni	43
4.14	Field of view of direct thermal instruments, Shot Tewa	44
4.15	Field of view of 90 degree indirect thermal instruments, Shot Tewa	44
4.16	Thermal irradiance as a function of time, Shot Tewa	45
4.17	Radiant exposure of direct thermal instruments, Shot Tewa	45
4.18	Radiant exposure of indirect thermal instruments, Shot Tewa	46
4.19	Comparison of measured and calculated thermal irradiance, Shot Tewa	46
4.20	Comparison of measured and calculated thermal irradiance, Shot Zuni	47
4.21	Comparison of measured and calculated thermal irradiance, Shot Flathead	47
5.1	Summary of maximum temperature rise, Shot Cherokee	53
5.2	Summary of maximum temperature rise, Shot Zuni	53
5.3	Summary of maximum temperature rise, Shot Flathead	54
5.4	Summary of maximum temperature rise, Shot Apache	54
5.5	Summary of maximum temperature rise, Shot Navajo	55
5.6	Summary of maximum temperature rise, Shot Tewa	55
5.7	Summary of maximum temperature rise, Shot Huron	56
5.8	Temperature time history of nacelle skin, Shot Flathead	56
5.9	Temperature time history of aileron and flap skin, Shot Flathead	57
5.10	Temperature time history of bomb bay door and lower fuselage, Shot Flathead	57
5.11	Temperature time history of arresting hook area, Shot Flathead	58
5.12	Temperature time history of quartz covered thermocouple compared to adjacent uncovered thermocouple, Shot Flathead	58
5.13	Temperature time history of aft portion of lower fuselage, Shot Flathead	59
5.14	Temperature time history of plastic radome, Shot Flathead	59
5.15	Temperature time history of tail turret, Shot Flathead	60
5.16	Temperature time history of elevator skin, Shot Flathead	60
5.17	Temperature time history comparing outer skin and internal beaded doubler, Shot Flathead	61
5.18	Temperature time history of lower rudder, Shot Flathead	61
5.19	Temperature time history of nacelle skin, Shot Zuni	62
5.20	Temperature time history of aileron and flap skin, Shot Zuni	62
5.21	Temperature time history of bomb bay door and lower fuselage, Shot Zuni	63
5.22	Temperature time history of arresting hook area, Shot Zuni	63

5.23	Temperature time history of quartz covered thermocouple compared to adjacent uncovered thermocouple, Shot Zuni	64
5.24	Temperature time history of aft portion of lower fuselage, Shot Zuni	64
5.25	Temperature time history of elevator skin, Shot Zuni	65
5.26	Temperature time history comparing outer skin and internal beaded doubler, Shot Zuni	65
5.27	Temperature time history of lower rudder, Shot Zuni	66
5.28	Temperature time history of nacelle skin, Shot Tewa	66
5.29	Temperature time history of alleron and flap skin, Shot Tewa	67
5.30	Temperature time history of bomb bay door and lower fuselage, Shot Tewa	67
5.31	Temperature time history of arresting hook area, Shot Tewa	68
5.32	Temperature time history of quartz covered thermocouple compared to adjacent uncovered thermocouple, Shot Tewa	68
5.33	Temperature time history of tail turret, Shot Tewa	69
5.34	Temperature time history of gray painted elevator skin, Shot Tewa	69
5.35	Temperature time history of blue painted elevator skin, Shot Tewa	70
5.36	Temperature time history comparing outer skin and internal beaded doubler, Shot Tewa	70
5.37	Temperature time history of lower rudder, Shot Tewa	71
5.38	Thermocouple lag calibration	71
6.1	Effect of absorptivity on calculated temperature time history	73
6.2	Effect of heat transfer coefficient on calculated temperature time history	74
6.3	Effect of maximum irradiance on calculated temperature time history	75
6.4	Comparison of measured and calculated temperature time history in blue painted elevator skin, Shot Tewa	76
6.5	Comparison of measured and calculated temperature time history in gray painted elevator skin, Shot Tewa	77
6.6	Comparison of measured and calculated temperature time history for white painted elevator skin, Shot Tewa	78
6.7	Comparison of measured and calculated temperature time history for white painted skin, Shot Zuni	79
6.8	Comparison of measured and calculated temperature time history for white painted skin, Shot Flathead	80
6.9	Effect of distance from leading edge of horizontal stabilizer on measured and calculated temperature time history, gray paint, Shot Tewa	81
8.1	Calculated overpressure versus yield factor	86
8.2	Calculated time of shock arrival versus yield factor	87
8.3	Comparison of center section and center of gravity accelerometers, Shot Tewa	89
8.4	Time history of measured and predicted center of gravity acceleration, Shot Zuni	89
8.5	Time history of measured and predicted center of gravity acceleration, Shot Flathead	89
8.6	Time history of measured and predicted center of gravity acceleration, Shot Apache	90
8.7	Time history of measured and predicted center of gravity acceleration, Shot Navajo	90
8.8	Time history of measured and predicted center of gravity acceleration, Shot Tewa	90

8.9	Time history of measured and predicted center of gravity acceleration, Shot Huron	90
8.10	Time history of measured and predicted wing root bending moment, Shot Apache	91
8.11	Time history of measured and predicted wing root bending moment, Shot Navajo	91
8.12	Time history of measured and predicted wing root bending moment, Shot Tewa	91
8.13	Time history of measured and predicted wing root bending moment, Shot Huron	92
8.14	Time history of measured and predicted wing fold joint bending moment, Shot Tewa	92
8.15	Time history of measured and predicted wing fold joint bending moment, Shot Huron	93
8.16	Time history of measured and predicted airplane pitching velocity, Shot Zuni	94
8.17	Time history of measured and predicted airplane pitching velocity, Shot Flathead	94
8.18	Time history of measured and predicted airplane pitching velocity, Shot Apache	95
8.19	Time history of measured and predicted airplane pitching velocity, Shot Navajo	95
8.20	Time history of measured and predicted airplane pitching velocity, Shot Tewa	96
8.21	Time history of measured and predicted airplane pitching velocity, Shot Huron	96
D.1	Thermal irradiance as a function of time, Shot Cherokee	111
D.2	Field of view of direct thermal instruments, Shot Cherokee	112
D.3	Radiant exposure of direct thermal instruments, Shot Cherokee	113
D.4	Radiant exposure of indirect thermal instruments, Shot Cherokee	113
D.5	Field of view of direct thermal instruments, Shot Apache	114
D.6	Field of view of 90 degree indirect thermal instruments, Shot Apache	114
D.7	Estimated direct thermal irradiance, Shot Apache	115
D.8	Estimated indirect thermal irradiance, Shot Apache	115
D.9	Radiant exposure of direct thermal instruments, Shot Apache	116
D.10	Radiant exposure of indirect thermal instruments, Shot Apache	116
D.11	Field of view of direct thermal instruments, Shot Navajo	117
D.12	Field of view of 90 degree indirect thermal instruments, Shot Navajo	117
D.13	Estimated direct thermal irradiance, Shot Navajo	118
D.14	Estimated indirect thermal irradiance, Shot Navajo	118
D.15	Radiant exposure of direct thermal instruments, Shot Navajo	119
D.16	Radiant exposure of indirect thermal instruments, Shot Navajo	119
D.17	Field of view of direct thermal instruments, Shot Huron	120
D.18	Thermal irradiance as a function of time, Shot Huron	120
D.19	Radiant exposure of direct thermal instruments, Shot Huron	121
D.20	Radiant exposure of indirect thermal instruments, Shot Huron	121
D.21	Temperature time history of plastic radome, Shot Zuni	122
D.22	Temperature time history of tail turret, Shot Zuni	122
D.23	Temperature time history of nacelle skin, Shot Apache	123
D.24	Temperature time history of aileron and flap skin, Shot Apache	123
D.25	Temperature time history of bomb bay door and lower fuselage, Shot Apache	124
D.26	Temperature time history of arresting hook area, Shot Apache	124

D.27	Temperature time history of quartz covered thermocouple compared to adjacent uncovered thermocouple, Shot Apache	125
D.28	Temperature time history of tail turret, Shot Apache	125
D.29	Temperature time history of elevator skin, Shot Apache	126
D.30	Temperature time history comparing outer skin and internal beaded doubler, Shot Apache	126
D.31	Temperature time history of lower rudder, Shot Apache	127
D.32	Temperature time history of nacelle skin, Shot Navajo	127
D.33	Temperature time history of aileron and flap skin, Shot Navajo	128
D.34	Temperature time history of bomb bay door and lower fuselage, Shot Navajo	128
D.35	Temperature time history of arresting hook area, Shot Navajo	129
D.36	Temperature time history of quartz covered thermocouple compared to adjacent uncovered thermocouple, Shot Navajo	129
D.37	Temperature time history of plastic radome, Shot Navajo	130
D.38	Temperature time history of tail turret, Shot Navajo	130
D.39	Temperature time history of elevator skin, Shot Navajo	131
D.40	Temperature time history comparing outer skin and internal beaded doubler, Shot Navajo	131
D.41	Temperature time history of lower rudder, Shot Navajo	132
D.42	Temperature time history of plastic radome, Shot Tewa	132
D.43	Temperature time history of tail turret, Shot Tewa	133
D.44	Temperature time history of nacelle skin, Shot Huron	133
D.45	Temperature time history of aileron and flap skin, Shot Huron	134
D.46	Temperature time history of bomb bay door and lower fuselage, Shot Huron	134
D.47	Temperature time history of arresting hook area, Shot Huron	135
D.48	Temperature time history of quartz covered thermocouple compared to adjacent uncovered thermocouple, Shot Huron	135
D.49	Temperature time history of plastic radome, Shot Huron	136
D.50	Temperature time history of tail turret, gray paint, Shot Huron	136
D.51	Temperature time history of tail turret, white paint, Shot Huron	137
D.52	Temperature time history of elevator skin, Shot Huron	137
D.53	Temperature time history comparing outer skin and internal beaded doubler, Shot Huron	138
D.54	Temperature time history of lower rudder, Shot Huron	138
D.55	Temperature time history of nacelle skin, Shot Cherokee	139
D.56	Temperature time history of aileron and flap skin, Shot Cherokee	139
D.57	Temperature time history of bomb bay door and lower fuselage, Shot Cherokee	140
D.58	Temperature time history of arresting hook area, Shot Cherokee	140
D.59	Temperature time history of quartz covered thermocouple compared to adjacent uncovered thermocouple, Shot Cherokee	141
D.60	Temperature time history of aft portion of lower fuselage, Shot Cherokee	141
D.61	Temperature time history of tail turret, Shot Cherokee	142
D.62	Temperature time history of elevator skin, Shot Cherokee	142
D.63	Temperature time history comparing outer skin and internal beaded doubler, Shot Cherokee	143
D.64	Temperature time history of lower rudder, Shot Cherokee	143

TABLES

2.1	Gust Instrumentation Availability	26
3.1	Summary of Event Participation	28

3.2	Comparison of Planned and Actual Yields and Positions	30
3.3	Flight and Environmental Parameters at Time of Explosion	31
3.4	Flight and Environmental Parameters at Time of Shock Arrival	31
4.1	Maximum Measured Irradiance and Radiant Exposure	33
4.2	Estimated and Effective Linear Attenuation Values	49
4.3	Atmospheric Conditions and Cloud Cover	49
6.1	Comparison of Measured and Calculated Temperature Rise	82
8.1	Measured and Calculated Peak Overpressure	85
8.2	Measured and Calculated Time of Shock Arrival	86
8.3	Effect of Shock Wave on Engine Performance Parameters	88
8.4	Dynamic Magnification Factors	93
C.1	Detailed Thermocouple Installations	103
C.2	Thermal Instruments for Shot Cherokee	106
C.3	Thermal Instruments for Shot Zuni	106
C.4	Thermal Instruments for Shot Flathead	107
C.5	Thermal Instruments for Shot Apache	107
C.6	Thermal Instruments for Shot Navajo	108
C.7	Thermal Instruments for Shot Tewa	108
C.8	Thermal Instruments for Shot Huron	109
C.9	Summary of Accelerometer Installations	109

SECRET

Chapter 1

INTRODUCTION

1.1 OBJECTIVES

Analytical studies of the high-altitude delivery capability of the A3D-1 aircraft showed that it was critical for thermal effects. This critical thermal response, coupled with uncertainties in the prediction of high-yield device phenomena, required thermal measurements on the aircraft in thermonuclear device tests to verify the suitability of the aircraft for its assigned primary mission.

The primary objectives of Project 5.8 of Operation Redwing as specified in BuAer Contract NOas 55-867c and BuAer letter Aer-CT-422, 09366 dated 19 May 1955 were:

- a. To determine temperature as a function of time in the instrumented skin.
- b. To correlate the temperature-time history of the instrumented areas with the measured and computed thermal field.
- c. To verify existing prediction methods for the effects field phenomena as applicable to airborne receiver, thermal radiant energy, thermal flux, overpressure, and time of shock arrival.
- d. To recommend thermal field limits for the A3D airplane backed by proven formulae for defining the thermonuclear weapon delivery capability of the A3D type aircraft.
- e. To verify the analytical methods of prediction of aircraft dynamic response to shock wave gust inputs within the limitations imposed by the scope of the structural response instrumentation.

1.2 BACKGROUND

Prior to the development of the A3D, the AJ Savage was the only Navy aircraft with a capability for the delivery of a megaton yield device. This capability was based on analytical predictions and was not verified by actual tests.

Naval aircraft (specifically the AD Skyraider, a light attack aircraft) participated in Project 5.1 in Operation Upshot-Knothole and in Project 8.1 in Operation Teapot. Both these tests series involved low yield devices. No other Naval aircraft with the capability for the delivery of atomic weapons participated in effects tests up to Operation Redwing.

The test results obtained by Project 5.1 during Upshot-Knothole (Reference 1) included data on overpressure, thermal radiation, and gust response. The data were obtained by both manned and unmanned aircraft. Loss of the AD drone during this operation, due to burning of skin panels, emphasized the need to minimize the thermal radiation effects by use of white paint on the lower surfaces of the aircraft.

Test results of Project 8.1 during Operation Teapot (Reference 2) included data on reflection of thermal radiation by terrain surface, temperature rise in aircraft skin, and spectral distribution of direct and reflected components of thermal radiation.

SECRET

FORMERLY RESTRICTED DATA

1.3 THEORY

To fulfill test objectives of this project the thermal analysis consisted of three parts: (1) comparing the time history of the thermal energy input measured in the test with the calculated value, (2) comparing the measured time history of the temperature rise with the time history computed from the measured thermal energy input, and (3) comparing the measured maximum temperature rise with that obtained by a simplified calculation which computed only maximum value rather than complete time history.

Methods used in the calculations of each of these phases are described in the following sections.

1.3.1 Thermal Energy Input. In computing the temperature time history in the aircraft skin, the significant device characteristic was the rate at which the thermal energy was released rather than the total amount of energy. In the case of an airplane in motion the air-stream has a cooling effect upon the aircraft skin. This, combined with the time history of the rate of energy release (reaching a maximum and then decreasing rapidly), results in the maximum temperature rise in the skin occurring before all the energy is released. Therefore, that portion of the thermal energy received after the aircraft skin has reached a maximum temperature is of no significance to the maximum temperature. For this reason, the majority of the analysis is concerned with the rate of energy release (irradiance) as a function of time rather than the total energy.

For the theoretical irradiance versus time relationship, which is commonly referred to as the thermal pulse, many sources and methods of scaling for device yield exist. The majority of data is in the form of a normalized thermal pulse. This is the ratio of the irradiance at a given time to the maximum irradiance (I/I_{\max}) plotted as a function of the ratio of time to the time to maximum irradiance (t/t_{\max}). Several sources for this relationship were considered, and it was found that the agreement between the various pulses and methods of scaling was quite good when the various pulses were scaled by their corresponding scaling methods to a yield of 10 Mt. It was concluded that the source of most of the data was the Mike shot of Operation Ivy, but a check of the method of scaling, or the determination of the value of the maximum irradiance, was not available.

The normalized thermal pulse used in the analysis presented in this report was obtained from Reference 3 and is shown in Figure 1.1. This pulse was selected because it was based on

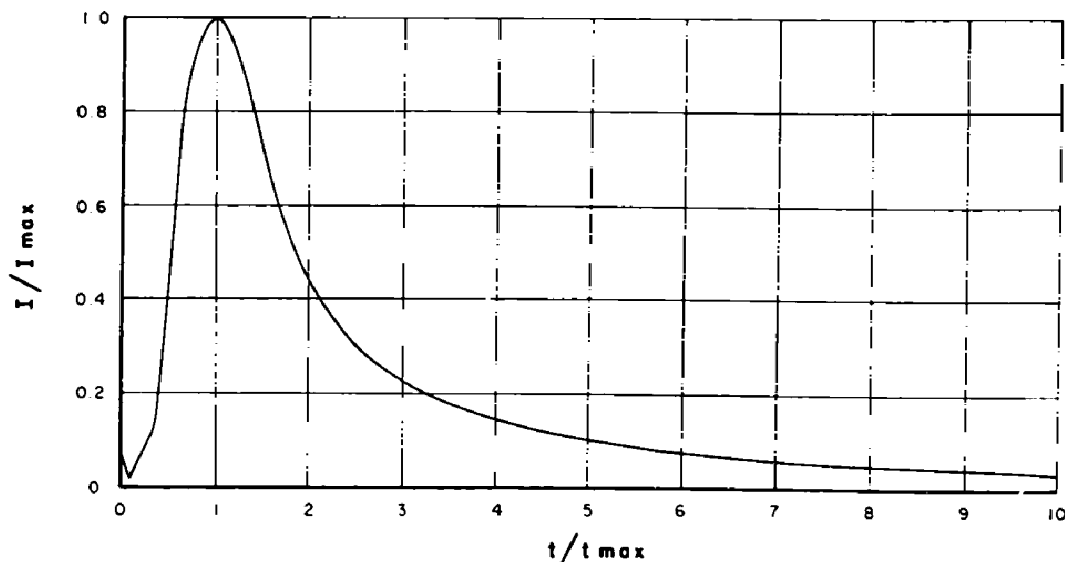


Figure 1.1 Normalized pulse of thermal irradiance.

an average of several yields from Operations Ivy and Castle and appeared to be the most reliable. Also, the cooling and flyaway correction factor which is analyzed in this report for use in the simplified calculation of the maximum temperature rise is based on this pulse. Therefore, comparison of the measured thermal inputs with those calculated from this pulse served as a check of the methods of computation. It also permitted a better analysis of the cooling and flyaway factors based on this pulse when maximum temperatures calculated with these factors were compared with the measured maximum temperature rise.

For the normalized pulse to be useful in the calculation of the irradiance with time, values for the time at maximum irradiance (t_{\max}) and the maximum irradiance (I_{\max}) must be obtained. Reference 3 states that the relationship between the time to maximum irradiance, maximum irradiance, and total thermal yield can be expressed by:

$$I_{\max} \times t_{\max} \times 2.02 = \text{total thermal yield}$$

It is generally accepted that the time for maximum irradiance in seconds is:

$$t_{\max} = 0.032W^{1/2}$$

and the total thermal yield is:

$$W_{TH} = 0.44 W^{0.94}$$

where W = total radiochemical yield (kt)

W_{TH} = total thermal yield (kt)

Therefore, an expression defining the maximum irradiance can be derived as follows:

$$I_{\max} \times t_{\max} \times 2.02 = 0.44 \times W^{0.94} = W_{TH} \quad (1.1)$$

Substituting the expression for t_{\max} gives:

$$I_{\max} = \frac{0.44W^{0.94}}{2.02 \times 0.032W^{1/2}} \text{ which gives:}$$

$$I_{W(\max)} = 6.8W^{0.44} \text{ (kt/sec)}$$

This is the maximum source irradiance in kt/sec and when the conversion of 1 kt = 10^{12} calories is used, the value for I_{\max} based on the cited pulse becomes:

$$I_{c(\max)} = 6.8 \times 10^{12} \times W^{0.44} \text{ (cal/sec)} \quad (1.2)$$

This represents the maximum irradiance (rate of thermal energy release) at the source, and from this the maximum irradiance received at a point in space in a vacuum can be obtained as:

$$I'_{(r)\max} = \frac{6.8 \times 10^{12} \times W^{0.44}}{4\pi r^2} \text{ (cal/cm}^2\text{/sec)} \quad (1.3)$$

where r is the slant range (cm)

It should be noted that the form of Equation 1.3 assumes an isotropic, isothermal spherical radiation source, also assumed valid by other analysts.

The in-vacuo irradiance is reduced in fact by the attenuation of the atmosphere through which it passes, and this factor can be included in the equation to give maximum irradiance as

a function of slant range:

$$I_{(r)_{\max}} = \frac{6.8 \times 10^{12} \times W^{0.44} \times e^{-k'r}}{4\pi r^2} \text{ (cal/cm}^2\text{/sec)} \quad (1.4)$$

where k' is the atmospheric attenuation (cm^{-1})

Equation 1.4 introduces the attenuation as $e^{-k'r}$ which is the form for a classical linear attenuation. It should be noted that this is an oversimplification when applied in a scattering atmosphere, in which field of view corrections may be significant.

For the cases in this analysis it is convenient to work with the slant range in feet; whereupon, the expression then becomes:

$$I_{(r)_{\max}} = \frac{8.57 \times 10^7 (6.8 \times W^{0.44})}{\overline{SR}^2 e^{kd}} \quad (1.5)$$

where $I_{(r)_{\max}}$ = maximum irradiance ($\text{cal/cm}^2\text{/sec}$)

W = total radiochemical yield in kt

\overline{SR} = slant range (feet)

k = attenuation coefficient per kilofeet (kilofeet^{-1})

d = slant range in kilofeet ($\overline{SR}/1000$) (kilofeet)

The above expression applies to the direct irradiance received on a surface normal to the explosion. However, some additional energy may be received by reflection from the terrain surface. The amount of this reflected energy may be obtained from either References 4, 5, or 6. In all cases the reflected energy is expressed in the form of the ratio of the reflected energy to the direct energy for a perfectly diffuse terrain surface. From this the reflected energy may be calculated as a function of the direct energy and the reflectance characteristics (albedo) of the terrain surface.

All the shots of Operation Redwing in which Project 5.8 participated were surface bursts except for Shot Cherokee. For a surface burst the fireball is distorted by the ground surface and is not a spherical shape. Therefore the area of the fireball seen is affected by the orientation of the receiver. For example, a receiver directly above would see a completely circular fireball area, while a receiver on the surface would see a hemispherical fireball or a half circle. Since the amount of fireball area seen affects the amount of radiation received, an additional factor is needed to account for this difference. The method proposed by Reference 7 was used for this correction. For a surface burst this correction factor reduces to the $\cos 2/3$ ($90-\theta$) where θ is the angle between the line from the fireball to the receiver and the horizontal.

With all the factors explained, the maximum irradiance at a point in space can be summarized as:

$$I_{\max} = \frac{8.57 \times 10^7 (6.8 \times W^{0.44})}{\overline{SR}^2 e^{kd}} (K_1 + \beta \frac{Q_{RN}}{Q_I}) \quad (1.6)$$

where I_{\max} = maximum irradiance ($\text{cal/cm}^2\text{/sec}$)

W = total radiochemical yield (kt)

β = albedo, or reflectance quality of terrain

$\frac{Q_{RN}}{Q_I}$ = ratio of reflected energy normal to receiver to direct energy at the receiver position

$K_1 = \cos 2/3$ ($90-\theta$)

θ = angle between line from receiver to fireball and horizontal (degrees)

\overline{SR} = slant range (feet)

k = attenuation coefficient per kilofeet (kilofeet^{-1})

d = slant range in kilofeet ($\overline{SR}/1000$) (kilofeet)

Equation 1.6 applies to the flux on a surface normal to the direct ray from the explosion. For a horizontal receiver, only the vertical component is of importance; in other words, the direct radiation, exclusive of the reflected term, resolved by the sine of the incidence angle. For a horizontal receiver this becomes:

$$I_{\max} = \frac{8.57 \times 10^7 (6.8 \times W^{0.44})}{SR^2 e^{kd}} (K_1 \sin \theta + \beta \frac{Q_{RN}}{Q_1}) \quad (1.7)$$

It should be noted that in each case the ratio of Q_{RN}/Q_1 is a summation of components of irradiation in a specific direction defined by the direct ray from burst point to receiver and is not the same for a receiver normal to the explosion and a horizontal receiver unless the receiver is directly above the explosion.

With the expression for maximum irradiance (I_{\max}) and the time to maximum irradiance (t_{\max}) developed, the irradiance (I) at any time (t) can be found from Figure 1.1 which is in the form of I/I_{\max} at t/t_{\max} .

In conjunction with the experimentally measured value of the maximum irradiance (I_{\max}), the theoretical value of I_{\max} as derived in Equation 1.7 can be used to determine an effective attenuation coefficient, since all other terms of Equation 1.7 are available from the test data. This attenuation should be thought of as an effective linear attenuation coefficient, since its value depends upon the thermal characteristics of the weapon or device being the same as those assumed in the developing of Equation 1.2, that is, that the total thermal yield is $0.44 \times W^{0.94}$ and that the irradiance time relationship is the same as the assumed normalized pulse. Derivation from the measured peak intensity, as outlined, presumes a propagation atmosphere comprised solely of extinction centers, so that there will be absorption only, and no scattering along the path. Lack of a known scattering law or scattering data requires and permits the rough comparison proposed in terms of effective linear attenuation coefficient.

While the attenuation coefficients determined in this manner may not be absolutely correct, they are useful as a comparison of the value that would be estimated from Reference 8. Also, since they are determined from the measured and calculated maximum irradiance, the estimated thermal inputs will agree with the measured at this point and will permit a more obvious comparison of the irradiance at times other than the time at maximum irradiance.

1.3.2 Thermal Response. With the thermal input available from the experimental data as measured by the radiometers, the predicted time history of the temperature rise in representative skin panels was computed in a step-by-step numerical integration of the following expression:

$$\Delta T = \frac{aI\Delta t}{G} - \frac{\bar{h}T\Delta t}{G} \quad (1.8)$$

where ΔT = temperature rise in small time increment (F)

a = absorptivity of surface

Δt = selected small time increment (secs)

I = average irradiance during small time increment, mean of $I(t + \Delta t)$ and $I(t)$ (cal/cm²/sec)

T = temperature rise at time t above ambient conditions prior to beginning of thermal pulse

G = thermal capacity of material (cal/cm²/°F) $G = \rho C_p t$, where, ρ = density of material (lb/in³), C_p = specific heat (cals/lb/°F), and t = skin thickness (inches). When t is expressed in inches, this reduces to: $G = 0.885t$ (cal/cm²/°F) for 75 ST Aluminum Alloy

\bar{h} = heat transfer coefficient as determined from Reference 8 (cal/cm²/sec/°F)

The values of G and \bar{h} used in the above expression are average values based on a constant temperature. As a check of the validity of this assumption a detailed cooling calculation was made for a typical case allowing the convective heat transfer coefficient and the specific

heat of the metal to vary with temperature, and the maximum temperature rise was within 2½ percent of that based on a constant temperature. The derivation of the heat transfer coefficient is shown in Appendix B.

The other phase of correlating the temperature rise is the calculation of the maximum temperature rise directly from the device yield and aircraft position at time of burst. This is obtained from the expression:

$$\Delta T = \left(\frac{a}{G} \right) \frac{8.57 \times 10^7 (0.44W^{0.94})}{SR^2 e^{kd}} (K_1 \sin \theta + \beta \frac{Q_{RN}}{Q_1}) (1 - FH) \quad (1.9)$$

It can be seen that this is similar in form to the equation for determining the maximum irradiance (Equation 1.7). The term $[8.57 \times 10^7 (0.44W^{0.94})]/SR^2$ is also the same as the accepted empirical value of $Q_{total} = 37.7W^{0.94}/d^2$, when d is the slant range in thousands of feet.

The factor (1-FH) is the cooling and flyaway factor and accounts for the aerodynamic cooling of the airstream over the surface and the increase in slant range of the aircraft during the time interval for the release of the total thermal energy. Curves for determining this parameter are presented in Reference 3 as a function of $\eta \bar{h}/G$ for various values of the parameter ηK_3 . The terms of these parameters are defined as follows:

- η = time to maximum irradiance (secs)
= $0.032 W^{0.5}$ (sec)
- W = radiochemical yield in kilotons (kt)
- \bar{h} = average heat transfer coefficient (cal/cm²/sec/°F)
- G = thermal capacity of material (cal/cm²/°F)
- $K_3 = V_{BR} (k + 2/d)$
- V_{BR} = aircraft radial velocity (kilofeet/sec)
= $\frac{V}{1000} \cos \theta$
- V = aircraft true ground speed (feet/sec)
- θ = angle between line from explosion to airplane and horizontal (degrees)
- k = attenuation coefficient per kilofeet (kilofeet⁻¹)
- d = slant range in kilofeet (SR/1000) (kilofeet)

Equation 1.9 was used to check the prediction system used for the simplified calculation of the maximum temperature rise with the measured and calculated temperature time histories.

1.3.3 Gamma Radiation. The gamma radiation was of insignificant magnitude in all the tests participated in by this project. For the positioning calculations the methods as specified in Reference 9 were used.

1.3.4 Shock Wave Effects. The overpressure and shock arrival data for a 1 kt yield were obtained from Reference 9. The scaling for altitude and yield were done by the modified Sachs scaling method as presented in Reference 10. A detailed description of these scaling laws is presented in Appendix A.

1.3.5 Gust Loads. In the preliminary stages of the program, it was not felt that gust loads would be as critical for the structure as the thermal radiation. Calculations had indicated that for high altitude deliveries, structure temperature limits would be reached before structural strength for gusts was exceeded. As a consequence, the airplane was instrumented for the tests primarily as a vehicle for the investigation of thermal effects. At a late stage of the program, in fact, after the first test shot, Cherokee, and prior to the second test shot, Zuni, the Task Group 7.4 Positioning Safety Committee questioned the validity of the blast response predictions. Consequently, it was decided to provide the airplane with as much blast response instrumentation as could be installed on short notice and under the difficult conditions which existed in the field. This instrumentation was necessarily incomplete, but it was hoped that the data would indicate whether the predicted gust response was significantly conservative or unconservative.

Chapter 2

PROCEDURE

2.1 OPERATION

2.1.1 Description of the A3D-1 Airplane. The A3D-1 airplane is a twin engine, swept wing, jet airplane which is intended for use as a high-altitude bomber having relatively long range and high performance. The airplane has an internal bomb bay capable of carrying special weapons. The power plants are Pratt and Whitney J57P-6 engines.

The A3D-1 airplane has a limit load factor of 2.67 at 55,942 pounds. At the weight at shock time, which was approximately 49,000 pounds for each of the tests, the allowable load factor was 3.05 g.

The skin thicknesses on the surfaces of the airplane which are exposed to radiation are listed below. All these skins are 75 ST6AL.

	Skin Thickness (inches)
Landing flap	0.032
Aileron	0.025 and 0.040
Elevator: upper surface	0.016
lower surface	0.025 (These skins are backed by a beaded sheet 0.016 thick which is spot-welded to the outer skin surface.)
Rudder	0.016
Minimum gage for structure (lower surface of fuselage, gear doors, etc.)	0.025

The airplane was painted white on the lower surfaces of the wing, horizontal stabilizer, and fuselage, and gull gray on the sides and top of the fuselage, sides of the vertical, and upper surfaces of the wings and horizontal stabilizer. For two shots, Tewa and Huron, one section of the lower surface of the elevator was painted gull gray and another insignia painted blue in order to obtain higher temperature rises.

The white areas of the standard production airplane are painted with Insignia Gloss White Lacquer, Mil Spec MIL-L-7178, a Mil Spec white paint. However, the white areas of the test airplane used for these tests were painted with a special Sherwin-Williams white paint CA 10023, which laboratory tests showed could withstand a greater temperature rise before charring than the Mil Spec white paint.

2.1.2 Shot Participation. The A3D aircraft (Project 5.8) participated in Shots Cherokee, Zuni, Flathead, Apache, Navajo, Tewa, and Huron. These events were selected for their suitability in providing weapon inputs consistent with the project objectives.

2.1.3 Criteria for Selecting Desired Aircraft Positions. Desired aircraft positions were selected so that if the maximum assumed errors accumulated to place the aircraft nearer the explosion, the effects would not exceed a 400F temperature rise, gamma radiation of 0.6 rem, overpressure of 1.5 psi, and an increase in load factor due to the gust of 1.5 g based on a rigid body analysis but with a lift curve slope for a flexible wing.

2.1.4 Positioning of Aircraft for Test. The intended and attained position was tail-on in a radial runout at time zero. In all tests except Cherokee the aircraft was flown on a straight and level course directly over ground zero. Although the A3D aborted Shot Cherokee, it had been planned that the basic flight path would be offset 5,000 feet from ground zero with a turn to place the aircraft radial to the explosion.

2.1.5 Systems for Positioning Aircraft. The primary positioning system for the A3D-1 aircraft was the Raydist tracking system. This system was originally planned to provide after-the-fact positioning data only but was modified to compare the actual position against a programmed time position and to present the azimuth and range error to the pilot by ultra-high-frequency (UHF) telemetering to an Instrument Landing System (ILS) indicator in the cockpit. This system provided data in two dimensions, azimuth and range, and the ASB/CP-66 radar bombing system provided accurate absolute altitude. Since the ASB/CP-66 also provided continuous range and bearing to a ground radar reference point, it served as a standby system in the event of a Raydist failure. During the test operation, when Shots Apache and Huron were moved to Eniwetok Atoll, the ASB/CP-66 was the only positioning means available since the Raydist transmitting stations could not be used for this site because of the orientation of the reference lines of the transmitting stations.

2.2 INSTRUMENTATION

The instrumentation installed in the A3D-1 aircraft to record weapon effects and aircraft response is summarized in this section.

2.2.1 Scope of Instrumentation. Thermocouples were installed to measure the temperature of various critical aircraft surfaces and of several test specimens of structural materials. The amount of aerodynamic cooling in thin skins of the elevator and lower fuselage was investigated by comparison of the temperature readings of quartz covered thermocouples with those of uncovered thermocouples at the same location. A sketch showing the thermocouple locations is shown in Figure 2.1.

Radiometers and calorimeters were installed to point directly at the explosion and vertically downward to provide information on the direct and indirect irradiance and radiant exposure and some information of the spectral distribution.

Calorimeters were also installed in the cockpit to measure the scattered-in radiation in the crew's compartment.

Two gun sight aiming point (GSAP) cameras pointed directly at the explosion to check the orientation of the direct calorimeters. Two GSAP cameras pointed vertically downward photographing the cloud cover and terrain beneath the aircraft.

An overpressure pickup was installed on a boom to measure free stream overpressure at time of shock arrival. Two additional pressure pickups were installed on the sides of the fuselage to supplement the overpressure data by measurement of the pressures on the fuselage skin panels.

Instrumentation for measuring engine data was installed to determine effects of shock wave passage on engine operation. This instrumentation included installations necessary to measure engine temperatures and pressures, compressor rotor speeds, bleed valve position, and fuel control operation.

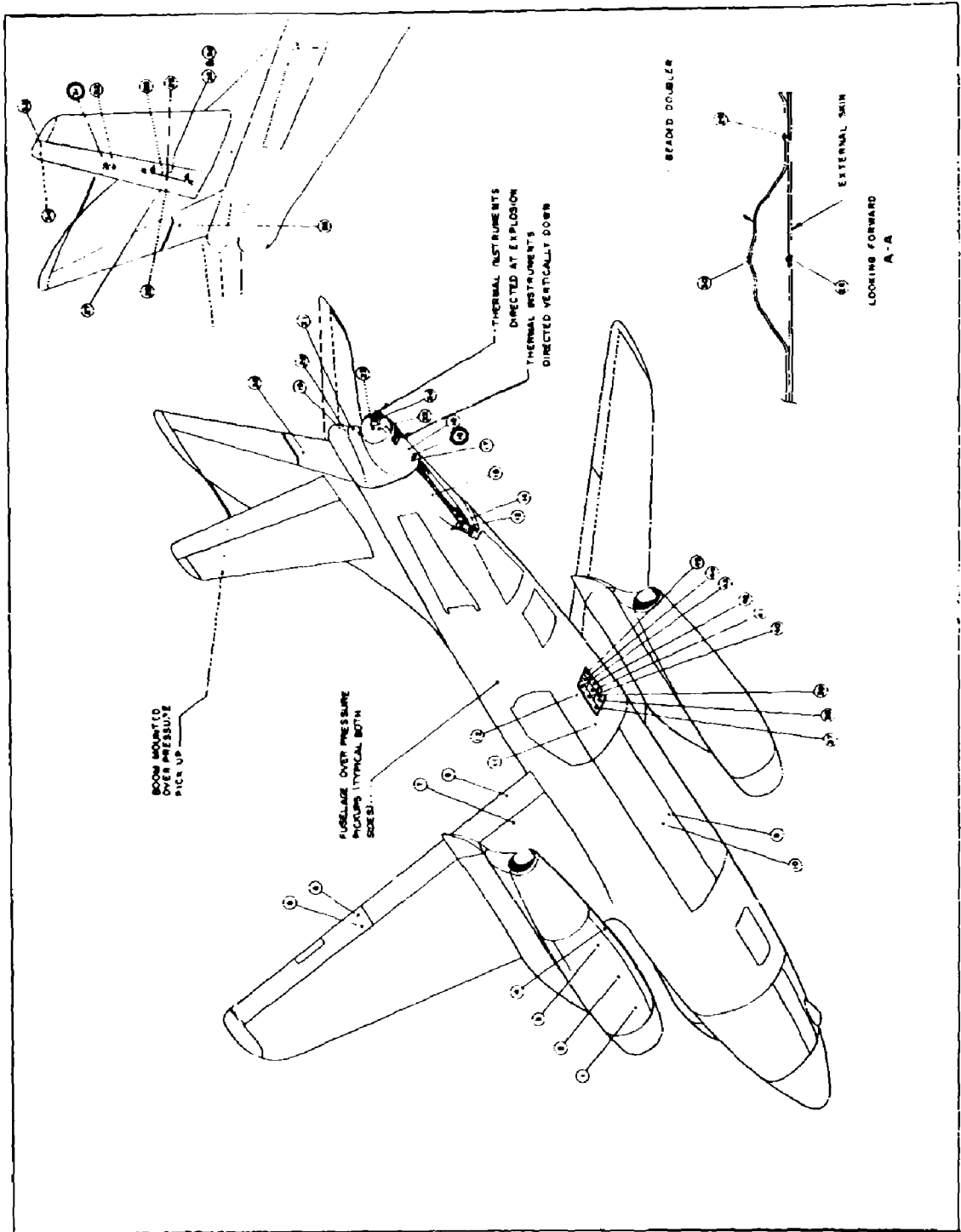


Figure 2.1 Instrumentation locations. (See Table C.1, for key to installation.)

Special instrumentation was installed to measure such items as time of explosion, control surface position, airspeed, altitude, and amount of nuclear radiation.

All recording instruments were equipped with synchronized counters. Oscillographs recorded time of explosion by means of one of the channels connected to a photo cell. Correlation of counter number, timing lines, and a 50 cycle timing trace on the oscillograph paper gave accurate timing on any record, or between records.

Originally the measurements of the aircraft response to the gust were limited to the center of gravity load factor, the aircraft pitch angle, and the pitch velocity. The instruments used were vertical accelerometers, an aircraft attitude gyro, and a pitch rate gyro. However, as the tests progressed it was desired to obtain as much additional information as possible. Therefore, strain gages were installed at the wing root and at the fold joint to provide some indication of the wing bending response. A list of the gust response instrumentation and its availability for each test shot appears in Table 2.1.

TABLE 2.1 GUST INSTRUMENTATION AVAILABILITY

Shot	Zuni	Flathead	Apache	Navajo	Tewa	Huron
C.G. Vertical Accelerometer	X	X	X	X	X	X
Pitch Rate	X	X	X	X	X	X
Center Section Vertical Accelerometer					X	
Strain Gage L.H. Center Section			X	X	X	X
Strain Gage R.H. Center Section			X	X	X	X
Strain Gage R.H. Front Spar Fold Joint					X	X
Strain Gage R.H. Rear Spar Fold Joint					X	X

Since no laboratory calibration of the wing strain gages was possible, it was necessary to rely upon steady-state air calibrations for correlation of strain gage response with wing bending moment. To accomplish this, steady-state symmetrical maneuvers were executed while simultaneously recording strain gage response and center of gravity load factor. From these data the strain gage response per unit of center of gravity acceleration was determined.

A detailed description of the instrumentation is presented in Appendix C.

2.2.2 Oscillograph Recorded Data. The following data were recorded on a total of two 36-channel and two 12-channel oscillographs. The paper traveled through the oscillographs at a speed of 10 in/sec.

- Time zero (t_0), determined by a photoelectric cell.
- Skin and structural temperatures and temperature rise (ΔT), measured by conventional thermocouple techniques.
- Thermal irradiance (I) and radiant exposure (Q), measured by radiometers and calorimeters furnished by the Naval Radiological Defense Laboratories (NRDL).
- Free stream overpressure (ΔP), measured by a pressure pickup mounted on a boom well forward of the vertical fin. Two static pressure taps were also installed on either side of the fuselage.
- Acceleration of center of gravity and tail, measured by accelerometers in the vertical plane.
- Structural strain, measured by strain gages.
- Aircraft pitch rate and attitude, measured by aircraft gyros.
- Engine temperatures and pressures, measured by thermocouples and pressure transducers.
- Stabilizer, elevator, and rudder positions, measured by selsyn type instruments.

2.2.3 Data Recorded on Photo Recorder. The following data in the photo recorder were presented on visual indicating instruments and photographed by a 35 mm camera:

- a. Airspeed
- b. Altitude
- c. Outside air temperature
- d. Stabilizer, elevator, and rudder positions
- e. Engine turbine speeds, N_1 and N_2
- f. Normal acceleration
- g. Engine inboard and outboard bleed valve position
- h. Attitude (pitch)

2.2.4 Method of Instrumentation Operation. All instruments were checked and calibrated prior to each shot. For the actual test the instrumentation was started at the time count 5 seconds prior to time zero. Data were continuously recorded until approximately 50 seconds after shock arrival. The oscillographs were automatically calibrated when the instrumentation was turned on and off by introducing known resistances into the circuits of all the galvanometers.

Chapter 3

RESULTS AND DISCUSSION OF SHOT PARTICIPATION, AIRCRAFT POSITIONS, AND FLIGHT ENVIRONMENTAL DATA

The results of Project 5.8 test participation are presented in this and the following chapters. Chapters are organized to include data for a particular effect from representative shots. Because of the interdependence of the various parts of the data, such as the thermal input and temperature time history, the discussion of each phase immediately follows the presentations of results. This is done to maintain a logical progression and understanding of the interdependent factors. Where data have been of insufficient magnitude to justify logical conclusions it has not been included in the main body of the report. These omitted data are presented in Appendix D, in the event they may be useful to other projects combining data from all weapon test reports.

3.1 SHOT PARTICIPATION

Table 3.1 is a summary of the test events in which the A3D-1 airplane participated.

TABLE 3.1 SUMMARY OF EVENT PARTICIPATION

Event	Yield*	Date	Time†	Type	Location
Cherokee	3.8 Mt	21 May 1956	05:50:38	Airburst 4320 ± 150	Bikini (Able)
Zuni	3.5 Mt	28 May 1956	05:56:00	Surface	Bikini (Tare)
Flathead	380 kt	12 June 1956	06:26:00	Barge	Bikini (Off Dog)
Apache	1.9 Mt	9 July 1956	06:06:00	Barge	Eniwetok (Off Flora)
Navajo	4.8 Mt	11 July 1956	05:56:00	Barge	Bikini (Off Dog)
Tewa	5.0 Mt	21 July 1956	05:46:00	Barge	Bikini (Off Dog)
Huron	270 kt	22 July 1956	06:16:00	Barge	Eniwetok (Off Flora)

*Naval Air Special Weapons Facility (NASWF) letter Serial No. 00173 dated Nov. 23, 1956. This reference quoted the yields from FC/AFSWP Secret R.D. letter Serial FCWTI 972.5 of 13 Nov. 1956. Yields are said to be accurate within ± 5 percent.

†Approximate local time.

3.2 AIRCRAFT POSITIONS AND FLIGHT ENVIRONMENTAL DATA

In understanding the level of the data obtained in these tests it must be appreciated that several factors can reduce the magnitude of the effects received. Test aircraft positions for a desired response level must be selected for a detonation of magnitude equal to the positioning

yield, a magnitude that may be substantially greater than the predicted or actual yield. In addition, the test position must consider the maximum positioning errors possible. In actual test the yield variations and positioning errors may so combine, that the effects magnitudes are low indeed. The planned and actual test conditions are presented in Table 3.2.

It will be noted that in all cases the actual yield was lower than the one required for positioning, also that with the exception of Shots Flathead, Navajo, and Tewa, the horizontal distances were greater than planned. For these reasons the observed data were of a much lower magnitude than anticipated.

Tables 3.3 and 3.4 present the flight and environmental parameters which were significant for the data analysis at the time of explosion and for the time of shock arrival, respectively.

3.2.1 Accuracy of Aircraft Position. For Shots Zuni, Flathead, Navajo, and Tewa the horizontal distances were determined by Raydist and the altitudes by the aircraft ASB bombing equipment. The distances were reported by Raydist to be accurate to approximately ± 50 feet; the radar altitudes were probably accurate to ± 50 feet.

Because of a Raydist failure, no data were available for Shot Cherokee. Therefore the positions were estimated with the ASB radar ranging. The Shot Cherokee position data were of unknown accuracy, as the horizontal distance at the time of explosion was not obtained by the aircraft crew because of temporary flash blindness. The distance estimate was obtained from a radar range made at an estimated time after the explosion and reduced back to time zero by calculation from the aircraft speed. Shots Apache and Huron occurred at Eniwetok Atoll and the Raydist equipment was not available for positioning or tracking. Therefore distances were obtained using the ASB equipment. For Shot Apache the measurement of the horizontal distance was probably accurate within ± 1000 feet and the altitude within ± 50 feet. For Shot Huron the horizontal distance was of unknown accuracy because there was insufficient time after passing over ground zero to rotate the periscope sight and positively relocate the target.

3.2.2 Comments on Positioning Methods. Raydist failures occurred on two of the test shots, Cherokee and Zuni. On Shot Cherokee this was because of a power failure at one of the transmitting stations; on Zuni the difficulty was a blown fuse in the control van aboard the USS *Baudoeng Strait*. This was corrected approximately 6 seconds before shot time, so that positioning data at time of explosion and shock arrival were available.

For Shots Flathead, Navajo, and Tewa the Raydist positioning system provided excellent aircraft positions.

The ASB radar positioning system did not prove capable of positioning the test aircraft to within ± 2000 feet. Based on the difference between actual and planned positions in Zuni (+5600 feet) and Apache (+4600 feet) it would appear that no better than ± 5000 -foot accuracy could be predicted for the ASB/CP 66 system as aircraft track-time programming equipment in its present configuration. This inaccuracy, of course, had no bearing on the accuracy or adequacy of the ASB/CP 66 system for measuring range or functioning as designed. The major difficulty in the system was in the necessity for hand calculation of time-late, or time-early, during the run-in, by visual reference to a rapidly changing range dial. The large range errors of Shots Apache and Zuni may be attributed partly to a natural psychological reaction of the crew to err on the conservative side.

Although it did not fulfill the desired positioning accuracy, the ASB radar system was extremely useful as a backup system and permitted participation in Shots Cherokee and Zuni when Raydist failures occurred. Participation on Shots Apache and Huron, planned originally for Bikini but changed to Eniwetok, required use of ASB as the primary positioning system.

It is believed that if the reliability of the Raydist system could be improved, it would provide an excellent aircraft positioning system. A detailed evaluation of the Raydist equipment and of the radar bombing systems for the test aircraft positioning is reported in References 13 and 20.

TABLE 3.2 COMPARISON OF PLANNED AND ACTUAL YIELDS AND POSITIONS

Event	Cherokee	Zuni	Flathead	Apache	Navajo	Tewa	Huron
Yield							
Positioning	6.0 Mt	5.0 Mt	760 kt	5 Mt	10 Mt	15 Mt	300 kt
Actual	3.8 Mt	3.5 Mt	380 kt	1.90 Mt	4.8 Mt	5.0 Mt	270 kt
Aircraft positions							
At explosion (t_0)							
Horizontal distance (ft)							
Planned	33,000	26,400	12,800	21,400	27,400	29,800	12,800
Actual	57,500*	32,060	12,740	26,000†	28,170	30,000	16,800‡
Absolute altitude (ft)							
Planned	34,000	28,000	14,000	26,000	36,000	36,500	12,000
Actual	34,100	28,170	14,050	26,000	36,100	36,316	12,050
At shock arrival							
Horizontal distance (ft)							
Planned	91,200	72,000	34,400	55,500	69,500	80,200	37,100
Actual	190,000*	96,470	32,930	81,500†	79,670	96,700	48,000‡
Absolute altitude (ft)							
Planned	34,000	28,000	14,000	26,000	36,000	36,500	12,000
Actual	34,100	27,900	14,050	26,500	36,000	35,900	12,050
Time of shock arrival (sec)							
Planned	72.8	57.0	27.0	42.6	52.6	63.0	30.3
Actual	176	81.56	27.18	67.86	68.26	80.87	39.03
Aircraft true heading (deg)							
At explosion							
Planned	132	071	124	276	124	124	276
Actual	222	071	124	276	124	117	286
At shock arrival							
Planned	132	071	124	276	124	124	276
Actual	--	071	124	276	124	117	286
Aircraft true bearing to Ground zero (deg)							
At explosion							
Planned	132	071	124	276	124	124	276
Actual	222	070.5	122.5	277	116.5	114	287
At shock arrival							
Planned	132	071	124	276	124	124	276
Actual	--	068.5	122.5	277	117	114	286

*These distances are approximate as they are based on calculation and ASB/CP-86 observations at times other than the explosion. This was necessitated by Raydist failure, and the fact that the abort flight path was used due to early bomb release. These values are quoted but are not used in the analysis of the test results. See paragraph 3.2.1.

†These distances are of questionable accuracy as they are based on ASB measurements, rather than Raydist. See paragraph 3.2.1.

‡Distances are approximate, being based on ASB observations which are of questionable accuracy due to poor target resolution. See paragraph 3.2.1.

TABLE 3.3 FLIGHT AND ENVIRONMENTAL PARAMETERS AT TIME OF EXPLOSION

Event	Cherokee	Zuni	Flathead	Apache	Navajo	Tewa	Huron
Yield (kilotons)	3800	3500	380	1900	4800	5000	270
Absolute altitude (feet)	34,100	28,170	14,050	26,000	36,100	36,310	12,050
Horizontal distance (feet)	57,500*	32,060	12,740	26,000†	28,170	30,000	16,800‡
Burst height (feet)	4320	0	0	0	0	0	0
Slant range (feet)	64,750*	42,680	18,570	36,770†	44,590	47,100	20,680‡
True airspeed (knots)	495	486	456	484	457	454	446
True airspeed (ft/sec)	836	820	771	817	772	767	753
Pressure altitude (feet)	30,850	26,080	13,040	24,000	33,570	34,200	11,300
Ambient pressure (psi)	4.19	5.20	9.97	5.70	3.70	3.59	9.60
Ambient air temperature (°R)	434	463	504	467	427	421	508
Wind speed (knots)	21	14	15	08	06	07	19
Wind direction (degrees)	220	160	80	260	210	300	80
Ground speed (ft/sec)	801	821	753	804	772	755	782
Airplane weight (lb)	48,500	47,470	47,870	48,570	48,670	47,230	45,640
Lift coefficient	0.2205	0.1919	0.1385	0.1819	0.2885	0.2875	0.1308
Mach number	0.818	0.759	0.700	0.771	0.761	0.761	0.680
Angle of attack (degrees, FRL§)	-0.3	-0.5	-1.0	-0.6	+0.6	+0.4	-0.9
Stabilizer angle¶ (degrees)	+4.2	+0.8	+1.67	+1.35	+0.58	+0.1	+0.09
Elevator angle** (degrees)	-5.5	-2.2	-3.3	-3.6	-0.80	-3.0	-2.1

*These distances are approximate as they are based on calculation and ASB/CP-66 observations at times other than the explosion. This was necessitated by Raydist failure, and the fact that the abort flight path was used due to early bomb release. These values are quoted but are not used in the analysis of the test results. See paragraph 3.2.1.

†These distances are of questionable accuracy as they are based on ASB measurements, rather than Raydist. See paragraph 3.2.1.

‡Distances are approximate, being based on ASB observations which are of questionable accuracy due to poor target resolution. See paragraph 3.2.1.

§FRL is Fuselage Reference Line.

¶Plus sign indicates stabilizer has positive angle of attack (leading edge up) relative to fuselage reference line.

**Minus sign indicates elevator has negative angle of attack (leading edge down) relative to stabilizer.

TABLE 3.4 FLIGHT AND ENVIRONMENTAL PARAMETERS AT TIME OF SHOCK ARRIVAL

Event	Cherokee	Zuni	Flathead	Apache	Navajo	Tewa	Huron
Time of shock arrival (sec)	176	81.56	27.18	67.86	68.26	80.87	39.03
Absolute altitude (feet)	34,100	27,900	14,050	25,500	36,000	35,900	12,050
Horizontal distance (feet)	190,000	96,470	32,440	81,500	79,670	96,700	48,000
Slant range (feet)	192,320*	100,430	35,350	85,400†	87,420	103,150	49,490‡
True airspeed (knots)	479	463	462	480	453	455	466
True airspeed (ft/sec)	809	782	780	811	765	769	787
Pressure altitude (feet)	31,530	25,600	12,990	24,060	33,540	34,340	11,235
Ambient pressure (psi)	4.070	5.312	8.990	5.681	3.706	3.569	9.631
Ambient air temperature (°R)	434	462	506	467	429	424	508
Ambient air density (slugs/ft ³)	0.787×10^{-3}	0.965×10^{-3}	1.49×10^{-3}	1.020×10^{-3}	0.725×10^{-3}	0.706×10^{-3}	1.59×10^{-3}
Ambient speed of sound at airplane altitude (ft/sec)	1021.2	1053.7	1102.7	1059.3	1015.3	1009.4	1104.9
Airplane weight (lb)	48,520	47,470	47,870	48,570	48,670	47,230	45,640
Lift coefficient	0.243	0.207	0.136	0.186	0.296	0.291	0.119
Mach number	0.790	0.743	0.706	0.769	0.754	0.762	0.712
Angle of attack (degrees, FRL§)	-0.05	-0.35	-1.0	-0.50	+0.60	+0.55	-1.25
Stabilizer angle¶ (degrees)	+2.0	+0.6	+1.68	+1.31	+0.50	+1.0	+0.9
Elevator angle** (degrees)	-2.25	-2.6	-3.8	-3.9	-1.1	-4.3	-2.1

*These distances are very approximate as they are based on calculation and ASB/CP-66 observations at times other than the explosion. This was necessitated by Raydist failure, and the fact that the abort flight path was used due to early bomb release. These values are quoted but are not used in the analysis of the test results. See paragraph 3.2.1.

†These distances are of questionable accuracy as they are based on ASB measurements, rather than Raydist. See paragraph 3.2.1.

‡Distances are approximate, being based on ASB observations which are of questionable accuracy due to poor target resolution. See paragraph 3.2.1.

§FRL is Fuselage Reference Line.

¶Plus sign indicates stabilizer has positive angle of attack (leading edge up) relative to fuselage reference line.

**Minus sign indicates elevator has negative angle of attack (leading edge down) relative to stabilizer.

Chapter 4

RESULTS AND DISCUSSION OF THERMAL INPUT DATA

Results of thermal quantities as measured by radiometers and calorimeters are presented in this section. Radiometers measured the rate of energy received as a function of time (irradiance), and calorimeters gave the total thermal energy (radiant exposure) received with time.

In order to show the fields of view of the various instruments, diagrams are presented for each shot showing the geometrical relationship of the fields of view to the fireball for both the direct and indirect instruments. These are especially useful in obtaining an understanding of the data from the indirect measurements with a 90-degree field of view. For example, in Shot Zuni it illustrates that the indirect radiometer with a 90-degree field of view never actually saw the fireball; the energy recorded by this instrument would be low compared to the amount received by an instrument with a 160-degree field of view, or a horizontal aircraft skin structure which would receive energy from 2π steradians. Therefore, on some of the radiometer results it will be noted that irradiance values have been estimated by differentiating the radiant exposure data measured by the calorimeters.

Three types of filters were used on the instruments, quartz, Corning 2-58, and Corning 5-76. Where the Corning filters were used this was noted on the data. Because of the inconsistency of some calorimeter readings, no attempt has been made in this report to determine the broad band spectral distribution of the thermal energy.

The basic thermal data are presented for certain representative shots. Sufficient data are shown to justify the conclusions of this report. A detailed discussion of the results of Shots Flathead, Zuni, and Tewa is included in this section. Data which merely substantiated the material presented are omitted from this section and are presented in Appendix D. Table 4.1 presents the maximum values of irradiance and radiant exposure recorded for all the shots.

4.1 SCATTERED RADIATION

Two calorimeters were installed in the cockpit of the airplane to measure the scattered radiation. One was pointed directly forward and the other was pointed out the left side of the cockpit. Since the instruments were inside the cockpit, they were behind the Plexiglas. Neither of these instruments detected any measurable trace of scattered thermal energy. This was somewhat surprising in view of the amount of the bomb light that was scattered into the cockpit area.

Instruments were checked prior to each test and appeared to be functioning properly.

The sensitivity of the instruments in the cockpit to measure the scattered radiation was increased as the tests progressed. For the first shot, Cherokee, these instruments had approximately three times the sensitivity of the direct and indirect instruments. For Shot Tewa the sensitivity was 100 times as great as the direct and indirect instruments.

TABLE 4.1 MAXIMUM MEASURED IRRADIANCE AND RADIANT EXPOSURE

Shot	Time to maximum irradiance	Maximum irradiance*		Radiant exposure*	
		Direct	Indirect	Direct	Indirect
	seconds	cal/cm ² /sec	cal/cm ² /sec	cal/cm ²	cal/cm ²
Flathead	0.68	9.85	7.24	14.0 - 14.6	9.9
Zuni	1.8	6.44	4.16†	23.7	14.0
Tewa	2.05	6.25‡	4.70‡	23.0	16.1
Cherokee§	1.5	3.4	--	14.3 - 15.1	6.4 - 7.0
Apache§	1.5†	5.85¶	4.05¶ - 4.70**	16.4	11.9
Navajo§	2.6†	5.76¶	4.55**	24.5	18.3
Huron§	0.60	5.50	--	6.7	3.9

*Values are correct for filter factors, but not for aircraft flyaway.

†Estimated from direct irradiance.

‡Estimated from radiant exposure data.

§Data from these shots are of questionable reliability, see paragraph 4.3.

¶Estimated from direct calorimeter.

**Estimated from indirect calorimeter.

During these tests the airplane was flying in clear air during all the thermal pulses. Therefore, although these data indicate that there was no scattered radiation, it cannot be assumed that all atmospheres are zero-scattering.

4.2 REFLECTED ENERGY FROM TERRAIN SURFACE

Analysis of portions of the film taken of the fireball from the direct camera station and the radiometer data indicated that in the time of interest of the thermal pulse, albedo, or reflectance quality, of the ocean surface was low. Individual frames from the film are shown in Figures 4.1 to 4.3.

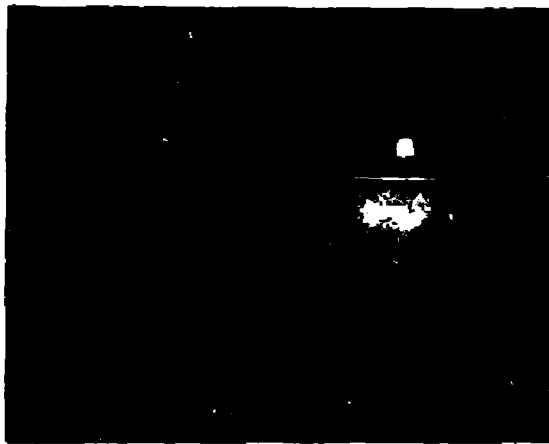
These films show the albedo was low until the water became frothed by the passage of the shock wave and at the time of maximum irradiance the area outside the fireball which had been frothed by the shock wave was quite small.

To present an indication of the possible magnitude of the surface reflection, the vertical component of the reflected energy has been estimated for Tewa based on study of the fireball photographs (Figure 4.1). The results of this analysis show that the incremental area included in the total diameter of the shock frothed water contributes approximately 75 percent of the reflection from the infinite field. Of this area the fireball covers the portion which contributes approximately 41 percent. Therefore of the reflectance computed for the infinite plane, 41 percent is shadowed by the fireball, 34 percent is from shock frothed water, and the remaining 25 percent is from the undisturbed ocean surface.

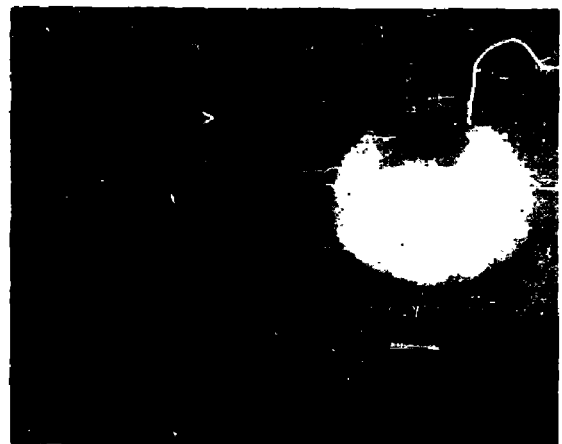
The ratio of the vertical component of the reflected energy to the direct, as determined from Reference 4 at the airplane position in Shot Tewa, is approximately 0.31 for a 100 percent reflection diffuse surface. Therefore if values for the surface albedo of 0.4 for the shock frothed water and 0.1 for the undisturbed ocean surface (Reference 14) are used, the total reflected energy can be estimated as:

$$\begin{aligned}
 \text{Area covered by fireball} &= 0 \times 41 \text{ percent} \times 0.31 = 0 \\
 \text{Shock frothed area} &= 0.4 \times 34 \text{ percent} \times 0.31 = 0.042 \\
 \text{Undisturbed ocean area} &= 0.1 \times 25 \text{ percent} \times 0.31 = 0.008 \\
 \text{Total reflected energy} &= 0.05 \text{ (5 percent) of direct}
 \end{aligned}$$

This case for Shot Tewa has the longest time to maximum irradiance so the effect on other shots with shorter times will be less than the 5 percent. From Figure 4.2 it is obvious that the shock frothed area for Shot Flathead is much smaller than for Shot Tewa.



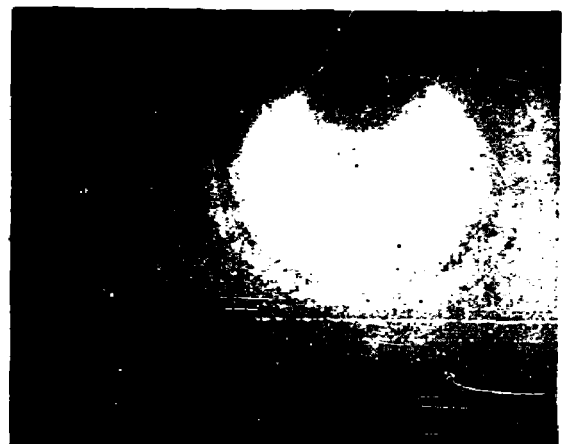
$t = 0.5$ SECONDS



$t = 1.5$ SECONDS

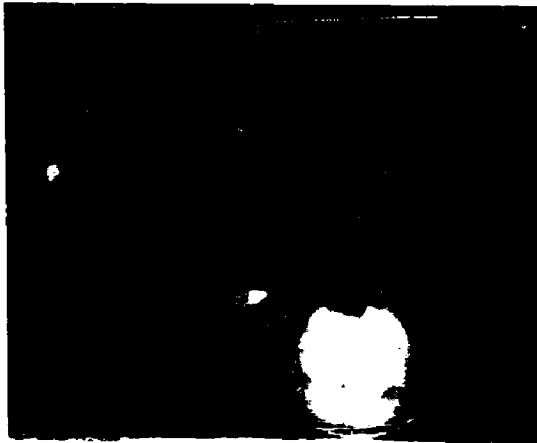


MAXIMUM IRRADIANCE
 $t = 2.25$ SECONDS

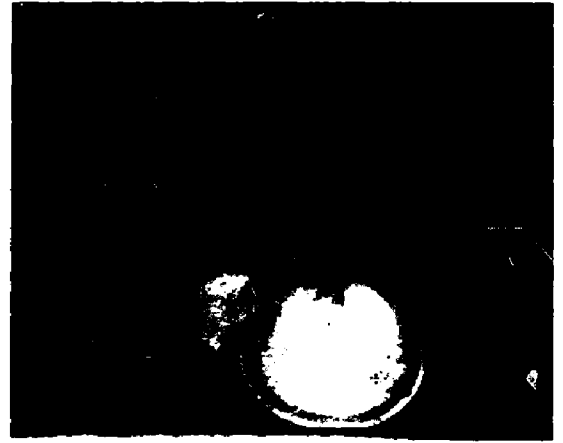


$t = 5.0$ SECONDS

Figure 4.1 Fireball and reflection area at various times, Shot Tewa.



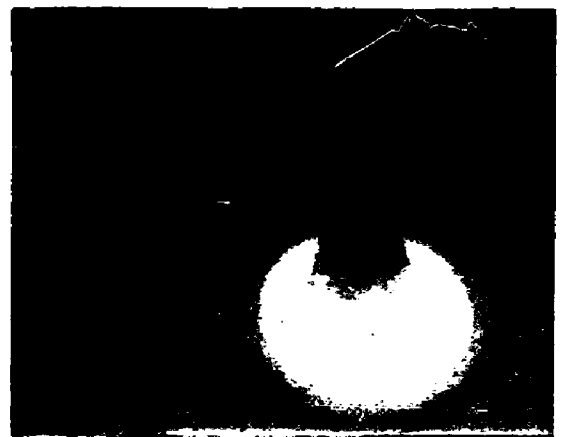
$t = 0.5$ SECONDS



MAXIMUM IRRADIANCE
 $t = 0.65$ SECONDS

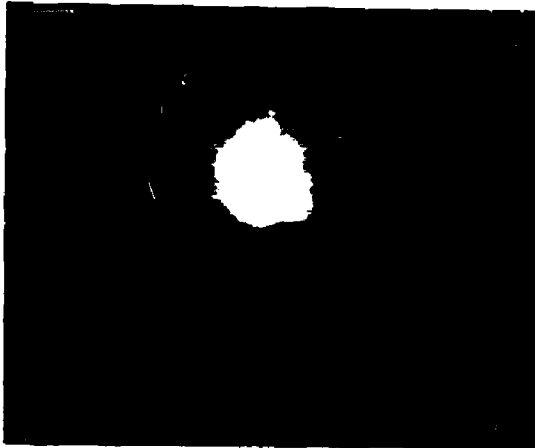


$t = 1.0$ SECONDS

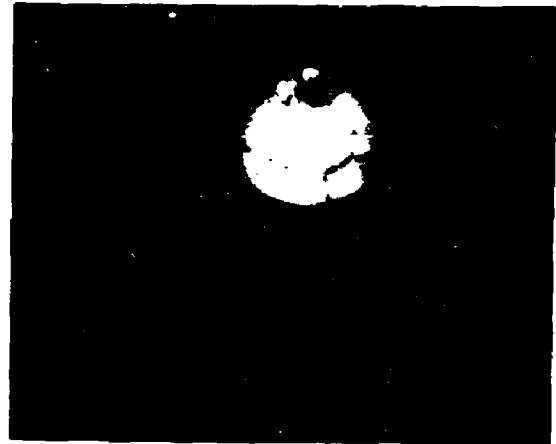


$t = 4.0$ SECONDS

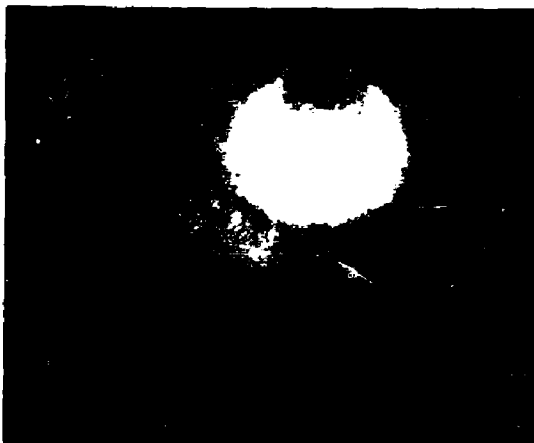
Figure 4.2 Fireball and reflection area at various times, Shot Flathead.



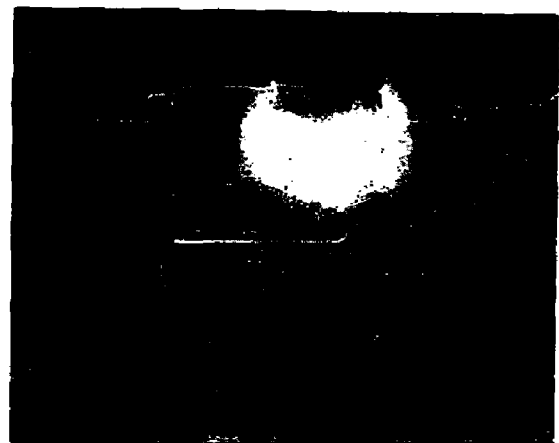
$t=0.625$ SECONDS



MAXIMUM IRRADIANCE
 $t=1.4$ SECONDS



$t=2.0$ SECONDS



$t=4.0$ SECONDS

Figure 4.3 Fireball and reflection area at various times, Shot Apache.

For this reason the reflected energy has been assumed as negligible in the analysis of the data from these tests. Neglecting the reflection component in this analysis has only a minor effect on the computed thermal field inputs. As discussed later in the report, the pertinent comparisons require the assumption of an attenuation coefficient, and neglecting the reflected component results in the calculation of an attenuation coefficient at the time of maximum irradiance slightly lower than would be calculated if the reflected component were included in the direct. The reduction in the attenuation would be such that it made up for the neglected 5 percent of irradiance received. For example, the calculated attenuation for Shot Tewa would be 0.0085 if the reflection were neglected and 0.0086 if the 5 percent reflected energy were included. It should be stressed that neglecting the reflection would only apply for conditions over water because the reflective qualities of the surface are low until the shock wave has passed over it.

A further justification for considering the reflected energy as negligible is obtained from an analysis of the direct and indirect radiometer measurements obtained from Shot Flathead. (Figures 4.4 and 4.5.) With a surface albedo of 0.4 and the ratio of reflected to direct energy of Reference 4, the reflected energy received by the direct radiometer, which is normal to the explosion, would be approximately 15 percent of the direct. The reflected energy received by the indirect radiometer, which is a receiver horizontal to the terrain surface, would be approximately 11 percent of the direct. Then, if the values measured by the direct radiometer were resolved to give the energy received by the horizontal receiver (the indirect radiometer), they should give values greater than those measured by the indirect radiometer by an amount equal to the resolved portion of the 4 percent difference, or approximately 3 percent. However, as can be seen from Figure 4.6, when the vertical component of the irradiance is obtained by multiplying the direct by the sine of the angle, the values so obtained agree exactly with those obtained from the indirect radiometer.

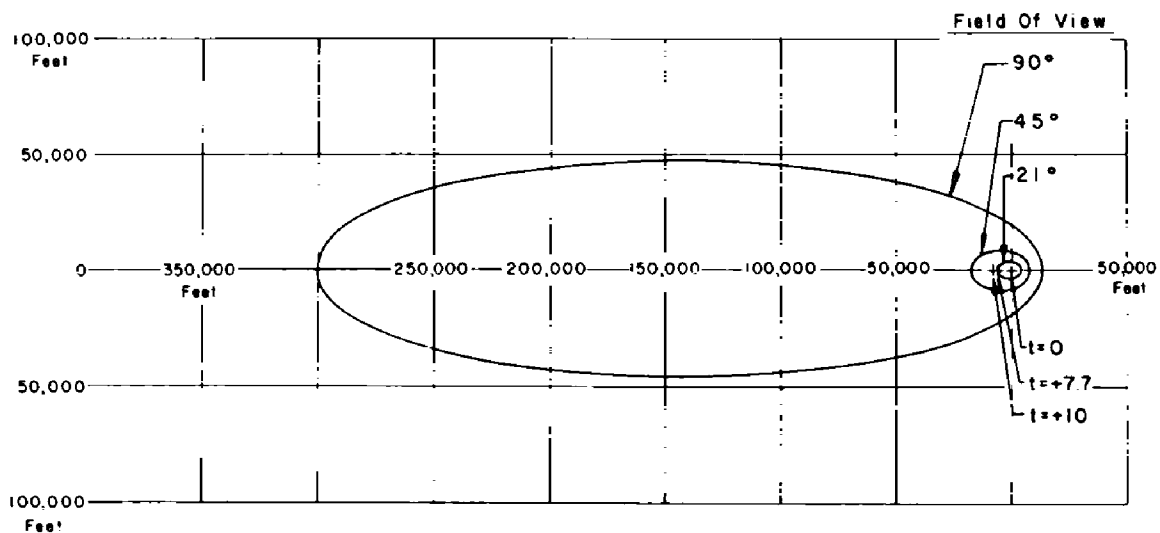
4.3 DISCUSSION OF RADIOMETER AND CALORIMETER MEASUREMENTS

The basic thermal data for Shots Flathead, Zuni, and Tewa (see Figures 4.6 to 4.21) are presented as:

1. Field of view of the instruments
2. Irradiance, from radiometer measurements, versus time
3. Direct thermal radiant exposure, measured by fireball line of sight calorimeters, versus time
4. Indirect thermal radiant exposure, measured by vertical view calorimeters, versus time.

In analyzing the radiometer and calorimeter data, it was noted that various discrepancies appeared in the results. For example, the thermal inputs measured by the two 160-degree indirect calorimeters in Shot Zuni differed by approximately 20 percent (Figure 4.13). The thermal inputs measured by the direct calorimeters in Shot Tewa (Figure 4.17) showed that the 90-degree instrument received more energy than the 160-degree instrument. Also, in some cases an integration of the radiometer data did not agree with the corresponding calorimeter, for example, the indirect data of Shot Zuni (Figure 4.13). As discussed in the preceding section, the energy measured by the indirect radiometer should also be close to the vertically resolved component of the direct radiometer for positions where the indirect instrument has the fireball in its field of view.

Because of the above noted discrepancies, great care has been used in the selection of the thermal input pulse used in the calculation of the temperature time history. As near as possible the pulse selected satisfied the following requirement, the direct and indirect radiometers agreed within reasonable limits when resolved by the sine of the angle; and when integrated, the direct and indirect radiometer data should check with observed calorimeters.



Note: + Symbol Indicates Position Of Fireball Relative To Field Of View At Time Noted.

Figure 4.4 Field of view of direct thermal instruments, Shot Flathead.

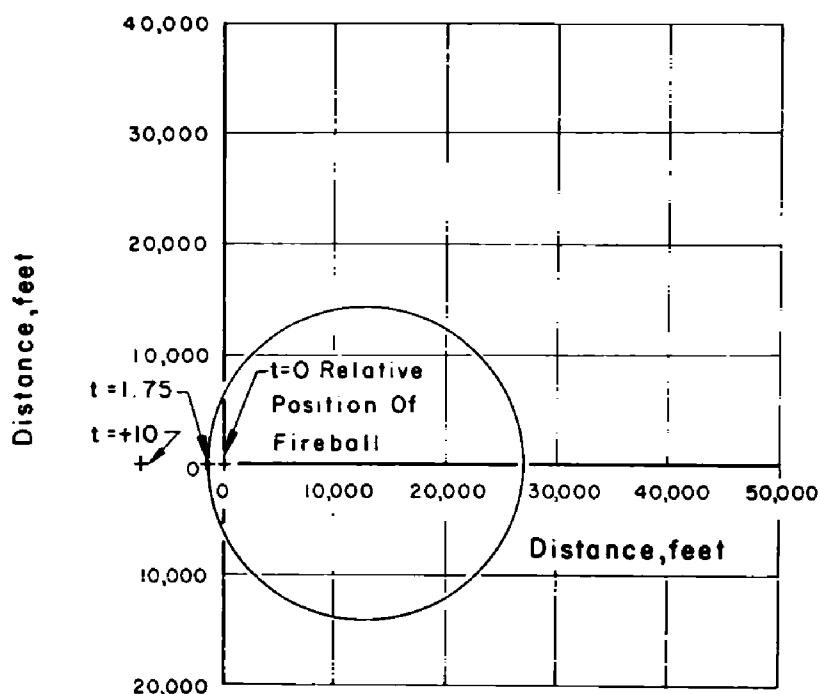


Figure 4.5 Field of view of 90-degree indirect thermal instruments, Shot Flathead.

The radiometer and calorimeter data are presented and discussed in detail in the following sections.

4.3.1 Shot Flathead. The radiometer data are shown in Figure 4.6. Also shown is the indirect irradiance obtained by resolution of the vertical component of the direct irradiance. It will be noted that the agreement between the measured indirect and the resolved direct irradiance is excellent.

When the direct radiometer is integrated it agrees well with the direct calorimeters, and it will be seen that the 160 degree, 90 degree, and 45 degree direct instruments agree well with each other (Figure 4.7). The integration of the measured indirect radiometer does not show as much total energy received as the indirect calorimeters, and there is appreciable discrepancy between the various indirect instruments (Figure 4.8). Integrating the indirect component from the direct radiometer shows closer agreement to the lowest value recorded by the calorimeters. Therefore, in view of the excellent agreement of the direct calorimeters and radiometers, and the agreement of the direct and the integration of the direct and indirect radiometers, the lowest value of the indirect calorimeters (which agrees with the integrated indirect radiometer) is believed to be most logical.

4.3.2 Shot Zuni. A good example of the effect of the fireball being in the field of view is found in analyzing the results of Shot Zuni. Here it is seen that the correlation between the direct instruments is excellent. When integrated, the direct radiometer (Figure 4.11) agrees well with the two 160-degree and the 90-degree direct calorimeters, whose agreement with each other is also excellent (Figure 4.12). However, when the indirect radiometer (Figure 4.11) is integrated it shows much less total energy received than either of the indirect calorimeters (Figure 4.13). An inspection of the location of the fireball relative to the field of view of the 90-degree indirect instrument shown in Figure 4.10 shows that the fireball is always out of the field of view. The direct instruments always see the fireball, except for the 21-degree field, after approximately 7 seconds.

In view of this it is reasonable that the indirect radiometer with the 90-degree field of view would not agree with the 160-degree instrument. Also, for this reason, it would not be suitable for use in determining the thermal input into a horizontal skin surface which receives energy from a 180-degree field. Therefore, to obtain a pulse for this use the vertical component of the direct radiometer was calculated and is shown in Figure 4.11. When it is integrated it agrees well with the lower of the two 160-degree calorimeters. Therefore, this calculated indirect pulse was used for the temperature rise calculations, and the lower of the two calorimeters was taken as the more accurate.

4.3.3 Shot Tewa. Another interesting fact of analyzing the radiometer data occurred in Shot Tewa. The irradiance as measured by the indirect radiometer is shown in Figure 4.16. The direct radiometer is not shown, as it was obviously in error. When integrated it reached a total value nearly double that recorded by the calorimeter, and the maximum irradiance recorded was higher than would be obtained from conservative calculations using thermal yield.

When the indirect radiometer was integrated it fell far below the values measured by the calorimeters, Figure 4.18. Also, when the direct irradiance was calculated from the measured indirect by dividing by the sine of the angle and the resulting pulse integrated, it also fell below the direct calorimeter recorded values.

In this case the low reading of the indirect radiometer could not be explained by the fireball being outside the field of view until approximately 8.3 seconds, and the discrepancy occurred well before this time.

With neither radiometer providing a reasonable time history of the irradiance, it was necessary to estimate the thermal pulse from calorimeter traces. When this was done for the 160-degree indirect calorimeters, the resulting thermal pulse was found to give too much energy when resolved, integrated, and compared with the direct instruments. The next calorimeter to be differentiated was the 160-degree direct instrument RD 230. When vertically resolved and integrated, this estimated irradiance agreed well with the 90-degree indirect calorimeter but

[Text continues on page 48.]

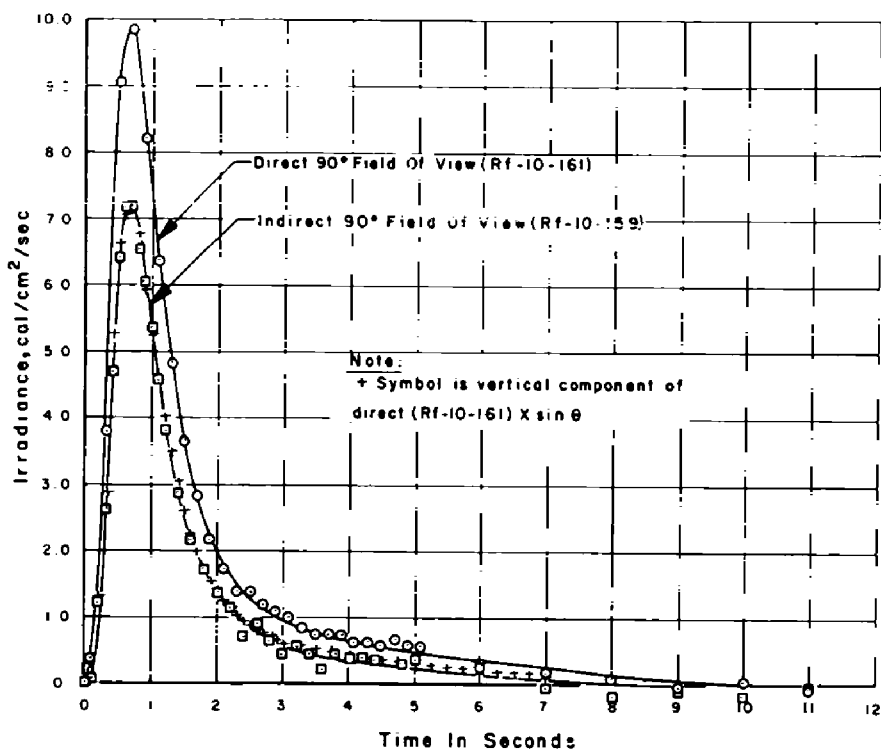


Figure 4.6 Thermal Irradiance as a function of time, Shot Flathead.

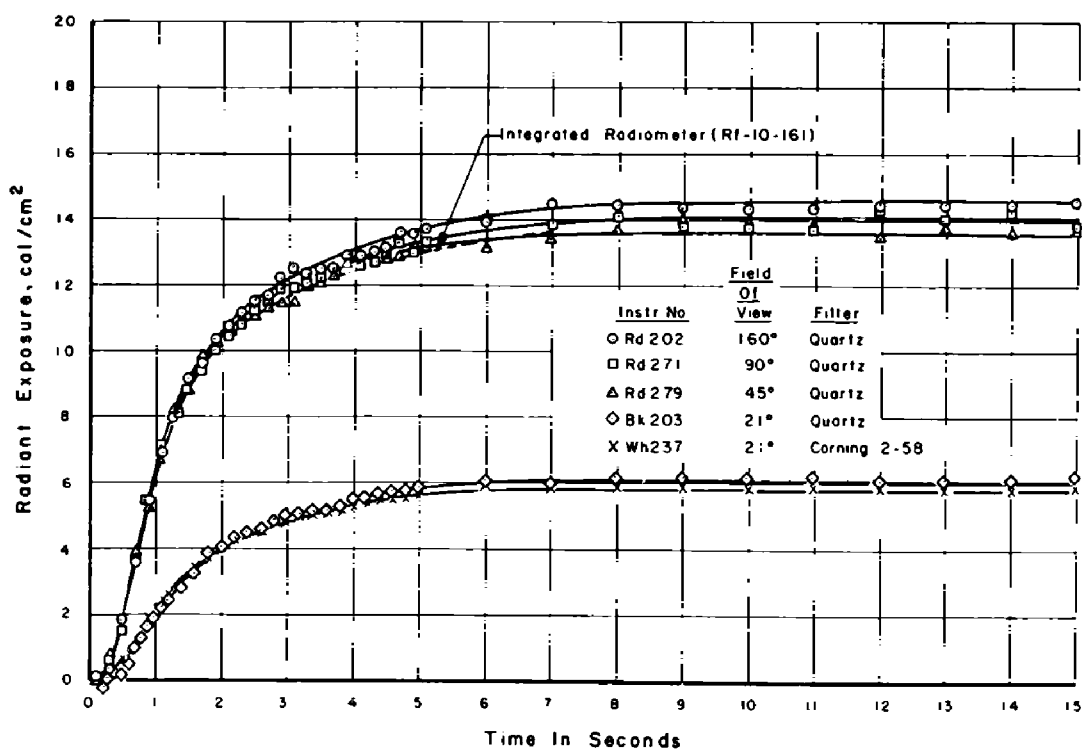


Figure 4.7 Radiant exposure of direct thermal instruments, Shot Flathead.

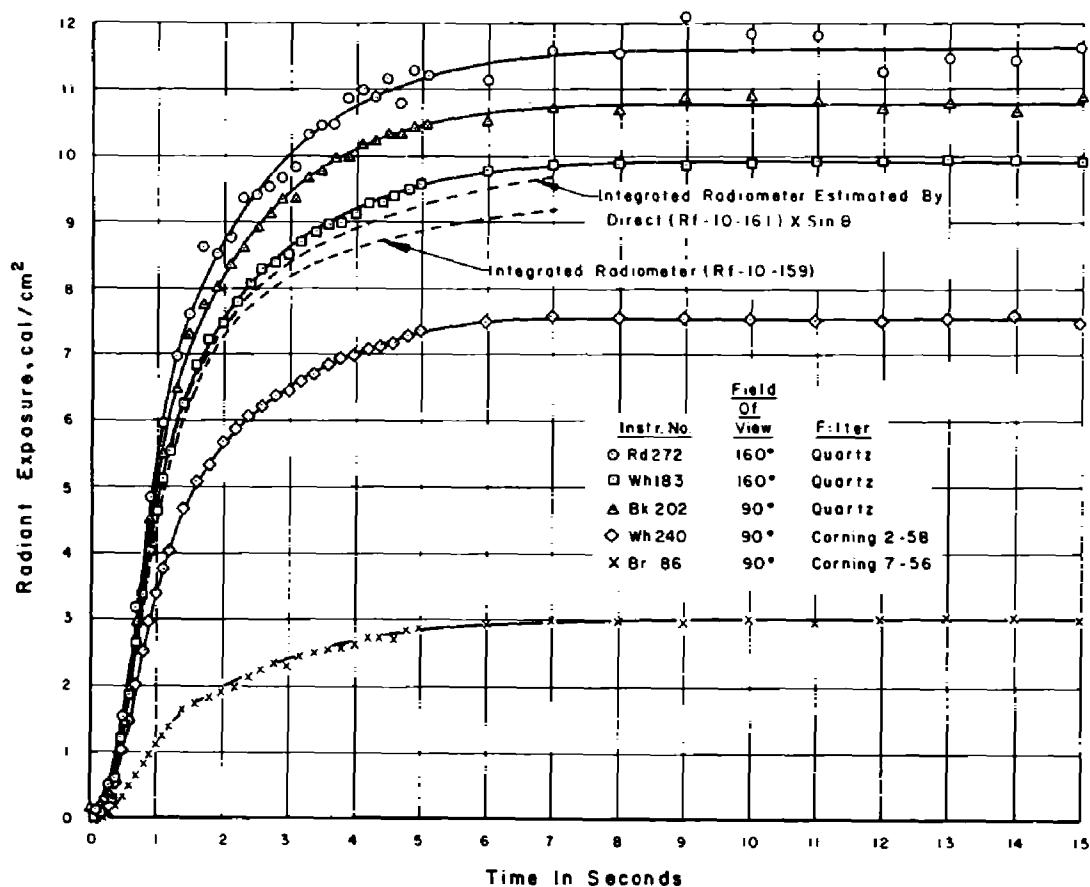


Figure 4.8 Radiant exposure of indirect thermal instruments, Shot Flathead.

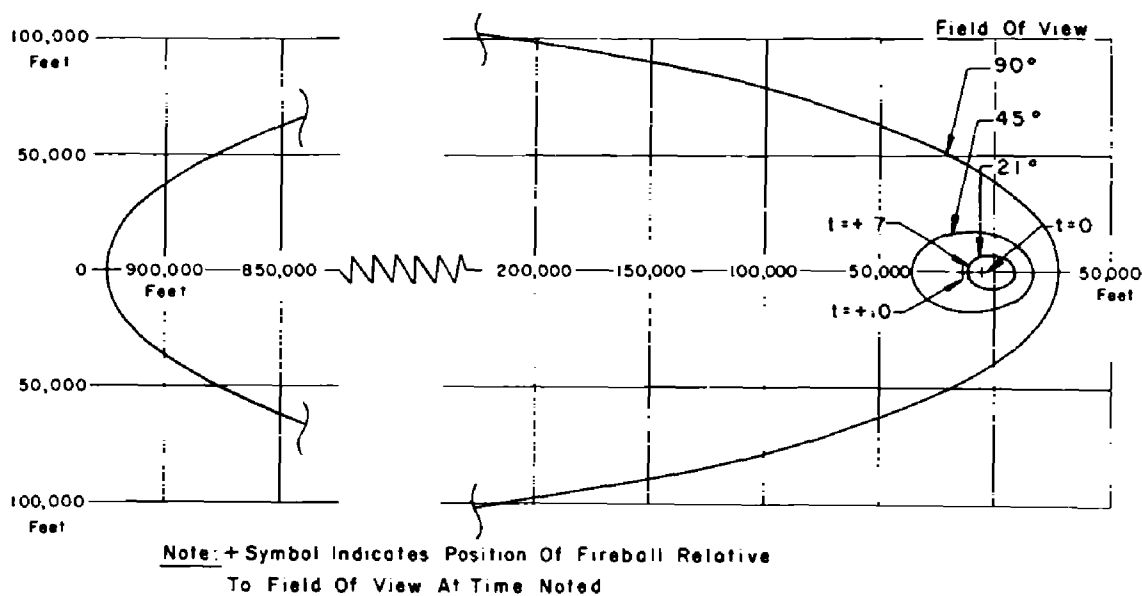


Figure 4.9 Field of view of direct thermal instruments, Shot Zuni.

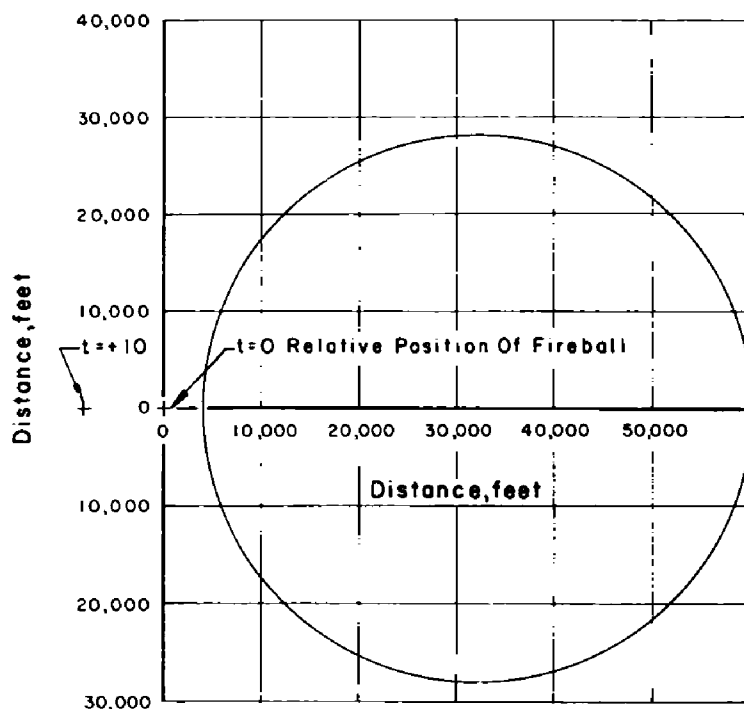


Figure 4.10 Field of view of 90-degree indirect thermal instruments, Shot Zuni.

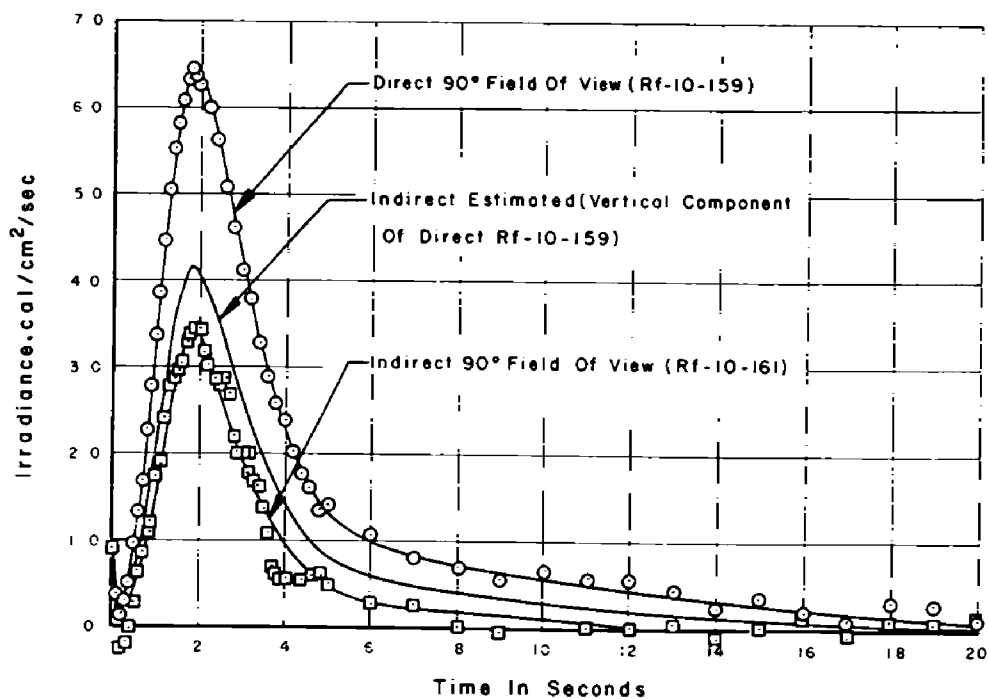


Figure 4.11 Thermal irradiance as a function of time, Shot Zuni.

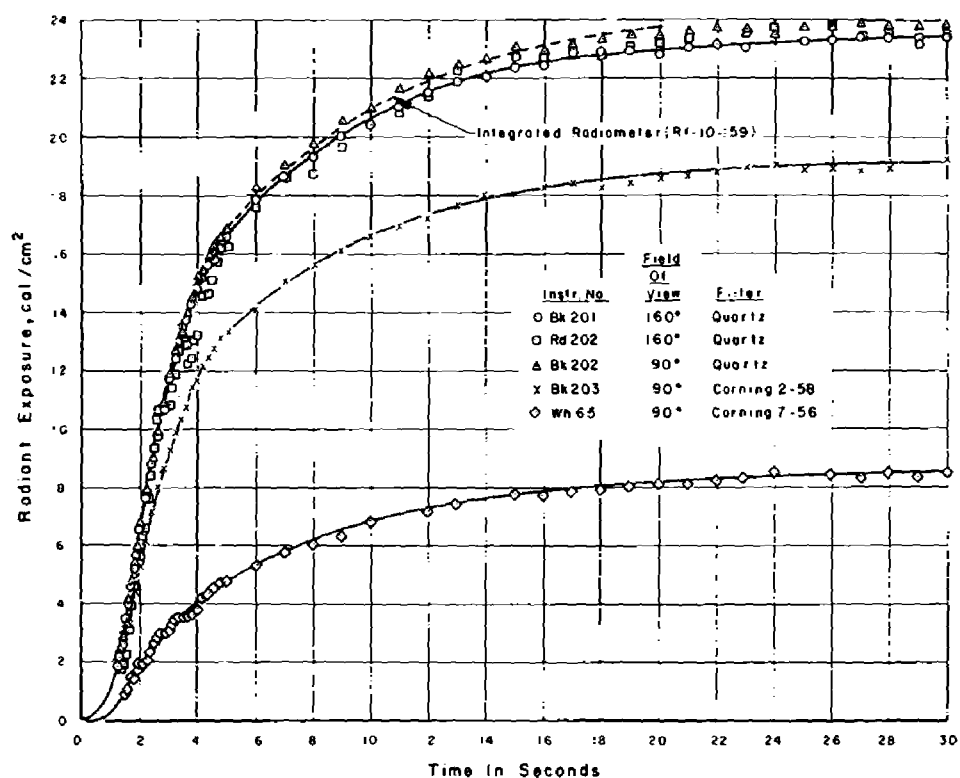


Figure 4.12 Radiant exposure of direct thermal instruments, Shot Zuni.

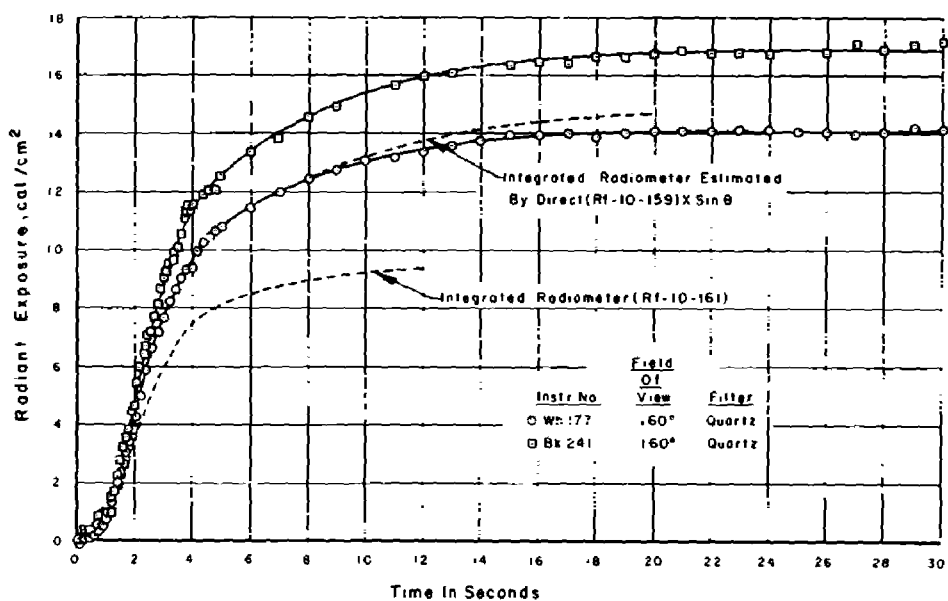


Figure 4.13 Radiant exposure of indirect thermal instruments, Shot Zuni.

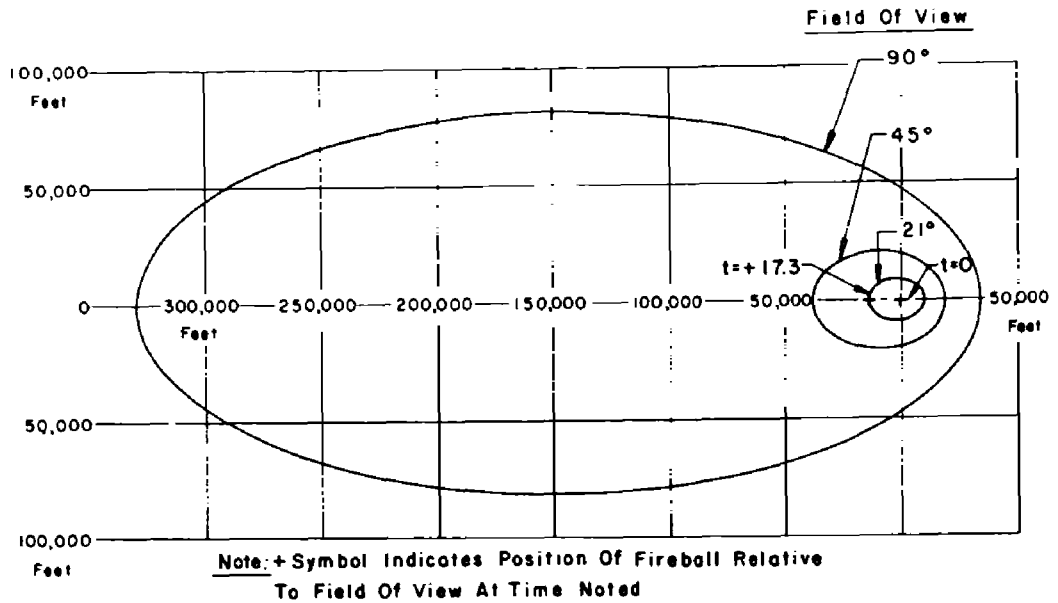


Figure 4.14 Field of view of direct thermal instruments, Shot Tewa.

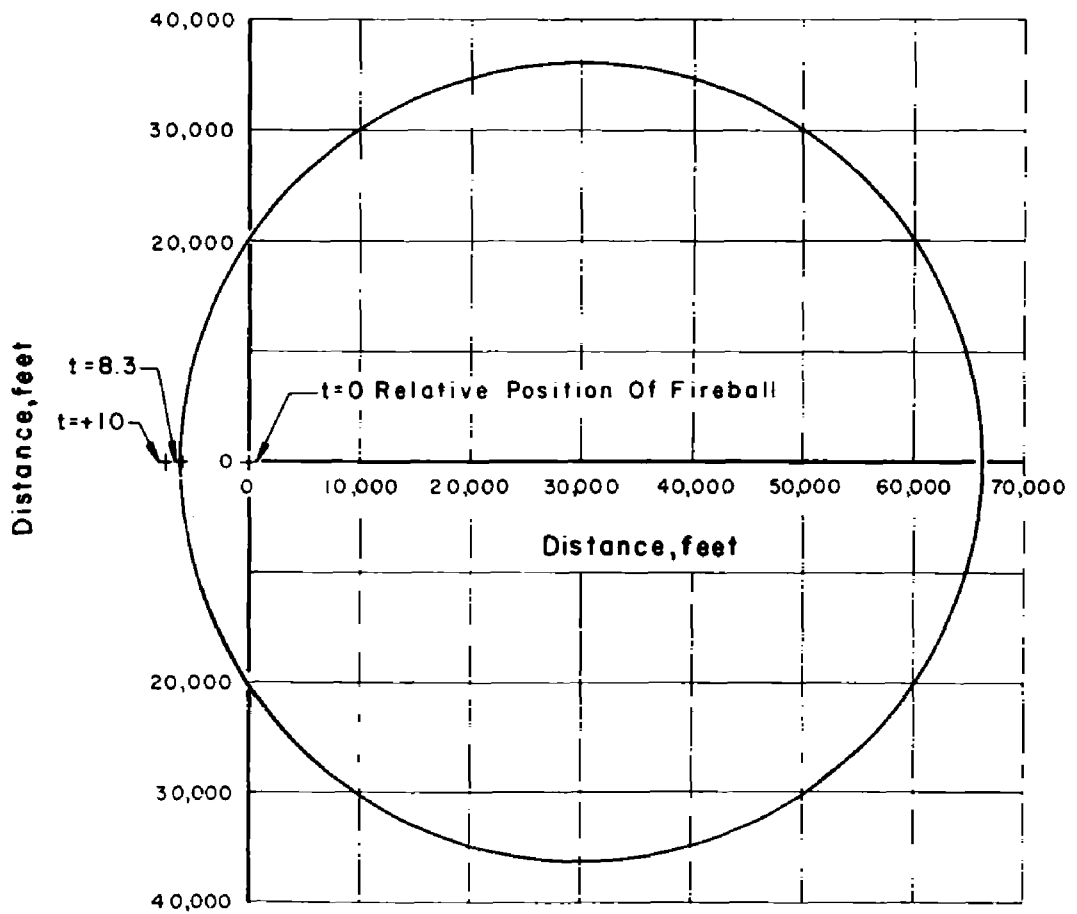


Figure 4.15 Field of view of 90-degree indirect thermal instruments, Shot Tewa.

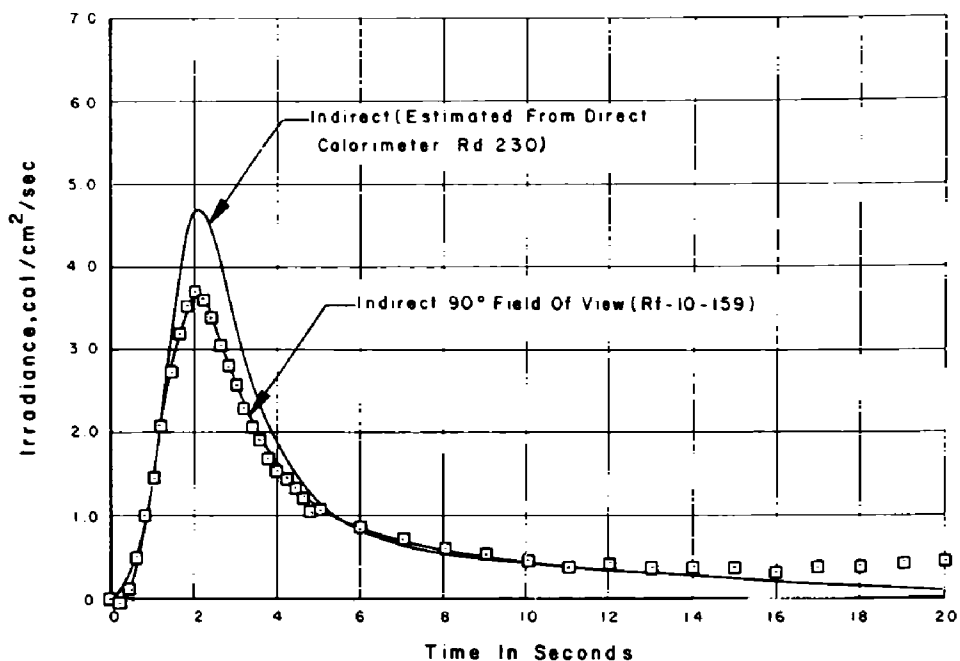


Figure 4.16 Thermal irradiance as a function of time, Shot Tewa.

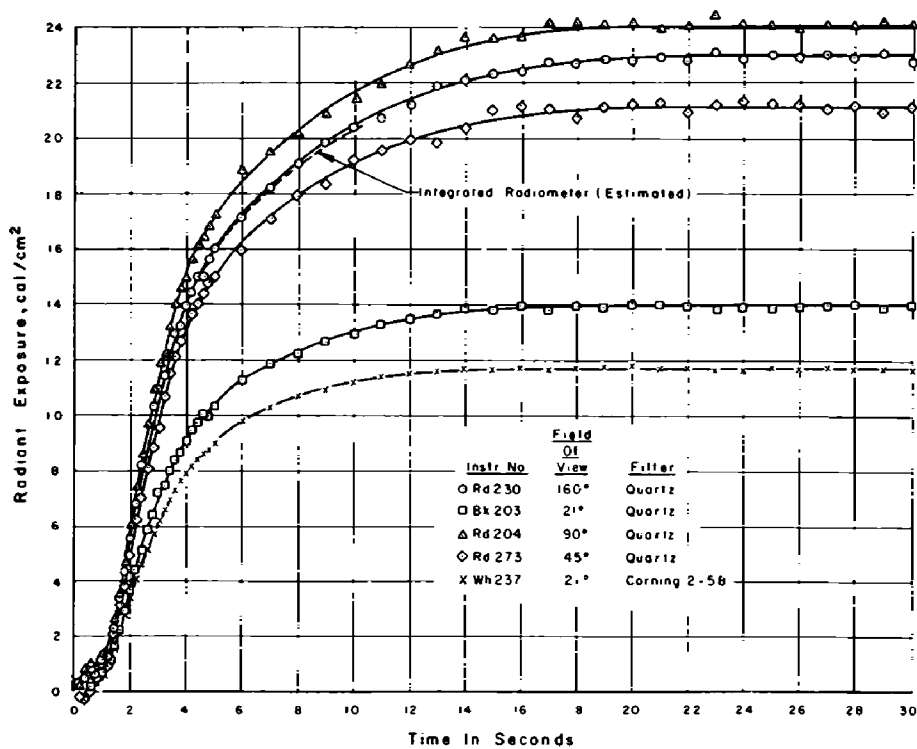


Figure 4.17 Radiant exposure of direct thermal instruments, Shot Tewa.

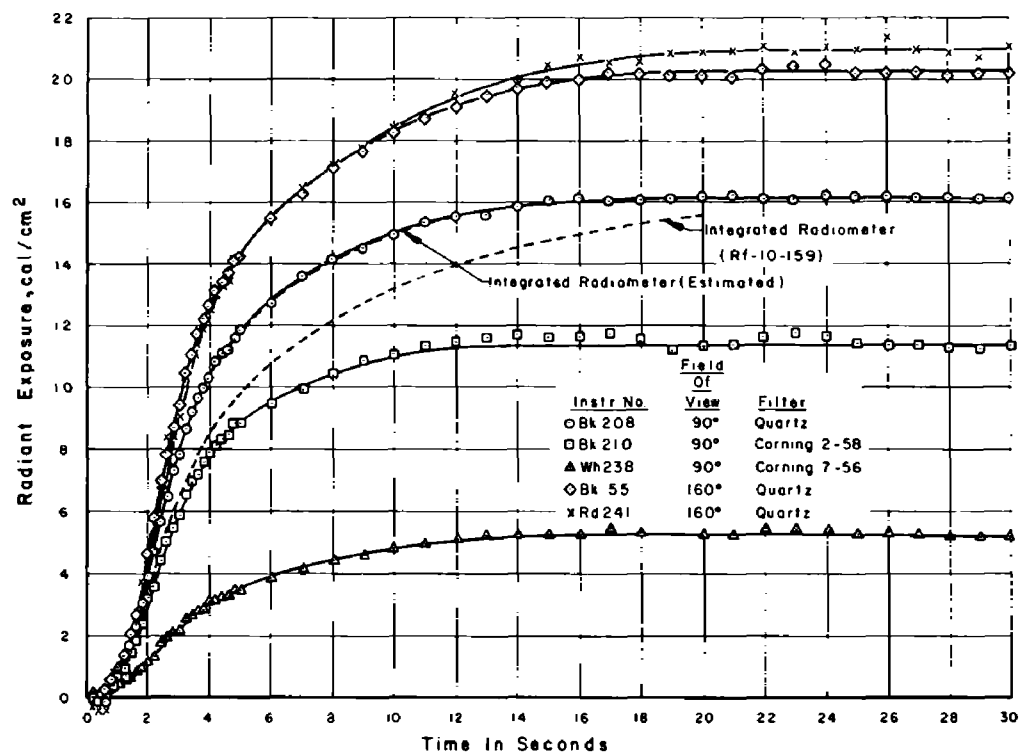


Figure 4.18 Radiant exposure of indirect thermal instruments, Shot Tewa.

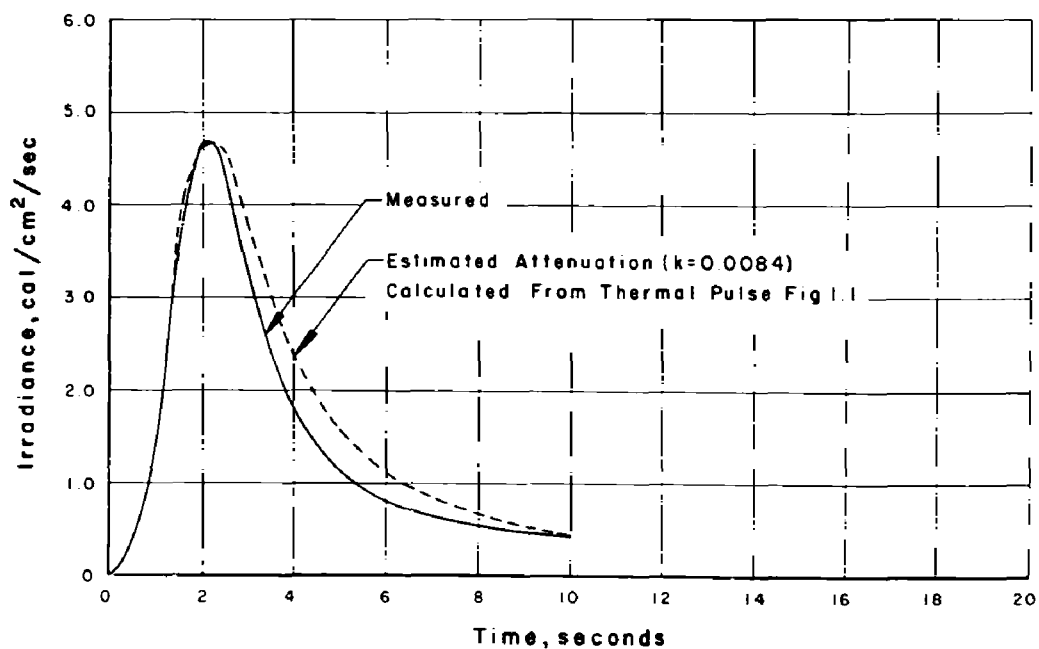


Figure 4.19 Comparison of measured and calculated thermal irradiance, Shot Tewa.

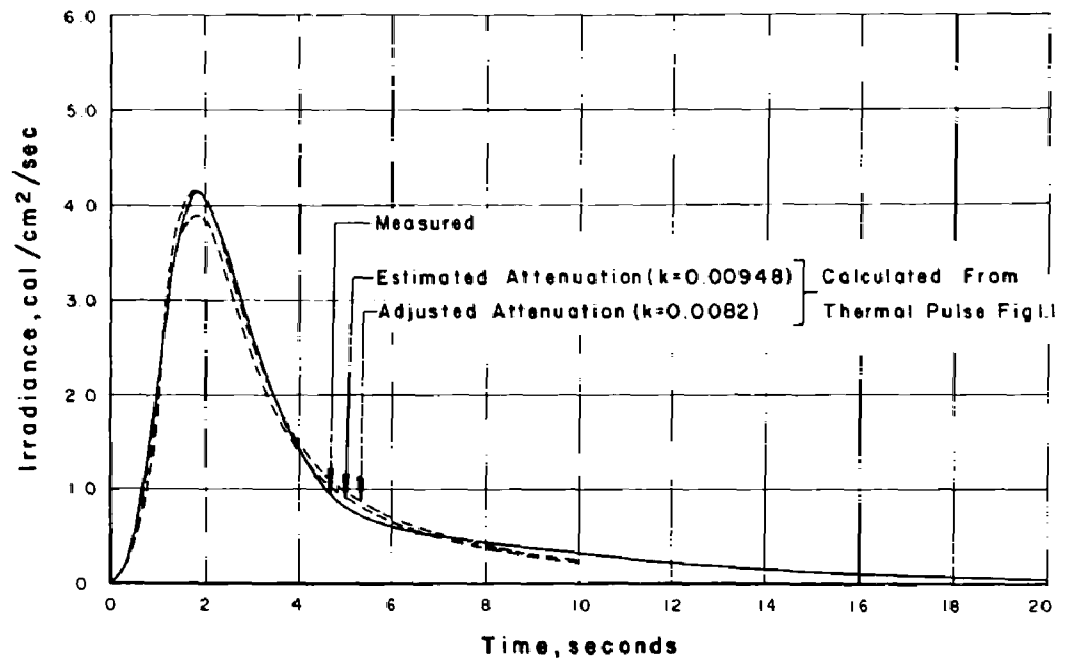


Figure 4.20 Comparison of measured and calculated thermal irradiance, Shot Zuni.

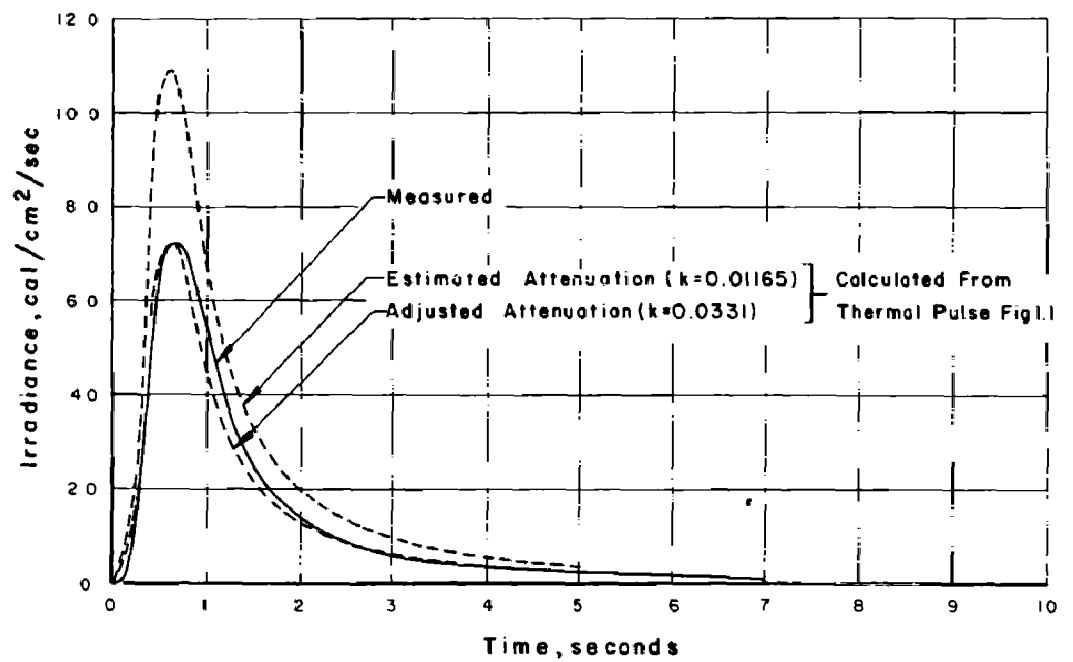


Figure 4.21 Comparison of measured and calculated thermal irradiance, Shot Flathead.

did not agree with the 160-degree indirect instruments. However, these same 160-degree instruments also appeared high for Shot Apache, and it may be that the 160-degree quartz filters produced a lens effect when used on the direct instruments. Therefore, the thermal pulse used for this shot was the one estimated by resolving the direct irradiance which was estimated from the direct calorimeters. This complication was necessary in order to obtain a pulse that would correlate between the direct and indirect data.

4.3.4 Shots Navajo, Apache, Cherokee, and Huron. The data for the remainder of the shots were not used in this analysis and are therefore not presented in the main body of this report.

Neither the direct nor the indirect radiometers functioned for Shots Navajo and Apache.

On Shot Cherokee, because of the uncertainty of the fireball location relative to the airplane and the field of view of the instruments, and the uncertainty of the aircraft position, no analysis of the thermal data from this shot was attempted.

Because of the lack of accurate aircraft position data, no attempt was made to analyze the thermal data on Shot Huron.

The data are shown in Appendix D in case they should prove useful to other agencies in correlating data from all projects.

4.4 CORRELATION OF MEASURED AND COMPUTED THERMAL FIELD

The computed thermal field is a function of the thermal pulse used for the source and the attenuation of the energy between the source and the receiver.

For the correlation in this study the normalized thermal pulse from Reference 3 (shown in Figure 1.1) was used, and the maximum irradiance of the source was determined from the analysis outlined in Section 1.3.1. This gave the time energy relationship of the source. Two time energy relationships at the receiver are covered in the following analysis. One is with the attenuation between the source and the receiver as determined from Reference 8. This represents a value which would be used for a delivery capability study and was also the method used for the test positioning calculations. The other was obtained by calculating the effective linear attenuation coefficient which gave the maximum irradiance as measured in the test for the calculated maximum irradiance at the source. This attenuation coefficient was obtained from Equation 1.7, Section 1.3.1. This brings the calculated and measured maximum irradiance into agreement and allows a study of the remainder of the calculated and measured pulses.

For purposes of comparison in this analysis, the attenuation determined from Reference 8 is called the estimated attenuation, and the value obtained by matching the maximum computed and measured irradiance is called the effective attenuation coefficient. It should again be emphasized that this effective attenuation coefficient assumes no scattering along the path of a direct ray (see Section 1.3.1).

Effective attenuation was determined from maximum irradiance rather than total energy received because it could be determined from the position of the airplane at the time of maximum irradiance. If the total energy were used, it would require assumption of an attenuation value, determination of the irradiance at the receiver versus time (taking into account the increase in distance of the airplane during the time of the energy release), and integration of the calculated irradiance versus time curve for comparison with the measured data. If the two did not agree, another value would be assumed and the process repeated until agreement was reached. Since both methods would be subject to the same basic assumptions (i.e., the pulse shape, and the total thermal yield was 0.44 W^{0.84}), it appears that the use of the maximum irradiance is more desirable. Determination of the attenuation from the maximum irradiance results in a value at a specific pulse time, which may be spectrally quite different than the average over the total thermal pulse. However, in the temperature time relationship of the aircraft structure, the conditions at and near the time of maximum irradiance are of more importance than an average value based on conditions which could vary greatly during the total thermal energy release.

The estimated values of attenuation from Reference 8 and the effective values are shown in Table 4.2. These are presented in two forms, as attenuation per kilofeet and as percent transmissivity per naut mi.

TABLE 4.2 ESTIMATED AND EFFECTIVE LINEAR ATTENUATION VALUES

	Airplane altitude	Effective linear attenuation adjusted at maximum irradiance		Estimated values from Reference 8			
		kilofeet ⁻¹	pct/mile	Exceptionally clear		Clear	
	feet			kilofeet ⁻¹	pct/mile	kilofeet ⁻¹	pct/mile
Cherokee	34,100	0.0061*	96.4	0.0080	95.3	0.0160	90.7
Zuni	28,170	0.0082	95.2	0.0095	94.4	0.0190	89.1
Flathead	14,050	0.0331	81.8	0.0117	93.2	0.0234	86.7
Apache	26,000	0.0134*	92.2	0.0098	94.2	0.0196	88.8
Navajo	36,100	0.0131	92.3	0.0085	95.0	0.0170	90.2
Tewa	36,310	0.0085	95.0	0.0084	95.1	0.0168	90.3
Huron	12,050	0.0387*	79.0	0.0119	93.0	0.0238	86.4

*These values are of questionable value due to uncertainty of aircraft positions.

Table 4.3 presents the atmospheric and cloud cover conditions which are of value in analyzing the attenuation results. It will be noted that for all events, with the exception of Shot Navajo, the cloud cover below the aircraft altitude was not too extreme. This was verified by a study of the movies taken from the direct and indirect camera station. However, for Shot Navajo the cloud cover was extremely heavy with large clouds obscuring much of the fireball. In view of this, it is somewhat surprising that the apparent attenuation for Shot Navajo was as low as it appeared to be. The heavy lower cloud cover during Shot Navajo undoubtedly contributed significant scattered flux to the measurement, and this indicated an apparent attenuation that was conceptually too low. The apparent attenuation derived as an effective equivalent linear attenuation is a less accurate method for comparing prediction with measurement as the scattering process becomes more significant.

TABLE 4.3 ATMOSPHERIC CONDITIONS AND CLOUD COVER

Obtained from official Joint Task Force 7 weather observations.

Shot	Cherokee	Zuni	Flathead	Apache	Navajo	Tewa	Huron
Surface visibility (naut mi)	10	8	10	10	10	10	10
Humidity at sea level (pct)	76	80	82	84	80	85	84
Low clouds—type*	CU	AC, AS	SC	SC	CU	CU	CU
Coverage	2/10	3/10—4/10	4/10	2/10	2/10	2/10	3/10
Bases (feet)	1800	8000	2000 (est)	2000	1800	2000	1800
Tops (feet)	2500	12,000	not observed	4000			10—15,000
Middle clouds—type*	none	CI	none	CU	CU	none	none
Coverage		4/10		2/10	6/10		
Bases (feet)		25,000		1500	2000		
Tops (feet)		27,000		25,000	7000 (est)		
High clouds—type*	CI	CI, CS	CS	CS	CS	CS	CS
Coverage	2/10	4/10—7/10	10/10	8/10	7/10	1/10	10/10
Bases (feet)	38,000	35,000	30,000 (est)	30,000	30,000	35,000	30,000
Tops (feet)	not observed	40,000	not observed	very thin	thin	36,000	very thin

*Standard cloud abbreviation.

With the exception of Shots Cherokee and Zuni, all the values estimated for an exceptionally clear day from Reference 8 are conservative in that they give less attenuation. The values estimated for a clear day would be conservative only for Shots Flathead and Huron.

The high values of attenuation for Shots Flathead and Huron, which were at comparatively low aircraft altitudes, and the good agreement with the exceptionally clear day estimates for the other shots at high altitudes indicate that there may be high attenuation in the lower part of the Marshall Islands atmosphere but that this is not true at the higher altitudes.

The calculated thermal fields are based on: (1) the normalized thermal pulse shown in Figure 1.1; (2) the determination of the maximum irradiance of the source from Equation 1.2; and (3) the determination of irradiance at the receiver from Equation 1.6. For comparison with the measured irradiance, the calculated thermal fields with the estimated attenuation for an exceptionally clear day, and the adjusted attenuation (summarized in Table 4.2) are shown in Figures 4.19, 4.20, and 4.21 for Shots Tewa, Zuni, and Flathead, respectively.

It will be noted that when the adjusted attenuation is used, the calculated curve for Shot Zuni agrees closely with the measured value. For Shot Tewa the measured decay of the irradiance is much greater than calculated, and for Shot Flathead the measured curve is shifted slightly in time, but the area under the curves would be about the same. For Shot Tewa the total area, or thermal energy, under the measured pulse would be less than assumed, and any temperatures computed from a method which considers the standard pulse would be too high.

The agreement obtained in these comparisons indicates that if the attenuation properties of the atmosphere can be predicted either as effective linear attenuation or by a combination of true attenuation and scattering considerations, the thermal field at the aircraft can be computed with acceptable accuracy.

Chapter 5

RESULTS AND DISCUSSION OF STRUCTURAL TEMPERATURE MEASUREMENTS

Sketches of the airplane showing the maximum temperature rise at each thermocouple location for each shot are presented in Figures 5.1 to 5.7. All the maximum temperatures were in the 0.025 skin, with the exception of Shot Apache, either on the nacelle, aft section of the fuselage, or the elevator. For Shots Tewa and Huron portions of the elevator were painted white, gull gray, and insignia blue.

5.1 QUARTZ COVERED THERMOCOUPLE FOR AERODYNAMIC COOLING

Two sections of the airplane, the lower surface of the aft section of the fuselage and the bottom surface of the elevator, were instrumented with a hemispherical quartz cover over a white painted disc of 0.025 dural skin with a thermocouple on the back. The quartz covered thermocouple was adjacent to a thermocouple in the aircraft skin. The purpose of the quartz covers was to eliminate the aerodynamic cooling of the airstream, thus permitting a comparison of a cooled and uncooled surface.

The quartz covered thermocouples did not provide a good indication of the aerodynamic convective cooling. From Figures 5.12, 5.23, and 5.32 (thermocouple Nos. 16, 17, 31, 32, of which 16 and 31 were quartz covered) it can be seen that the temperature reached a definite peak at a time only slightly greater than the time for the uncovered cooled thermocouple. Also, the decrease in temperature after reaching the peak was almost as great as for the cooled thermocouple.

If the quartz covered thermocouple was recording temperature without cooling, it would rise steadily to a constant value at the completion of the release of the thermal energy. Some of the heat would be conducted away to the surrounding structure, but it was hoped that this would be small. However, the time to peak and the steepness of the temperature decrease after the peak indicated that the conduction away of the heat was a large factor in the temperature recorded by the quartz covered thermocouple. Since the amount of heat lost to the surrounding structure was not known, it was not practical to arrive at a value of the cooling ratio from a source of data which included an unknown quantity of heat loss.

5.2 TEMPERATURE TIME HISTORY (FIGURES 5.8 to 5.37)

The time histories of the temperature rise in the aircraft structure are presented in this section. Sufficient data are included to illustrate all effects. Data of extremely low response or significance has been omitted and compiled in Appendix D.

It is believed that all the temperatures shown are slightly lower than the actual temperature. To increase the durability of the small thermocouple wire used, a spot of EC 801 cement

was placed over each thermocouple. This had the effect of adding a small amount of mass at the thermocouple junction, which served as a minor heat sink. After completion of participation in Operation Redwing, laboratory tests were conducted in a radiant heat source on a section of the instrumented elevator from the airplane used in this project. The section tested was that containing thermocouples 33, 34, and their spares, and the temperatures measured by these thermocouples were compared with temperatures measured by a special installation where the thermocouple wires were welded directly into the skin. The results of the check, Figure 5.38, indicated that thermocouple No. 33 with the cement gave a temperature reading 8 to 10 percent less than the welded thermocouple. This correction was not applied to the measured data as it would vary depending upon the amount of cement on each thermocouple, and although this was not the same in all cases it is believed the thermocouples tested were representative of the amount used.

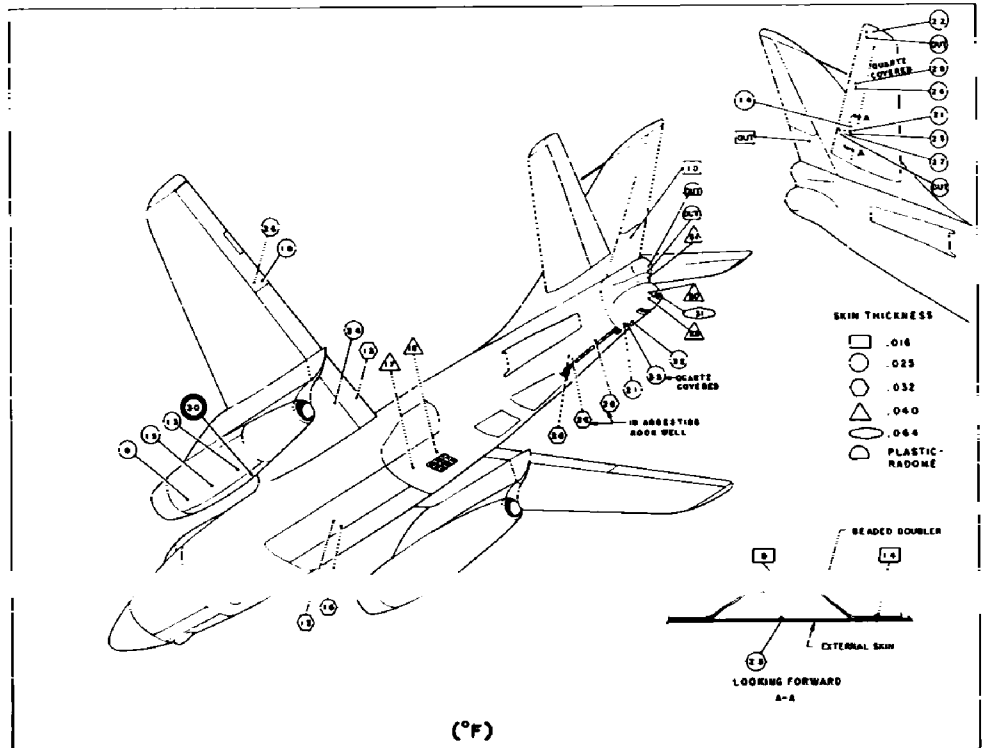


Figure 5.1 Summary of maximum temperature rise, Shot Cherokee.

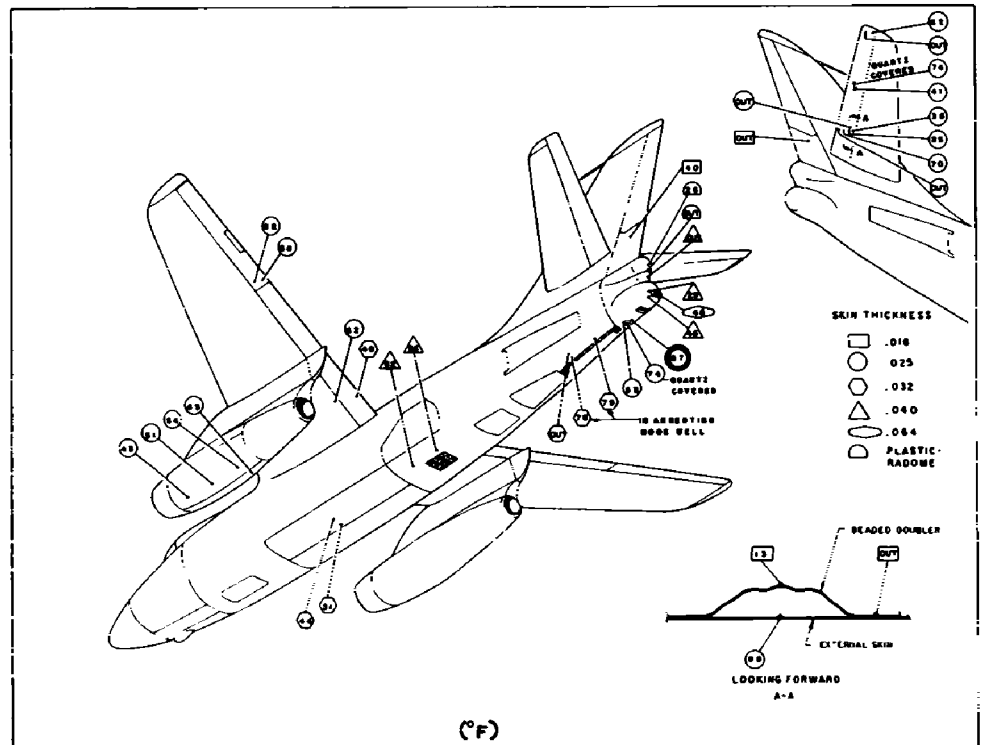


Figure 5.2 Summary of maximum temperature rise, Shot Zuni.

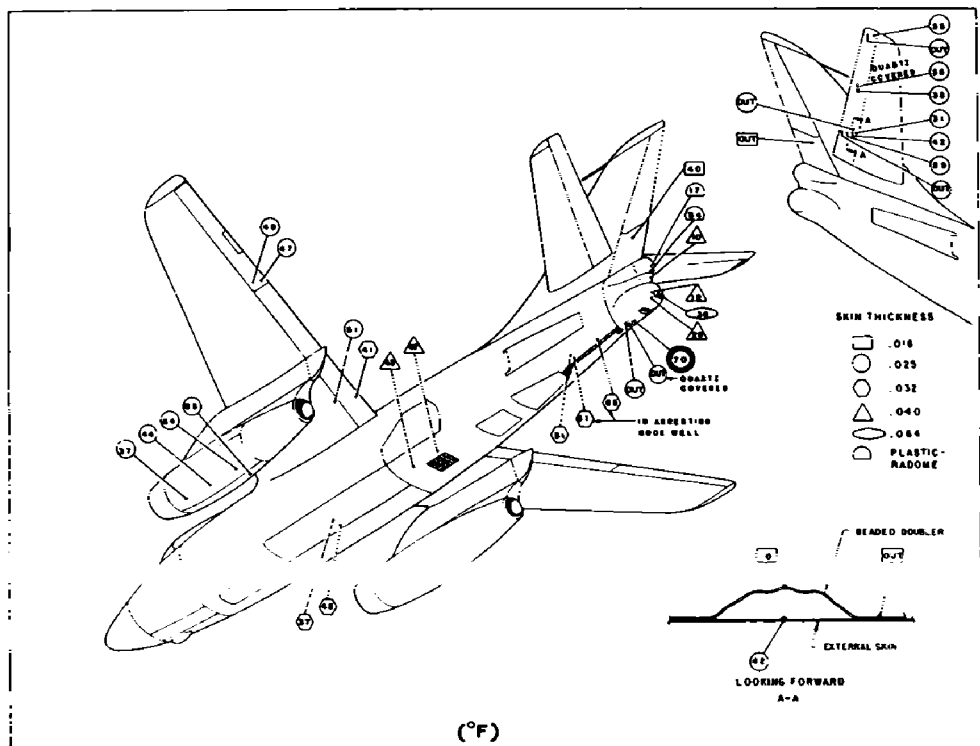


Figure 5.3 Summary of maximum temperature rise, Shot Flathead.

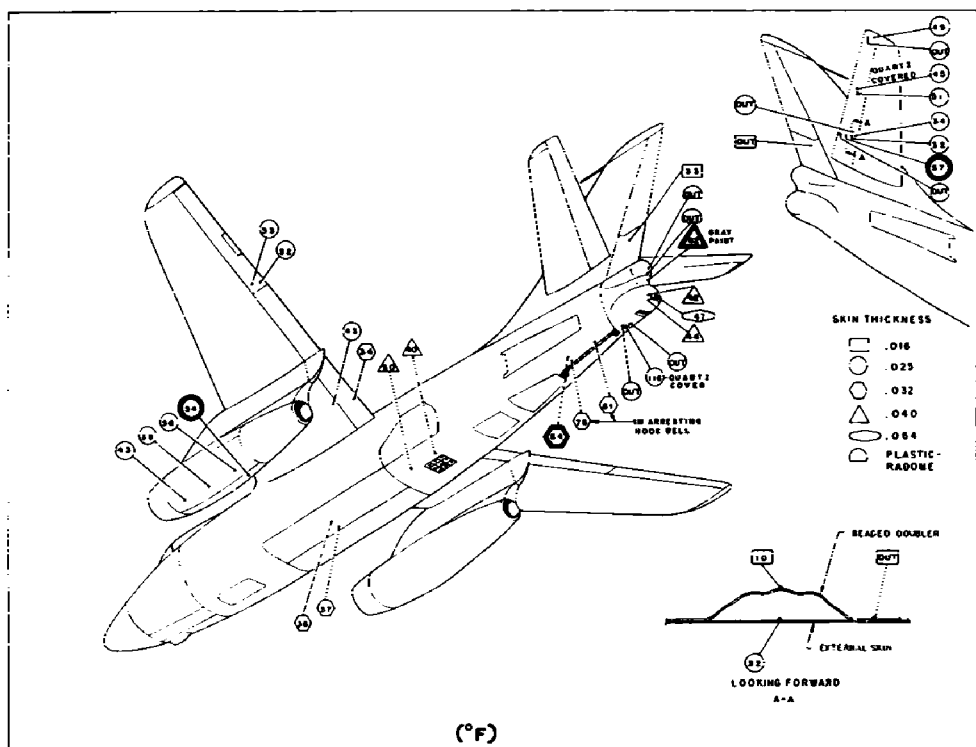


Figure 5.4 Summary of maximum temperature rise, Shot Apache.

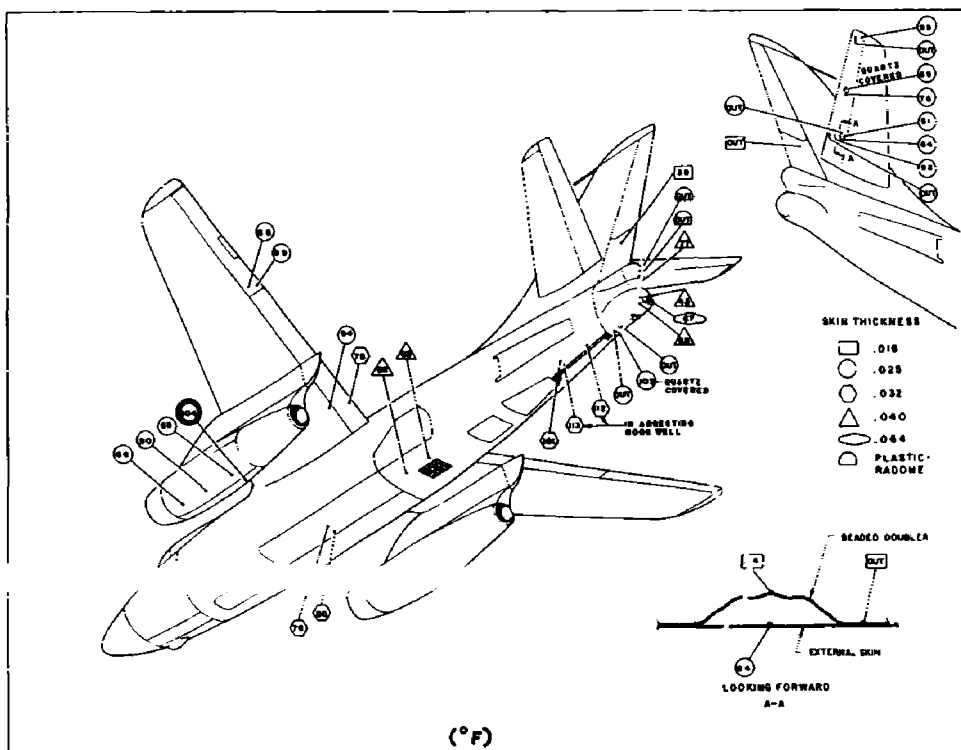


Figure 5.5 Summary of maximum temperature rise, Shot Navajo.

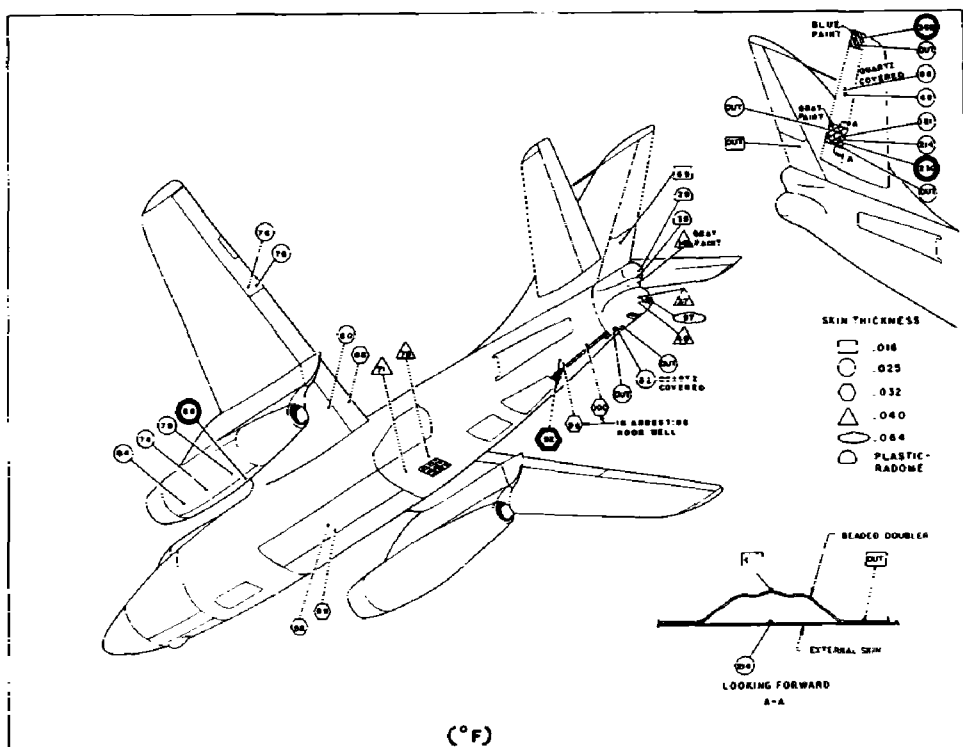


Figure 5.6 Summary of maximum temperature rise, Shot Tewa.

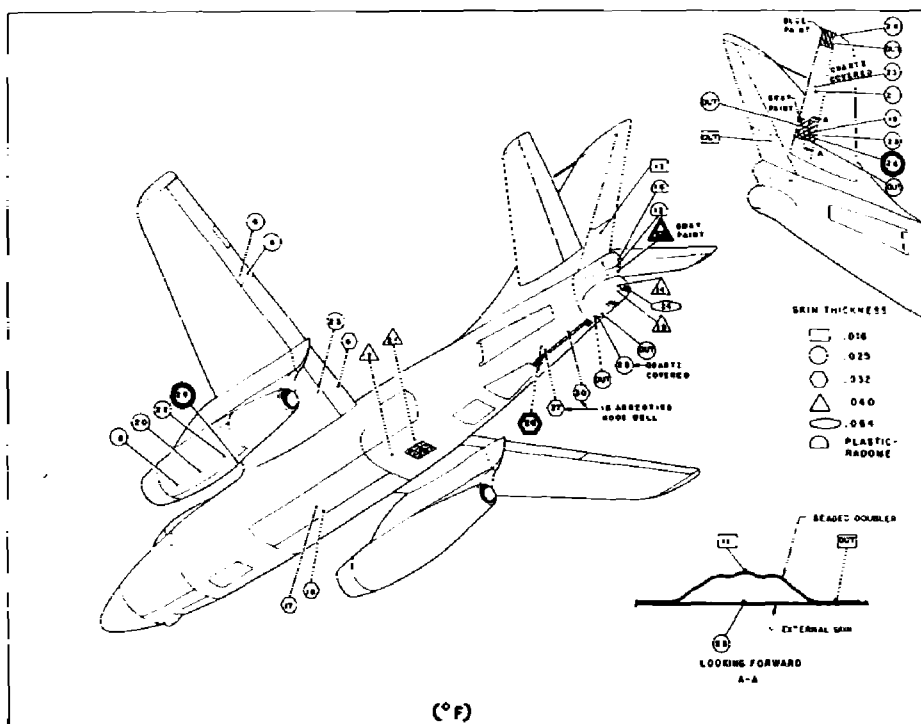


Figure 5.7 Summary of maximum temperature rise, Shot Huron.

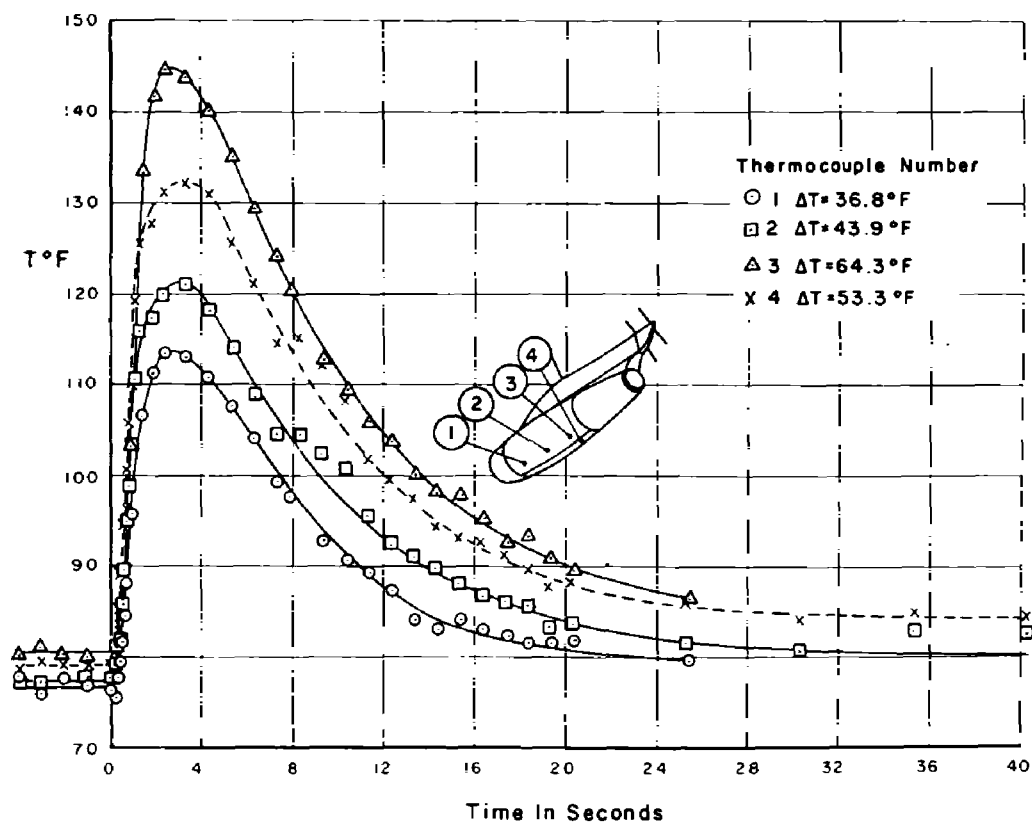


Figure 5.8 Temperature time history of nacelle skin, Shot Flathead.

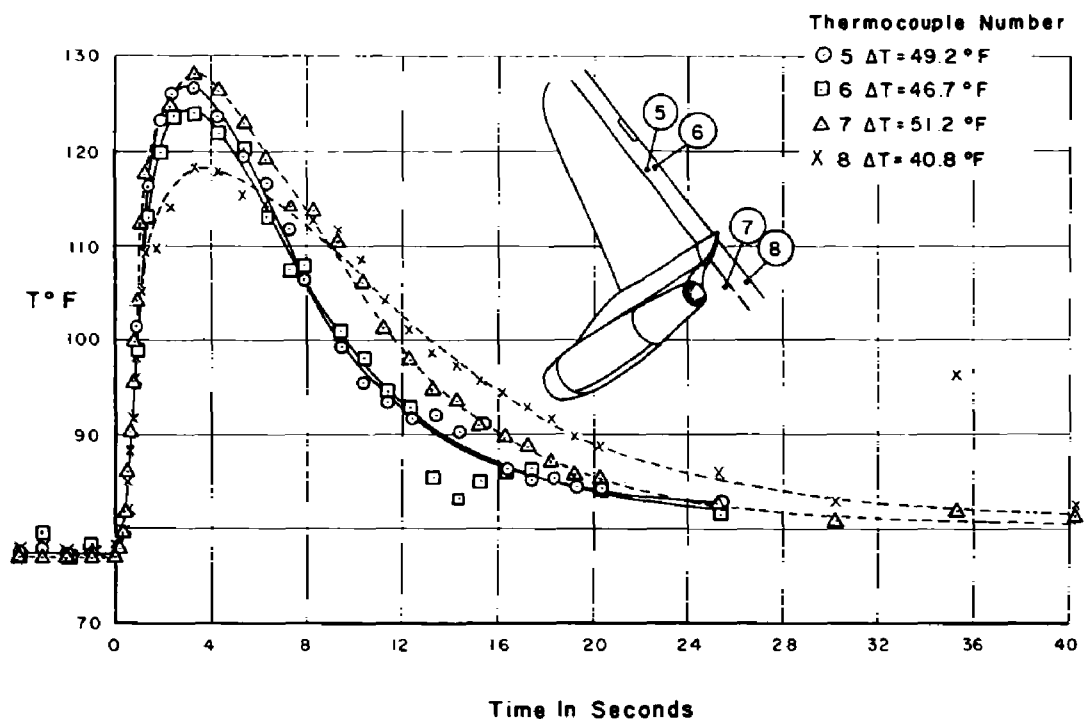


Figure 5.9 Temperature time history of aileron and flap skin, Shot Flathead.

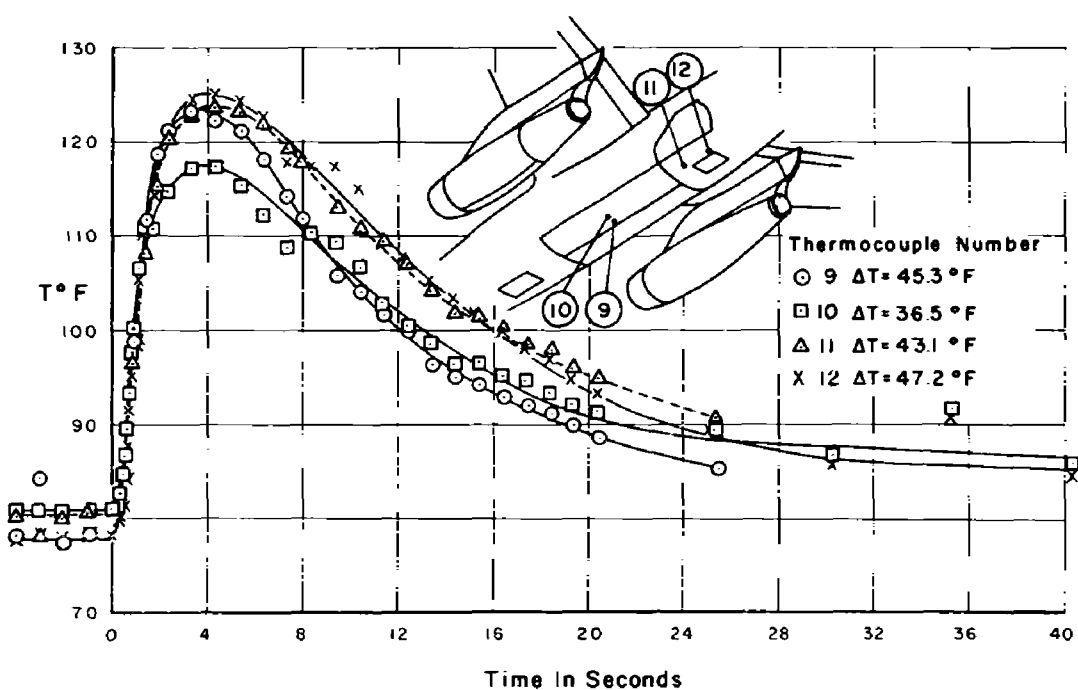


Figure 5.10 Temperature time history of bomb bay door and lower fuselage, Shot Flathead.

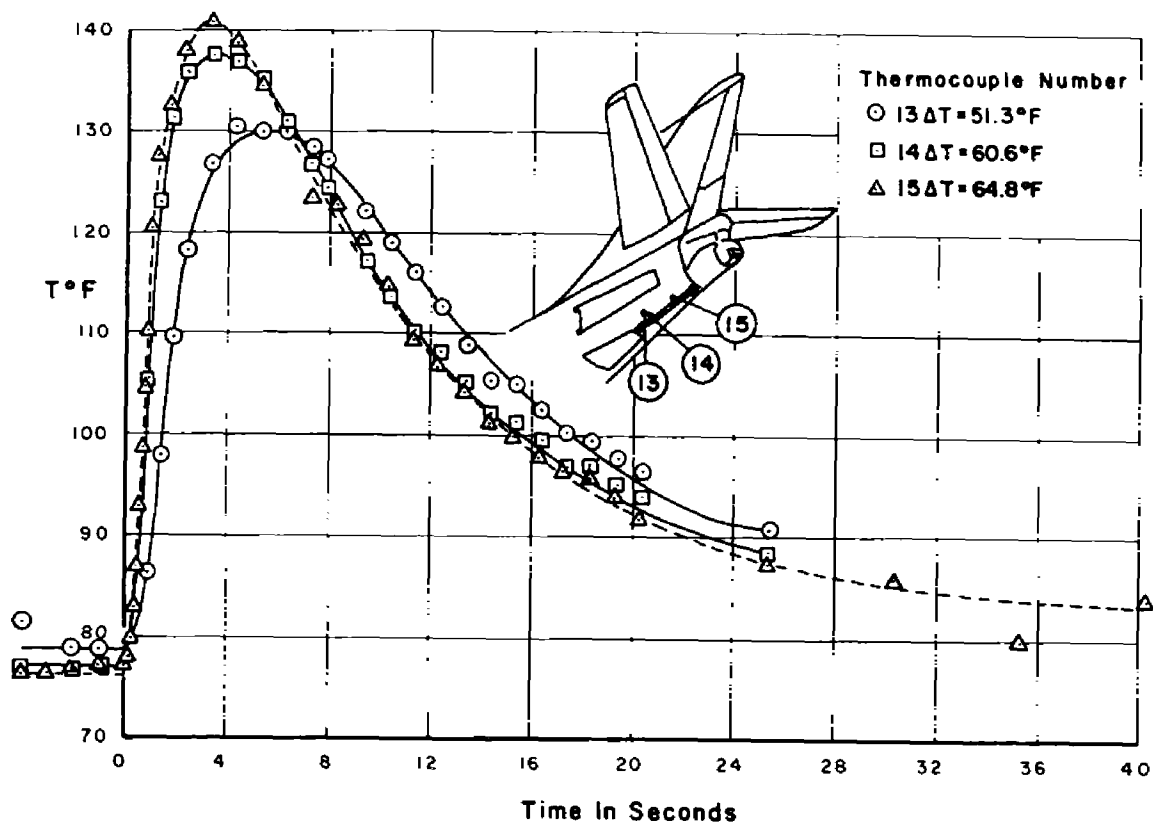


Figure 5.11 Temperature time history of arresting hook area, Shot Flathead.

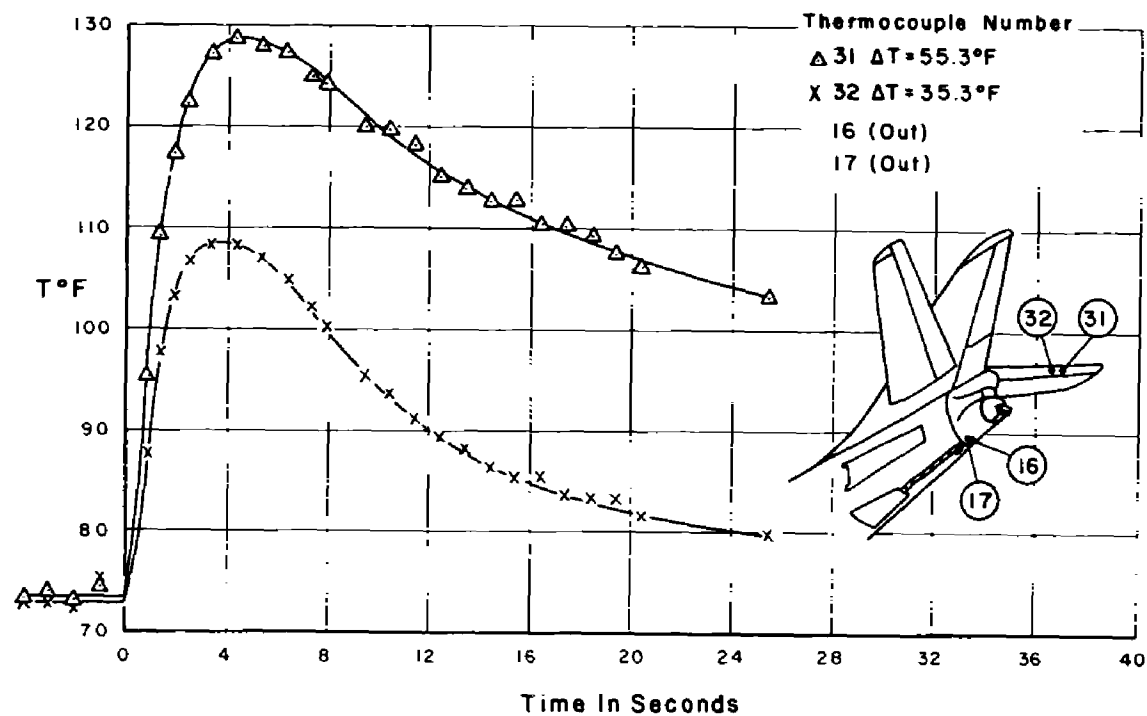


Figure 5.12 Temperature time history of quartz covered thermocouple compared to adjacent uncovered thermocouple, Shot Flathead.

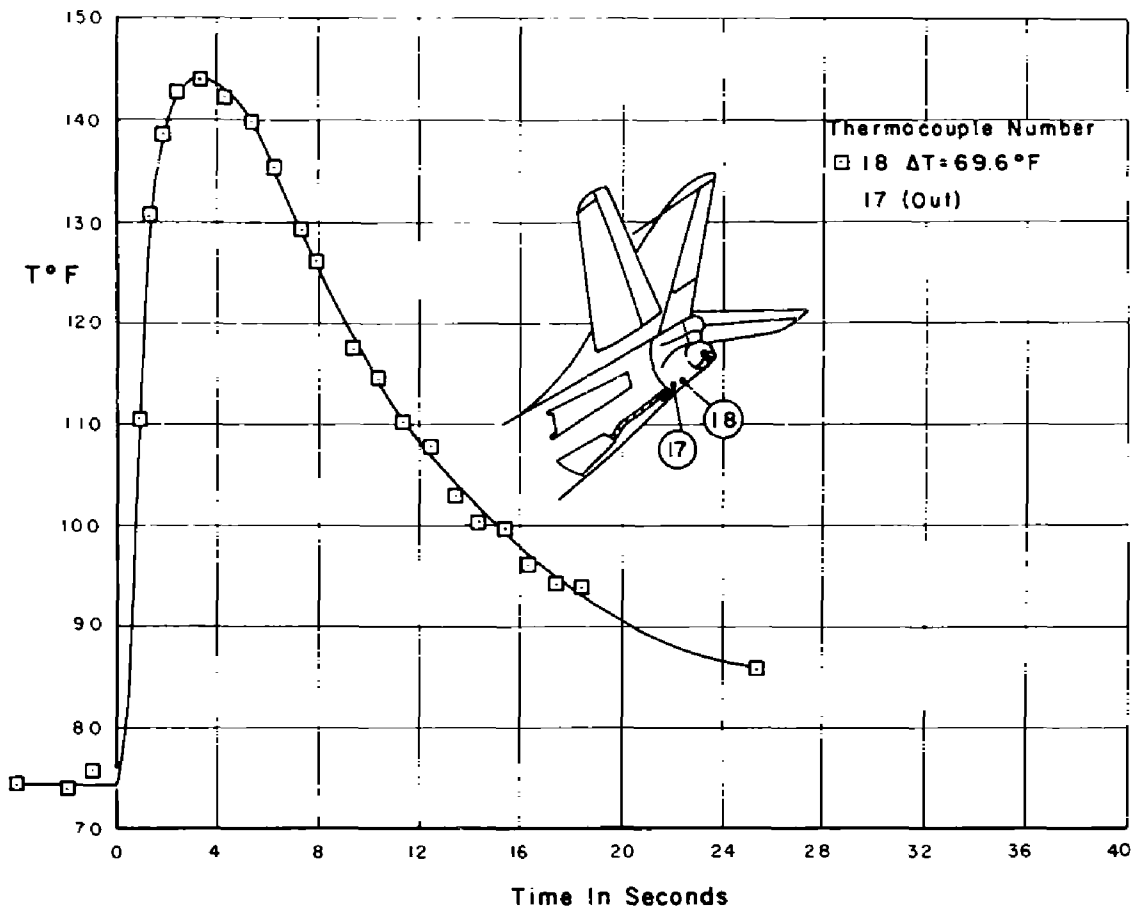


Figure 5.13 Temperature time history of aft portion of lower fuselage, Shot Flathead.

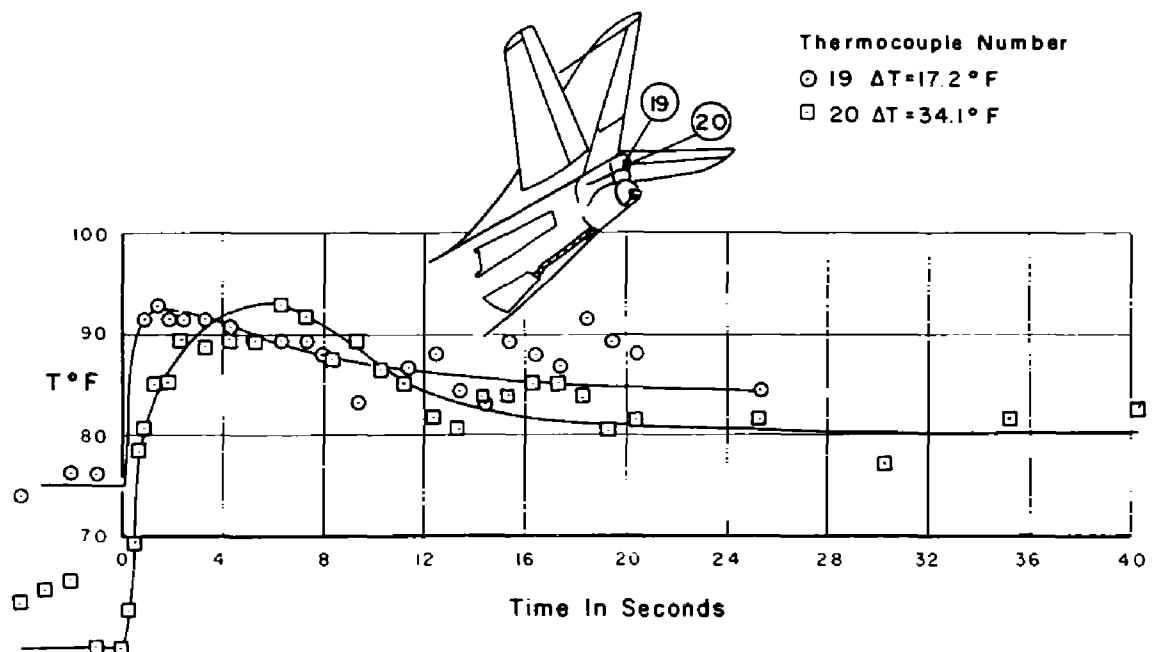


Figure 5.14 Temperature time history of plastic radome, Shot Flathead.

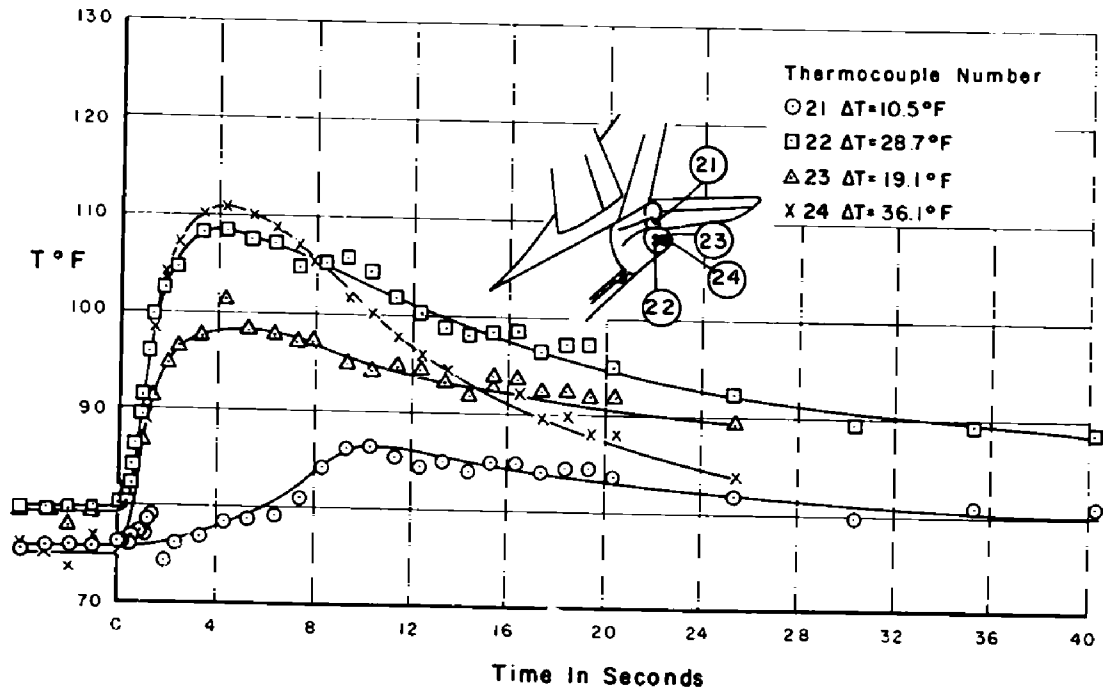


Figure 5.15 Temperature time history of tail turret, Shot Flathead.

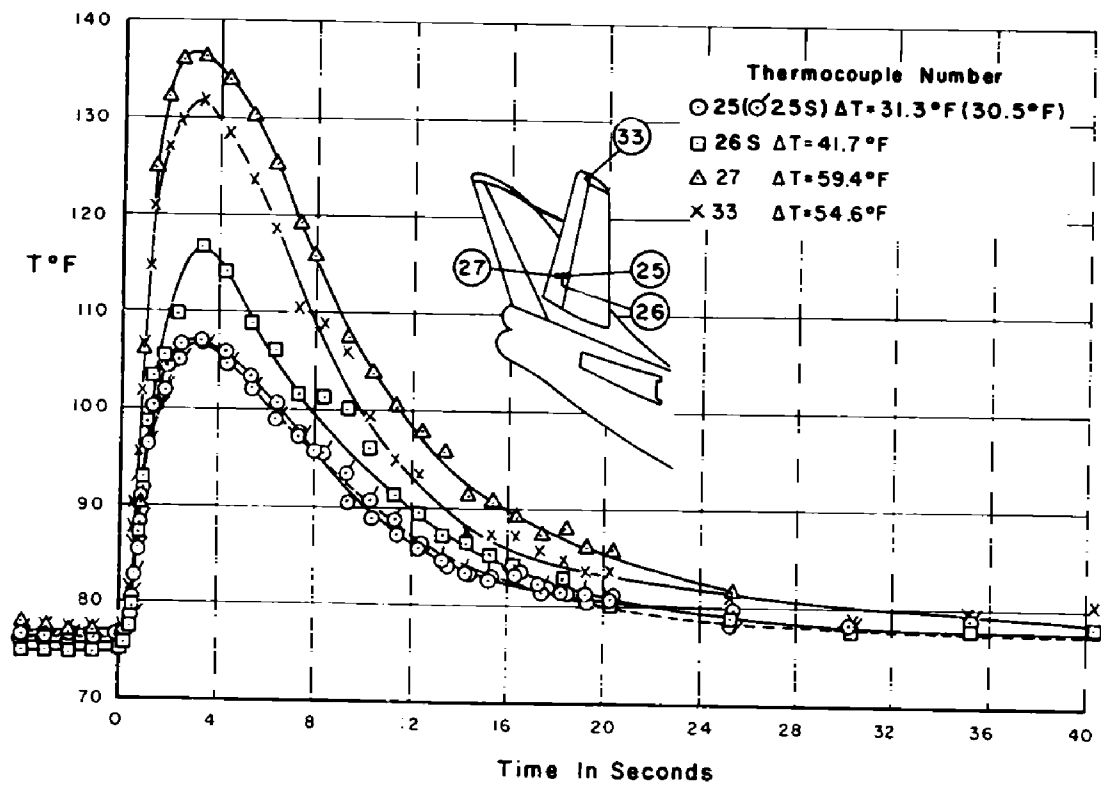


Figure 5.18 Temperature time history of elevator skin, Shot Flathead.

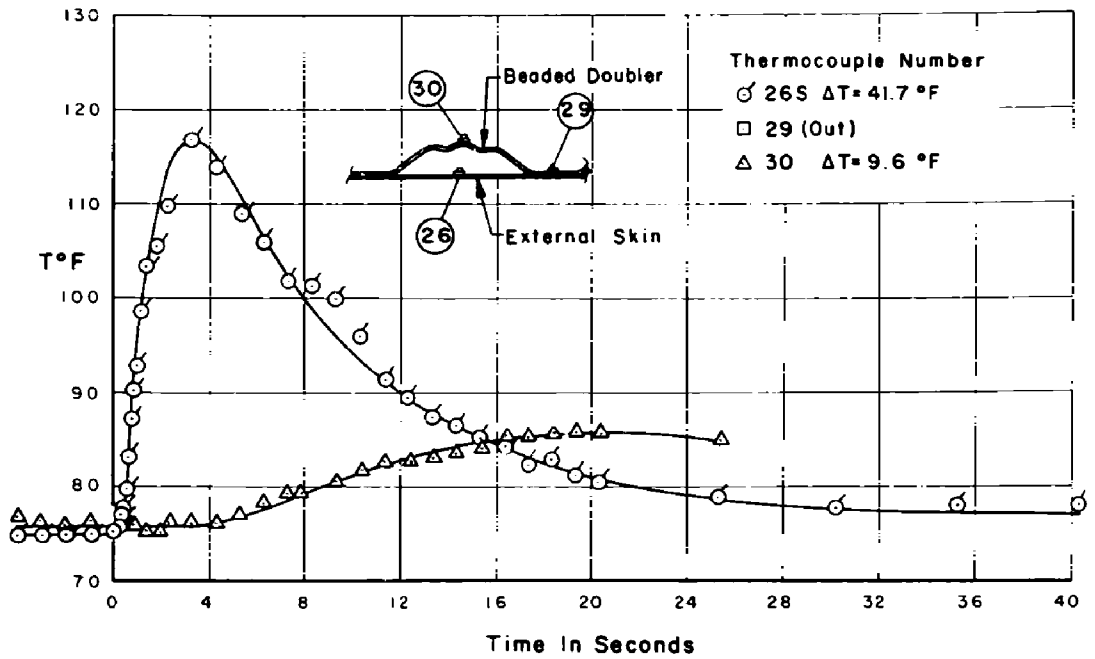


Figure 5.17 Temperature time history comparing outer skin and internal beaded doubler, Shot Flathead.

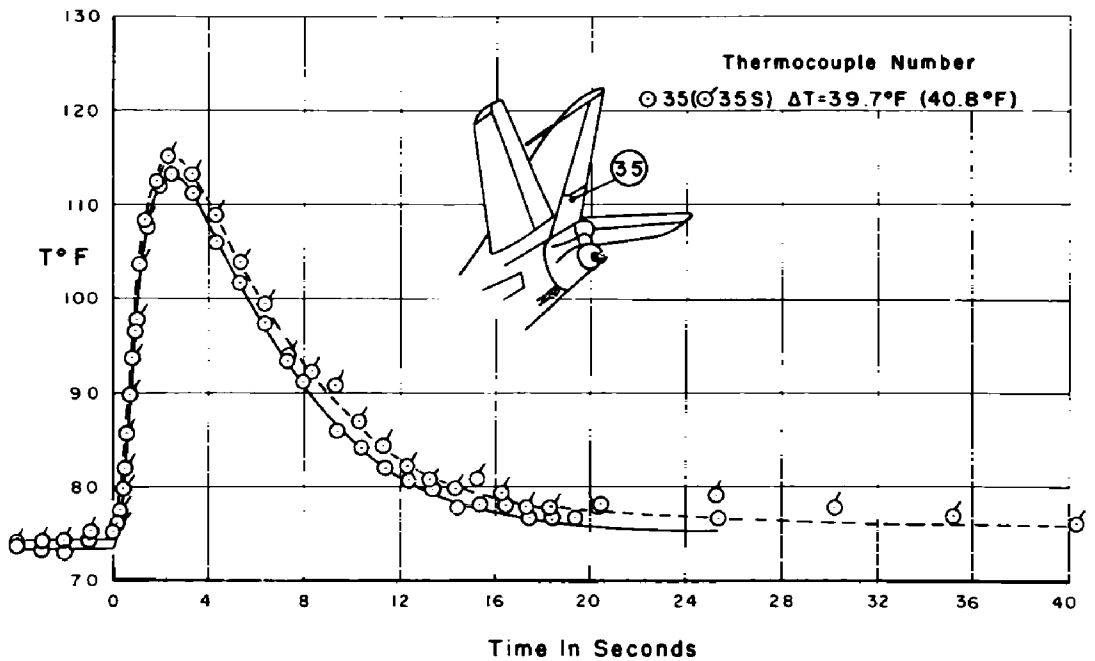


Figure 5.18 Temperature time history of lower rudder, Shot Flathead.

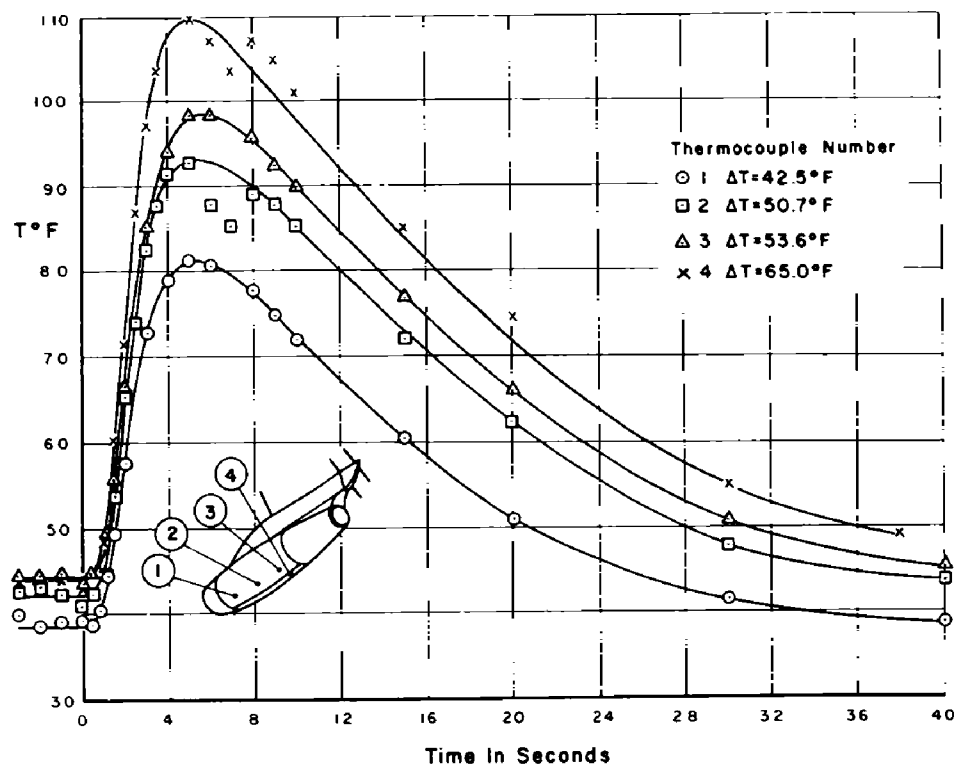


Figure 5.19 Temperature time history of nacelle skin, Shot Zuni.

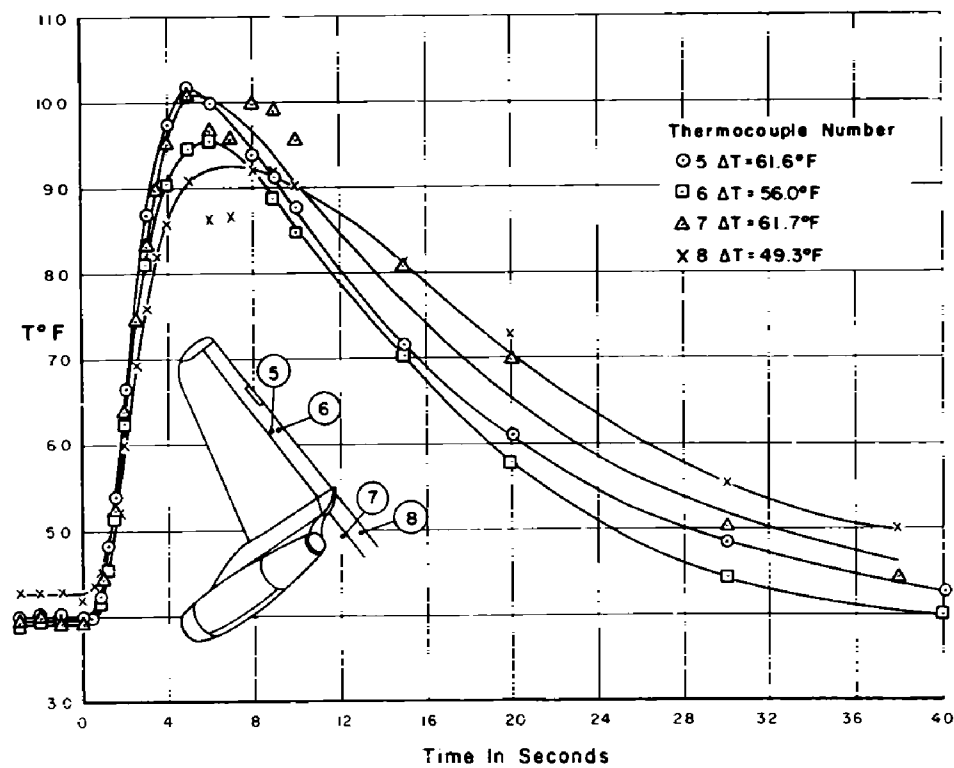


Figure 5.20 Temperature time history of aileron and flap skin, Shot Zuni.

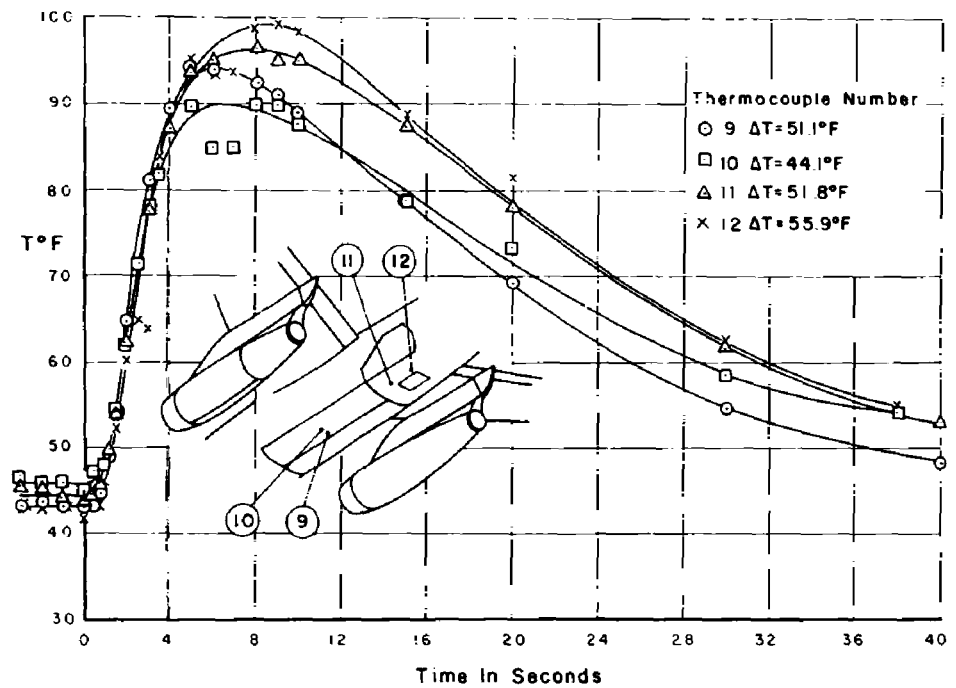


Figure 5.21 Temperature time history of bomb bay door and lower fuselage, Shot Zuni.

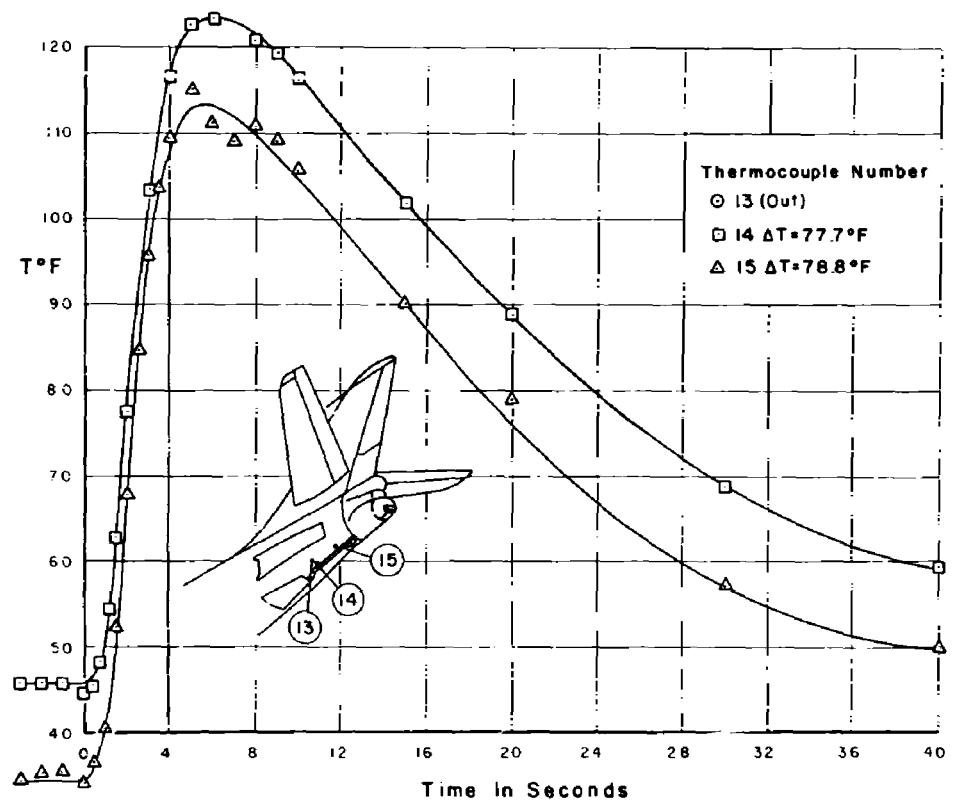


Figure 5.22 Temperature time history of arresting hook area, Shot Zuni.

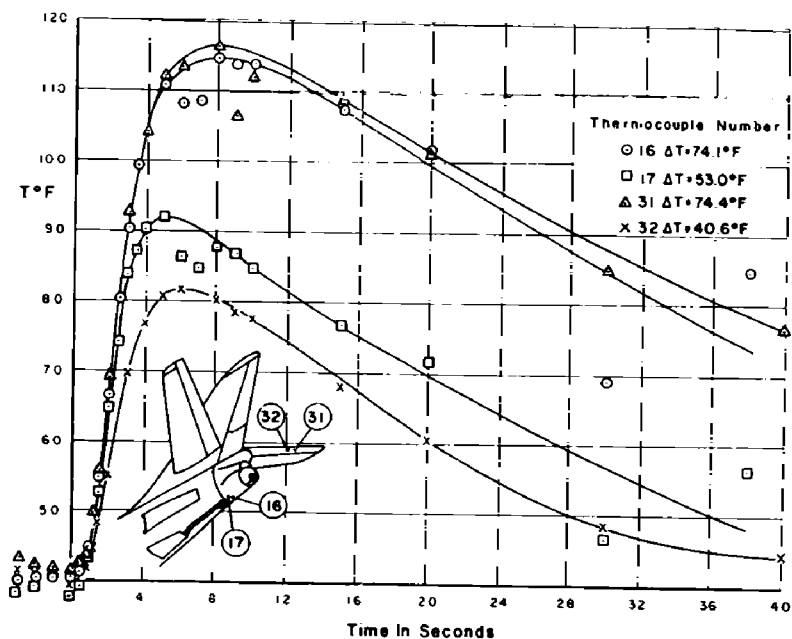


Figure 5.23 Temperature time history of quartz covered thermocouple compared to adjacent uncovered thermocouple, Shot Zuni.

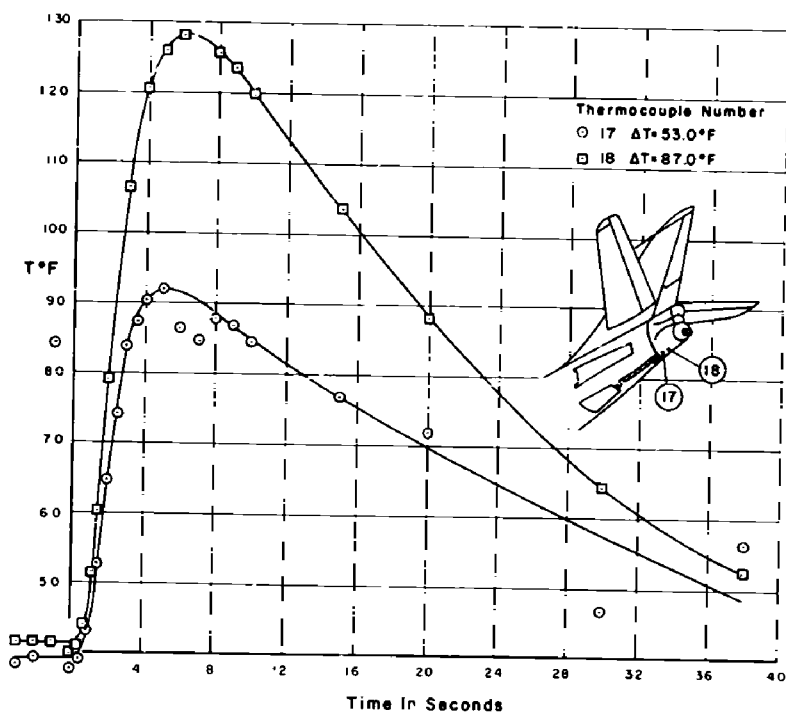
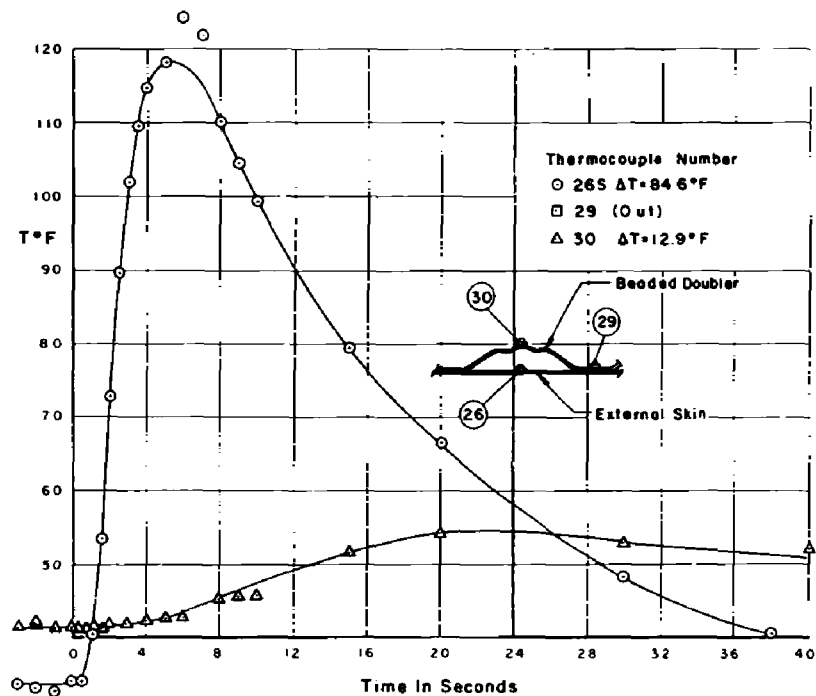
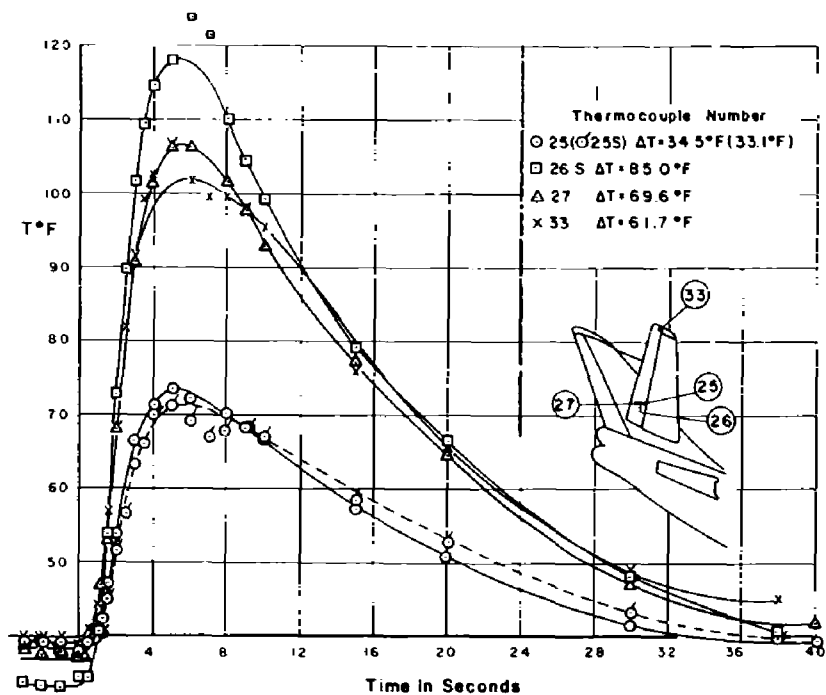


Figure 5.24 Temperature time history of aft portion of lower fuselage, Shot Zuni.



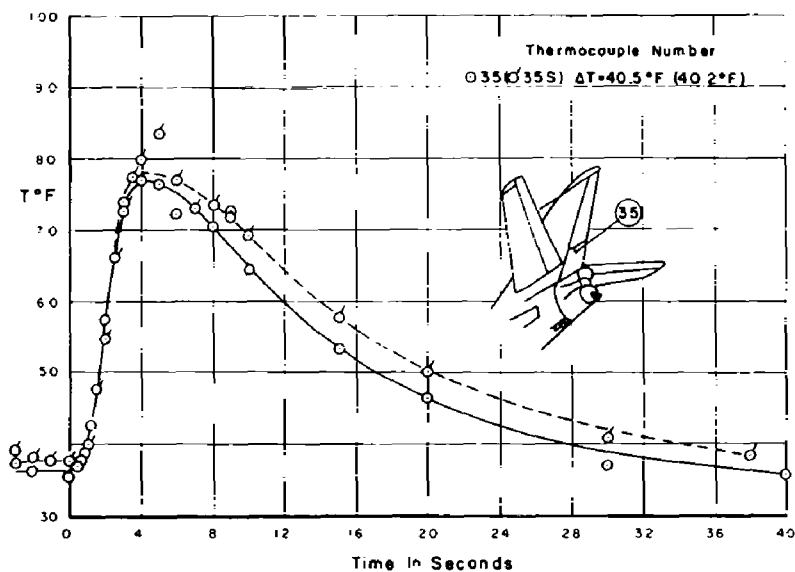


Figure 5.27 Temperature time history of lower rudder, Shot Zuni.

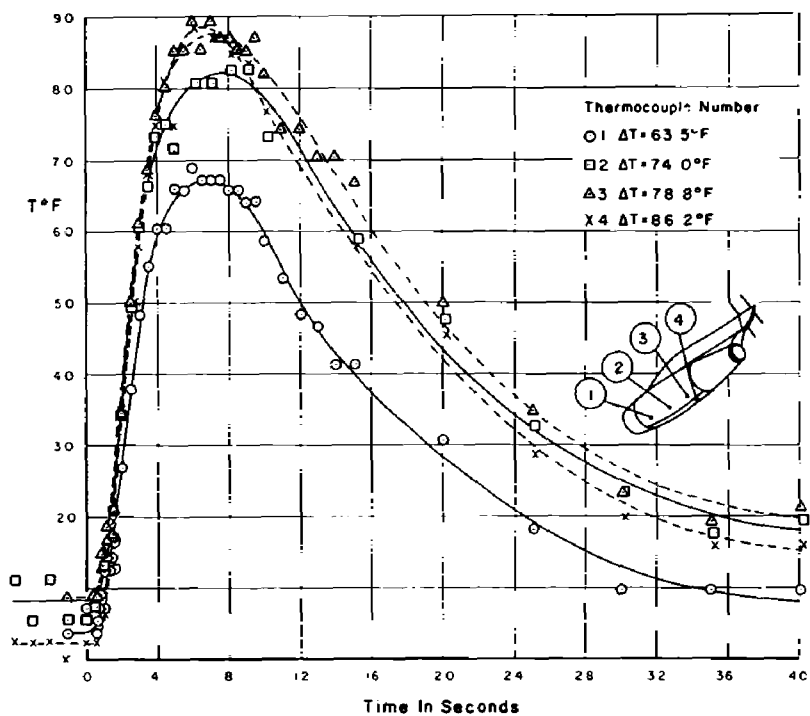


Figure 5.28 Temperature time history of nacelle skin, Shot Tewa.

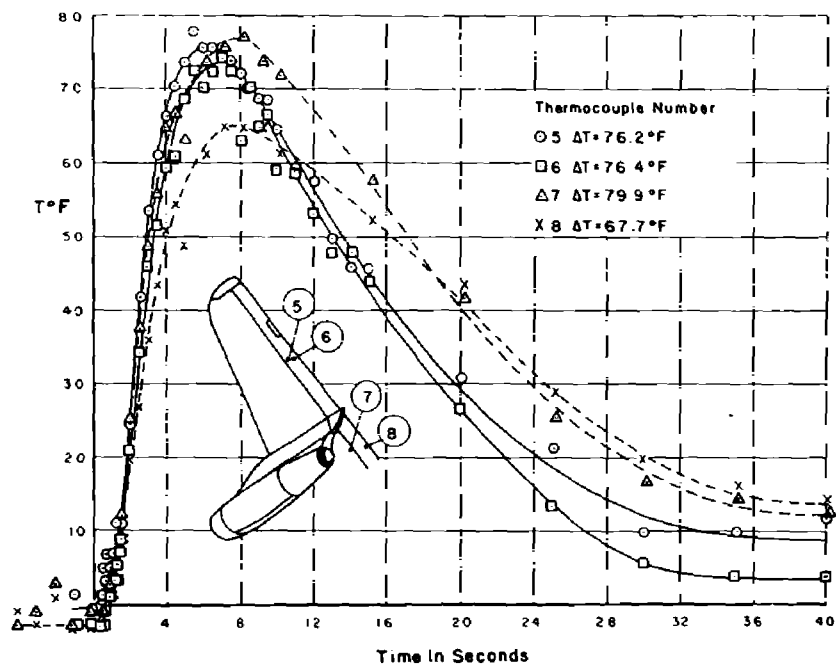


Figure 5.29 Temperature time history of aileron and flap skin, Shot Tewa.

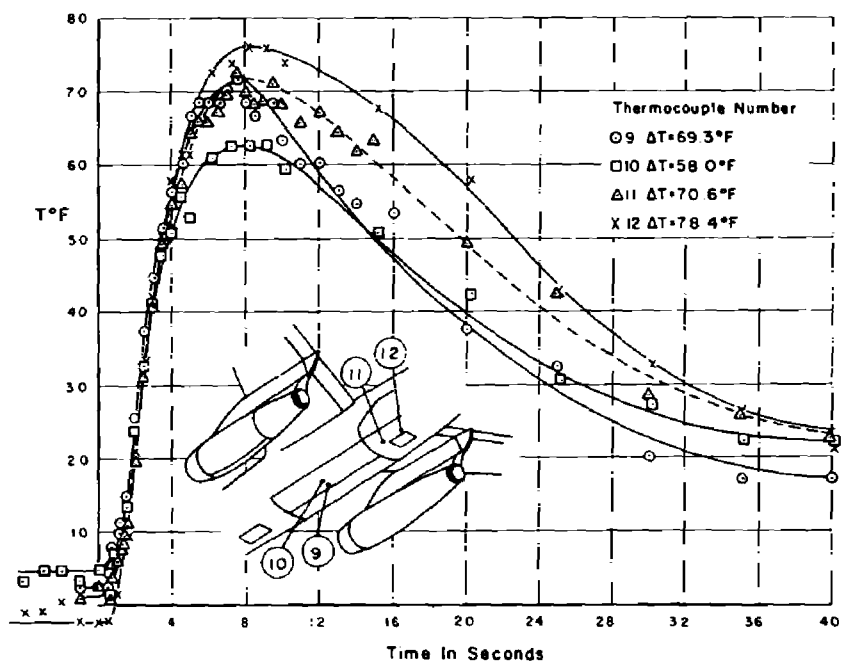


Figure 5.30 Temperature time history of bomb bay door and lower fuselage, Shot Tewa.

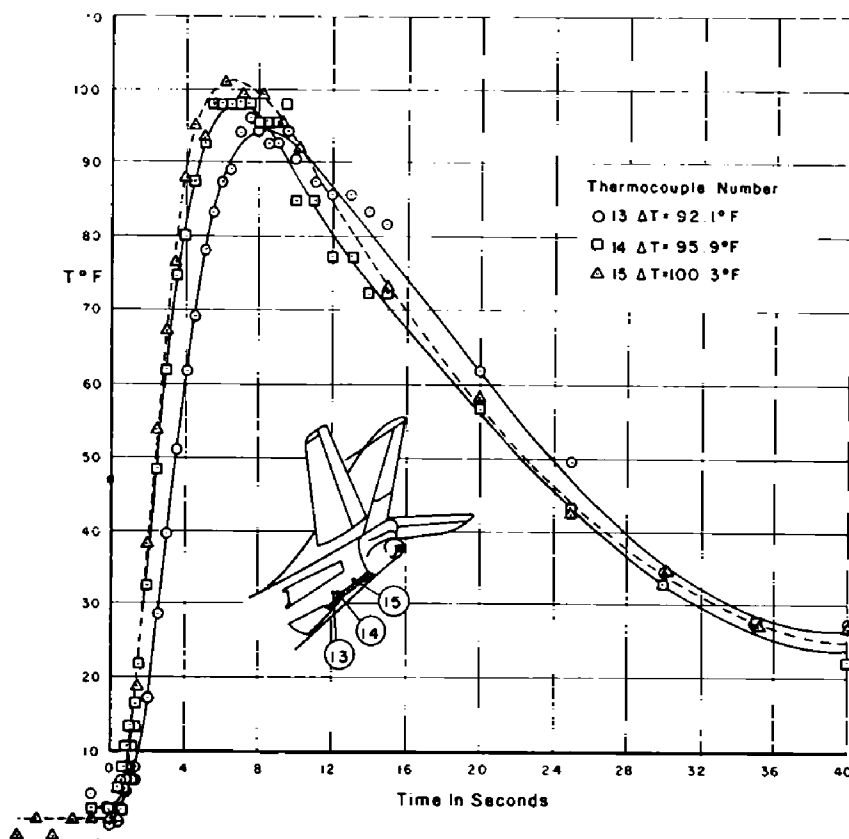


Figure 5.31 Temperature time history of arresting hook area, Shot Tewa.

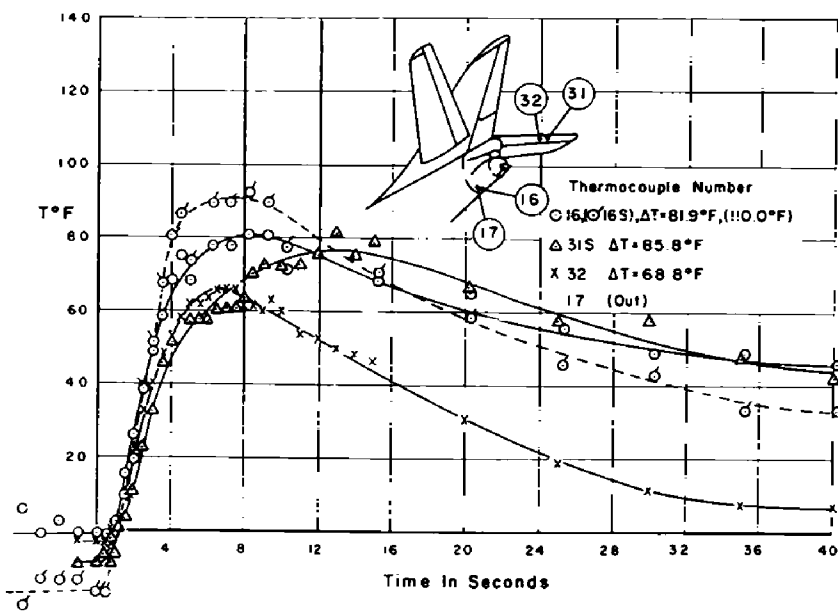


Figure 5.32 Temperature time history of quartz covered thermocouple compared to adjacent uncovered thermocouple, Shot Tewa.

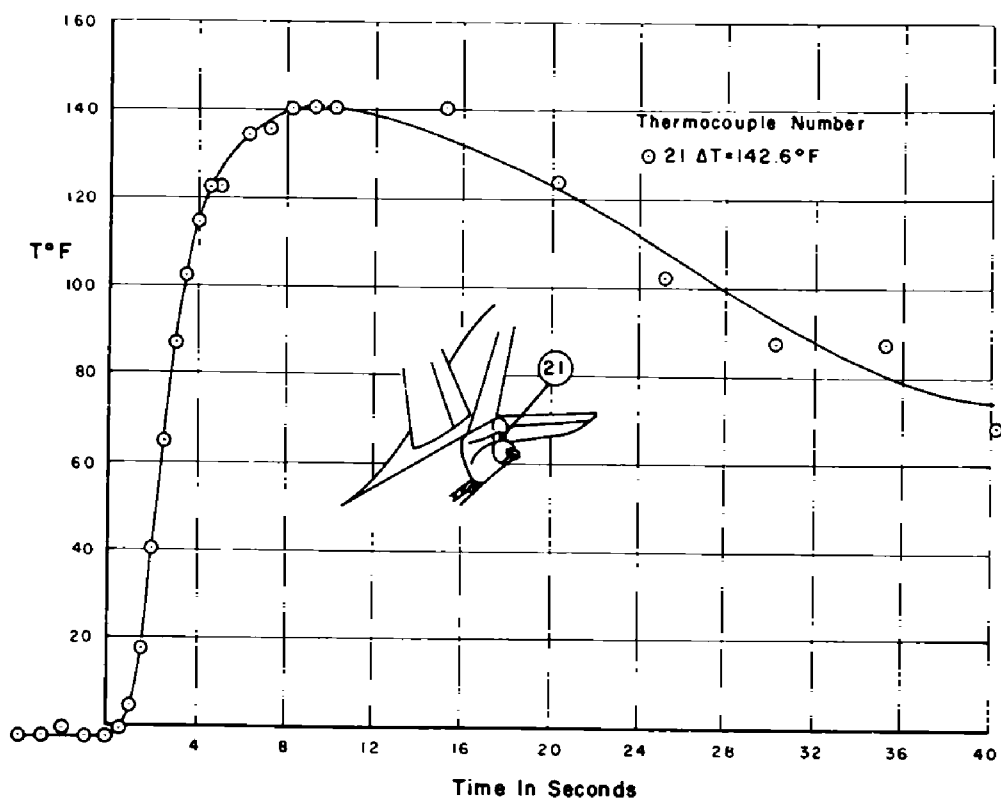


Figure 5.33 Temperature time history of tail turret, Shot Tewa.

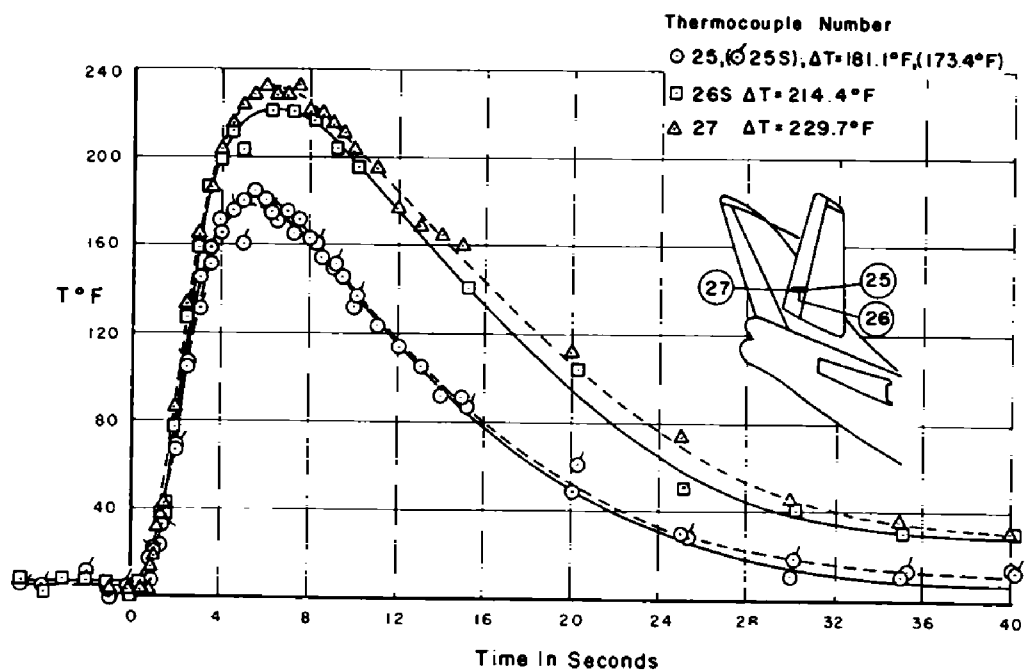


Figure 5.34 Temperature time history of gray painted elevator skin, Shot Tewa.

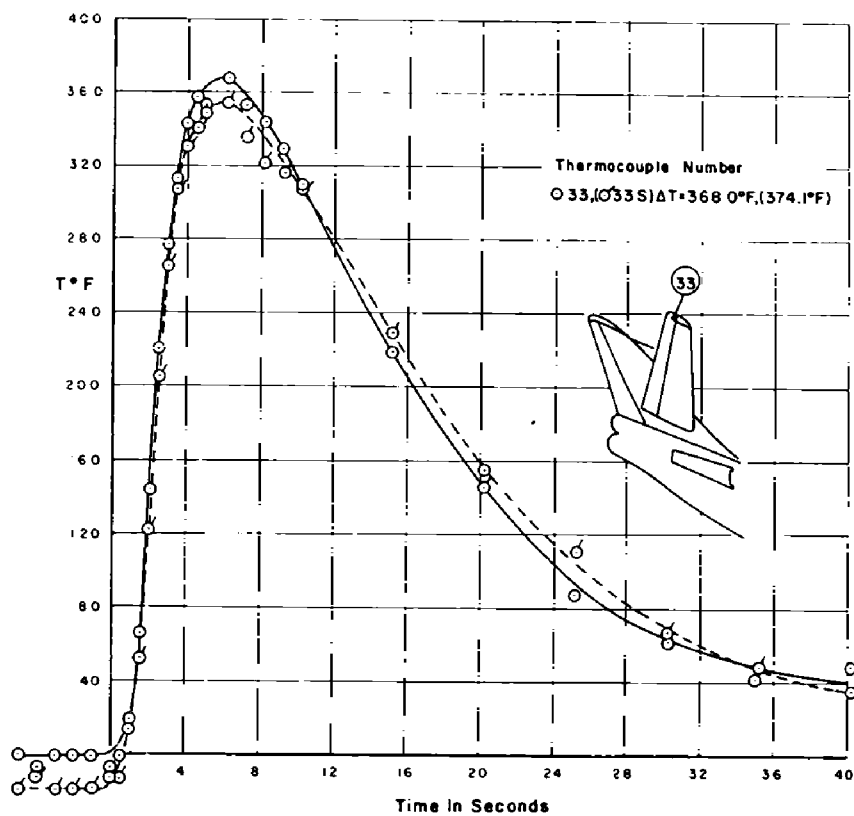


Figure 5.35 Temperature time history of blue painted elevator skin, Shot Tewa.

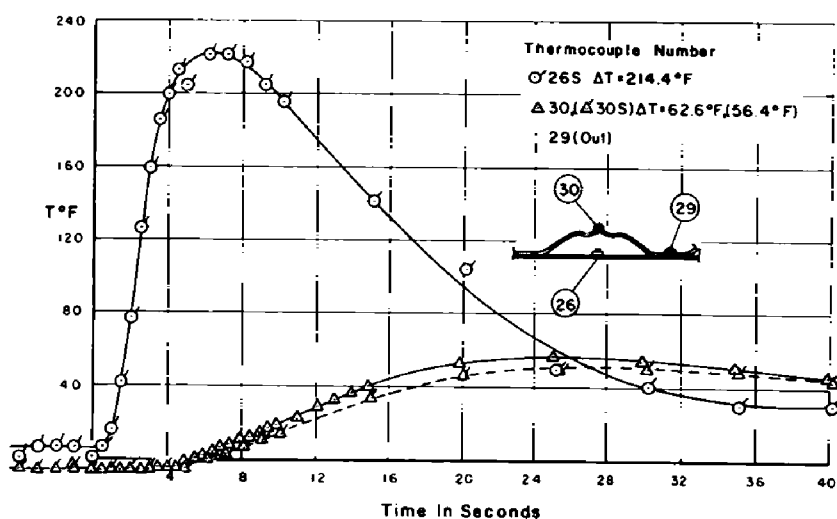


Figure 5.36 Temperature time history comparing outer skin and internal beaded doubler, Shot Tewa.

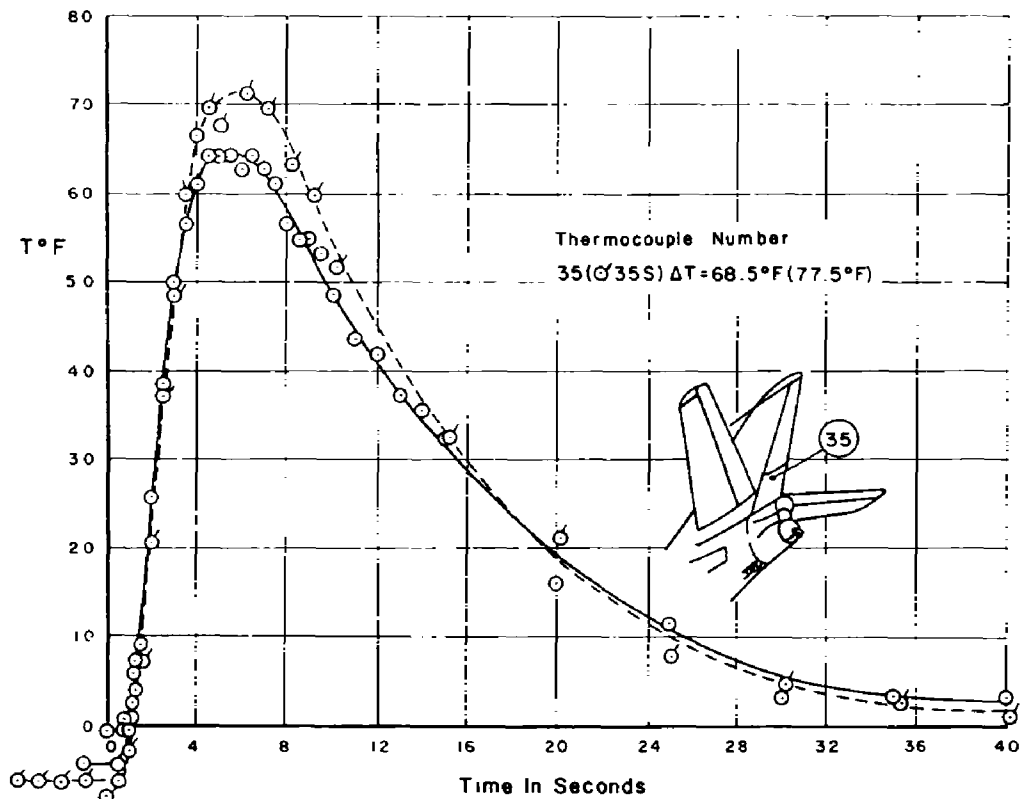


Figure 5.37 Temperature time history of lower rudder, Shot Tewa.

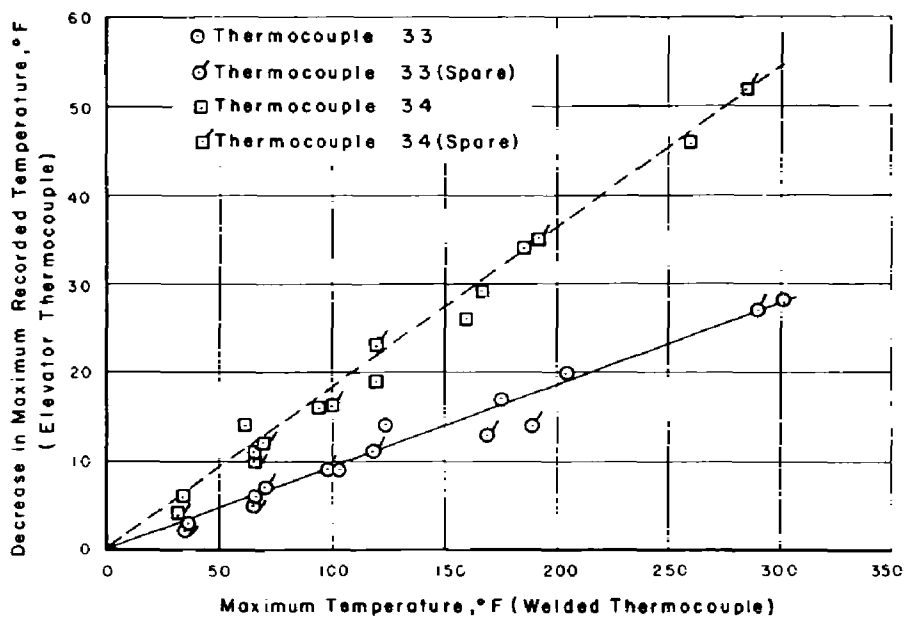


Figure 5.38 Thermocouple lag calibration, laboratory check of lag in maximum recorded temperature, typical thermocouple installations from flight, airplane elevator when compared with welded low lag thermocouple.

Chapter 6

RESULTS AND DISCUSSION OF TEMPERATURE RISE CALCULATED FROM MEASURED THERMAL INPUT

With the rate at which the thermal energy is received determined from the irradiance versus time data obtained from the indirect radiometer, or as estimated from the direct radiometer or calorimeter data, the time history of the temperature in selected areas can be calculated. Also the simplified method of calculating the maximum temperature rise can be checked.

6.1 CALCULATION OF TEMPERATURE TIME HISTORY

The time history of temperature rise in a specific area was determined by a step-by-step solution of Equation 1.8 in Section 1.3.2. The irradiance relationship used was the one which appeared the most reasonable when considered with all the measured thermal data. The other factors required are the absorptivity of the surface (a) and the heat transfer coefficient (\bar{h}). The absorptivity values which were found to give the best correlation were 0.2 for the white paint, 0.55 for the gray paint, and 0.9 for blue. The white and gray values are in approximate agreement with measurements made in the field with a spectrophotometer, but no such measurements were made for the blue paint.

With regard to the values of the paint absorptivity, it should be noted that although the above quoted values gave good data correlation, the actual value was probably somewhat higher. Examination of the equation for calculating the temperature shows that the value of the absorptivity appears as a ratio of the absorptivity to the thermal capacity of the material (the factor a/G). In this analysis the thermal capacity has been used as that for the aluminum skin. Actually there was a film of paint over the aluminum skin, which would increase the thermal capacity of the complete system somewhat. If this increase in thermal capacity were taken into account, the same ratio of the factor a/G could be obtained by a similar increase in the absorptivity of the paint. If a similar adjustment were made in the heat transfer coefficient, the identical data correlation would be obtained.

The heat transfer coefficient was determined by the method outlined in Appendix B.

If the temperature rise were examined only from the standpoint of the maximum temperature rise obtained, it would be possible to correlate any temperature by adjusting the absorptivity and heat transfer coefficient. However, when the time history of the temperature rise is considered, the two parameters cannot be assumed arbitrarily, due to their effect not only on the maximum temperature but on the time to reach the maximum temperature. If the absorptivity is changed, only the temperature is effected while the time to peak is unchanged. If the

heat transfer coefficient is changed, the time to maximum temperature is changed as well as the maximum temperature. Also, the peak value of the irradiance can change the time at which the maximum skin temperature is obtained even though the time for maximum irradiance is unchanged. These effects are illustrated in the following discussion.

Figure 6.1 illustrates that decreasing the absorptivity reduces the maximum temperature rise, but does not effect the time to peak.

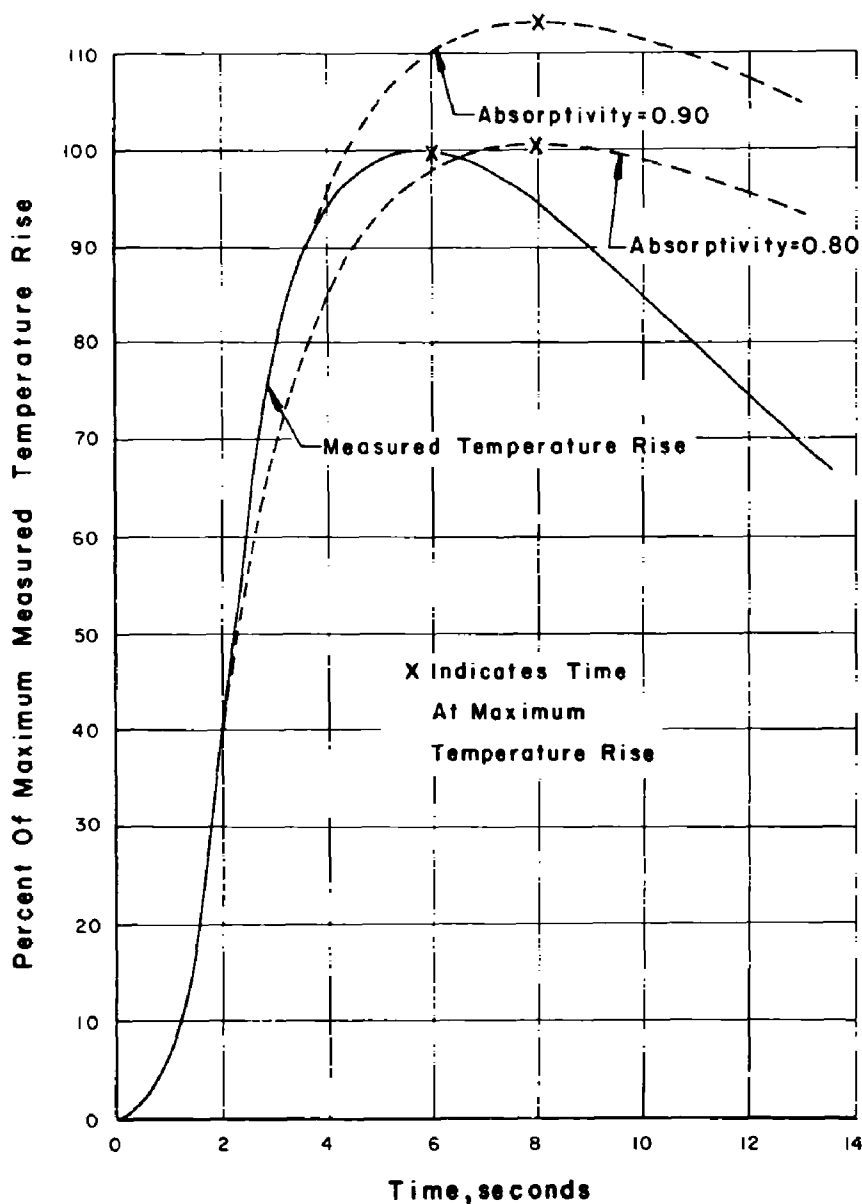


Figure 6.1 Effect of absorptivity on calculated temperature time history.

Figure 6.2 illustrates the effect of increasing the heat transfer coefficient. This decreases both the maximum temperature rise and the time to peak. It can be seen that further increase would bring the time into agreement, but the temperature would be lower than measured. How-

ever, as seen in the previous example, the temperature could be increased without affecting the time correlation by an increase in the absorptivity.

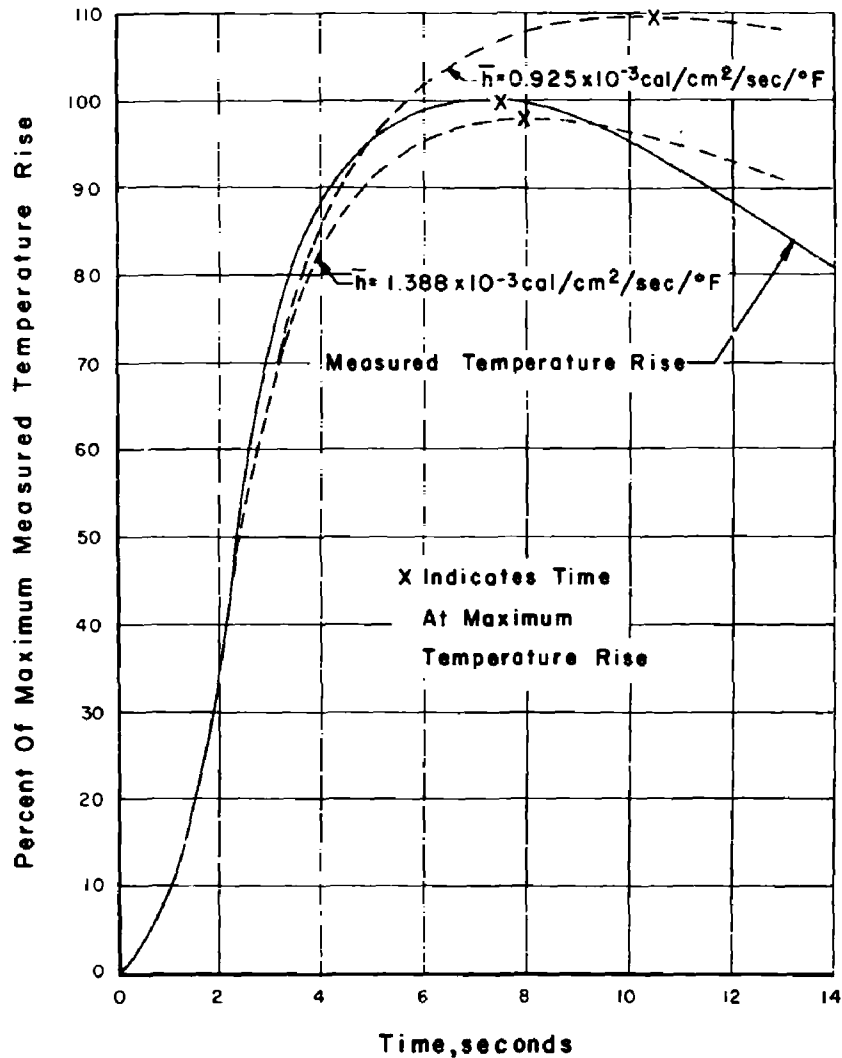


Figure 6.2 Effect of heat transfer coefficient on calculated temperature time history.

Figure 6.3 shows the effect of changing the peak irradiance value even though the time to peak is not changed. The two irradiance time relationships used were the measured and estimated indirect from Shot Tewa. It can be seen that this changes the time to maximum temperature as well as the maximum temperature and illustrates the importance of carefully selecting the proper thermal pulse data.

With this explanation of the background and technique used, the actual correlation of results will be discussed.

To illustrate the results of the temperature correlation, the data obtained for Shot Tewa will be discussed in detail as it illustrates all the basic factors. Data are available for white, gray, and blue painted skin surfaces which offer more opportunity to check the effect of the various parameters.

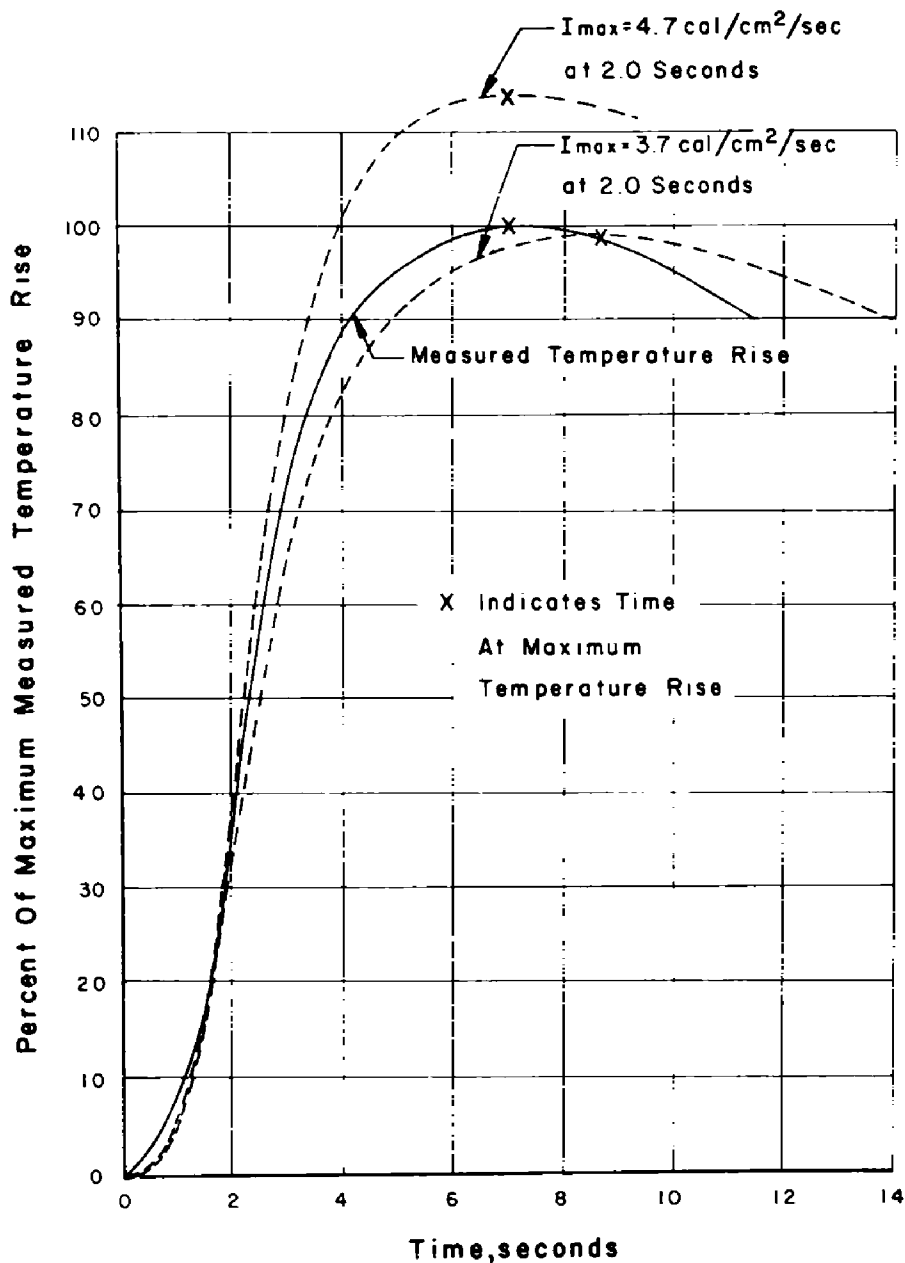


Figure 6.3 Effect of maximum irradiance on calculated temperature time history.

The measured temperature rise on the blue paint section of the elevator and the calculated temperature rise using an absorptivity of 0.9 and the heat transfer coefficient as calculated in Appendix B are presented in Figure 6.4. Calculated temperatures are shown for the thermal pulse as measured by the indirect radiometer, and for the thermal pulse estimated from the calorimeter data as discussed in Section 4.3.3. The measured temperature rise is 368 degrees at 5.8 seconds, the measured thermal pulse gives 370 degrees at 8.2 seconds, and the estimated thermal pulse gives 428 degrees at 6.8 seconds.

Similar plots are presented for the gray painted surface for an absorptivity of 0.55 in Figure 6.5. Here the measured temperature rise is 229 degrees at a time of 6.5 seconds, the measured indirect pulse gives 232 degrees at 8.6 seconds, and the estimated pulse gives 287 degrees at 7.0 seconds.

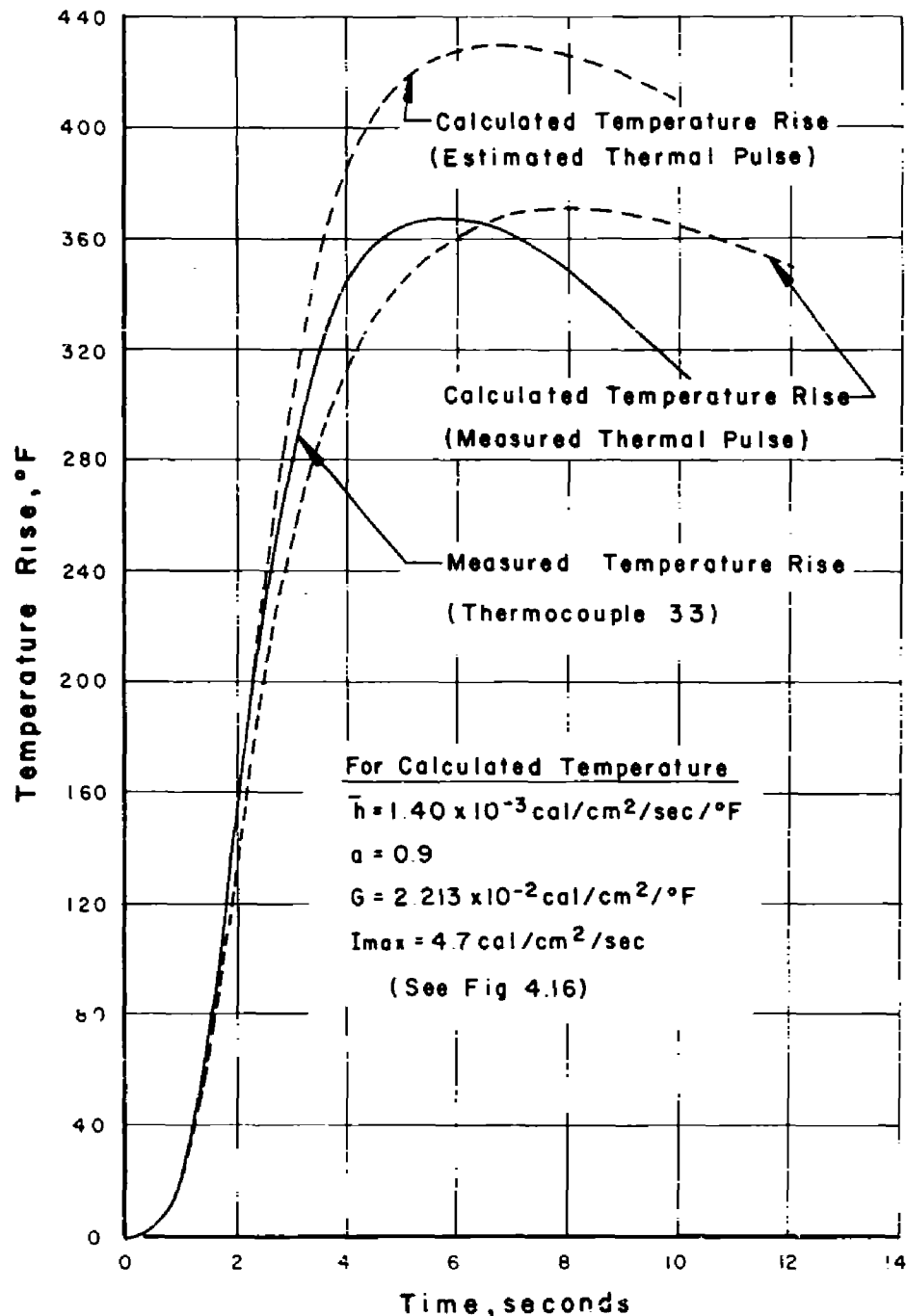


Figure 6.4 Comparison of measured and calculated temperature time history in blue painted elevator skin, Shot Tewa.

The results for the white surface with an absorptivity of 0.2 are shown in Figure 6.6. The measured temperature rise is 86 degrees at 6.6 seconds, and the calculated values for the measured and estimated thermal pulses are 85 degrees at 8.6 seconds, and 97 degrees at 7.0 seconds, respectively.

These comparisons for the three paint surfaces show that the measured pulse gives good agreement in the value of the maximum temperature, but the time to peak temperature is much greater than measured. When the estimated pulse is used, the calculated time to peak comes

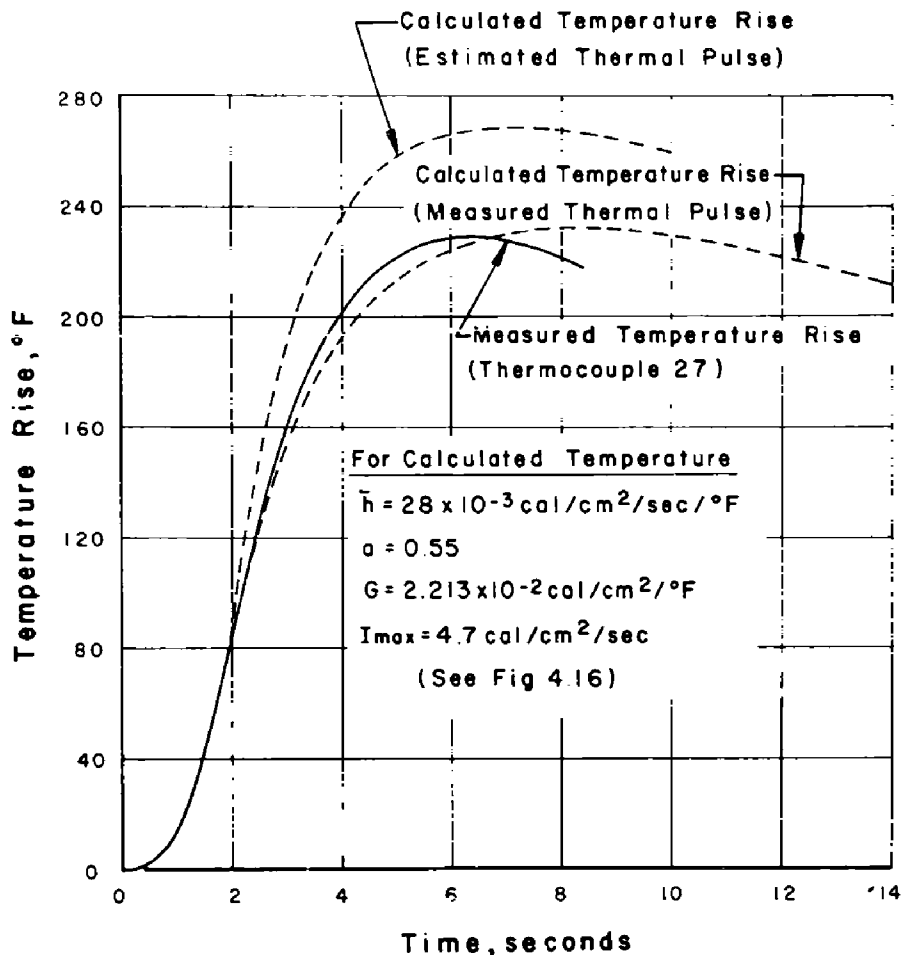


Figure 6.5 Comparison of measured and calculated temperature time history in gray painted elevator skin, Shot Tewa.

into much closer agreement, but the temperatures are higher than measured. Although no quantitative numerical analysis of the discrepancy can be made, certain factors which would effect the temperature rise can be mentioned and a rough approximation of their effect considered.

For the blue painted section the laboratory tests discussed previously in Section 5.2 show that for this actual thermocouple the EC 801 cement over the thermocouple junction reduced the recorded temperature approximately 9 percent when compared to the welded thermocouple without cement. If this correction were applied to the measured temperature, it would raise the 368 degrees to 405 degrees, $(368/0.91)$.

Another source of difference is that no allowance was made in the calculated time history for the heat conducted from the skin surface to the surrounding structure. Accurate evaluation of this quantity of heat would be a complicated process of indefinite accuracy and is not attempted here. However, a rough approximation of the magnitude may be obtained from a brief study of the temperature recorded at the top of the beaded doubler behind the elevator skin panel, (Thermocouple 30).

The maximum rate at which the heat was conducted into the beaded doubler was determined by measuring the slope of the comparatively straight-line portion of the temperature time history (Figure 5.36). This value was found to be approximately 4.5 degrees per second for a total temperature rise of the outside skin of 220 degrees. If the assumption is made that

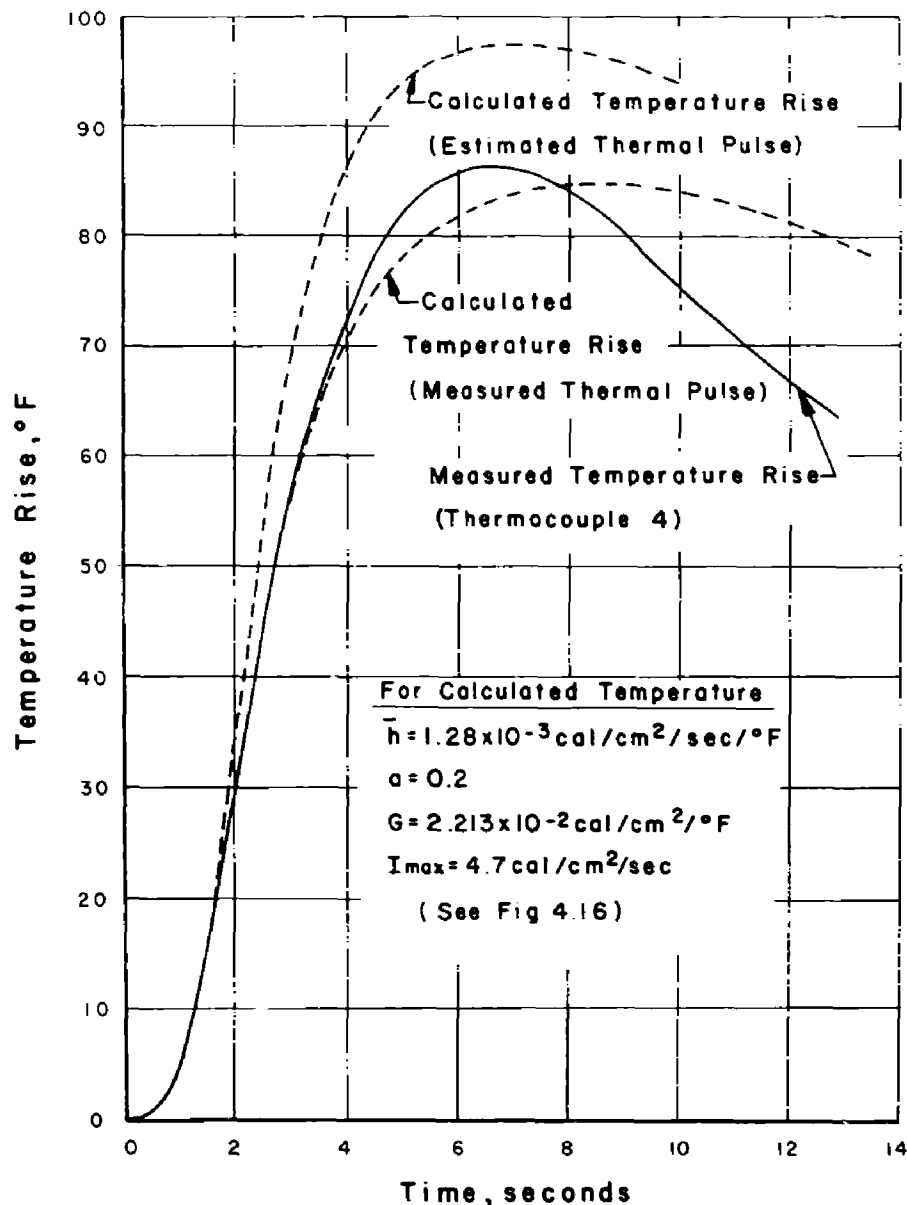


Figure 6.6 Comparison of measured and calculated temperature time history for white painted elevator skin, Shot Tewa.

the rate of temperature increase in the doubler, which is immediately behind the skin and spot welded to it at frequent intervals, was caused by an equivalent loss of heat in the outer skin, the maximum rate at which the temperature was reduced in the outer skin can be estimated. Since the inner doubler is 0.016 inch and the outer skin is 0.025 inch, the rate at which the temperature is reduced by conduction would be $(4.5 \times 0.016/0.025)$ or 2.9 deg/sec. Since the time at which the measured temperature peaked is 5.8 seconds, the correction to the calculated temperature would be $(2.9 \times 5.8) = 17$ degrees. This would correct the calculated temperature to 411 degrees. Thus the corrected agreement would be 405 degrees measured and 411 degrees calculated. It should be stressed that the above discussion is only a rough approximation. It assumes the estimated rate was effective throughout the rise to peak temperature, and no correction was applied for the gradient between the outer and inner skin faces. However, it did in-

dicate the approximate magnitude of the correction and partly explained the discrepancy between the measured and calculated maximum temperature rise.

The time to maximum temperature was measured to be 5.8 seconds and calculated to be 6.6 seconds. However, if a rigorous correction for conduction were included, it would have the same effect as an increase in the heat transfer coefficient which would decrease the time to peak.

The above corrections can be applied to the gray and white painted skin panels. For the gray panel the corrected measured temperature becomes, $(229/0.91)$, 252 degrees at 6.5 seconds, and the corrected calculated temperature becomes 248 degrees, $(267 - 2.9 \times 6.5)$, at 7 seconds. For the white the corrected measured temperature would be, $(88.5/0.91)$, 97 degrees at 6.6 seconds, and the calculated temperature of 97 degrees at 7.0 seconds. This temperature would not require the correction for the beaded doubler construction as it did for the nacelle where this type of construction was not used.

For Shot Zuni the maximum temperature recorded was in the 0.025 skin at the aft end of the lower surface of the fuselage. The comparison of the measured and calculated temperature time histories is shown in Figure 6.7. There is probably not a great deal of correction needed

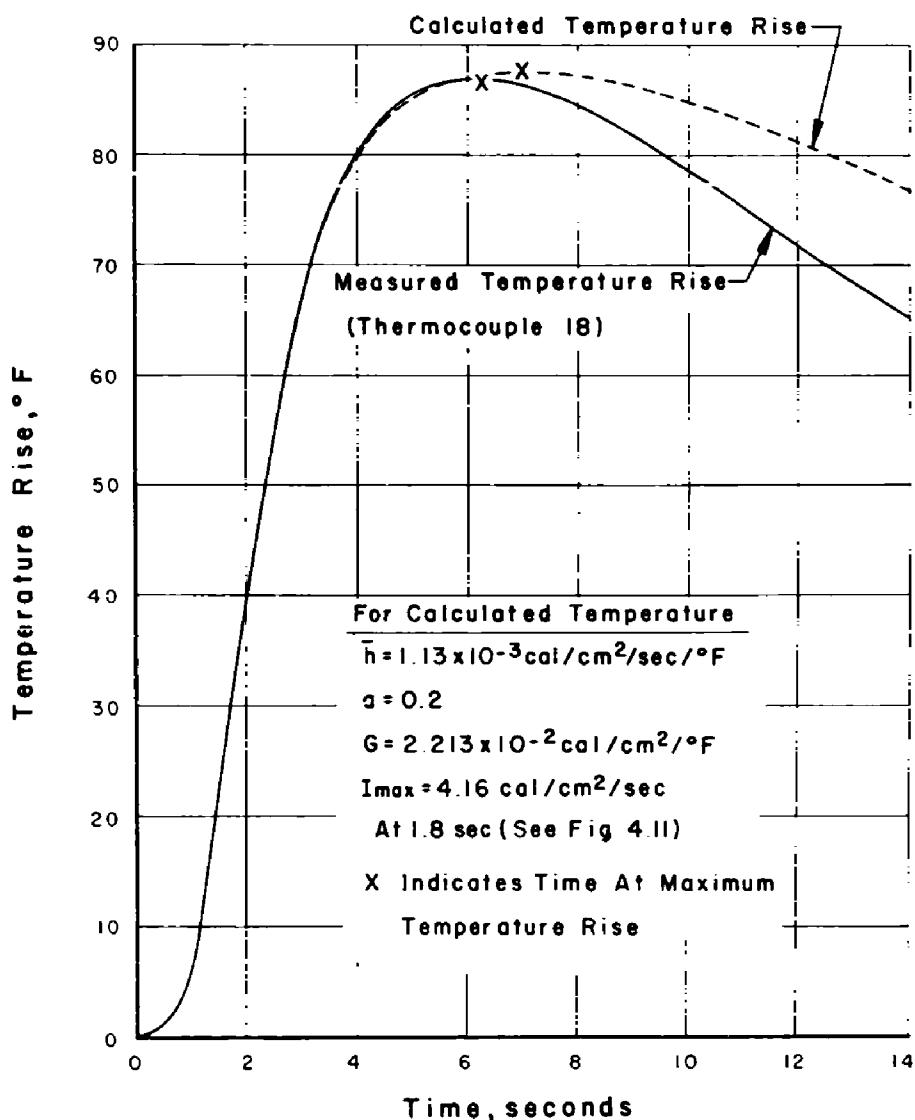


Figure 6.7 Comparison of measured and calculated temperature time history for white painted skin, Shot Zuni.

at these temperatures. The thermocouple was accessible in the fuselage and therefore did not have as much of the EC 801 cement as the thermocouples inside the elevator. The calculated temperature would not require a conduction correction because the skin was a fairly large panel without a backing beaded doubler. The measured temperature rise was 87 degrees, and the calculated was 87.5 degrees. The time measured to peak was about 6.3 seconds, and the calculated was 7.0 seconds.

The temperature time history comparison for Shot Flathead is shown in Figure 6.8. The measured temperature rise is 69.5 degrees, and the calculated is 64.5 degrees. The time to

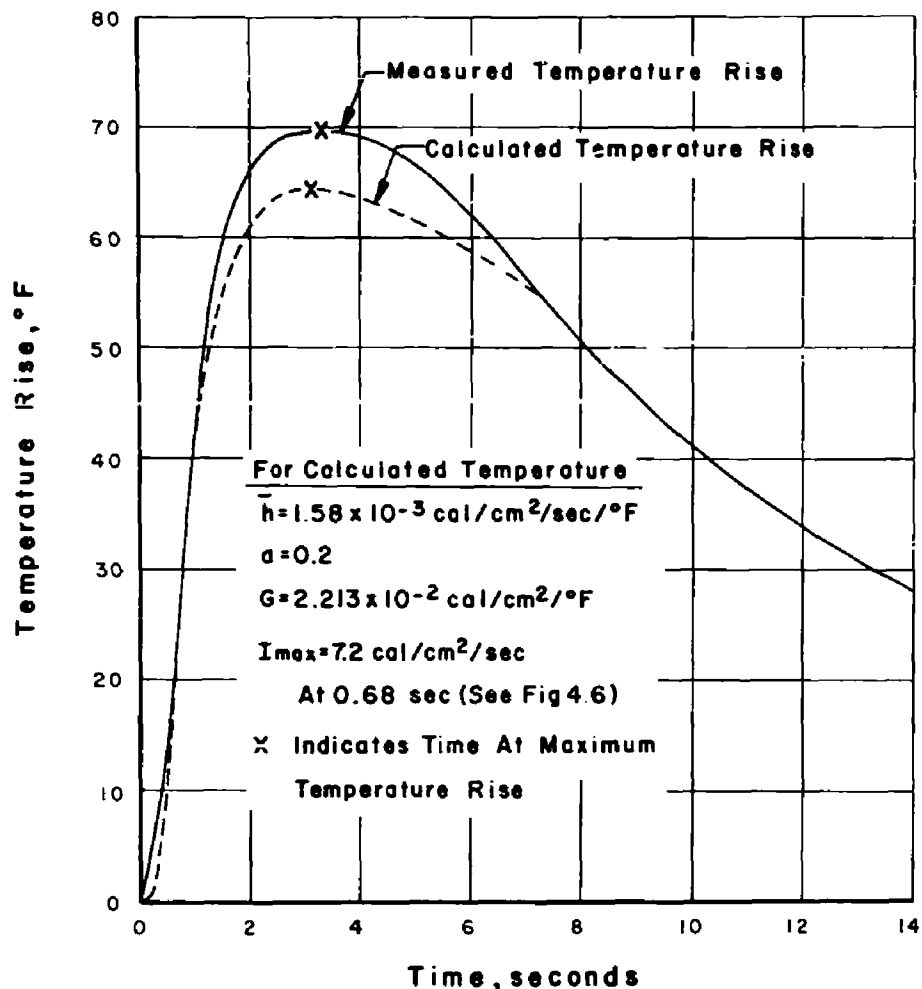


Figure 6.8 Comparison of measured and calculated temperature time history for white painted skin, Shot Flathead.

the maximum temperature was measured to be approximately 3 seconds, and the calculated time was 2.5 seconds.

It will be noted that in all the comparisons shown the predicted temperature decay history is far less rapid than the measured. This could possibly be explained as a lag in the measuring thermocouple which would read higher when the cooling effect was greater than the heating input. Also, the conduction of heat from the outer face would be greatest at the maximum temperature difference between the inner and outer skin and neglecting the term in the calculation would reduce the predicted temperature decay.

The agreement of the calculated and measured temperature time histories for the cases of the maximum rise has been shown to be good. However, the locations checked were all near

the trailing edge of the particular surface, such as elevator, nacelle, or fuselage. When the locations further forward were checked, the measured temperature rise was less than would have been calculated.

To illustrate this effect, time histories of the three locations on the elevator were calculated for Shot Tewa. The three locations were 5.4 feet, 6.0 feet, and 6.8 feet, respectively, from the leading edge of the horizontal stabilizer. The corresponding heat transfer coefficients that were computed from Appendix B are 1.34×10^{-3} , 1.30×10^{-3} , and 1.28×10^{-3} cal/cm²/sec/F.

The calculated time histories are shown in Figure 6.9. These show that the calculated effect of chord position is only 3 or 4F. However, the measured temperature rises for the same locations, as shown in Figure 6.9, indicate a difference in temperature of approximately 46F.

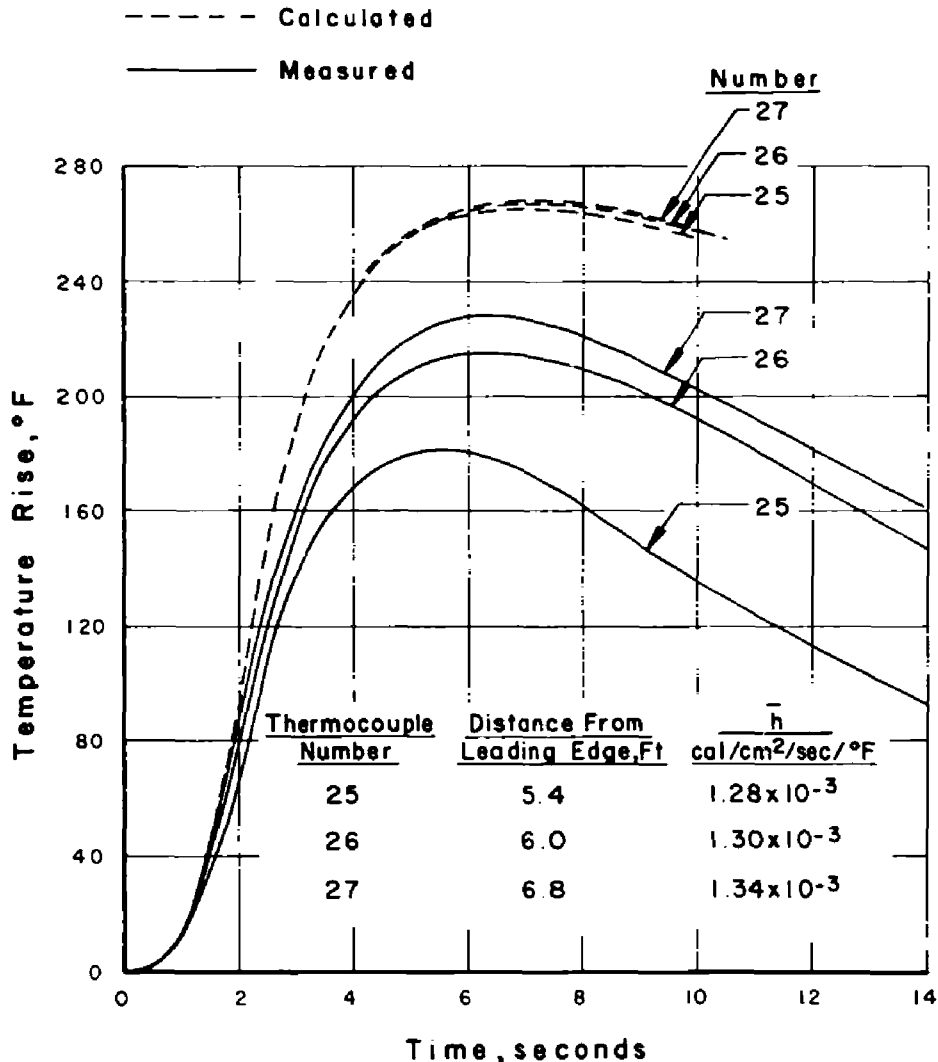


Figure 6.9 Effect of distance from leading edge of horizontal stabilizer on measured and calculated temperature time history, gray paint, Shot Tewa.

This large variation with distance from the leading edge is apparent on other shots as well, as is indicated by the maximum temperature rise summaries, Figures 5.1 to 5.7.

These discrepancies are pointed out to illustrate that the method of computing the heat transfer coefficient appears to be satisfactory for the maximum temperature rise condition at the trailing edge of a surface. However, it does not appear to be accounting adequately for the effect of distance from the leading edge along the surface.

Also, the absolute magnitude of the heat transfer coefficient has not actually been checked, only the ratio of heat transfer coefficient to the thermal capacity of the material (the factor \bar{h}/G in Equation 1.8).

Therefore, it appears that there is still a definite need to improve the method of calculating the heat transfer coefficient.

6.2 SIMPLIFIED CALCULATION OF MAXIMUM TEMPERATURE RISE

For the calculation of an airplane delivery study, or an aircraft position for participation in a special weapons test, the maximum temperature rise is usually of more significance than the time history of the temperature. Therefore, it is extremely convenient to calculate the temperature rise as though the aircraft was stationary and to use a factor to account for the aerodynamic cooling and the increase of the aircraft slant range during the thermal pulse rather than perform the more laborious time history calculations. This factor is commonly called the cooling and fly-away factor and is defined as the ratio of the temperature reached by the moving aircraft with aerodynamic cooling and fly-away to that which would be reached if the aircraft were a stationary receiver. Treating the airplane as a stationary receiver with a factor to account for the cooling and fly-away requires the comparatively simple calculation shown in Equation 1.9, Section 1.3.2, while the rigorous solution of the moving aircraft requires the laborious step-by-step calculations of Equation 1.8, Section 1.3.2.

The maximum temperature rise computed by the two methods, and the measured temperature rise is shown in Table 6.1. The step-by-step solution is shown for both the measured

TABLE 6.1 COMPARISON OF MEASURED AND CALCULATED TEMPERATURE RISE

	Measured maximum temperature rise	Calculated maximum temperature rise		
		Step-by-step method		
		Measured pulse	Standard pulse	Simplified method
	°F	°F	°F	°F
Tewa-Blue	368(405*)	429(411†)	500	510
Tewa-Gray	229(252*)	267(248†)	313	319
Tewa-White	89(97*)	97	113	116
Zuni-White	87	88	89	86
Flathead-White‡	70	65	67	61
Flathead-White§	55 (59*)	59 (56†)	55	54

*Corrected for thermocouple lag (see paragraph 5.2).

†Corrected for heat conduction (see paragraph 6.1).

‡Aft fuselage (Thermocouple 18).

§Elevator (Thermocouple 33).

thermal field and the thermal field computed from the normalized pulse published in Reference 3, as the cooling and fly-away factors of Reference 3 are based on the published pulse. The same values of attenuation and heat transfer coefficients were used in both methods.

To simplify the comparison, all calculations are with the effective linear attenuation (Table 4.2). Thus, the peak irradiances are the same for the calculated thermal pulse and the measured.

From Table 6.1 the complete link of the temperature correlation can be seen. As expected, the maximum temperature rise computed by the simplified method agreed well with the value computed by the step-by-step calculation from the published normalized standard pulse upon which the cooling and fly-away factors were based. Therefore, in the yield range covered in

this analysis (370 kt to 5 Mt), the cooling and fly-away factor of Reference 3 gives satisfactory results if the actual pulse is identical or nearly so to the published normalized pulse.

The step-by-step calculation from the calculated thermal input agreed well with that calculated from the measured thermal input for Shots Zuni and Flathead, but gave too high a value for Shot Tewa. A study of the thermal pulses in Figures 4.19 to 4.21 shows that for Shot Tewa the actual measured pulse had much less area under it so that the energy received was less, and therefore the temperature rise was less.

As discussed previously in Section 6.1 the calculated temperature time history agreed well with the measured time history.

The results show that the simplified method of computing maximum temperature rise using the cooling and fly-away factors of Reference 3 gives excellent results if the actual thermal pulse is identical, or nearly so, to the normalized pulse used in the analysis of Reference 3. In cases where these calculations differ from the measured results, the reason is seen to be in the thermal pulse of the device. Unless an actual pulse is supplied for a specific weapon, it appears that the normalized pulse can be used with satisfactory results.

Chapter 7

RESULTS AND DISCUSSION, GAMMA RADIATION

No significant levels of gamma radiation were recorded or expected during these tests; consequently, no discussion is presented.

Chapter 8

RESULTS AND DISCUSSION, SHOCK WAVE EFFECTS

8.1 OVERPRESSURE

The peak values of measured and calculated overpressure are presented in Table 8.1. Some discrepancies exist between the three sources of overpressure, which were the boom on the vertical fin and one on either side of the fuselage. It is believed these were within the experimental accuracy of the instruments and recording system because of the low level of overpressure. For this same reason no reliable time history data of the overpressures were obtained.

TABLE 8.1 MEASURED AND CALCULATED PEAK OVERPRESSURE

Event	Maximum overpressure (psi)			
	Boom	L.H. fuselage	R.H. fuselage	Calculated
Cherokee*	0.10	0.15	0.00	0.125
Zuni	0.33	0.36	0.34	0.332
Flathead	0.64	0.73	0.69	0.674
Apache*	0.36	0.39	0.31	0.325
Navajo	0.37	0.41	0.36	0.386
Tewa	0.31	0.34	--	0.306
Huron*	0.41	0.44	--	0.371

*Aircraft positions are of doubtful accuracy.

Shown for comparative purposes are the values which were calculated using the method of modified Sachs scaling outlined in Appendix A for the actual yield times a factor of two, to account for being in the Mach region, and the actual aircraft position at shock arrival.

Calculated overpressures, using a yield multiple of two, agreed well with measured values. Since yield factor is somewhat of a question in calculations of this type, Figure 8.1 is shown to present the calculated overpressure as a function of the yield factor for each of the shots. Only those shots for which accurate positions are known are included. Also shown are the values as measured by the boom mounted instrument. This figure shows that the calculated overpressure agrees with the boom measured value between a range of yield factor of 1.8 and 2.0 for all the shots presented. The overpressure measured by the fuselage source is usually higher, but it is believed the boom mounted instrument is probably the more reliable. The yield factor of two appears to be valid for these tests with the positions in the Mach region.

8.2 TIME OF SHOCK ARRIVAL

The time of shock arrival as measured and calculated using the method of modified Sachs scaling as outlined in Appendix A is shown in Table 8.2. Calculations of the shock arrival time

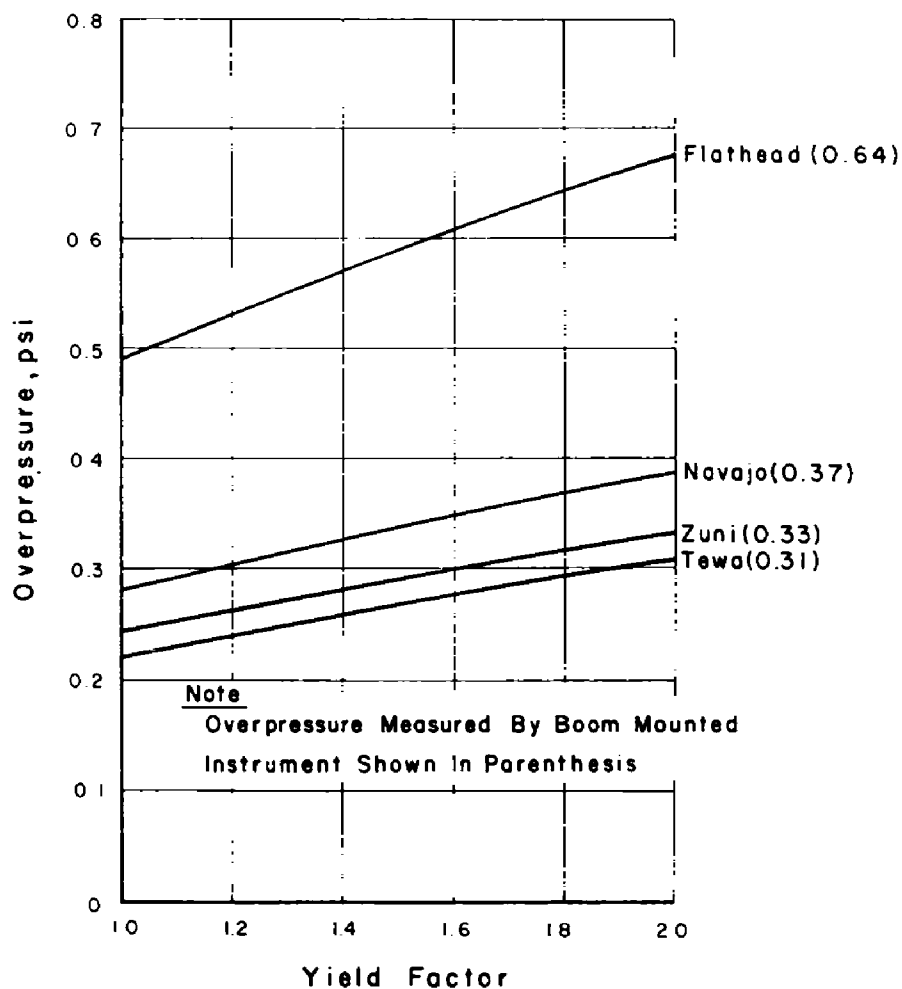


Figure 8.1 Calculated overpressure versus yield factor.

TABLE 8.2 MEASURED AND CALCULATED TIME OF SHOCK ARRIVAL

Event	Measured	Calculated†	Calculated‡	Time Error†	Time Error‡
	sec	sec	sec	percent	percent
Cherokee*	176	166.3	157.0	-5.5	-10.9
Zuni	81.56	79.5	76.4	-2.6	-6.5
Flathead	27.18	26.2	25.8	-3.6	-5.0
Apache*	67.86	67.8	65.2	-0.1	-3.9
Navajo	68.26	67.3	63.4	-1.5	-7.1
Tewa	80.87	82.2	77.1	+1.7	-4.5
Huron*	39.03	38.9	38.2	-0.3	-2.2

*Aircraft positions are of doubtful accuracy.

†Based upon speed of sound at aircraft altitude.

‡Based upon speed of sound at average altitude between the aircraft and burst point.

were made using the speed of sound at the aircraft altitude and at the average altitude between the aircraft and the explosion. All calculations are for twice the bomb yield as the airplane was always in the fused shock region.

It can be seen that agreement obtained with aircraft altitudes is excellent and better than with average altitude. For Shots Cherokee and Huron, the apparent discrepancy was probably due to the uncertain accuracy in the determination of the aircraft position at shock arrival.

Figure 8.2 shows the effect of yield factor on time of shock arrival. The variation with yield factor is quite small, and no valid conclusions can be made. However, it can be seen from Table 8.2 that the use of a yield factor of 2.0, as indicated by the overpressure data, gives satisfactory agreement.

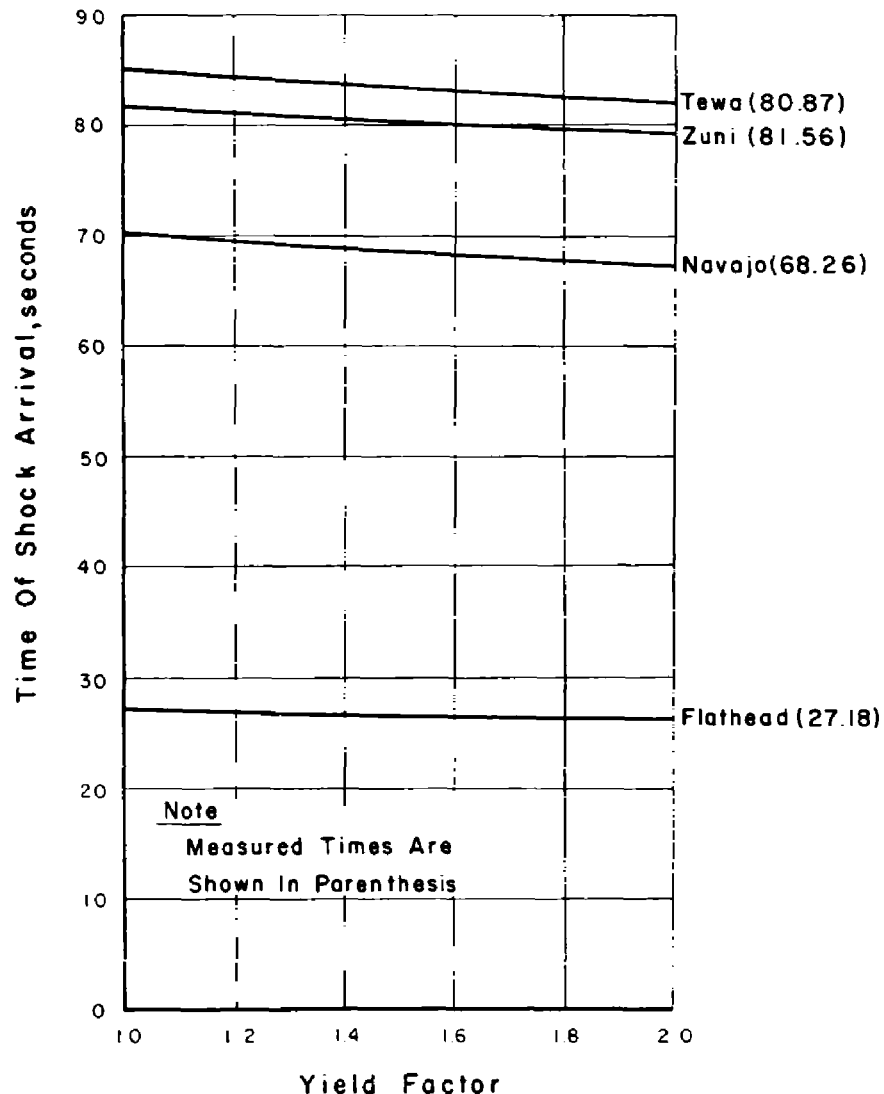


Figure 8.2 Calculated time of shock arrival versus yield factor.

8.3 ENGINE OPERATION

Analysis of the engine data obtained during flight of the A3D radially outbound from the test explosions indicates that there were no violent reactions of the engines due to the passage

of the blast waves encountered. The maximum effect of shock waves on engine performance parameters is shown in Table 8.3. Unfortunately, for accurate analysis purposes, the observed changes in engine performance were so small that they could be within the accuracy of the measuring and recording equipment.

TABLE 8.3 EFFECT OF SHOCK WAVE ON ENGINE PERFORMANCE PARAMETERS

Event	Conditions before shock					Conditions after shock				
	P_{t_1}/P_{t_2}	$N_1/\sqrt{\theta_{t_1}}$	$N_2/\sqrt{\theta_{t_1}}$	P_{s_a}/P_{t_1}	F_N	P_{t_1}/P_{t_2}	$N_1/\sqrt{\theta_{t_2}}$	$N_2/\sqrt{\theta_{t_2}}$	P_{s_a}/P_{t_2}	F_N
		rpm	rpm		lb		rpm	rpm		lb
Zuni	1.6	5589	9390	7.47	1780	1.60	5592	9403	7.72	1840
Flathead	1.68	5497	9223	7.88	2950	1.68	5489	9240	8.10	3100
Apache	2.85	5757	9511	9.62	6240	2.79	5746	9522	9.57	6190
Navajo	3.04	5886	9651	8.81	6060	3.54	5905	9670	10.58	6430
Tewa	3.56	5899	9662	11.14	5890	3.33	5911	9668	10.69	5730

P_{t_1} - Total pressure taken at a station just aft of turbine.

P_{t_2} - Total pressure taken at a station just forward of compressor face.

N_1 - Low pressure compressor rotor speed (rpm).

N_2 - High pressure compressor rotor speed (rpm).

θ_{t_1} - The ratio of temperature just forward of compressor divided by 518.4 °R.

P_{s_a} - Static pressure taken behind shock wave.

F_N - Net thrust = gross thrust - ram thrust (lb).

8.4 AIRPLANE RESPONSE TO GUST LOADING

Results of the gust investigation for Operation Redwing consisted of the set of measured time histories of airplane response together with the corresponding time histories of predictions as obtained from the analog computer results presented in References 11 and 12. These appear in Figures 8.3 through 8.21. As mentioned in Section 2.2.1 quantities measured were center of gravity acceleration, wing bending moment, and airplane pitch rate. Discussion of results is divided into three parts, each corresponding to a measured quantity.

Analysis of the gust response data indicated the inadequacy of the instrumentation for correlation between measurements of acceleration and wing stresses. There is little reason to believe that more thorough wing instrumentation and calibration would not have resulted in acceptable agreement with analytical prediction of wing responses.

It is seen that the prediction method provides a reasonable index to the mean center of gravity acceleration but fails to reproduce the high frequency response which was experienced. The few bending moment records obtained failed to verify the predictions; this is also true of the pitching velocities.

Despite the limitations of the gust response instrumentation, sufficient experimental data were obtained to substantiate the pretest conclusion that A3D response to gusts would not be the limiting factor for high altitude delivery missions. The aircraft response shown in Figures 8.3 through 8.9 when considered in light of the limit load factors discussed in Section 2.1.1 precluded establishing wing stresses as a limiting consequence of the delivery mission being considered.

8.4.1 Center of Gravity Acceleration. The most obvious feature of the measured response for the center of gravity accelerometer is the presence in the early stages of the response of several high frequency acceleration components which do not appear in the predicted curves. Frequencies varying from approximately 11 to 30 cps are apparent. In the course of the tests an accelerometer was installed on the wing center section at the airplane center of gravity. It was hoped that a comparison of the acceleration at this point with the center of gravity accelerometer response would indicate the influence of local mounting on the high frequency acceleration component. Both instruments were used to record acceleration for Shot Tewa. A comparison of the two responses is shown in Figure 8.3, and it can be seen that they

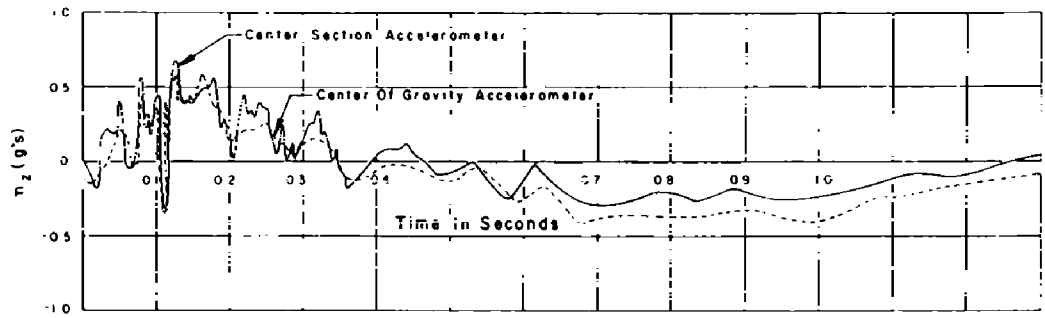


Figure 8.3 Comparison of center section and center of gravity accelerometers, Shot Tewa.

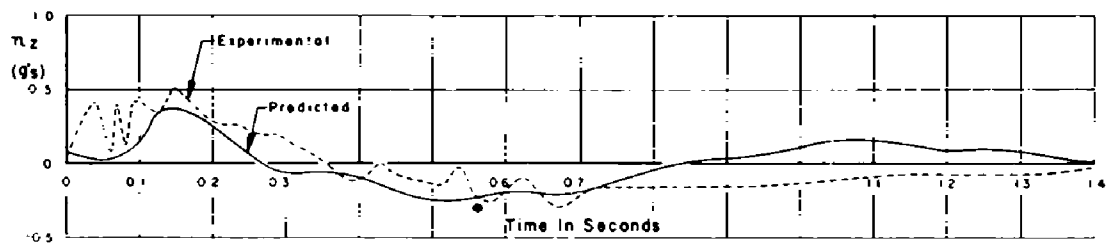


Figure 8.4 Time history of measured and predicted center of gravity acceleration, Shot Zuni.

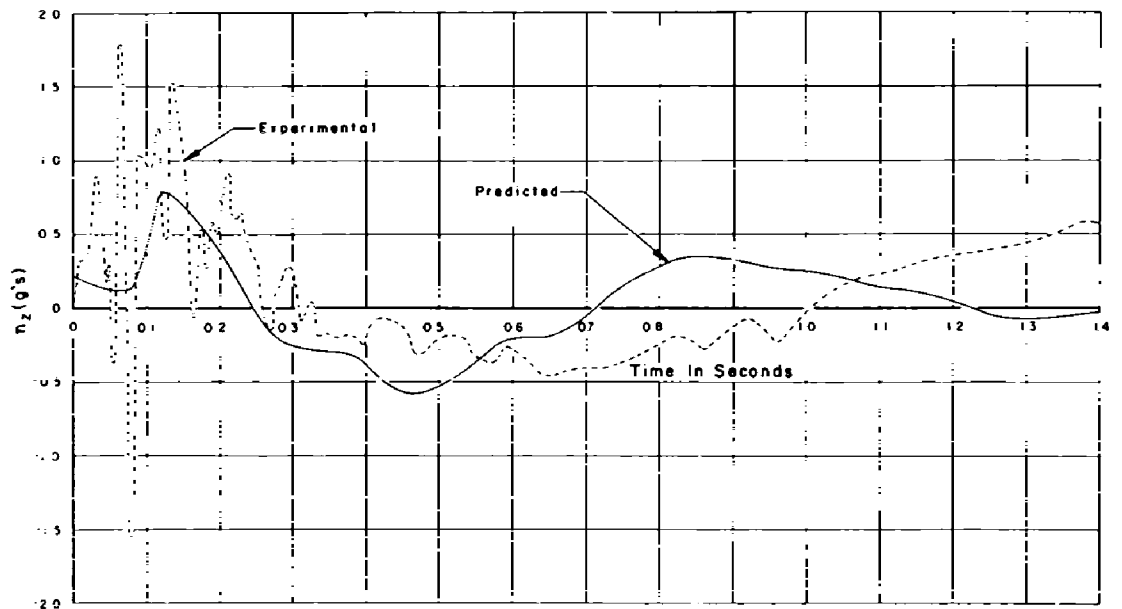


Figure 8.5 Time history of measured and predicted center of gravity acceleration, Shot Flathead.

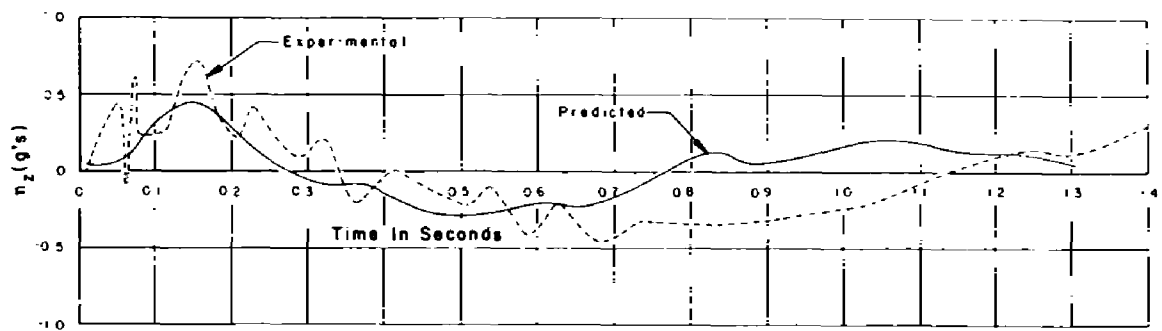


Figure 8.6 Time history of measured and predicted center of gravity acceleration, Shot Apache.

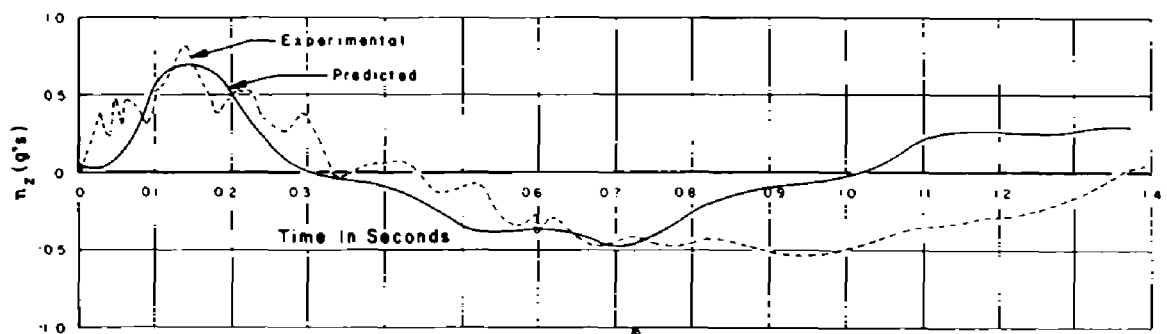


Figure 8.7 Time history of measured and predicted center of gravity acceleration, Shot Navajo.

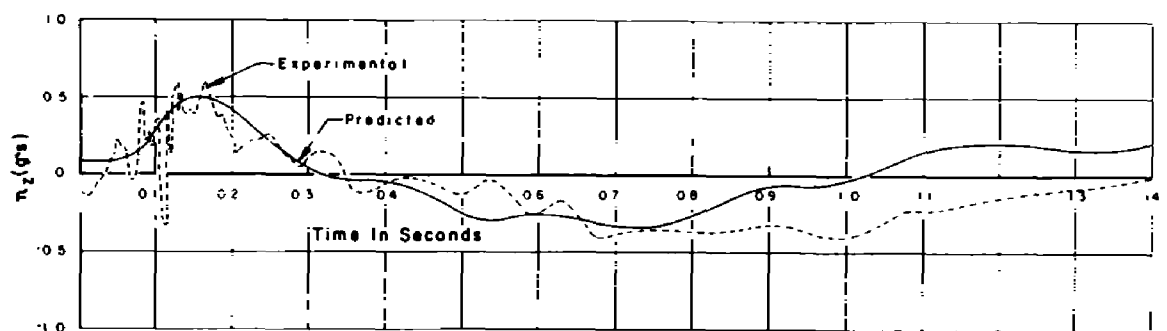


Figure 8.8 Time history of measured and predicted center of gravity acceleration, Shot Tewa.

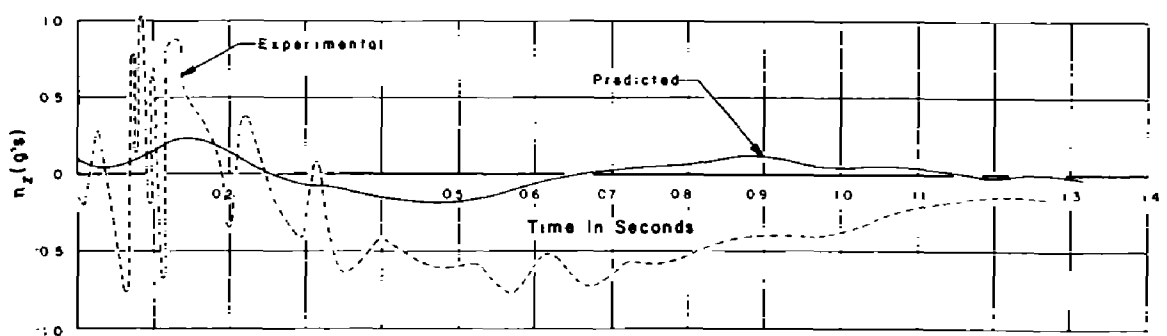


Figure 8.9 Time history of measured and predicted center of gravity acceleration, Shot Huron.

are substantially identical in the frequency sense. This was taken as an indication that the high frequency vibration affected a substantial portion of the fuselage. Although a discussion of the wing strain gage response is reserved for a subsequent paragraph it is useful to point out here that high frequency components were absent from the wing response as evidenced by Figures 8.10 through 8.13. This was taken as evidence that while the fuselage is excited by the gust to high frequency low amplitude vibration, the airplane as a whole responds only to the lower frequency acceleration components.

Except for the high frequency components the agreement with prediction is considered reasonable for all center of gravity accelerations measured in the tests, with the exception of Shot Huron, where uncertainty of exact aircraft position prohibited good response prediction.

Curves showing predicted and measured accelerations versus time are shown in Figures 8.4 through 8.9.

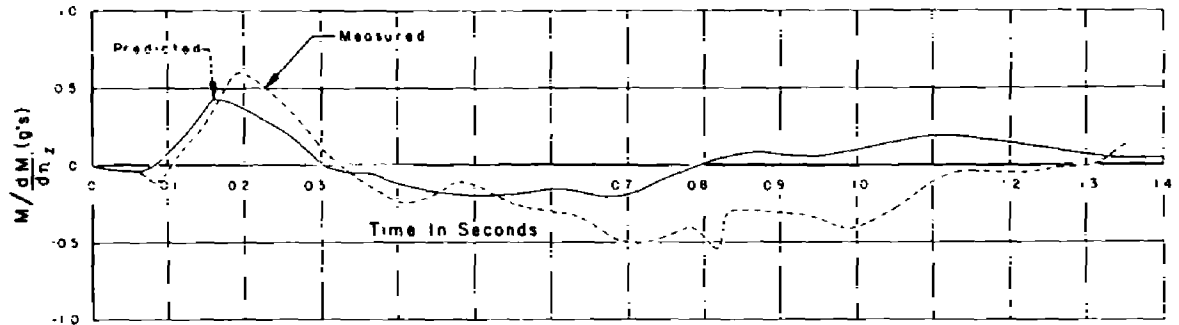


Figure 8.10 Time history of measured and predicted wing root bending moment, Shot Apache.

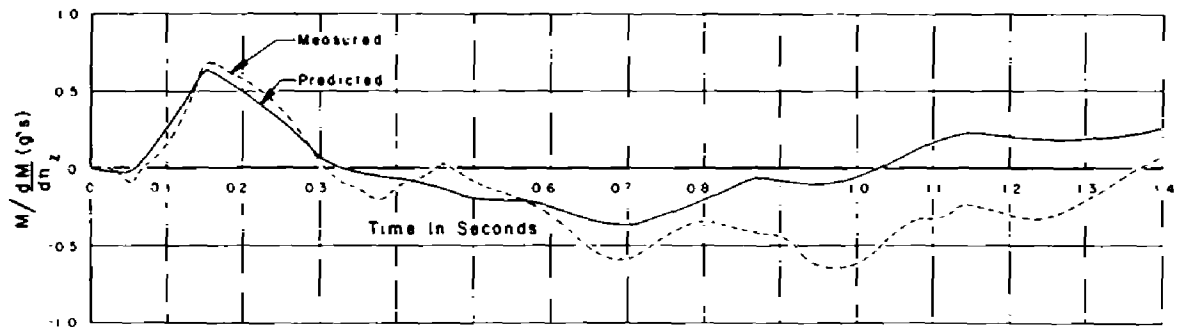


Figure 8.11 Time history of measured and predicted wing root bending moment, Shot Navajo.

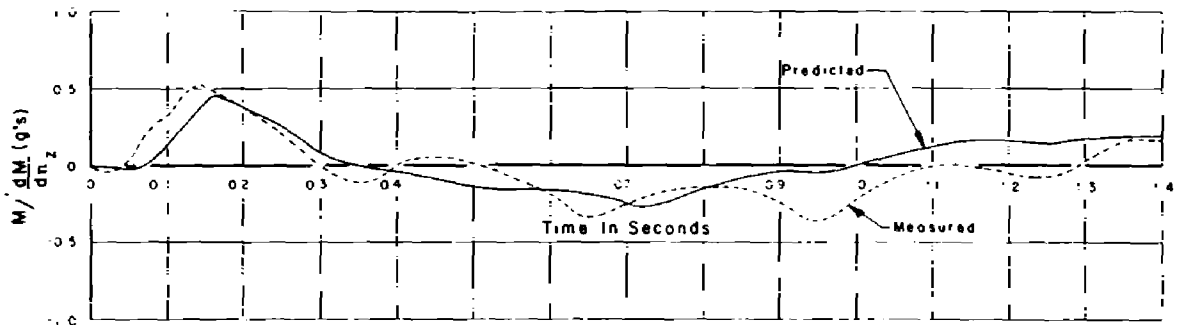


Figure 8.12 Time history of measured and predicted wing root bending moment, Shot Tewa.

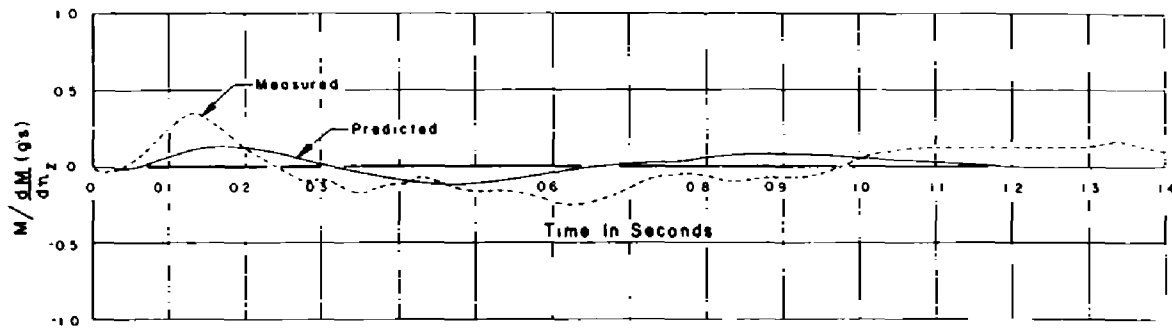


Figure 8.13 Time history of measured and predicted wing root bending moment, Shot Huron.

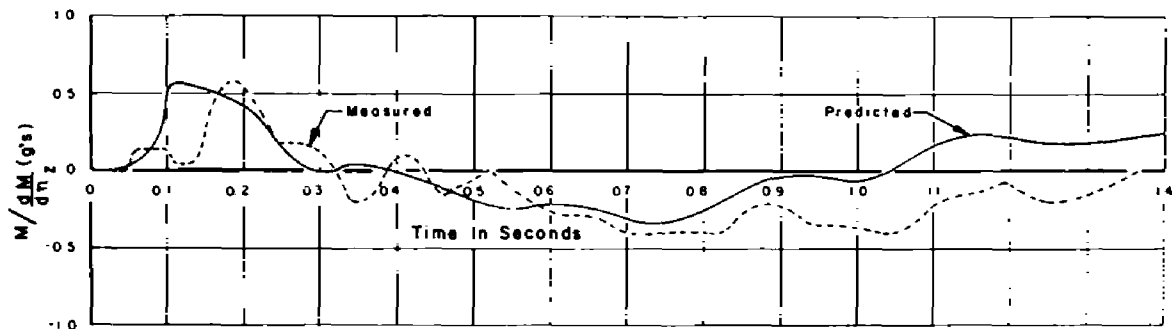


Figure 8.14 Time history of measured and predicted wing fold joint bending moment, Shot Tewa.

8.4.2 Wing Bending Moment. Wing strain gage data was reduced in a manner such that the quantity determined was wing bending moment per unit airplane center of gravity load factor (N). More specifically,

$$N = \frac{\Delta M}{\frac{dM}{dn_z}} \quad (g's)$$

where ΔM = local incremental wing bending moment (lb-in)

$\frac{dM}{dn_z}$ = analytically determined rate of change of local wing bending moment with respect to airplane center of gravity acceleration.
 $\left(\frac{g}{lb-in} \right)$

This quantity has no physical significance in itself, its utility being the fact that it is directly proportional to bending moment and can easily be determined from strain gage response. The so called dynamic magnification factor can also be determined from N since

$$DMF = \frac{\Delta M}{\Delta n_R \frac{dM}{dn_z}} \quad (\text{dimensionless})$$

where Δn_R is the rigid airplane sharp edge gust load factor, which gives

$$DMF = \frac{N}{\Delta n_R}$$

In general, the measured index (N) was found to exceed the analog predictions. Dynamic magnification factors are shown in Table 8.4. No results are given for Shot Huron because of in-

TABLE 8.4 DYNAMIC MAGNIFICATION FACTORS

Case	Wing root		Wing fold	
	Predicted	Measured	Predicted	Measured
Apache	0.74	1.04	--	--
Navajo	0.82	0.86	--	--
Tewa	0.76	0.89	0.95	0.98

sufficient knowledge of airplane position. Curves of N (the bending moment index) versus time are given in Figures 8.10 through 8.15.

8.4.3 Pitching Velocity. Test measurements of pitching velocity indicated serious discrepancy with predicted results. It was found that a greater pitching velocity was predicted than measured for all test cases.

Curves of predicted and measured pitching velocity versus time are given in Figures 8.16 through 8.21.

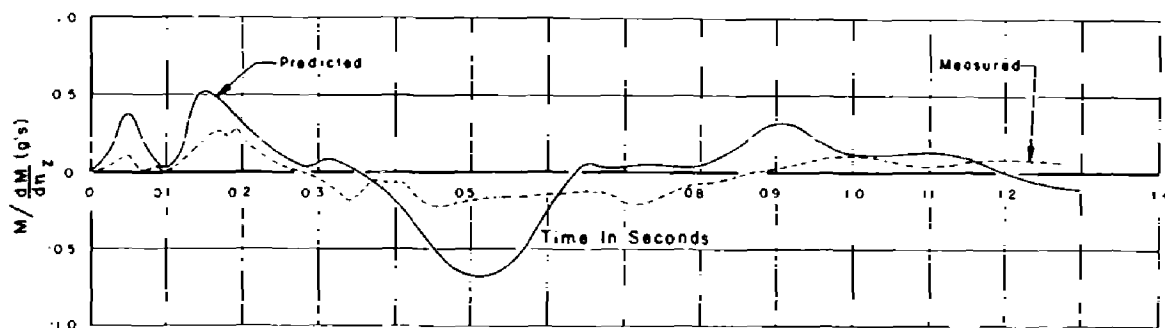


Figure 8.15 Time history of measured and predicted wing fold joint bending moment, Shot Huron.

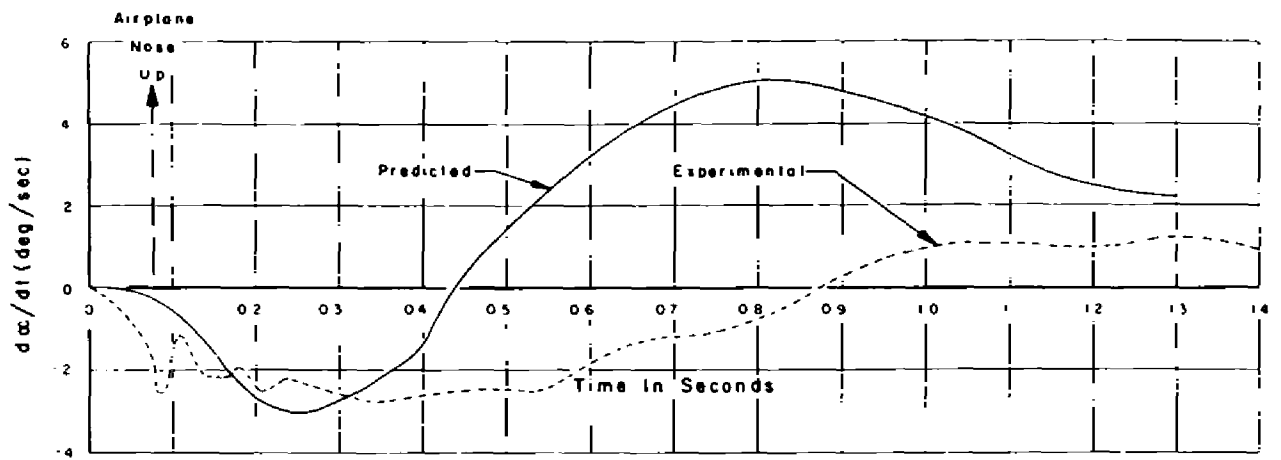


Figure 8.16 Time history of measured and predicted airplane pitching velocity, Shot Zuni.

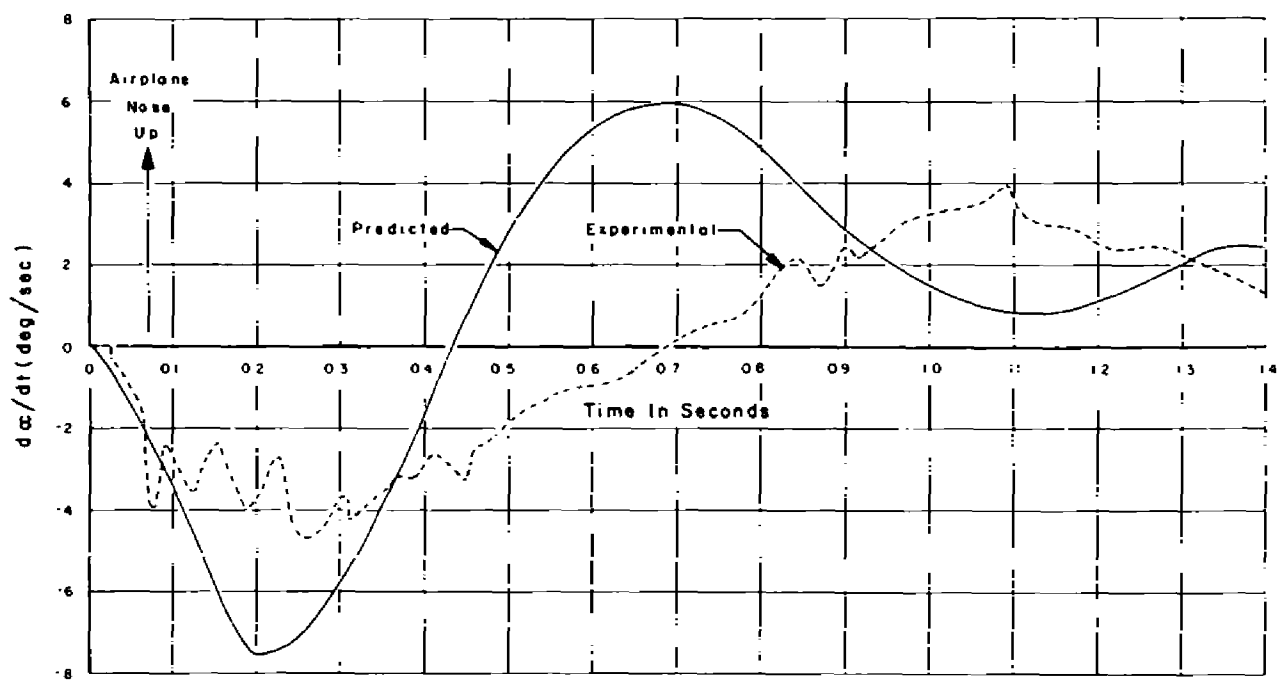


Figure 8.17 Time history of measured and predicted airplane pitching velocity, Shot Flathead.

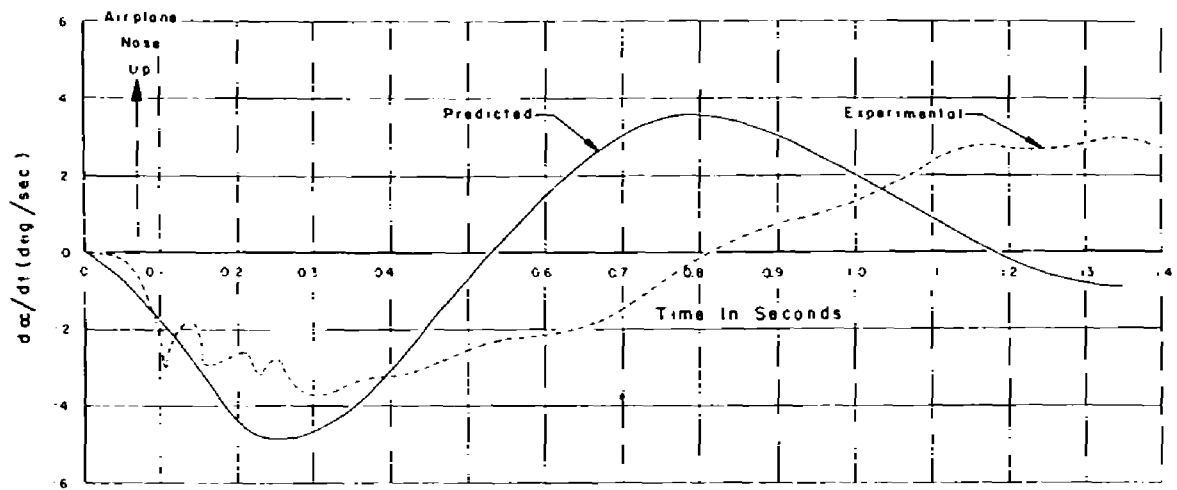


Figure 8.18 Time history of measured and predicted airplane pitching velocity, Shot Apache.

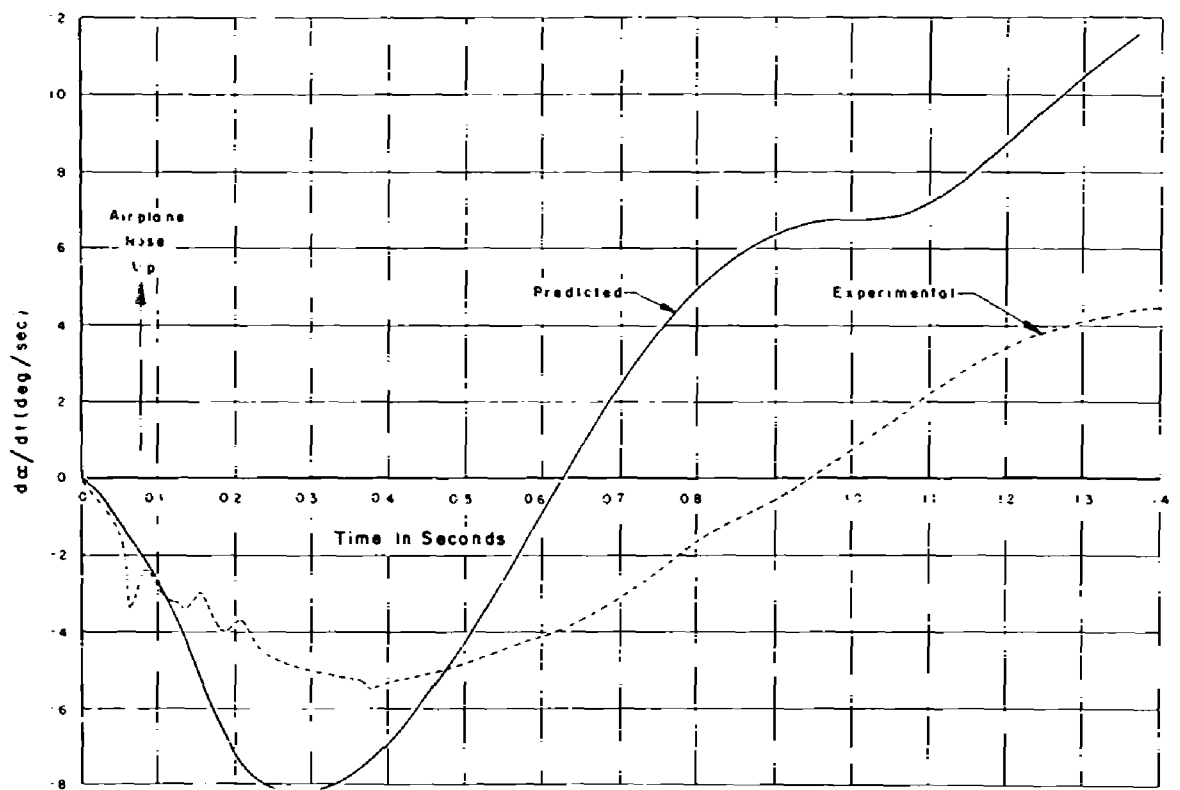


Figure 8.19 Time history of measured and predicted airplane pitching velocity, Shot Navajo.

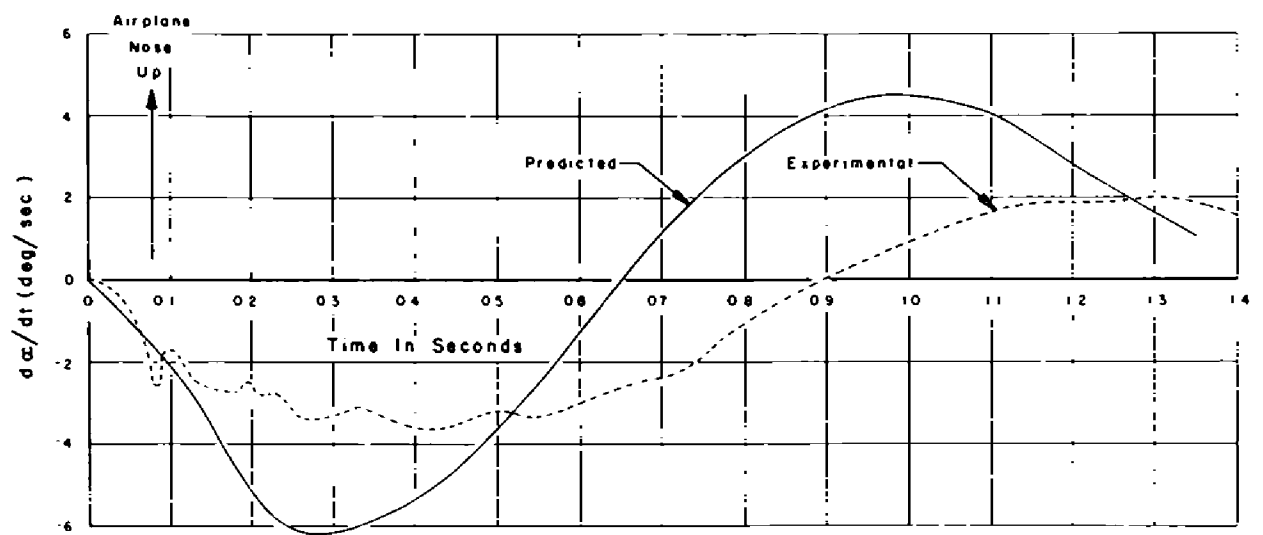


Figure 8.20 Time history of measured and predicted airplane pitching velocity, Shot Tewa.

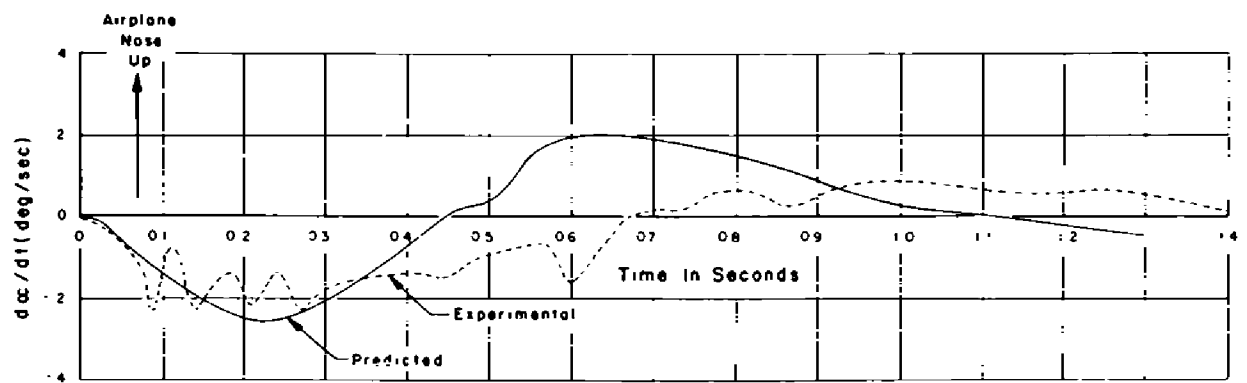


Figure 8.21 Time history of measured and predicted airplane pitching velocity, Shot Huron.

Chapter 9

DELIVERY CAPABILITY OF THE A3D AIRPLANE

One of the objectives of Project 5.8 in Operation Redwing was to define the limiting thermal fields and to provide a proven experimental basis for defining the thermonuclear weapon delivery capability of the A3D type aircraft.

Because of the low level of most of the temperature rises experienced, it was not possible to define an absolute upper limit of temperature rise in the aircraft structure. However, during the tests a section of the elevator reached 368 degrees without any damage whatsoever.

In analyzing the delivery capability of the A3D airplane, the prime factors were the effects of the weapon at some point in space, and the position in space of the delivering aircraft at the time of receiving the effects. Theoretical delivery capability studies of the A3D aircraft reported in References 15 and 16 were based on the weapon effects prediction methods used in this report. In view of the good agreement these methods have given with the experimental data when proper adjustments for actual test conditions were made, they may be considered valid. Therefore, the only questionable item remaining after these tests is the ability of the pilot to make good the calculated escape paths. This phase of the investigation is currently being conducted and when completed and combined with the results obtained in this project will permit definite conclusions of the delivery capability of the A3D airplane.

In the delivery capability studies of References 15 and 16, a limit in temperature rise of 350 degrees was used. Results of Project 5.8 indicate that this limit could be raised, at least to 400F. Even at the 350 degree limit the theoretical studies indicated that the A3D airplane could safely deliver an air burst of a 5 Mt yield weapon. Therefore, if the tests of the escape maneuver bear out the calculated flight paths of the capability studies, it can be concluded that the A3D-1 airplane can safely deliver at least a 5 Mt weapon using this escape maneuver.

If a surface burst is used, the capability based on the same weapon-effects prediction and airplane-flight paths is greater than 12 Mt.

For the A3D participation in Operation Redwing all the test positions, with the exception of Shot Cherokee, were closer to the explosion than if the airplane had dropped the device and executed a horizontal turn escape maneuver.

Chapter 10

CONCLUSIONS

The results of the tests participated in by Project 5.8 in Operation Redwing can be summarized in the following conclusions:

1. The weapon effects prediction methods used for these tests were satisfactory when proper adjustments for actual test conditions were made.
2. For a surface burst the reflected thermal energy from the ocean surface was much lower than predicted by existing theory.
3. The quartz covered thermocouples adjacent to uncovered thermocouples were not satisfactory as a method of determining the aerodynamic convective cooling.
4. The method of computing the heat transfer coefficient was satisfactory at or near the trailing edge of a surface, but did not account adequately for the effect of distance from the leading edge along the surface.
5. The method for calculating aircraft skin temperature rise gave good agreement with measured temperature rise for regions where the heat transfer coefficient was adequately represented.
6. A simplified method of computing the maximum temperature rise (rather than a laborious step-by-step solution of the temperature time history) gave excellent results.
7. There were no violent reactions of the engine because of passage of shock waves encountered.
8. Sufficient gust response data were obtained to confirm the calculations that the A3D airplane high altitude delivery capability would not be limited by gust effects.
9. When the effects methods discussed herein are combined with adequate escape maneuver data, the maximum delivery capability of the A3D-1 airplane can be determined.

Chapter 11

RECOMMENDATIONS

It is recommended that: (1) Studies and experimental investigations be conducted to improve the understanding and prediction of the atmospheric attenuation of the thermal radiation and (2) A program be initiated to experimentally determine, in flight, the heat transfer coefficient at various locations on the airframe surfaces. Such a program should include tests in a nuclear test series in order to determine the effect of the increase in skin temperature.

Appendix A

METHOD OF SCALING SHOCK WAVE EFFECTS

The following method of scaling shock wave effects for yield and altitude is known as the modified Sachs scaling method. This method uses a set of values versus slant range for 1 kt at sea level, and then corrects to receiver altitude and yield conditions by a set of equations.

The curves for 1 kt at sea level were taken from Reference 9, and the scaling equations are from Reference 10.

For convenience, the scaling relationships are summarized below. In all cases sea level conditions are for the NACA standard atmosphere.

Slant Range

$$R' = R_1 (E)^{1/3} \left(\frac{P_0}{P_a} \right)^{1/3} \quad (A.1)$$

Overpressure

$$\Delta P' = \Delta P_1 \left(\frac{P_a}{P_0} \right) \quad (A.2)$$

Time of Shock Arrival

$$t' = t_1 \left(\frac{C_0}{C_a} \right) (E)^{1/3} \left(\frac{P_0}{P_a} \right)^{1/3} \quad (A.3)$$

Density of Air Behind Shock Front

$$\rho' = \rho_1 \left(\frac{P_a}{P_0} \right) \quad (A.4)$$

Particle Velocity Behind Shock Front (Gust Velocity)

$$U' = U_1 \left(\frac{C_a}{C_0} \right)$$

Duration of Positive Phase

$$t'_+ = t_{+1} \left(\frac{C_0}{C_a} \right) (E)^{1/3} \left(\frac{P_0}{P_a} \right)^{1/3} \quad (A.5)$$

where R = slant range
 E = total radiochemical yield (kt)
 ΔP = overpressure
 P = ambient atmospheric pressure
 t = time of shock arrival
 ρ = density
 U = particle velocity behind shock front
 C = speed of sound
 t_+ = duration of positive pressure phase

Superscripts

' = desired yield and altitude conditions

Subscripts

₁ = values for 1 kt at sea level (Reference 9)
₀ = ambient conditions at sea level NACA standard atmosphere
_a = ambient conditions at desired altitude

All ambient conditions at altitude refer to receiver altitude. The original calculations for time of shock arrival used the ambient speed of sound at an average altitude between the receiver and the explosion. However, the results of these tests indicated that much better agreement with experimental results was obtained by using the ambient speed of sound at receiver altitude.

Appendix B

DETERMINATION OF HEAT TRANSFER COEFFICIENT

The heat transfer coefficient was determined by the following equation from Reference 17, Page 117:

$$\frac{N_{ux}}{Re P_r} = \frac{0.0296(Re)^{-1/4}}{1 + 0.87A(Re)^{-1/4}(P_r^{-1})}$$

substituting, $\frac{\bar{h}x}{k} = N_{ux}$

and,

$$A = 1.5(P_r)^{-1/4}$$

the equation becomes:

$$\bar{h}x = \frac{0.0296(Re)^{1/4} k P_r}{1 + 1.305(P_r)^{-1/4}(Re)^{-1/4}(P_r^{-1})}$$

which may be written as:

$$\bar{h}x = \frac{0.0296(Re)^{1/4} k P_r}{1 - \frac{1.305(1-P_r)}{(P_r)^{1/4}(Re)^{1/4}}} \quad (B.1)$$

The values of k were obtained from Reference 17 where they are given in units of Btu, hour, and square feet. It was convenient to use them in these units but to include a conversion factor in the expression so that the heat transfer coefficient was obtained in units of calories, square centimeters, and seconds.

Equation B.1 then becomes:

$$\bar{h}x = \frac{2.23 \times 10^{-6}(Re)^{1/4} k P_r}{1 - \frac{1.305(1-P_r)}{(P_r)^{1/4}(Re)^{1/4}}} \quad (B.2)$$

where \bar{h} = local heat transfer coefficient (cal/cm²/sec/F)
 x = distance from leading edge in streamwise direction (feet)
 Re = local Reynolds number based on distance from leading edge
 $= \frac{Vx}{\nu}$
 V = airplane velocity (ft/sec)
 ν = kinematic viscosity of air (ft²/sec)
 k = thermal conductivity of air (Btu/hr/ft/F)
 P_r = Prandtl number

In the determination of the heat transfer coefficient a reference temperature for the cooling air is required to determine Reynolds number, Prandtl number, and thermal conductivity of the air. The reference temperature used was obtained by the method of Reference 8 and is expressed by:

$$T^* = T_0 + \frac{\Delta T_v}{2} + \left(\frac{\Delta T}{4}\right) \quad (B.3)$$

where T^* = average temperature in the boundary layer during the thermal pulse (°F or °R)
 T_0 = ambient air temperature (°F or °R)
 ΔT_v = adiabatic temperature rise
 $= 0.666 V^2 \times 10^{-4}$ (°F or °R)
 V = airplane true airspeed (ft/sec)
 ΔT = temperature rise due to thermal energy of explosion (°F or °R)

This representation of T^* is a simple approximation of a complex relationship of the temperature variation in the boundary layer which varies with the distance from the skin and with time as the surface temperature is heated during the thermal pulse.

Appendix C

INSTRUMENTATION

C.1 RECORDING INSTRUMENTATION

Recording instrumentation consisted of two 36-channel oscillographs, two 12-channel oscillographs, and a photo panel recorder. The oscillograph recorded time of explosion by means of a channel connected to a photo cell. All recording instruments were equipped with synchronized mechanical counters. Correlation of counter number, timing lines on oscillograph paper, and a 50-cycle timing trace gave accurate timing on any record or between records.

C.2 INSTRUMENTATION FOR THERMAL MEASUREMENTS

The most extensive instrumentation on the A3D-1 aircraft was the thermocouples on the thin skin areas. These regions were investigated most thoroughly because they experienced the greatest temperature rise and hence would be the most critical from an escape standpoint. Thermocouple positions are numbered and are located as shown in Figure 2.1 and Table C.1.

General areas which were instrumented were the thin dural skins of the engine nacelle; the lower surfaces of the flap, alleron wing, and elevator; both sides of the rudder; the thin skin panels along the lower surface of the fuselage; the gun turret and turret radome. Most thermocouples were located on single thickness skins as far away from stiffeners or other heat absorbing structures as possible.

Locations on the turret and aft radome were selected because at some place on the curved surface the thermal rays were normal to the surface, causing increased heat, and also because the aerodynamic cooling was greatly reduced due to a comparatively thick boundary layer.

C.3 SPECIAL INSTRUMENTATION FOR THERMAL EFFECTS DATA

In order to investigate aerodynamic cooling, two thermocouples, one on the fuselage and one on the elevator, were protected from cooling by quartz

covers. Each covered thermocouple was located near an uncovered thermocouple in order that direct comparisons could be made between the temperatures of the cooled and uncooled skin surfaces. As a further indication of the aerodynamic cooling, thermocouples were located in the arresting hook well, where the aerodynamic cooling would be reduced. Thermocouple installations for the determination of aerodynamic cooling were No. 13 on the skin contour, and No. 14 for the hook well, No. 16, a quartz covered uncooled thermocouple, and No. 17 adjacent to it on the lower skin of turret structure, and Nos. 31 (quartz covered) and 32 on the lower skin of the right hand elevator. For detail location of these thermocouples refer to Figure 2.1 and Table C.1.

A special rack for mounting a maximum of nine test specimens was installed under the fuselage at the main landing gear wells. One thermocouple was attached to each specimen. This installation provided a means of testing the thermal effects on various types of material and paints. The results of the panel data and analysis are reported in the final report of Project 8.4, Operation Redwing.

C.4 MEASUREMENT OF THERMAL RADIATION RECEIVED BY AIRCRAFT

In order to evaluate more accurately the thermal effects on the A3D-1 aircraft, data were obtained to show the quantity of thermal radiation received at the aircraft. For this purpose, calorimeters and radiometers, which measured the amount of heat received and the rate at which the heat was received, were installed.

Six thermal instruments were mounted on the tail turret in order that they could be positioned to point directly at the explosion by operating the turret to the proper angle and locking it in place. An adjustment range from straight aft to 70 degrees down was provided.

Another set of six thermal instruments was pointed vertically downward; these were located in the lower surface of the turret structure approximately at Fuselage station 818.

TABLE C.1 DETAILED THERMOCOUPLE INSTALLATIONS

Thermo- couple number	Maximum temperature range	Thermocouple location	Streamwise distance	Skin thickness
			from local leading edge	
	°F		feet	inches
1	450	L. H. nacelle lower skin	3.53	0.025
2	450	L. H. nacelle lower skin	5.95	0.025
3	450	L. H. nacelle lower skin	9.00	0.025
4	450	L. H. nacelle lower skin	9.00	0.025
5	450	L. H. aileron lower skin	7.72	0.025
6	450	L. H. aileron lower skin	9.34	0.025
7	450	L. H. wing lower skin	9.89	0.025
8	450	L. H. flap lower skin	13.64	0.032
9	450	L. H. bomb bay door	31.64	0.032
10	450	L. H. bomb bay door	31.64	0.032
11	450	L. H. side fuselage lower skin	41.42	0.040
12	450	L. H. side fuselage lower skin	44.25	0.040
13	450	L. H. side fuselage lower skin	61.69	0.032
14	600	L. H. side fuselage lower skin	61.69	0.032
15	450	L. H. side fuselage lower skin	64.65	0.032
16	900	Turret struc- ture lower skin (quartz covered)	66.42	0.025
17	450	Turret struc- ture lower skin	66.42	0.025
18	450	Turret struc- ture lower skin	67.33	0.025
19	600	Aft surface of tail radome on airplane $\frac{1}{2}$	71.22	0.022
20	600	Aft surface of tail radome on airplane $\frac{1}{4}$	71.22	0.022

TABLE C.1 DETAILED THERMOCOUPLE INSTALLATIONS (Cont'd)

Thermo- couple number	Maximum temperature range	Thermocouple location	Streamwise distance from local leading edge	Skin thickness
			feet	inches
21	600	Aft surface of turret fairing on airplane &	71.22	0.040
22	600	On turret skin above L.H. gun fairing	71.22	0.040
23	600	On turret skin left of L.H. gun fairing	71.22	0.040
24	600	Aft face of L.H. gun fairing	71.22	0.064
25	450	Lower skin R.H. elevator	5.38	0.025
26	450	Lower skin R.H. elevator	6.03	0.025
27	450	Lower skin R.H. elevator	6.75	0.025
28	450	Lower skin R.H. elevator	7.52	0.025
29	450	Lower doubler on R.H. elevator	5.99	0.025 0.016
30	450	Peak of lower doubler R.H. elevator	6.03	0.016
31	900	Lower skin (quartz cover) R.H. elevator	5.46	0.025
32	450	Lower skin R.H. elevator	5.39	0.025
33	450	Lower skin R.H. elevator	3.83	0.025
34	450	Lower skin R.H. elevator	4.50	0.025
35	450	L.H. side lower rudder	13.56	0.016
36	450	R.H. side lower rudder	13.56	0.016
37-45	450	Test panel specimens for Project 8.4	13.56	

Two calorimeters were located in the cockpit to measure scattered thermal radiation in the crew's compartment. One was mounted near the pilot's headrest and pointed to the side through the window; the other was pointed forward through the windshield.

The thermal instruments were supplied with several full scale ranges, filters, and fields of view. The Naval Radiological Defense Laboratory (NRDL) was responsible for the selection of the instrument used and the calibration. NRDL also instructed and advised Douglas personnel in the use, maintenance, and installation of NRDL furnished equipment. The instruments used in each shot, their field of view, filter, and sensitivity are shown in Tables C.2 to C.8. Filters 2-58 and 7-56 were Corning filters and the numbers are their designation.

C.5 CAMERA INSTALLATIONS

Two GSAP cameras were mounted on the turret, along with the thermal instruments, so they could be pointed directly at the explosion.

Two additional GSAP cameras were mounted pointing vertically downward to show the field of the indirect thermal instruments and the terrain and cloud cover at the time of the explosion. These cameras were mounted with the six thermal instruments in the lower surface of the turret structure.

The GSAP cameras (16 mm) were equipped with 17-mm lenses which gave a field of view of 24 degrees 36 minutes vertical and 33 degrees 58 minutes horizontal.

Nuclear radiation shielding was not provided for these cameras since a tolerance of 10 r for regular film and 1000 r for microfilm was indicated.

C.6 OVERPRESSURE MEASUREMENTS

In order to measure the overpressure which was experienced when the shock wave passed the aircraft, pickups were installed which were capable of recording the time history of the overpressure pulse. The primary instrument for this measurement was a pickup located ahead of the vertical tail on a boom mounting. In addition to this instrument, two overpressure pickups were mounted, one on each side of the fuselage forward of the speed brakes (Figure 2.1). These fuselage pickups were added to insure that overpressure data were obtained in case of failure of the boom mounted system and also to provide a direct measurement of the pressures experienced by the fuselage skin panels.

C.7 ENGINE INSTRUMENTATION

Results from previous tests indicated the possibility of engine tail pipe temperature rise at shock arrival. In order to measure the effects of shock arrival on the J-57 engine in the A3D-1 aircraft the port engine was instrumented. The instrumentation included measurements of the inlet and outlet condi-

tions of pressure and temperatures, fuel manifold pressures, bleed valve positions, and low and high pressure compressor rotor speeds.

The above data measured the conditions which could contribute to compressor stall and/or flame-out.

C.8 MISCELLANEOUS INSTRUMENTATION

A time of explosion signal was provided by a photo cell, and recorded on each 36-channel and 12-channel oscillograph.

Position indicators were provided to show the angle of the stabilizer, elevator, and rudder. These positions were recorded on the 36-channel oscillographs with duplicate records on the photo recorder.

A summary of the miscellaneous instrumentation is given below.

Pressure pickup ahead of vertical tail on a boom mounting

- Pressure pickup port side of fuselage
- Pressure pickup starboard side of fuselage
- Turbine discharge total temperature (T_{t_1})
- Turbine discharge total pressure (P_{t_1})
- Compressor inlet total pressure (P_{t_2})
- Compressor inlet static pressure (P_{s_1})
- Free stream total temperature (T_{t_2})
- Pilot fuel manifold pressure (P_{f_p})
- Low pressure compressor discharge static pressure (P_{s_2})
- Compressor discharge static pressure (P_{s_3})
- Main fuel manifold pressure (P_{f_m})
- Low pressure compressor rotor speed (N_1)
- High pressure compressor rotor speed (N_2)
- Inboard intercompressor bleed valve (open or closed) indicating lights on photo recorder
- Outboard intercompressor bleed valve (open or closed) indicating lights on photo recorder
- Time of explosion
- Stabilizer position
- Elevator position
- Rudder position
- Normal aircraft acceleration in tail
- Pitch rate
- Normal aircraft center of gravity acceleration
- Airspeed
- Altitude
- Outside air temperature
- Normal aircraft acceleration
- Time (clock)
- Attitude (pitch)
- Iron-Constantan ice bath
- Chromel-Alumel ice bath
- Counter number
- 50 cycle time trace
- 1 second and 10 second timing traces
- Reference static pressure for overpressure measurement

The following flight conditions were recorded on the photo recorder; airspeed, altitude, outside air temperature, and time.

TABLE C.2 THERMAL INSTRUMENTS FOR SHOT CHEROKEE

Instrument	NRDL serial number	Station	Field of view	Filter	Calibration factor
			degrees		cal/cm ² /mv
Radiometer	RF-10-159	direct	90	quartz	1.30
Radiometer	RF-10-161	indirect	90	quartz	1.58
Calorimeter	RD-202	direct	160	quartz	2.60
Calorimeter	BK-201	direct	160	quartz	1.19
Calorimeter	BK-202	direct	90	quartz	1.17
Calorimeter	BK-203	direct	90	2-58	1.17
Calorimeter	WH-65	direct	90	7-56	0.623
Calorimeter	BK-200	indirect	160	quartz	1.17
Calorimeter	WH-177	indirect	160	quartz	0.581
Calorimeter	BR-78	indirect	21	quartz	0.447
Calorimeter	BR-71	indirect	21	2-58	0.458
Calorimeter	BR-86	indirect	21	7-56	0.427
Calorimeter	WH-66	cockpit (fwd)	90	quartz	0.618
Calorimeter	BR-77	cockpit (L.H.)	90	quartz	0.449

TABLE C.3 THERMAL INSTRUMENTS FOR SHOT ZUNI

Instrument	NRDL serial number	Station	Field of view	Filter	Calibration factor
			degrees		cal/cm ² /mv
Radiometer	RF-10-159	direct	90	quartz	1.30
Radiometer	RF-10-161	indirect	90	quartz	1.58
Calorimeter	BK-201	direct	160	quartz	1.19
Calorimeter	RD-202	direct	160	quartz	2.60
Calorimeter	BK-202	direct	90	quartz	1.17
Calorimeter	BK-203	direct	90	2-58	1.17
Calorimeter	WH-65	direct	90	7-56	0.623
Calorimeter	WH-177	indirect	160	quartz	0.581
Calorimeter	BK-211	indirect	160	quartz	1.17
Calorimeter	BR-78	indirect	21	quartz	0.447
Calorimeter	BR-71	indirect	21	2-58	0.458
Calorimeter	BR-86	indirect	21	7-56	0.427
Calorimeter	WH-66	cockpit (fwd)	90	quartz	0.618
Calorimeter	BR-77	cockpit (L.H.)	90	quartz	0.449

TABLE C.4 THERMAL INSTRUMENTS FOR SHOT FLATHEAD

Instrument	NRDL serial number	Station	Field of view	Filter	Calibration factor
			degrees		cal/cm ² /mv
Radiometer	RF-10-161	direct	90	quartz	1.58
Radiometer	RF-10-159	indirect	90	quartz	1.30
Calorimeter	RD-202	direct	160	quartz	2.60
Calorimeter	RD-271	direct	90	quartz	2.59
Calorimeter	RD-279	direct	45	quartz	2.59
Calorimeter	BK-203	direct	21	quartz	1.17
Calorimeter	WH-237	direct	21	2-58	0.574
Calorimeter	RD-272	indirect	160	quartz	2.60
Calorimeter	WH-183	indirect	160	quartz	0.562
Calorimeter	BK-202	indirect	90	quartz	1.17
Calorimeter	WH-240	indirect	90	2-58	0.601
Calorimeter	BR-86	indirect	90	7-56	0.427
Calorimeter	BR-54	cockpit (fwd)	90	quartz	0.439
Calorimeter	BR-77	cockpit (L.H.)	90	quartz	0.449

TABLE C.5 THERMAL INSTRUMENTS FOR SHOT APACHE

Instrument	NRDL serial number	Station	Field of view	Filter	Calibration factor
			degrees		cal/cm ² /mv
Radiometer	RF-50-166	direct	90	quartz	14.49
Radiometer	RF-50-174	indirect	90	quartz	5.90
Calorimeter	RD-230	direct	160	quartz	2.61
Calorimeter	RD-204	direct	90	quartz	2.62
Calorimeter	RD-273	direct	45	quartz	2.57
Calorimeter	BK-203	direct	21	quartz	1.17
Calorimeter	WH-237	direct	21	2-58	0.574
Calorimeter	RD-274	indirect	160	quartz	2.54
Calorimeter	BK-55	indirect	160	quartz	1.24
Calorimeter	BK-208	indirect	90	quartz	1.21
Calorimeter	BK-210	indirect	90	2-58	1.16
Calorimeter	WH-238	indirect	90	7-56	0.586
Calorimeter	XX-15	cockpit (fwd)	90	quartz	0.0208
Calorimeter	XX-17	cockpit (L.H.)	90	quartz	0.0220

TABLE C.6 THERMAL INSTRUMENTS FOR SHOT NAVAJO

Instrument	NRDL serial number	Station	Field of view	Filter	Calibration factor
			degrees		cal/cm ² /mv
Radiometer	RF-50-166	direct	90	quartz	14.49
Radiometer	RF-50-174	indirect	90	quartz	5.90
Calorimeter	RD-230	direct	160	quartz	2.61
Calorimeter	RD-204	direct	90	quartz	2.56
Calorimeter	RD-273	direct	45	quartz	2.57
Calorimeter	BK-203	direct	21	quartz	1.17
Calorimeter	WH-237	direct	21	2-58	0.574
Calorimeter	BK-55	indirect	160	quartz	1.24
Calorimeter	RD-274	indirect	160	quartz	2.54
Calorimeter	BK-208	indirect	90	quartz	1.21
Calorimeter	BK-210	indirect	90	2-58	1.16
Calorimeter	WH-238	indirect	90	7-56	0.586
Calorimeter	XX-17	cockpit (fwd)	90	quartz	0.0220
Calorimeter	XX-15	cockpit (L.H.)	90	quartz	0.0208

TABLE C.7 THERMAL INSTRUMENTS FOR SHOT TEWA

Instrument	NRDL Serial number	Station	Field of view	Filter	Calibration factor
			degrees		cal/cm ² /mv
Radiometer	RF-50-165	direct	90	quartz	8.26
Radiometer	RF-10-159	indirect	90	quartz	1.30
Calorimeter	RD-230	direct	160	quartz	2.61
Calorimeter	RD-204	direct	90	quartz	2.56
Calorimeter	RD-273	direct	45	quartz	2.57
Calorimeter	BK-203	direct	21	quartz	1.17
Calorimeter	WH-237	direct	21	2-58	0.574
Calorimeter	BK-55	indirect	160	quartz	1.24
Calorimeter	RD-241	indirect	160	quartz	2.57
Calorimeter	BK-208	indirect	90	quartz	1.21
Calorimeter	BK-210	indirect	90	2-58	1.16
Calorimeter	WH-238	indirect	90	7-56	0.586
Calorimeter	XX-17	cockpit (fwd)	90	quartz	0.0220
Calorimeter	XX-15	cockpit (L.H.)	90	quartz	0.0208

TABLE C.8 THERMAL INSTRUMENTS FOR SHOT HURON

Instrument	NRDL serial number	Station	Field of view	Filter	Calibration factor
			degrees		cal/cm ² /mv
Radiometer	RF-10-58	direct	90	quartz	1.54
Radiometer	RF-10-159	indirect	90	quartz	1.30
Calorimeter	WH-197	direct	160	quartz	0.598
Calorimeter	WH-58	direct	90	quartz	0.615
Calorimeter	WH-62	direct	45	quartz	0.689
Calorimeter	WH-191	direct	21	quartz	0.619
Calorimeter	WH-237	direct	21	2-58	0.574
Calorimeter	BR-89	indirect	160	quartz	0.436
Calorimeter	WH-238	indirect	90	quartz	0.586
Calorimeter	WH-180	indirect	90	quartz	0.610
Calorimeter	WH-196	indirect	90	2-58	0.611
Calorimeter	WH-161	indirect	90	7-56	0.587
Calorimeter	XX-18	cockpit (fwd)	90	quartz	0.0258
Calorimeter	XX-15	cockpit (L.H.)	90	quartz	0.0208

TABLE C.9 SUMMARY OF ACCELEROMETER INSTALLATIONS

Accelerometer location	Cherokee	Zuni	Flathead	Apache	Navajo	Tewa	Huron
Aircraft center of gravity	X	X	X	X	X	X	X
Tail compartment	X	X	X	X	X	X	X
Photo recorder	X	X	X	X	X	X	X
Inboard side of R.H. wing fold (wing station 344)		X	X	X	X	X	X
Outboard side of R.H. wing fold (wing station 355)			X				
R.H. wing station 422			X				
R.H. wing tip			X	X	X	X	X
Center wing						X	X
Center section							

Three dosimeters to measure nuclear radiation were installed, one each, in the cockpit, bomb bay, and tail compartment of the aircraft. A PDR-27C radiometer was located in the cockpit.

C.9 MEASUREMENT OF LOAD FACTOR INCREMENT DUE TO GUST

In the original planning for the A3D aircraft participation in Operation Redwing the measurement of thermal data was considered to be the primary consideration and the aircraft instrumentation was planned accordingly. As prescribed by Reference 14, gust response data was to be obtained by the measurement of aircraft center of gravity response. The instrumentation provided for this purpose included

two vertical accelerometers mounted near the aircraft center of gravity, one to be recorded on an oscillograph and the other on the photo recorder. Additional instrumentation which was added for correlation purposes included a vertical accelerometer in the tail of the aircraft, a pitch rate gyro, and an attitude gyro.

When the gust positioning criteria for the A3D aircraft was questioned at the EPG, it was decided to add instrumentation for possible further correlation of the gust response data. Table C.9 summarized the additional accelerometer installations. Strain gage installations were made later in the test program. These installations included strain gages installed on the center wing center section skin prior to Shot Apache and on the forward and aft wing spars at the wing fold joint prior to Shot Tewa.

Appendix D

ADDITIONAL TEST DATA

All the data obtained during the course of the tests and not shown in the main body of the report are included in this appendix. (Figs. D.1 through D.64.)

These data are of low level, or merely confirmed the data in the main body of the report. They are included in the event they might prove helpful to other agencies, possibly in correlating or checking data from other projects.

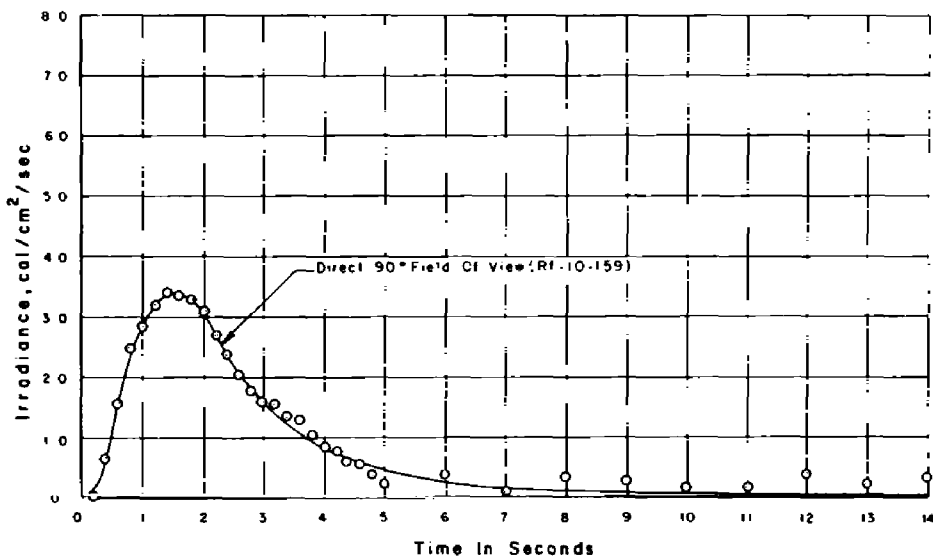


Figure D.1 Thermal Irradiance as a function of time, Shot Cherokee.

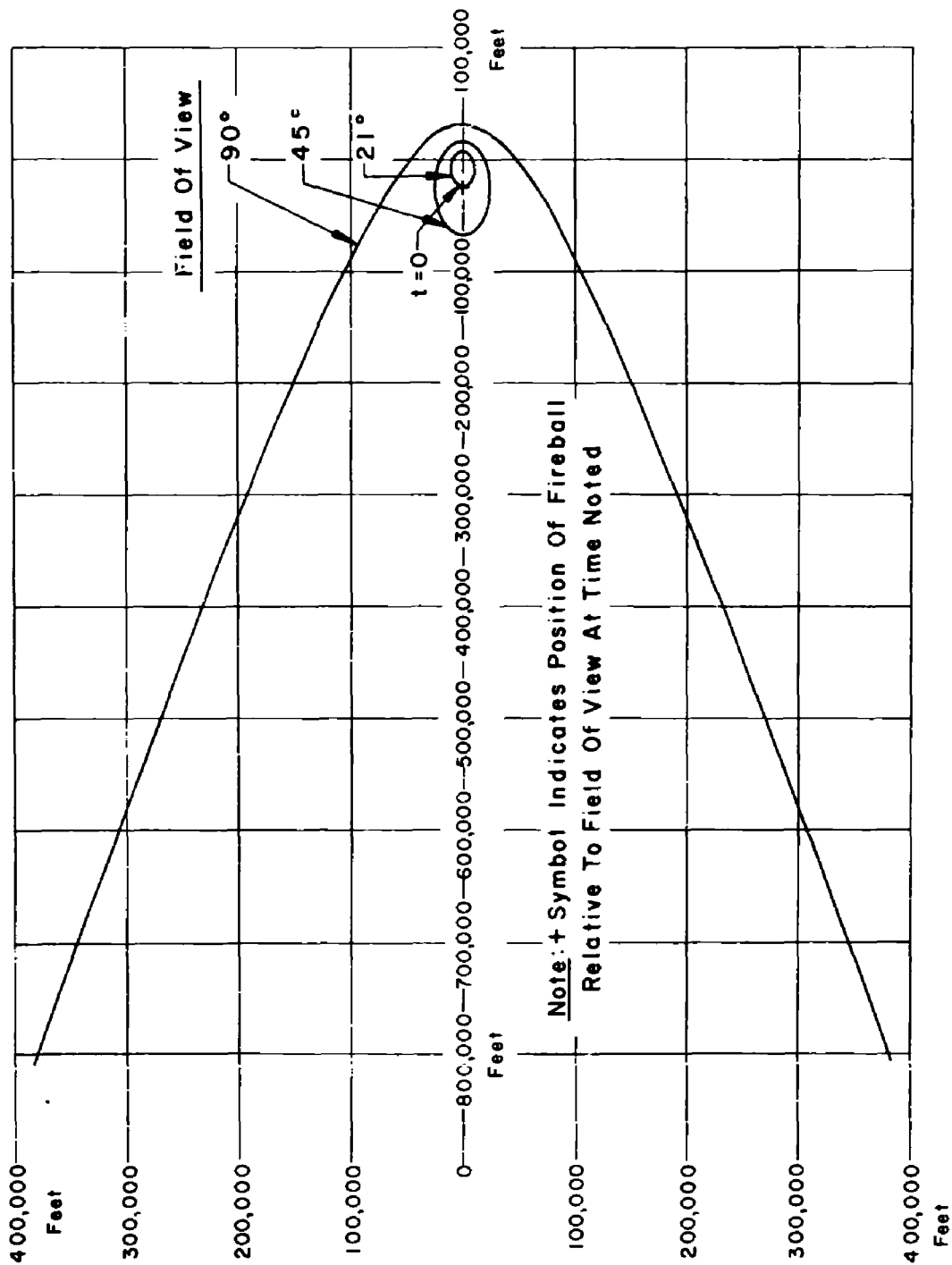


Figure D.2 Field of view of direct thermal instruments, Shot Cherokee.

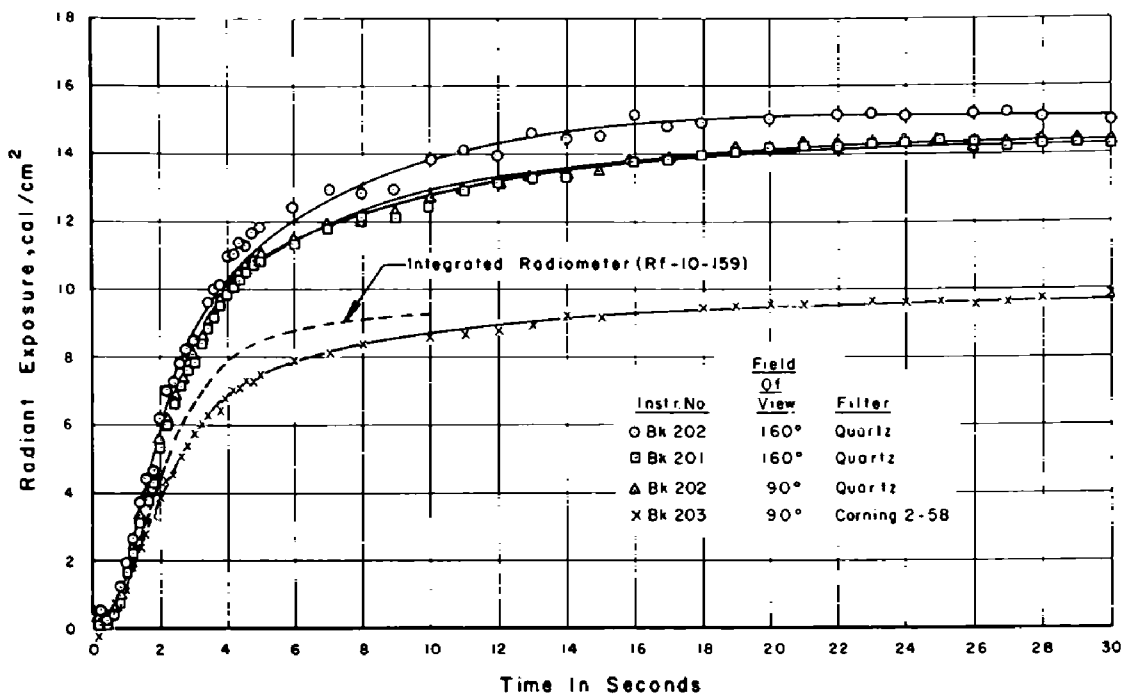


Figure D.3 Radiant exposure of direct thermal instruments, Shot Cherokee.

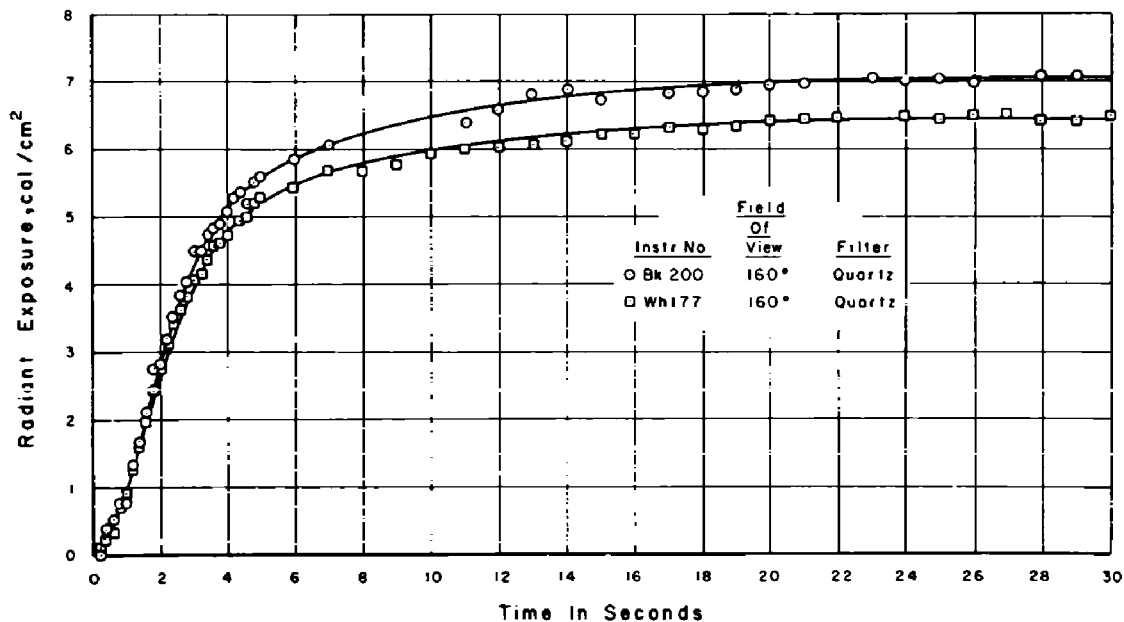
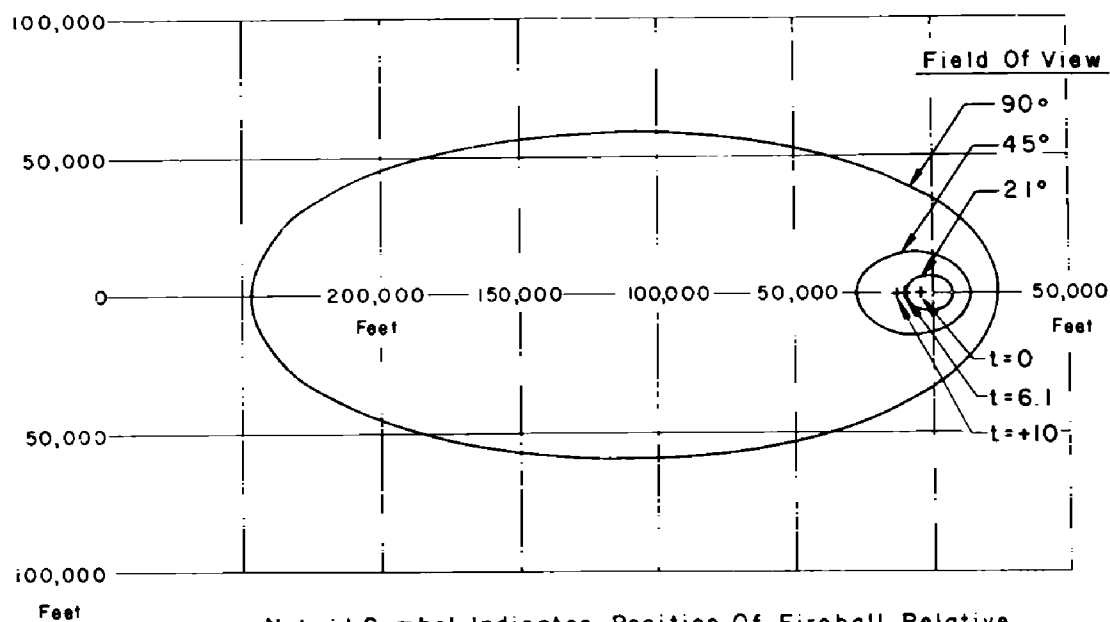


Figure D.4 Radiant exposure of indirect thermal instruments, Shot Cherokee.



Note: + Symbol Indicates Position Of Fireball Relative To Field Of View At Time Noted

Figure D.5 Field of view of direct thermal instruments, Shot Apache.

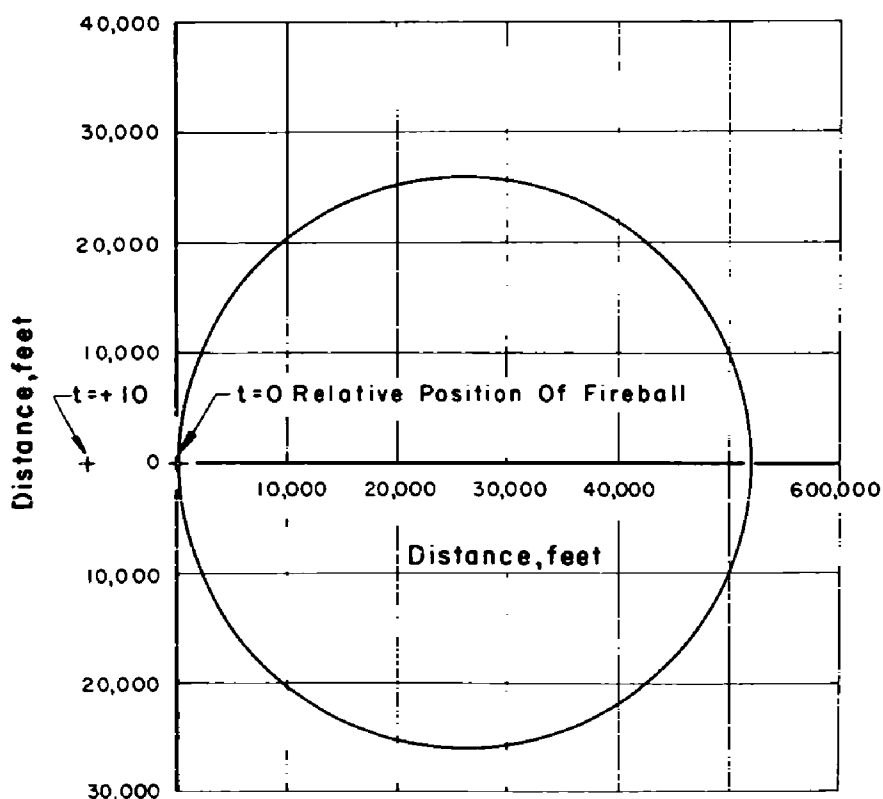


Figure D.6 Field of view of 90-degree indirect thermal instruments, Shot Apache.

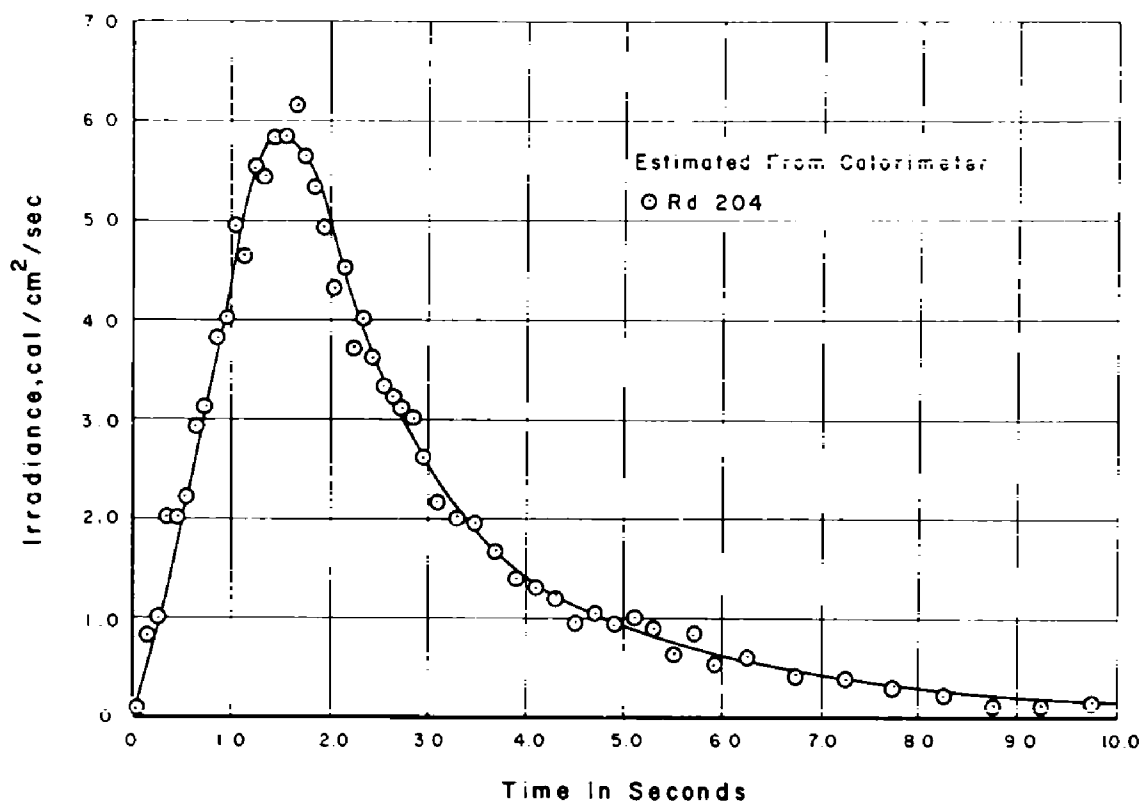


Figure D.7 Estimated direct thermal irradiance, Shot Apache.

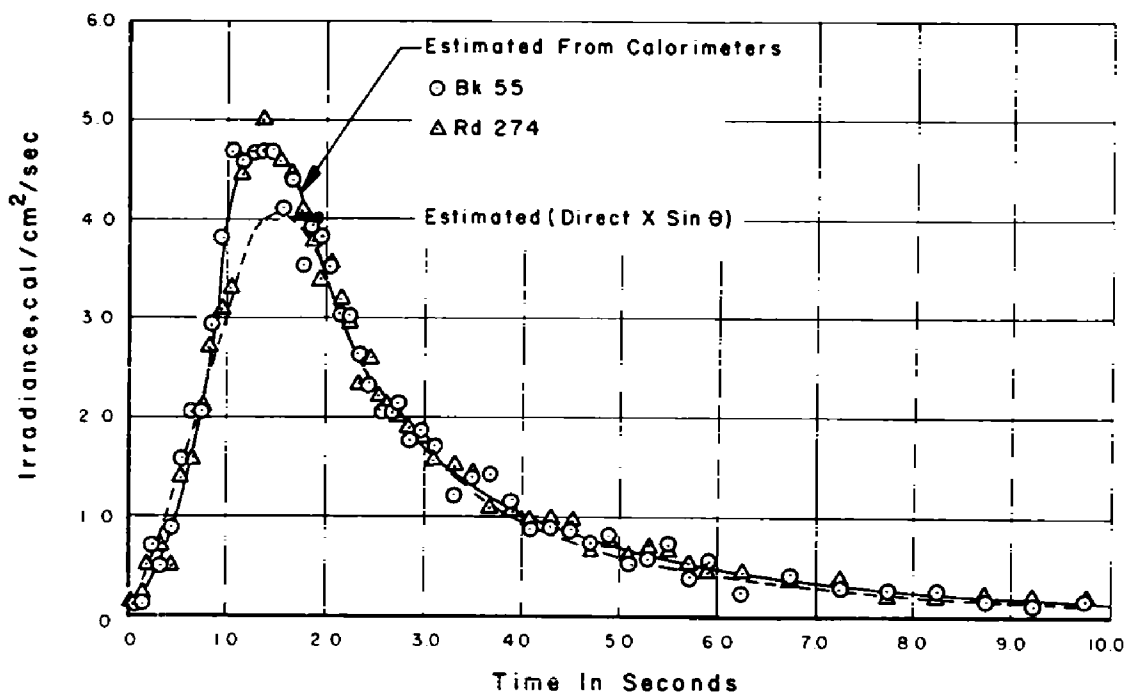


Figure D.8 Estimated indirect thermal irradiance, Shot Apache.

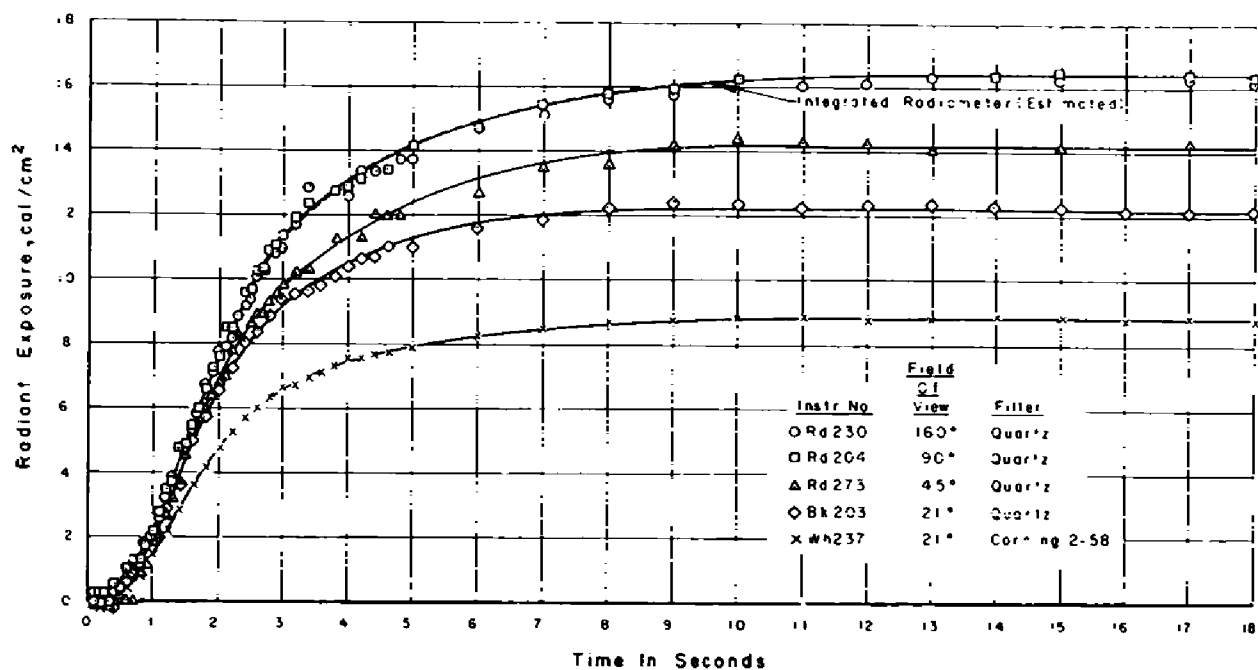


Figure D.9 Radiant exposure of direct thermal instruments, Shot Apache.

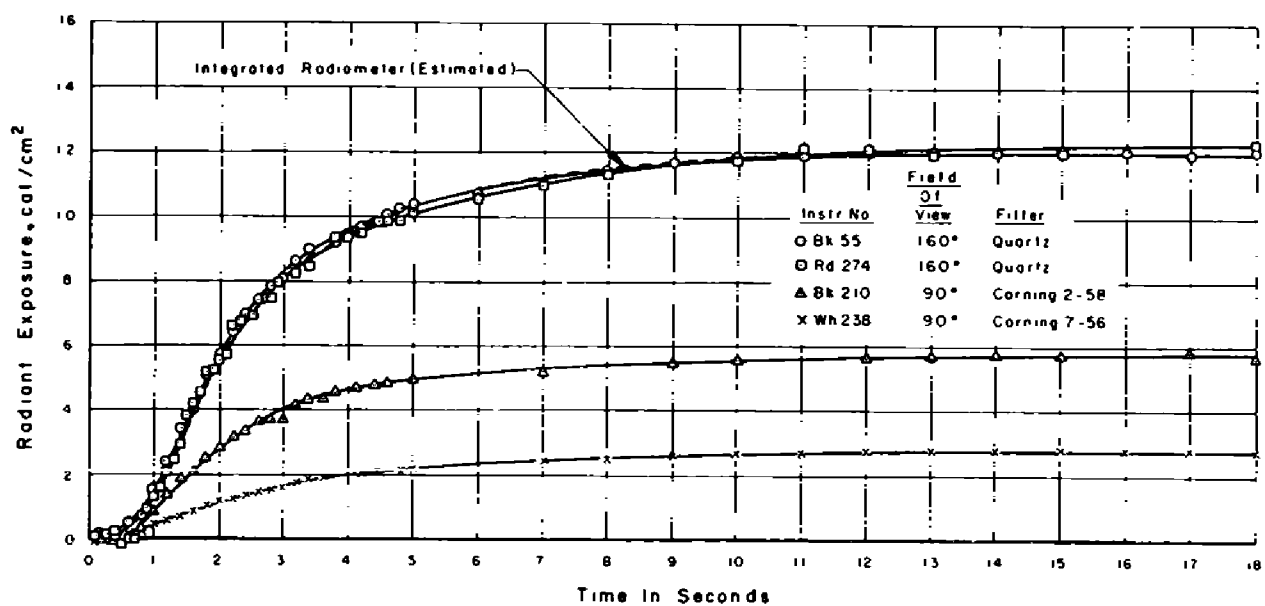


Figure D.10 Radiant exposure of indirect thermal instruments, Shot Apache.

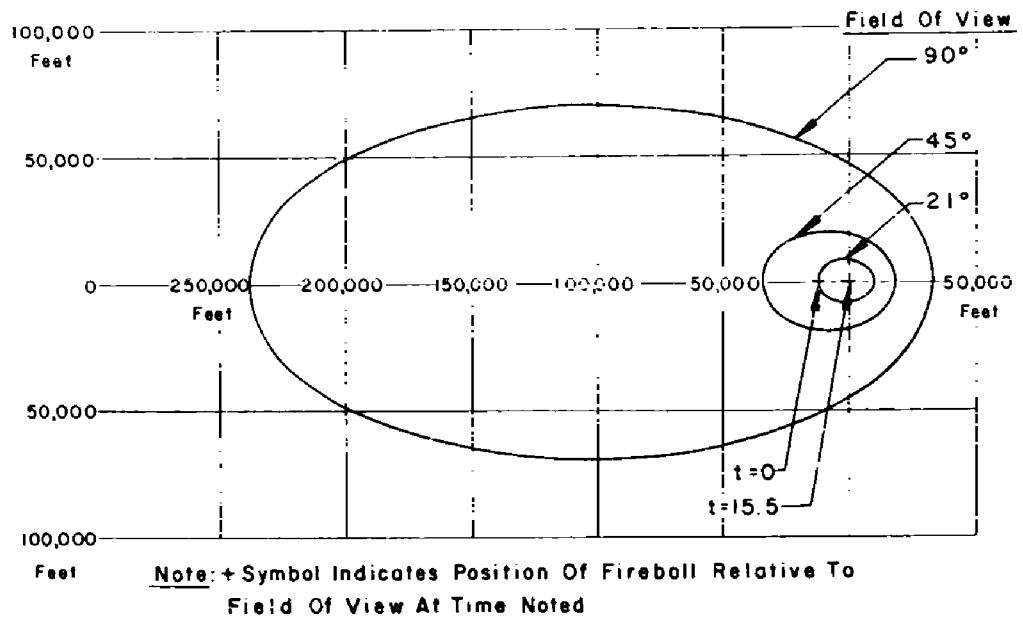


Figure D.11 Field of view of direct thermal instruments, Shot Navajo.

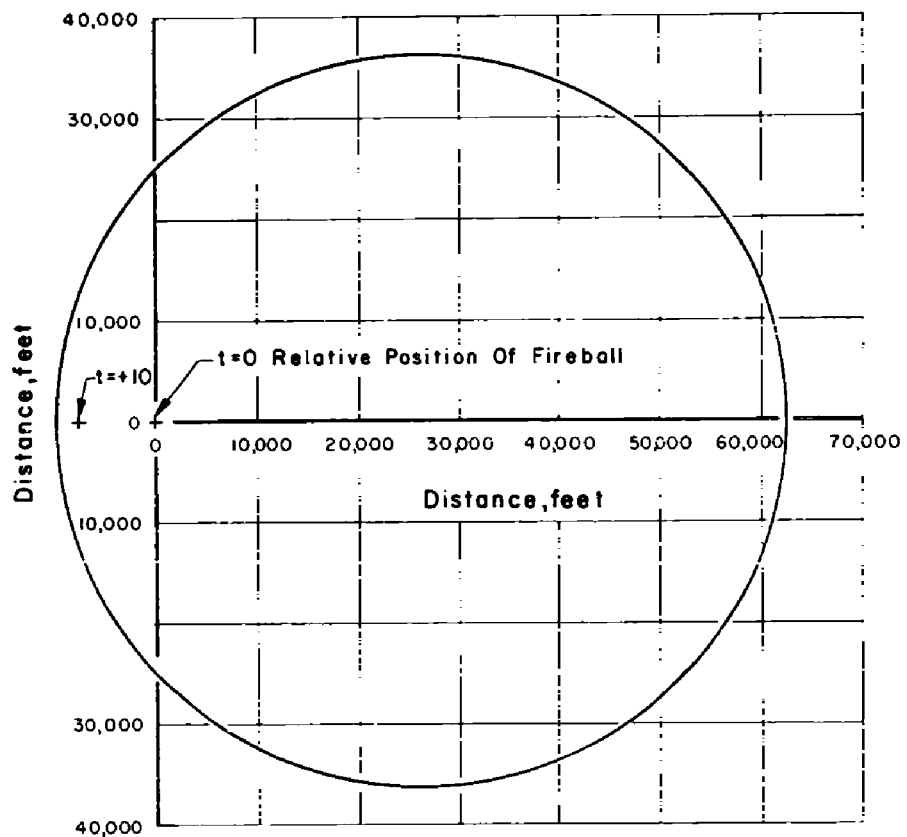


Figure D.12 Field of view of 90-degree indirect thermal instruments, Shot Navajo.

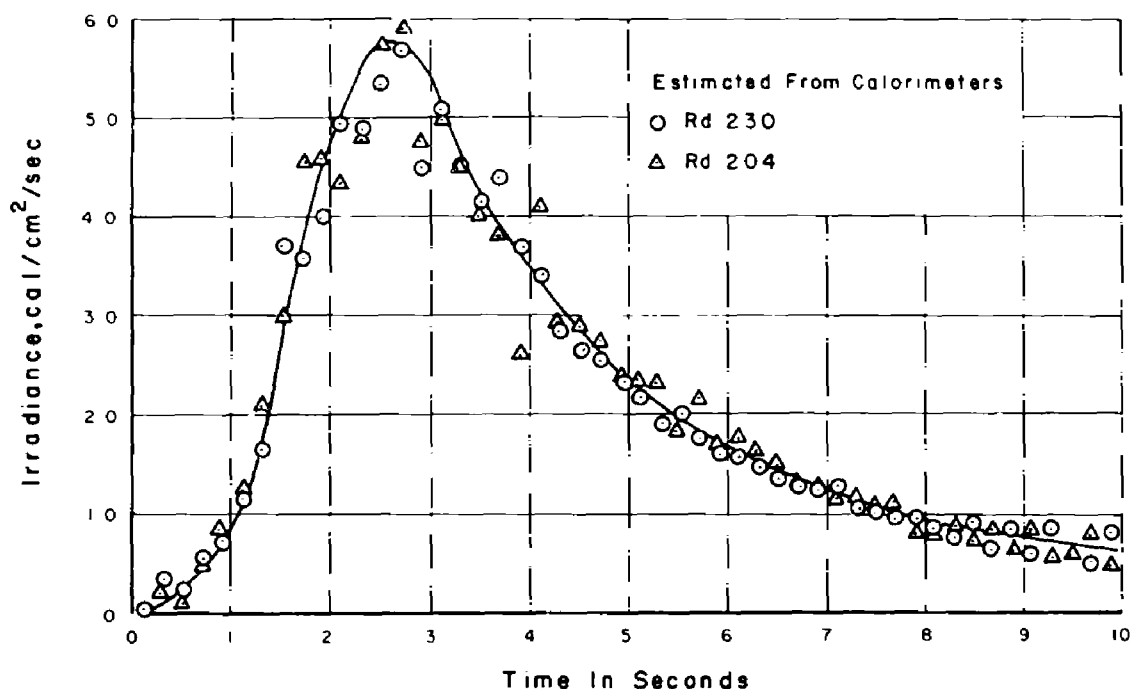


Figure D.13 Estimated direct thermal irradiance, Shot Navajo.

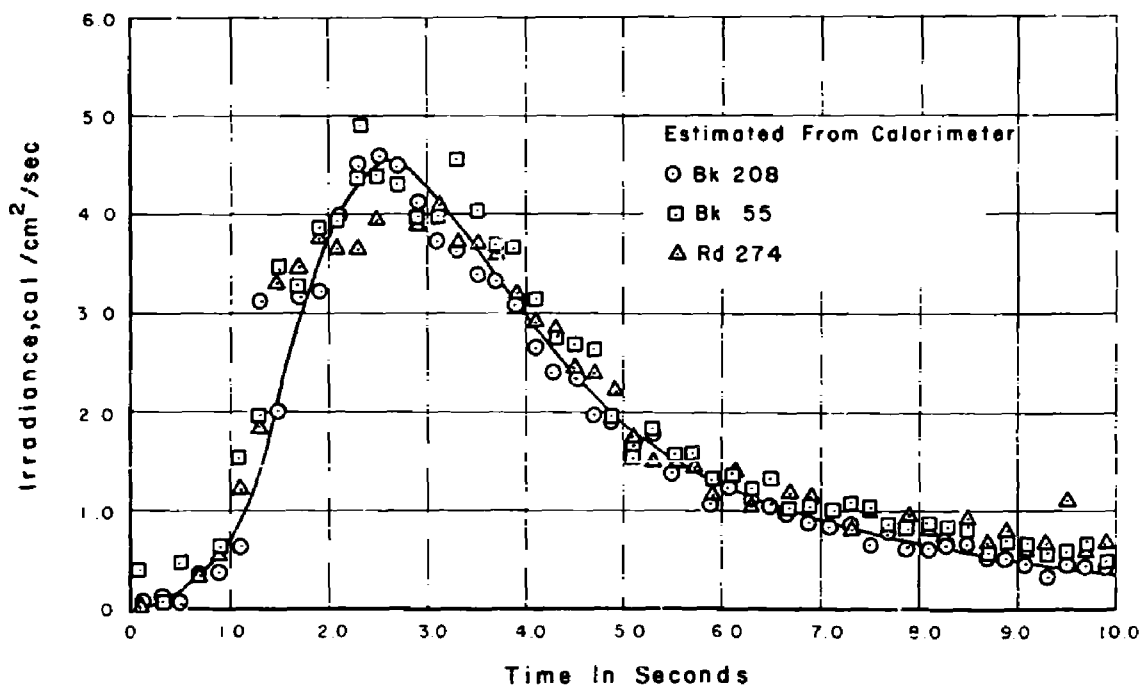


Figure D.14 Estimated indirect thermal irradiance, Shot Navajo.

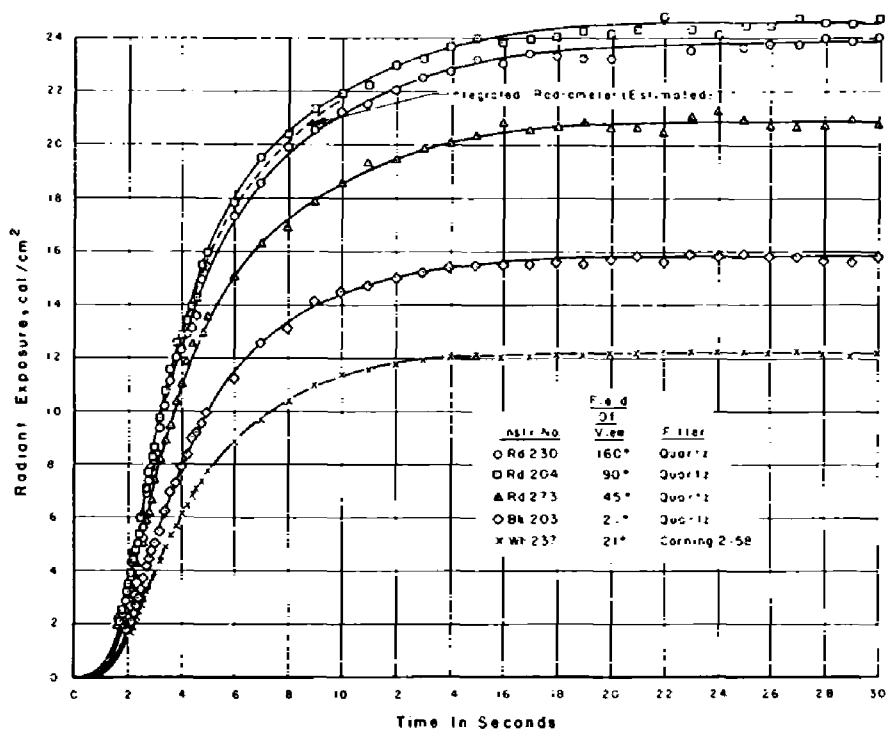


Figure D.15 Radiant exposure of direct thermal instruments, Shot Navajo.

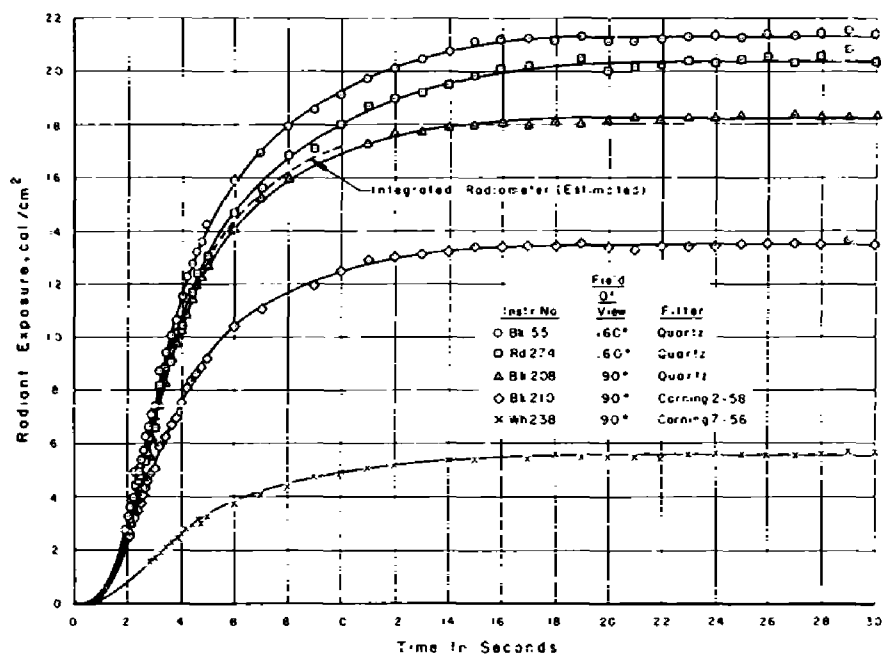


Figure D.16 Radiant exposure of indirect thermal instruments, Shot Navajo.

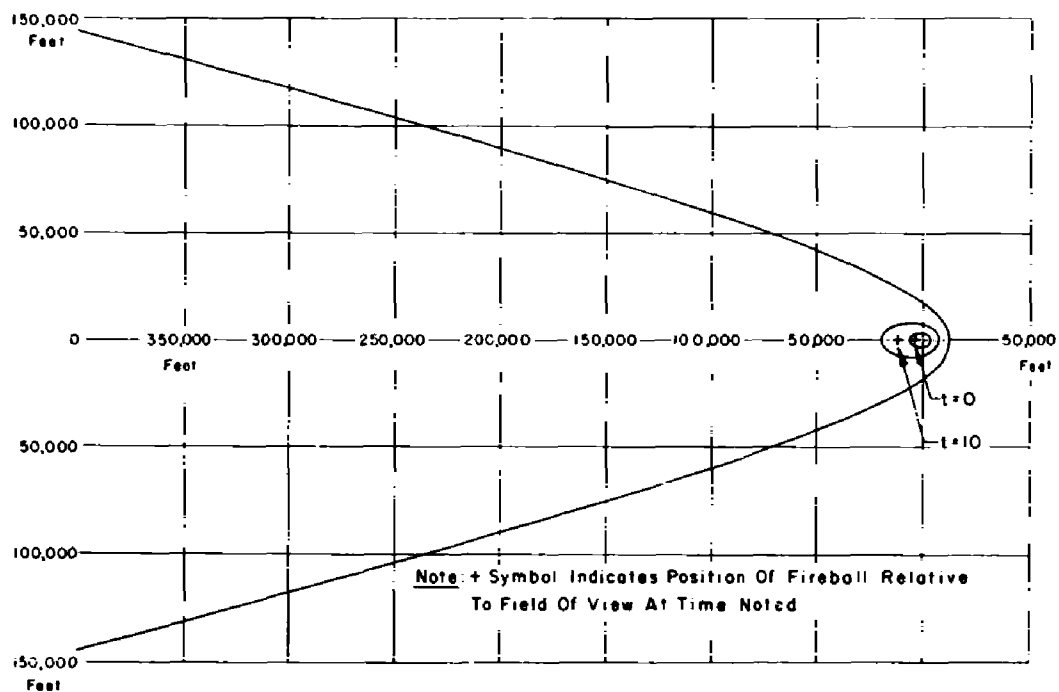


Figure D.17 Field of view of direct thermal instruments, Shot Huron.

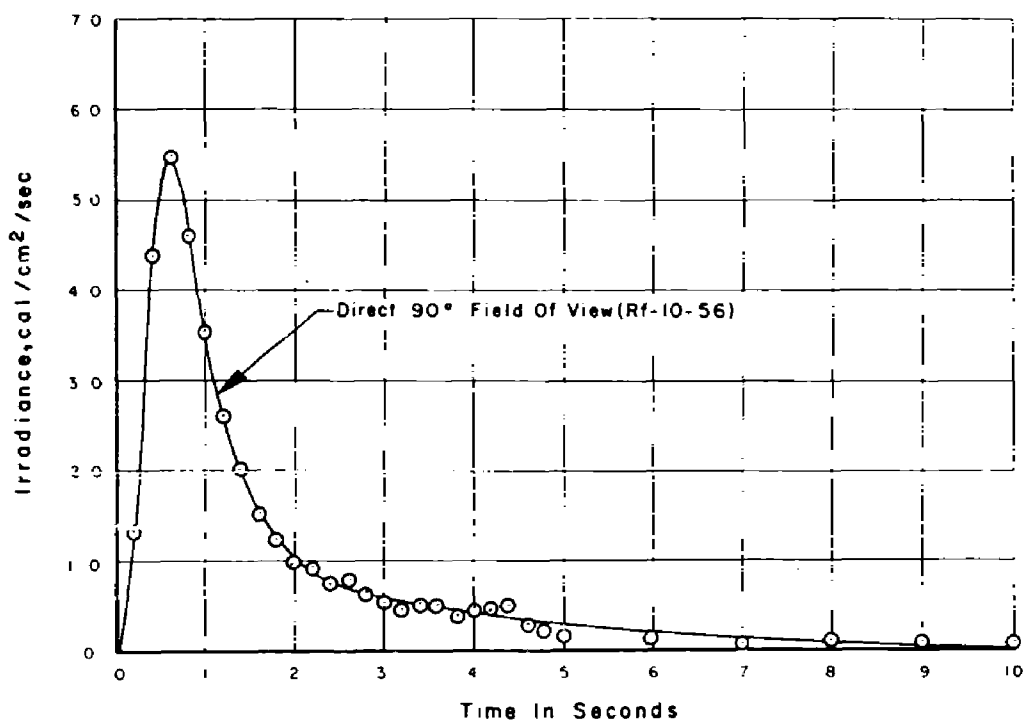


Figure D.18 Thermal irradiance as a function of time, Shot Huron.

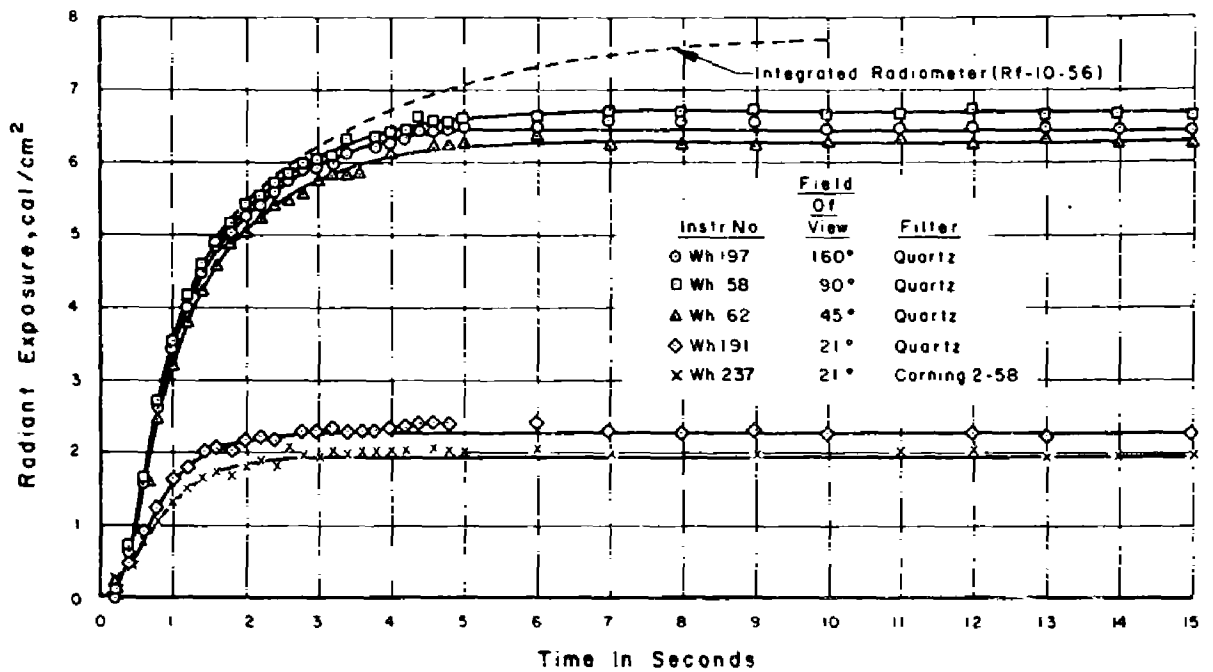


Figure D.19 Radiant exposure of direct thermal instruments, Shot Huron.

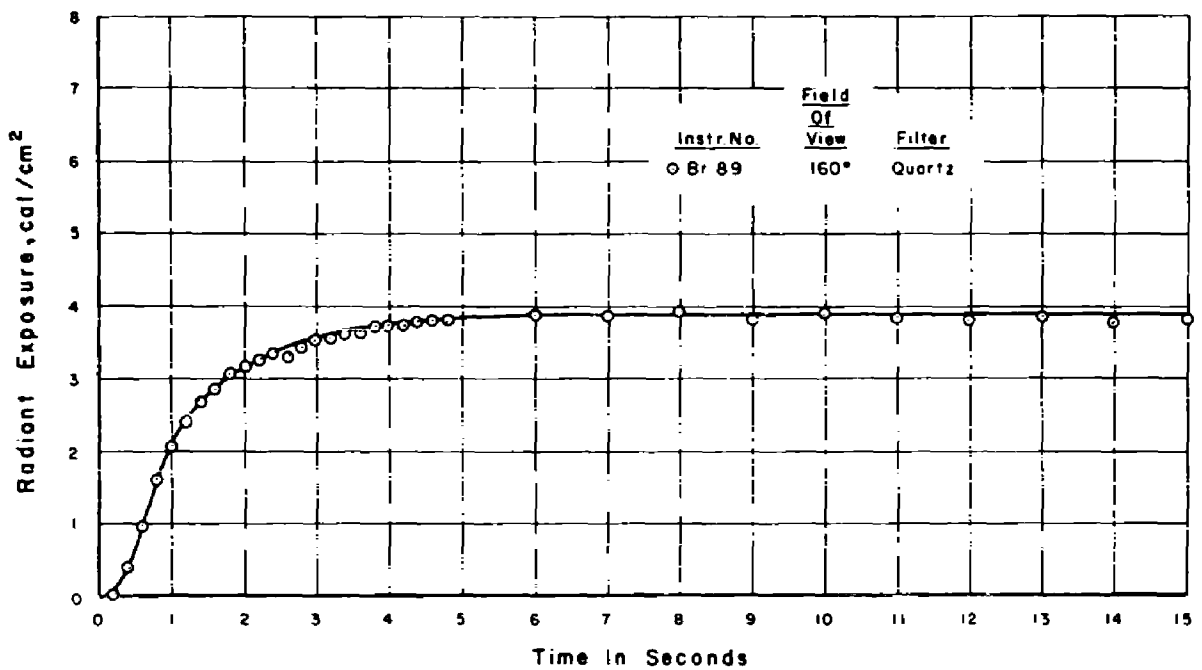


Figure D.20 Radiant exposure of indirect thermal instruments, Shot Huron.

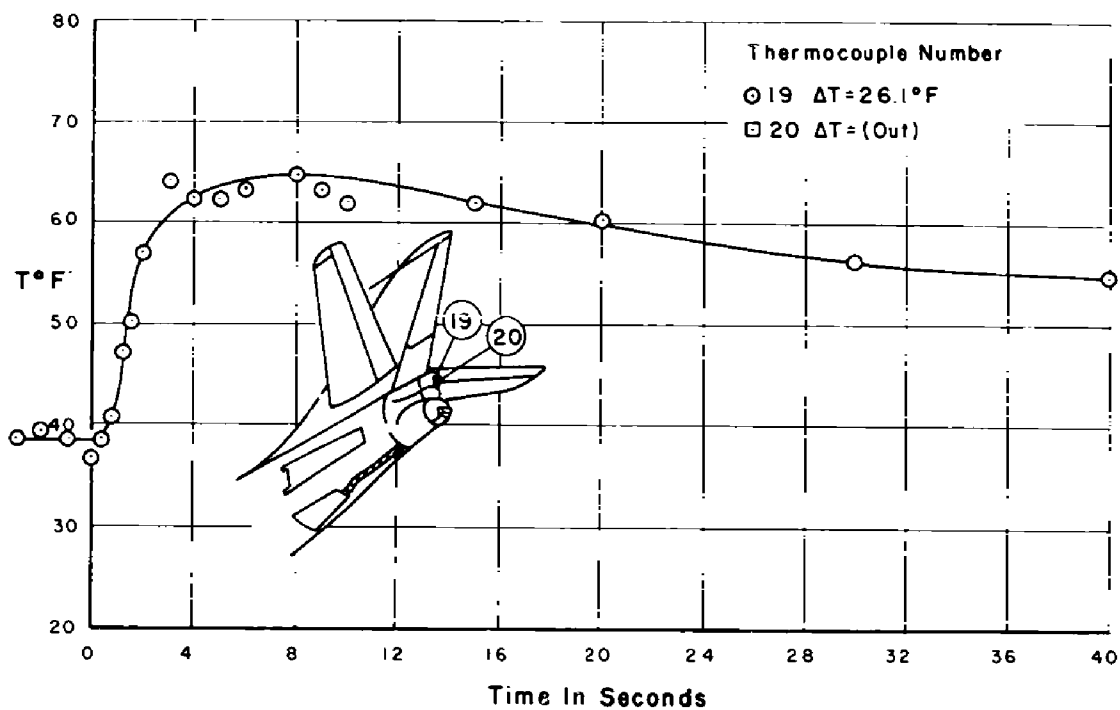


Figure D.21 Temperature time history of plastic radome, Shot Zuni.

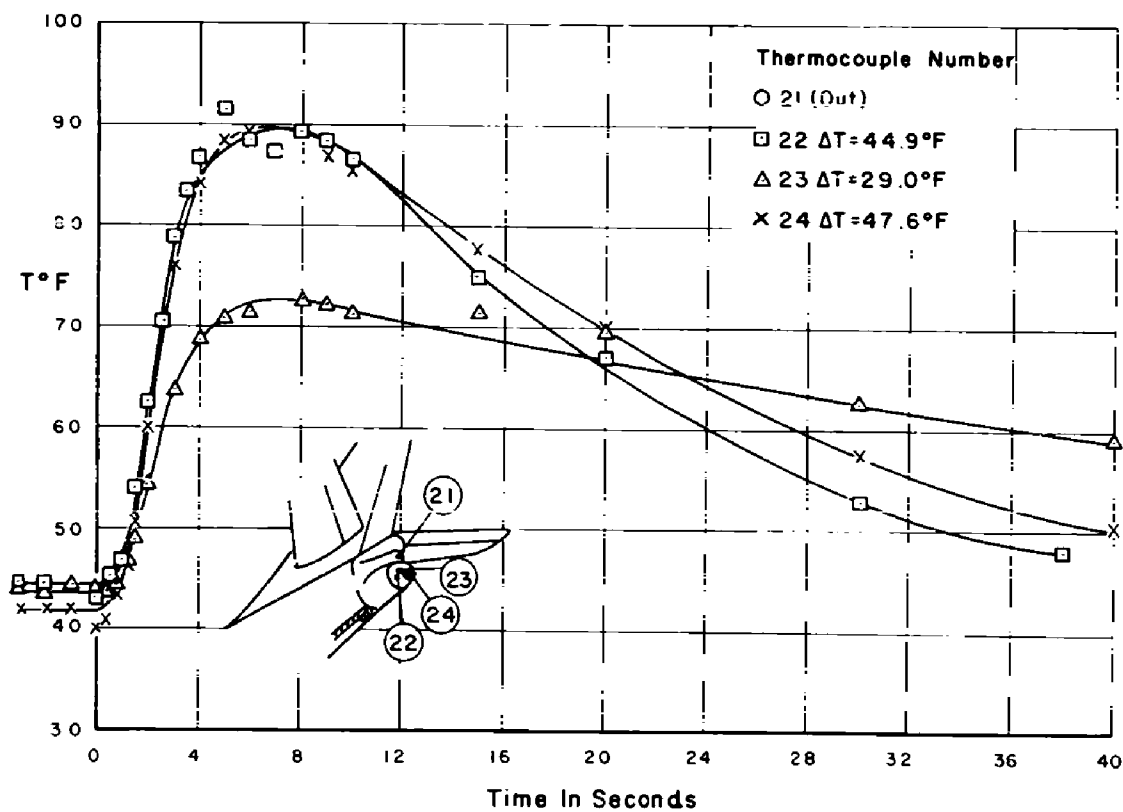


Figure D.22 Temperature time history of tail turret, Shot Zuni.

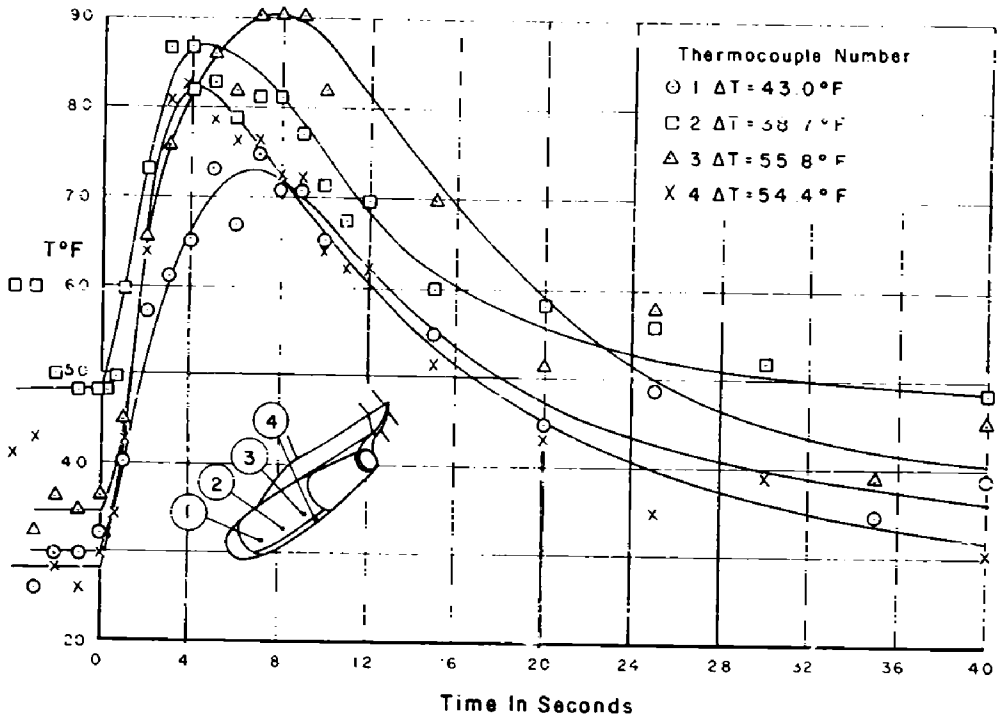


Figure D.23 Temperature time history of nacelle skin, Shot Apache.

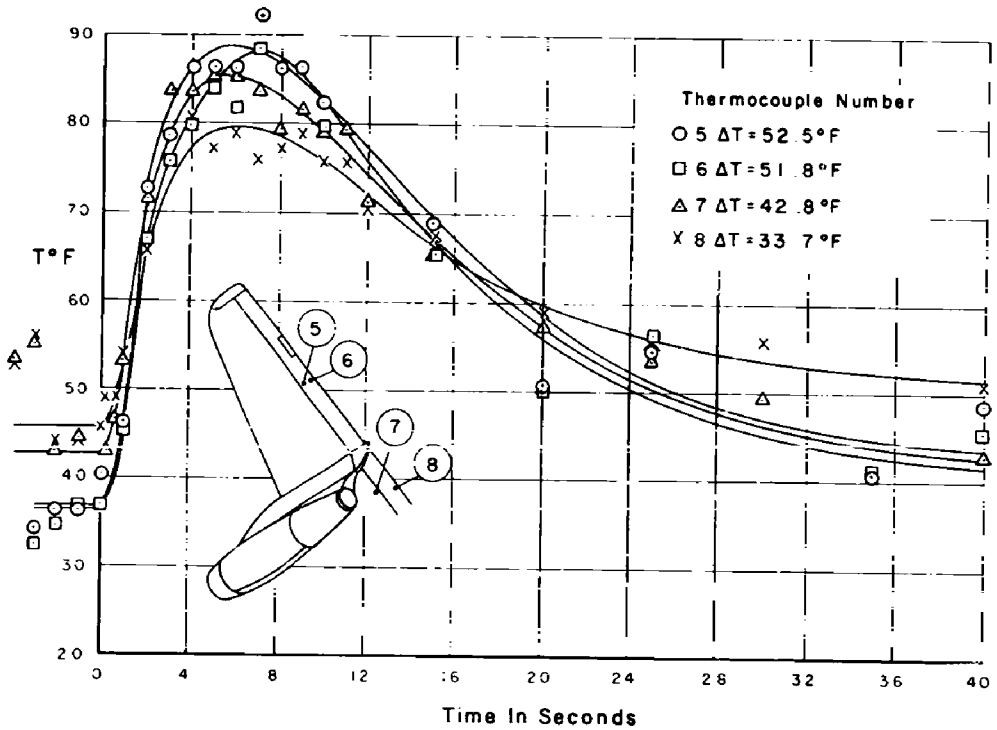


Figure D.24 Temperature time history of aileron and flap skin, Shot Apache.

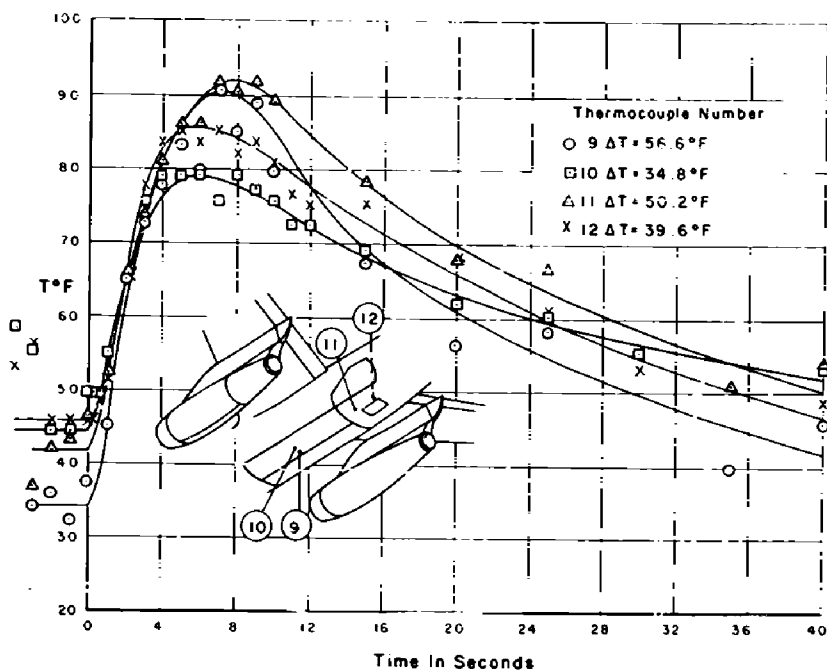


Figure D.25 Temperature time history of bomb bay door and lower fuselage, Shot Apache.

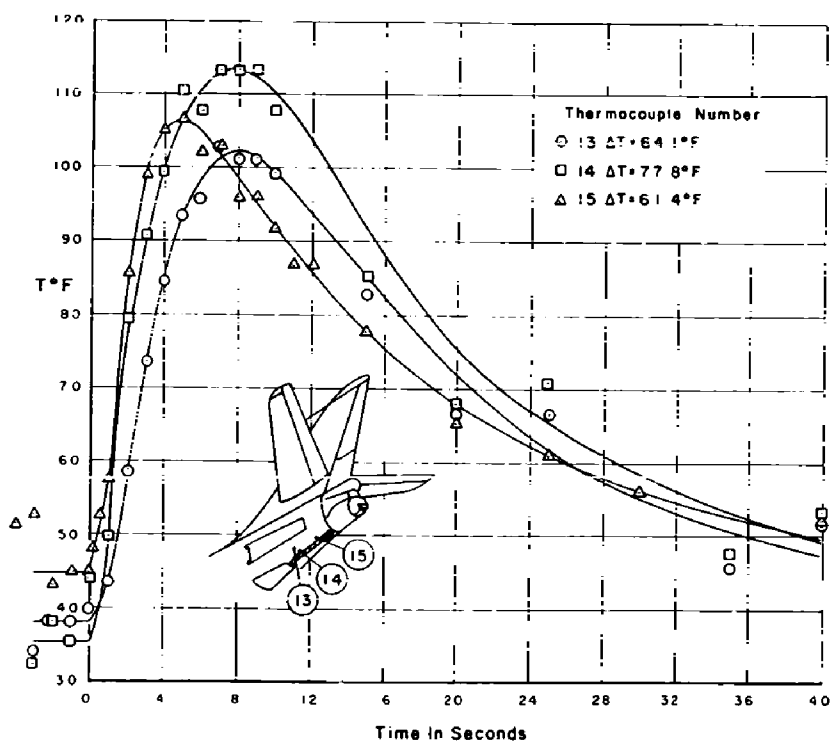


Figure D.26 Temperature time history of arresting hook area, Shot Apache.

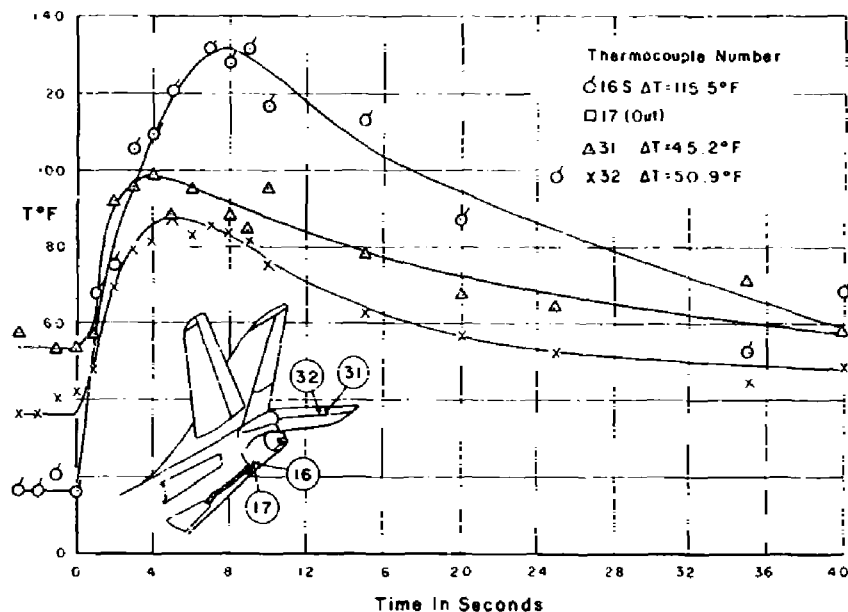


Figure D.27 Temperature time history of quartz covered thermocouple compared to adjacent uncovered thermocouple, Shot Apache

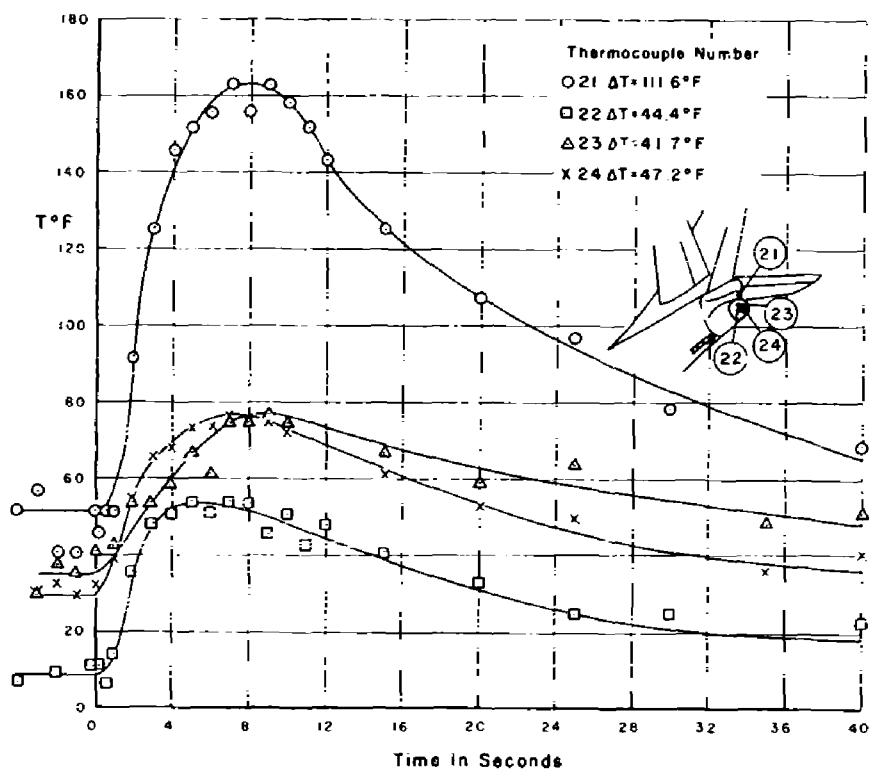


Figure D.28 Temperature time history of tail turret, Shot Apache

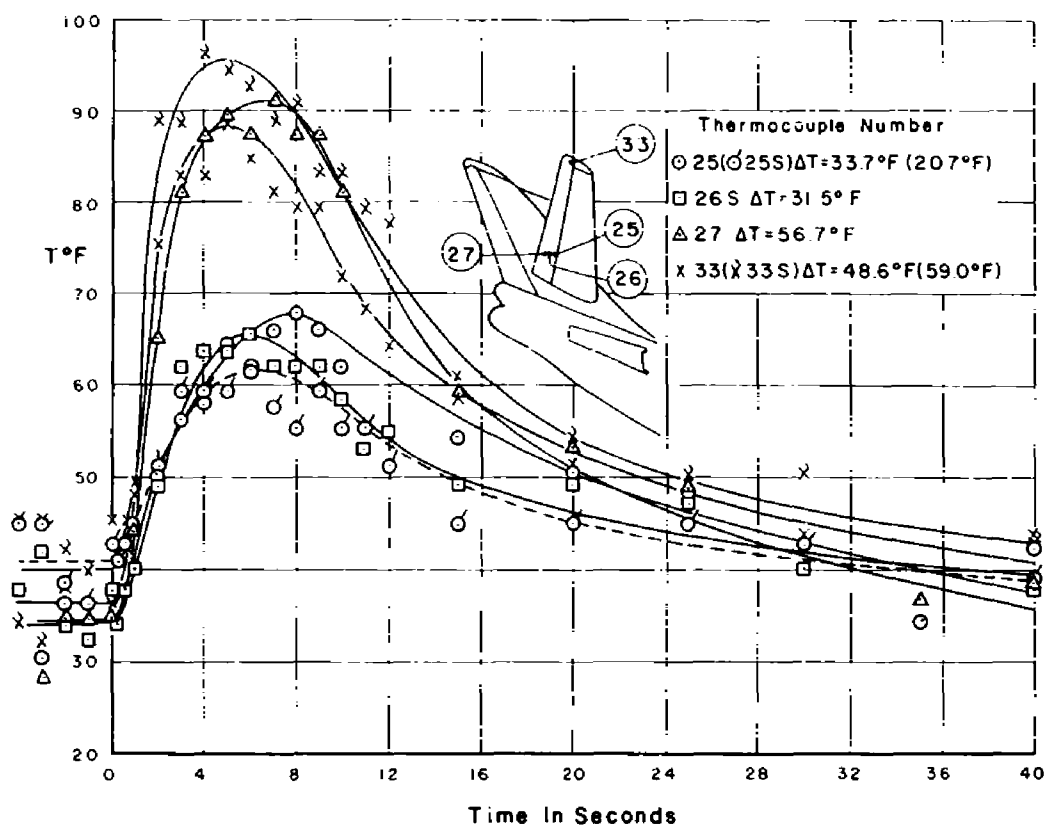


Figure D.29 Temperature time history of elevator skin, Shot Apache.

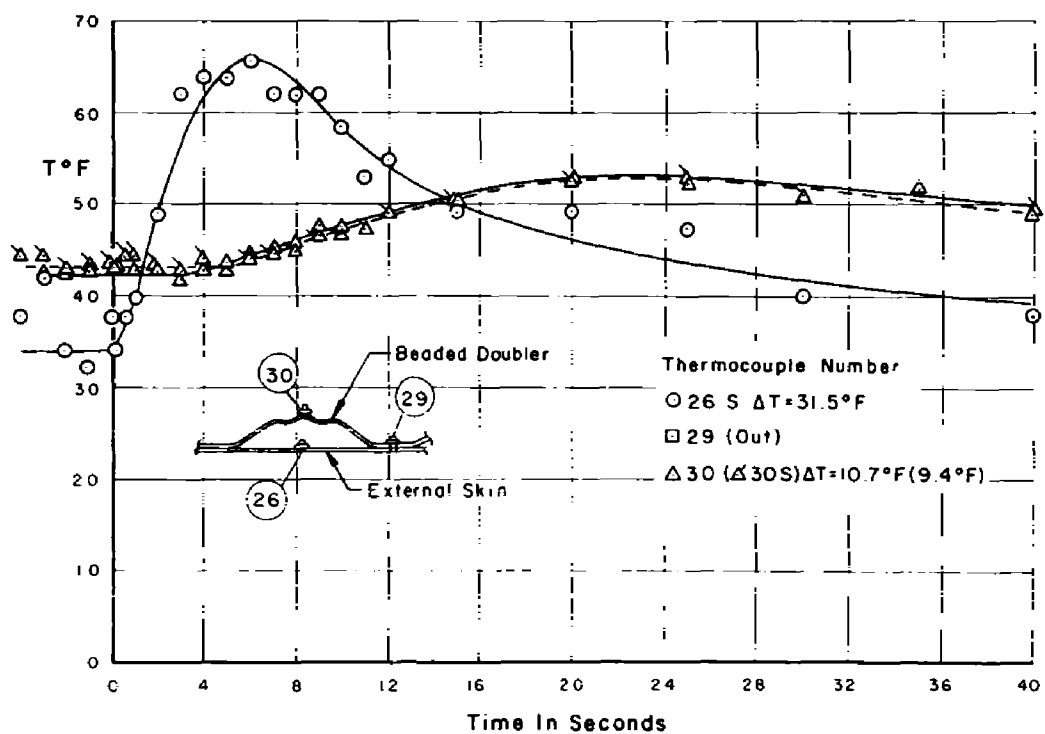


Figure D.30 Temperature time history comparing outer skin and internal beaded doubler, Shot Apache.

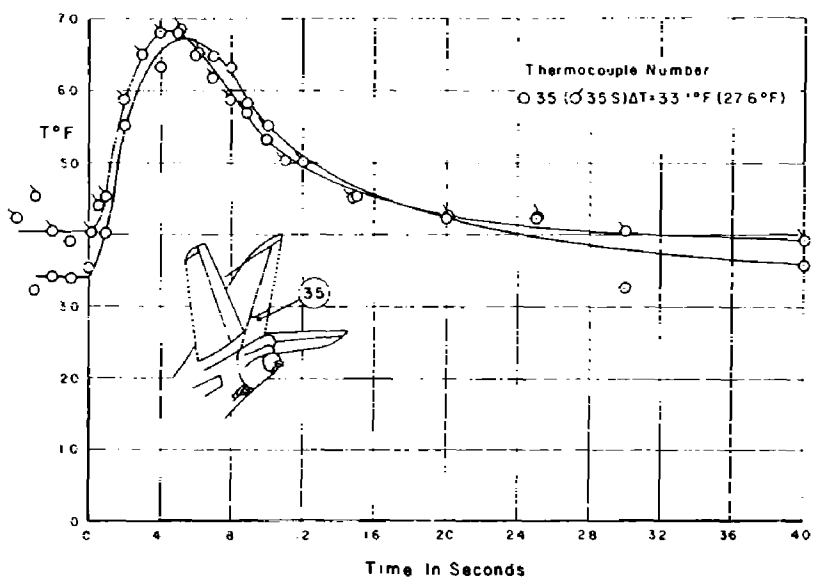


Figure D.31 Temperature time history of lower rudder, Shot Apache.

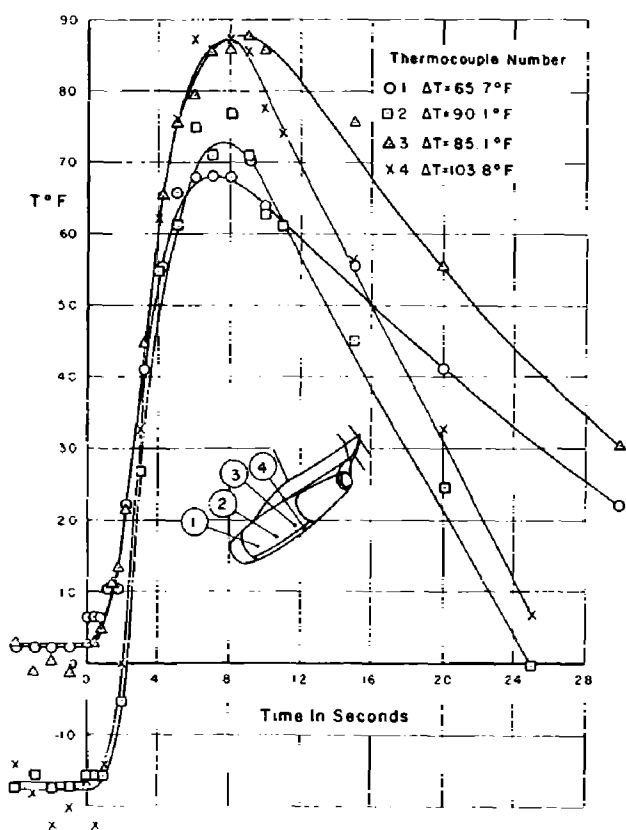


Figure D.32 Temperature time history of nacelle skin, Shot Navajo.

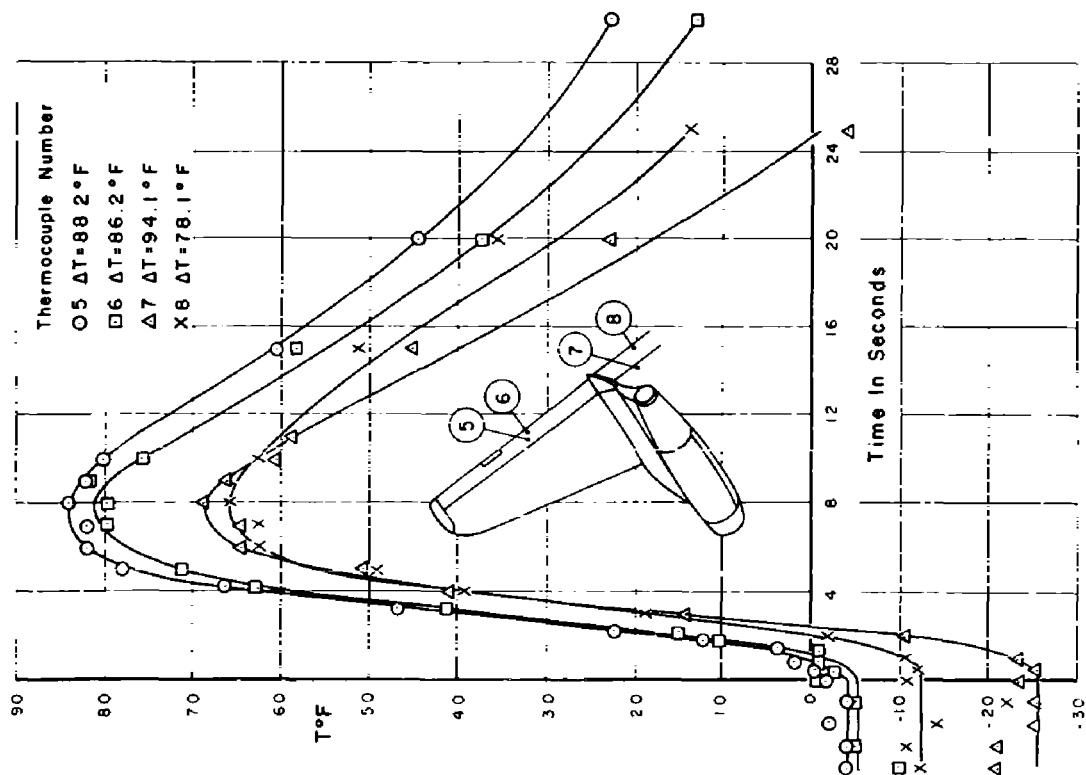


Figure D.33 Temperature time history of aileron and flap skin, Shot Navajo.

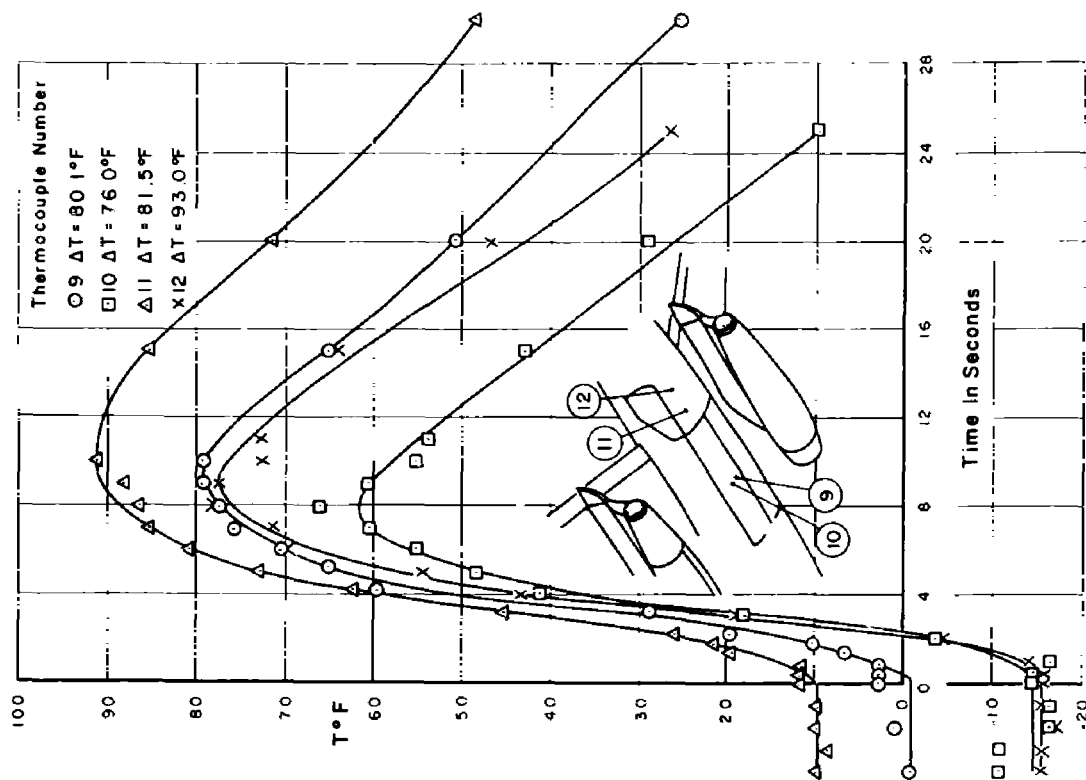


Figure D.34 Temperature time history of bomb bay door and lower fuselage, Shot Navajo.

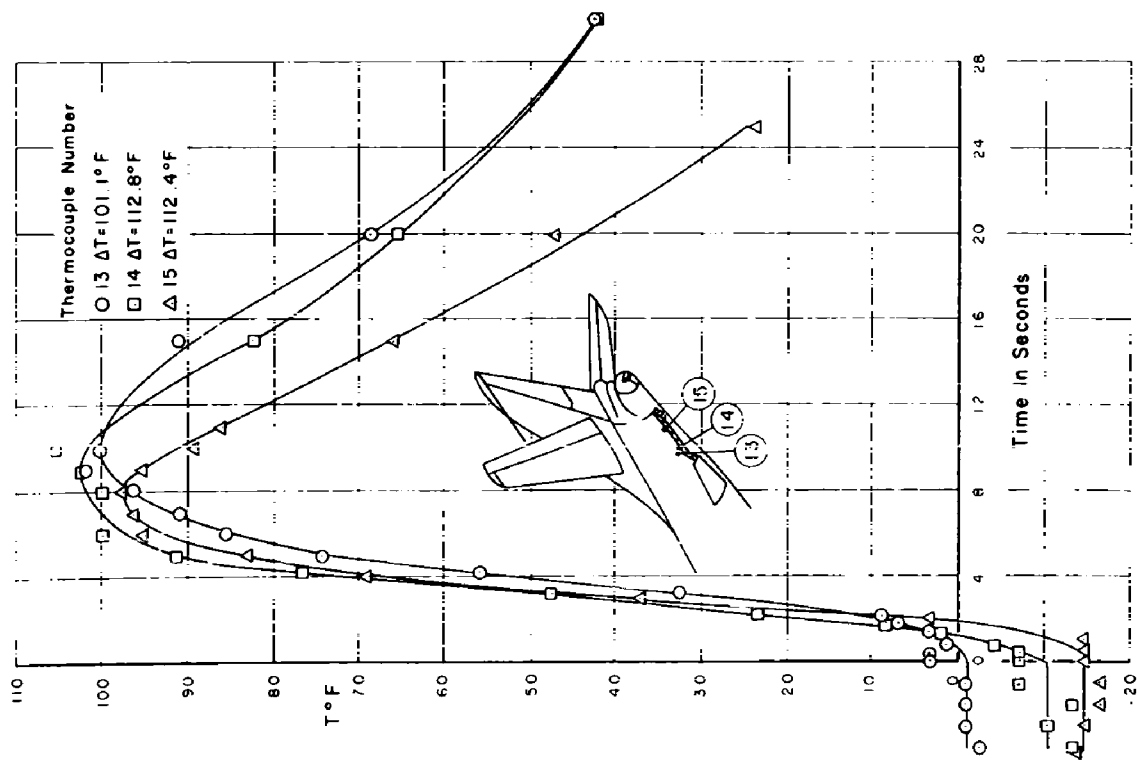


Figure D.35 Temperature time history of arresting hook area, Shot Navajo.

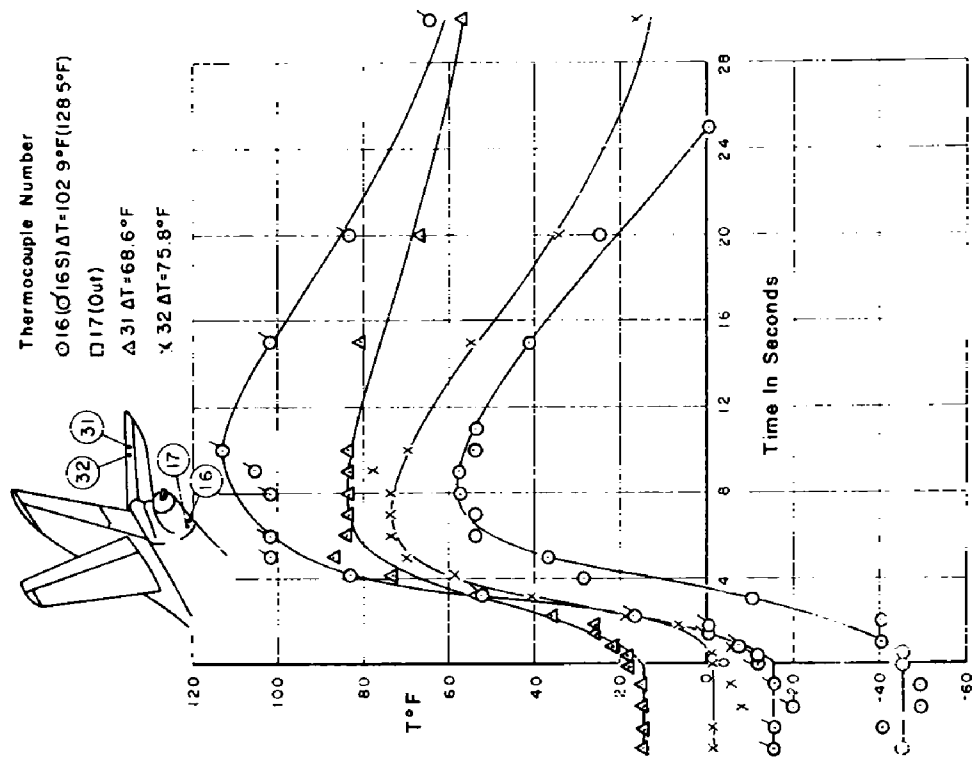


Figure D.36 Temperature time history of quartz covered thermocouple compared to adjacent uncovered thermocouple, Shot Navajo.

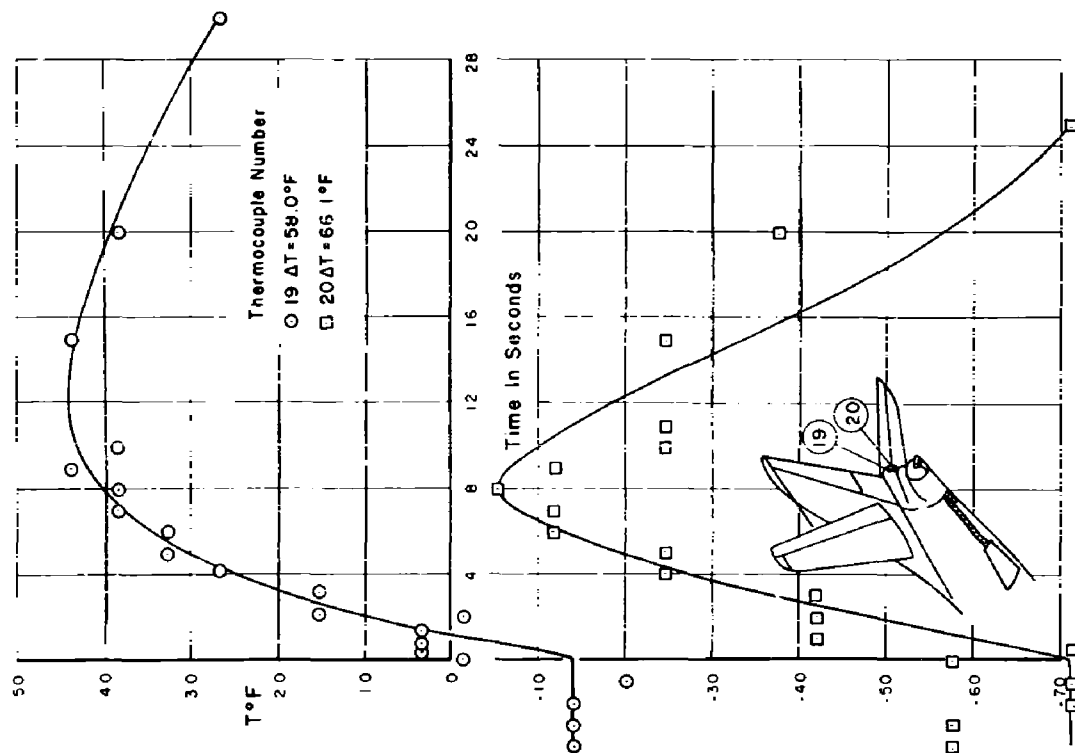


Figure D.37 Temperature time history of plastic radome, Shot Navajo.

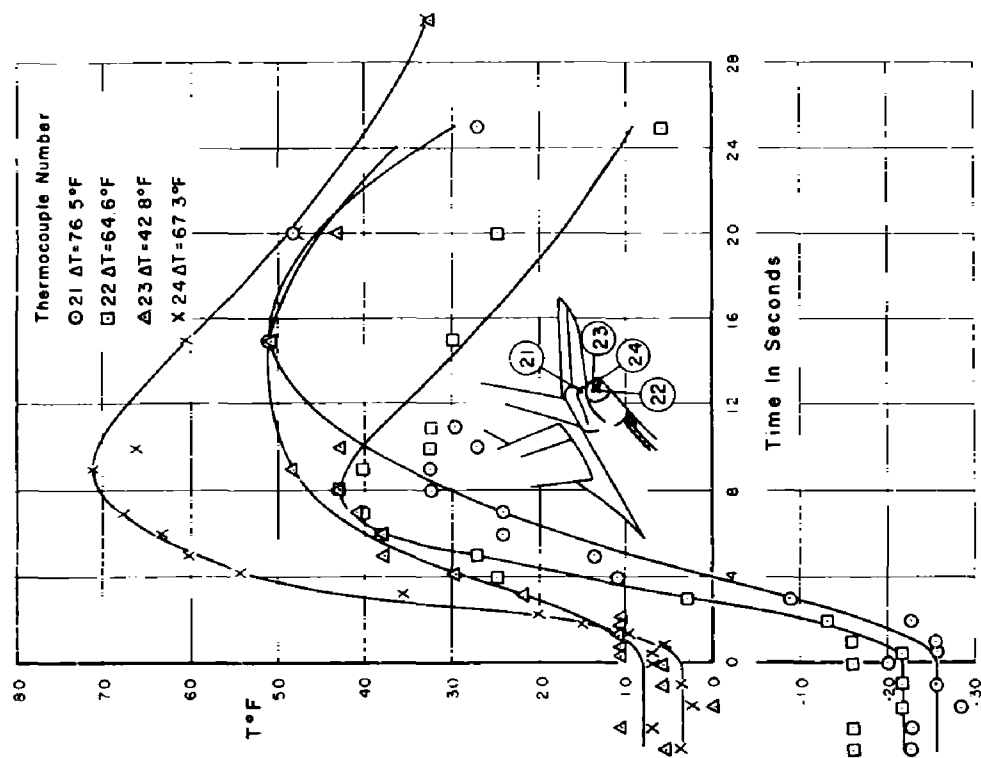


Figure D.38 Temperature time history of tail turret, Shot Navajo.

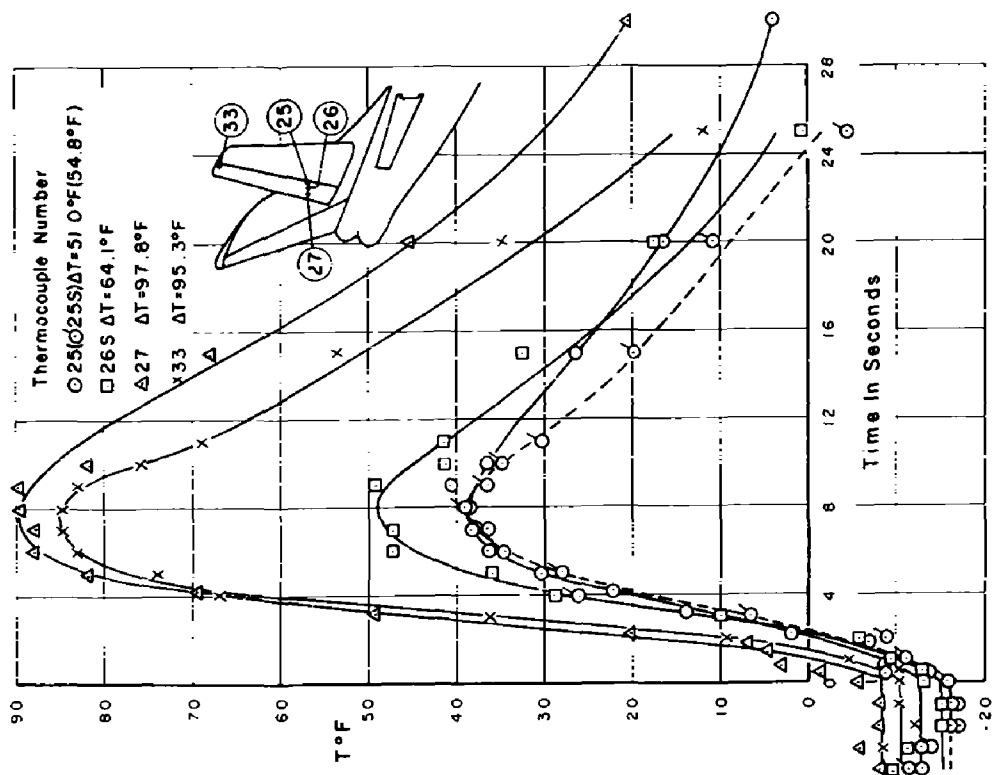


Figure D.39 Temperature time history of elevator skin, Shot Navajo.

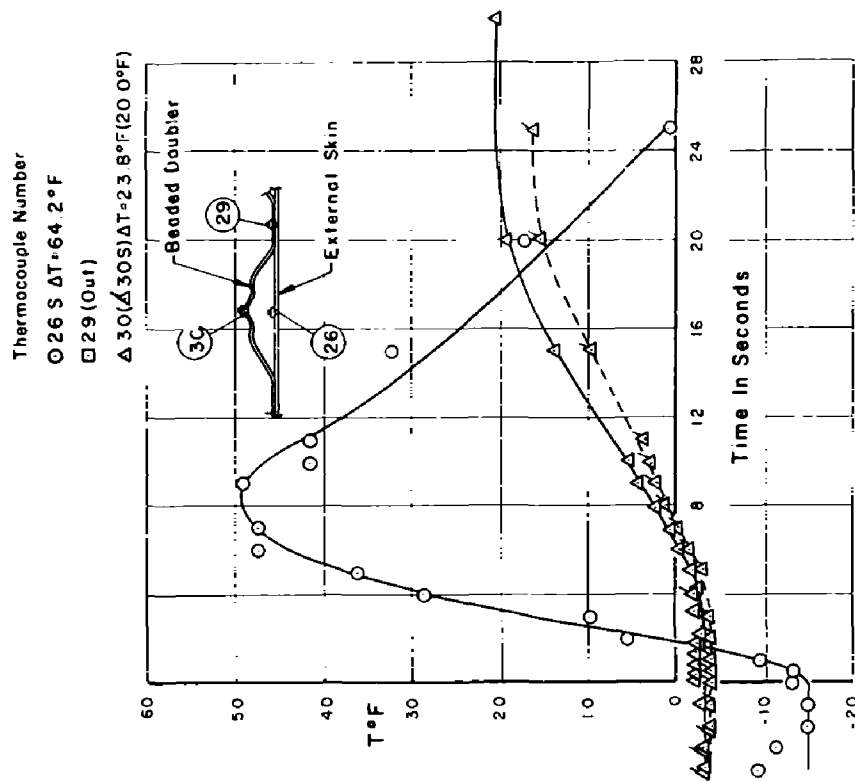


Figure D.40 Temperature time history comparing outer skin and internal beaded doubler, Shot Navajo.

Thermocouple Number
 35(\odot 35 S) $\Delta T=39.0^{\circ}\text{F}(43.3^{\circ}\text{F})$

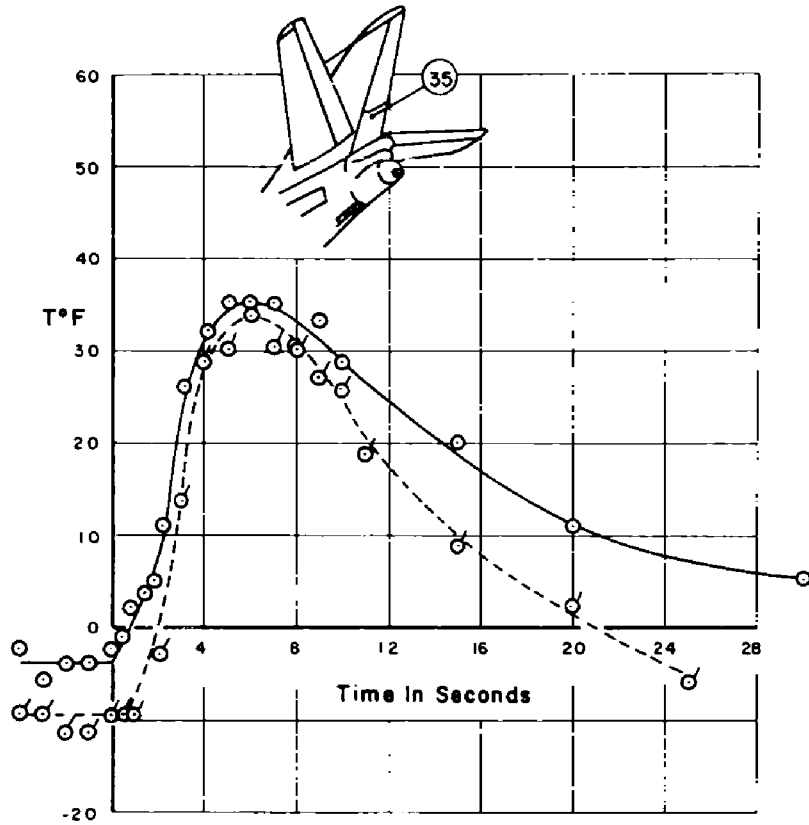


Figure D.41 Temperature time history of lower rudder, Shot Navajo.

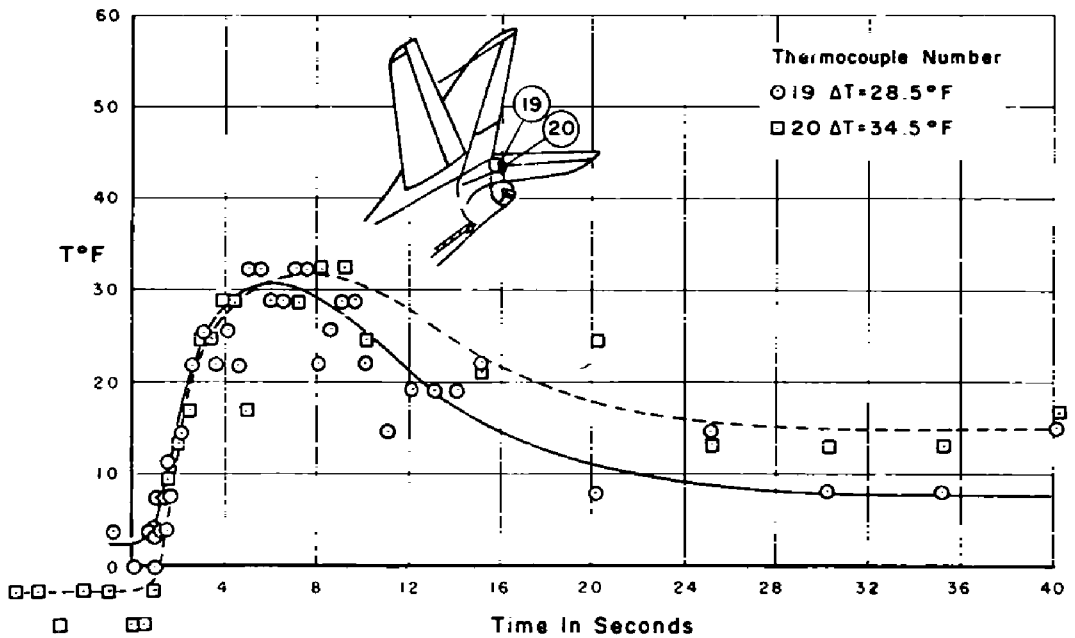


Figure D.42 Temperature time history of plastic radome, Shot Tewa.

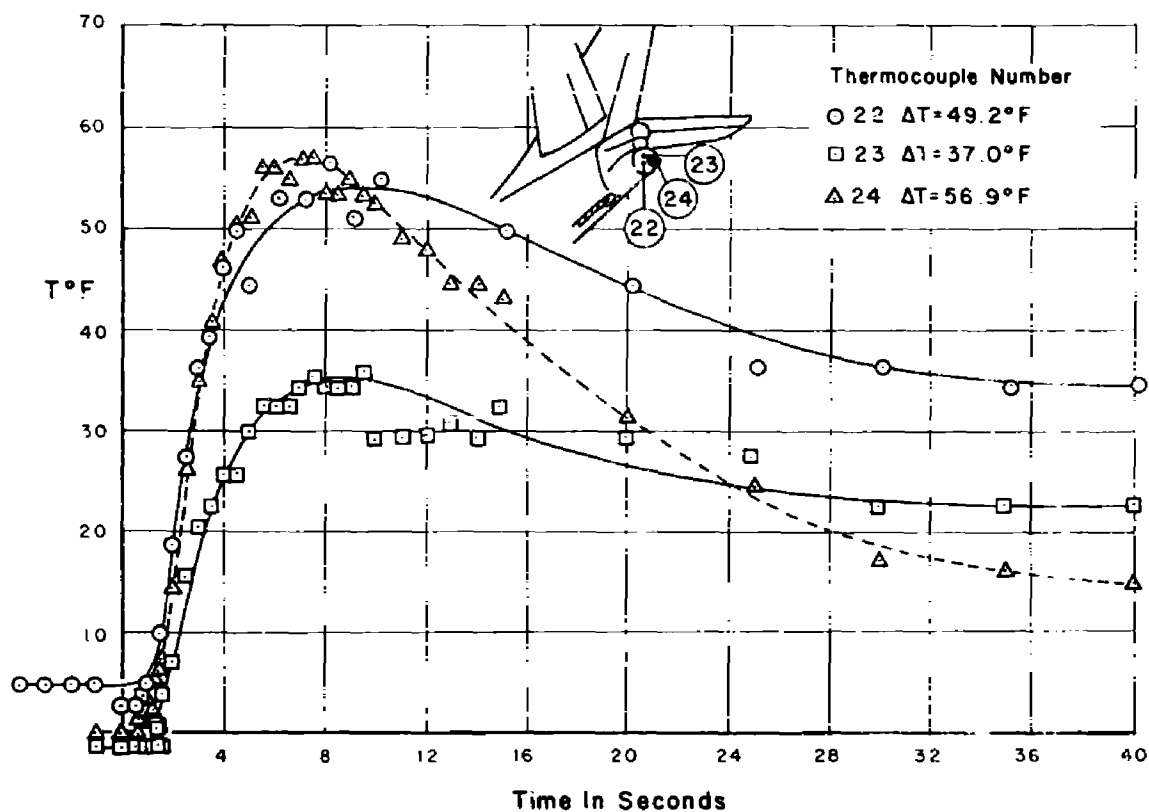


Figure D.43 Temperature time history of tail turret, Shot Tewa.

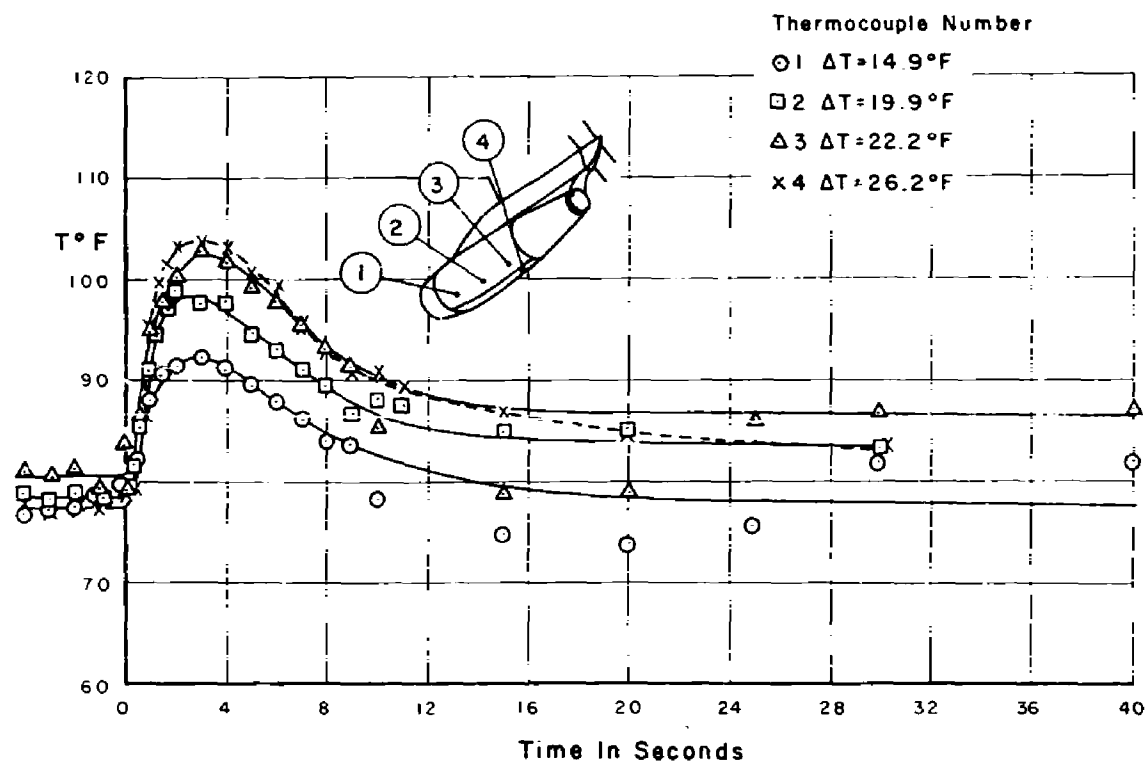


Figure D.44 Temperature time history of nacelle skin, Shot Huron.

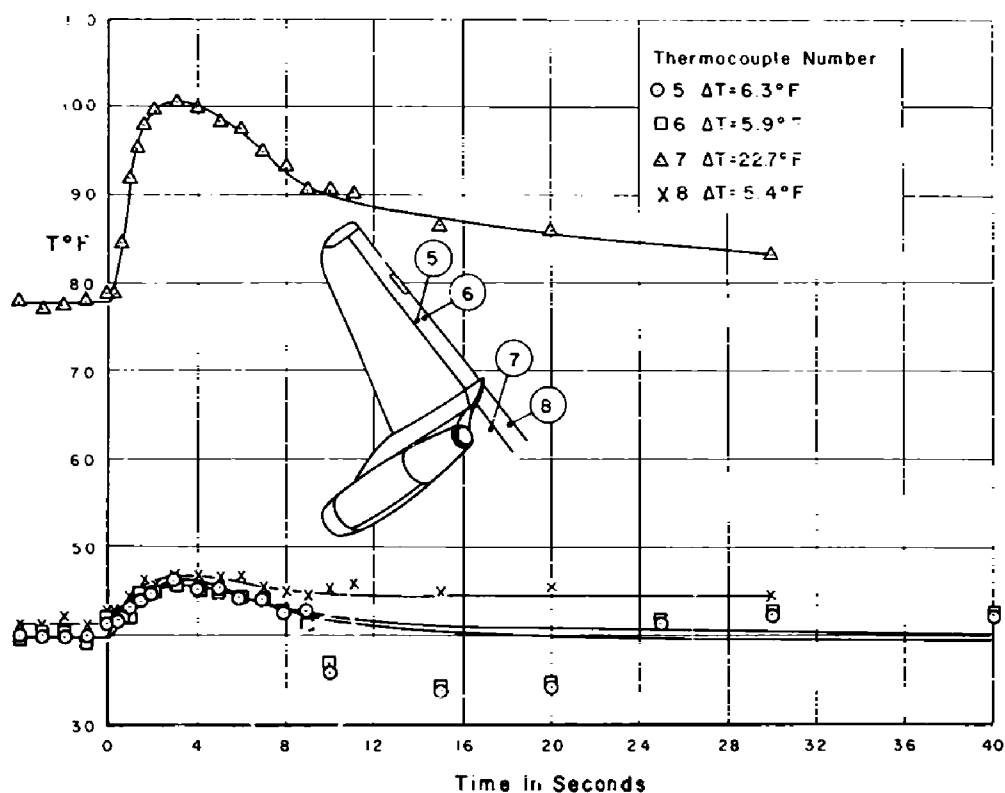


Figure D.45 Temperature time history of aileron and flap skin, Shot Huron.

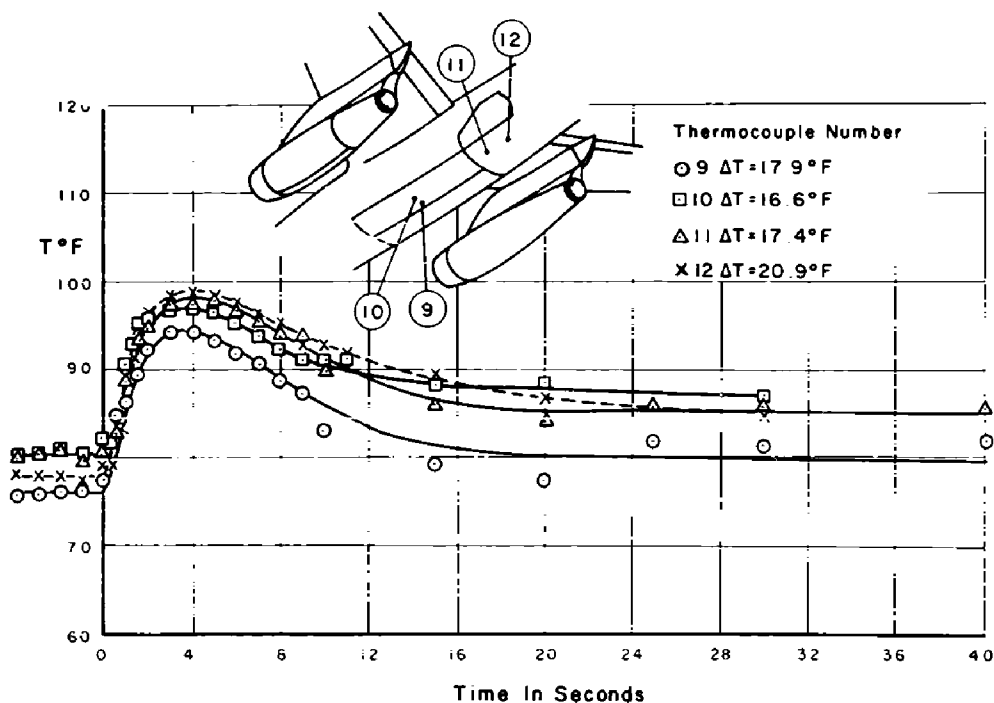


Figure D.46 Temperature time history of bomb bay door and lower fuselage, Shot Huron.

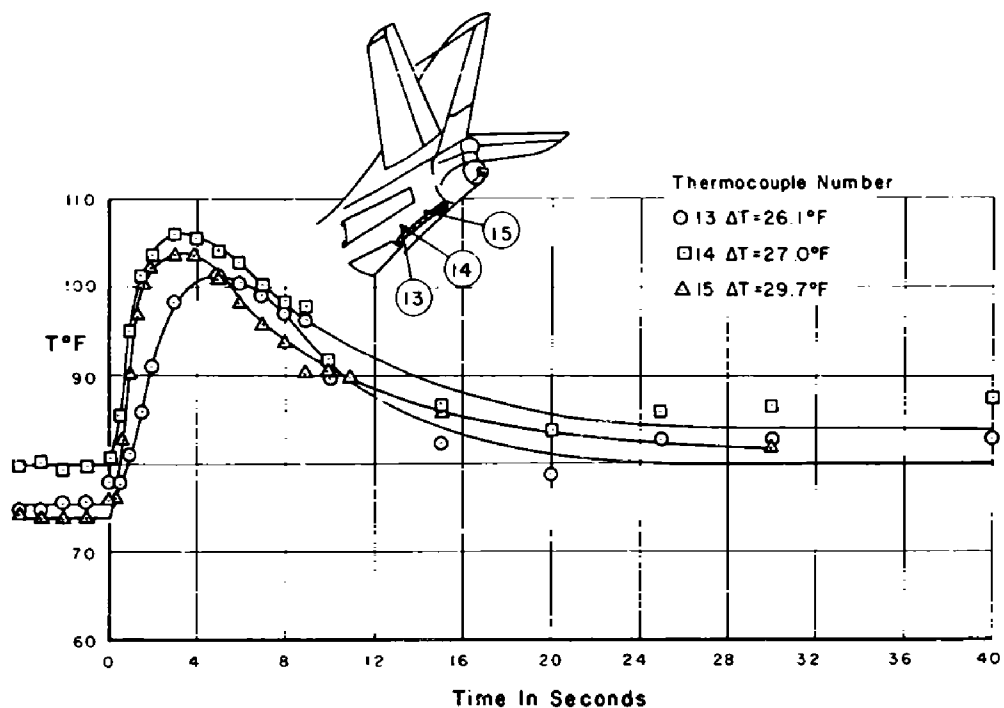


Figure D.47 Temperature time history of arresting hook area, Shot Huron.

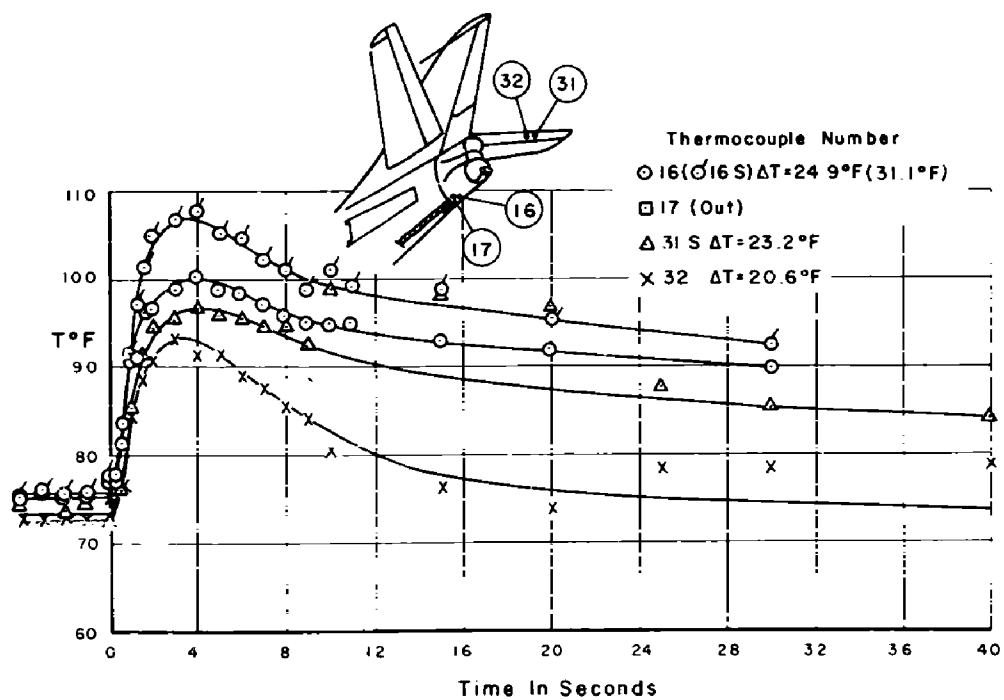


Figure D.48 Temperature time history of quartz covered thermocouple compared to adjacent uncovered thermocouple, Shot Huron.

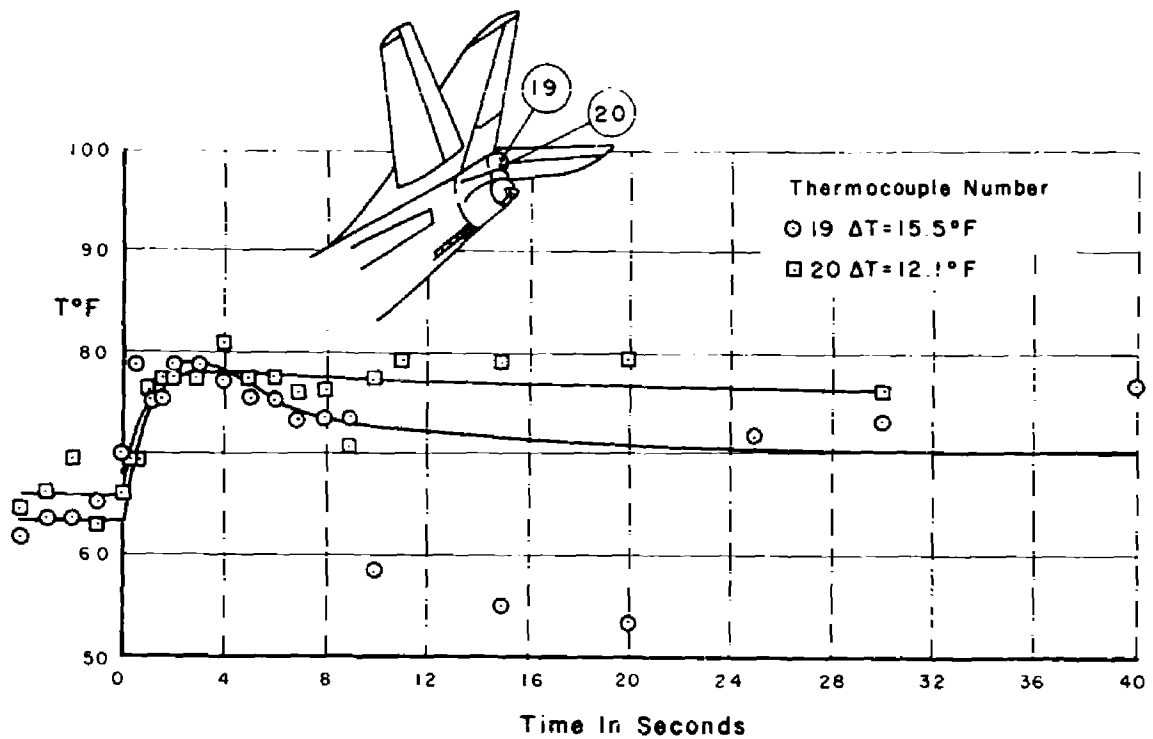


Figure D.49 Temperature time history of plastic radome, Shot Huron.

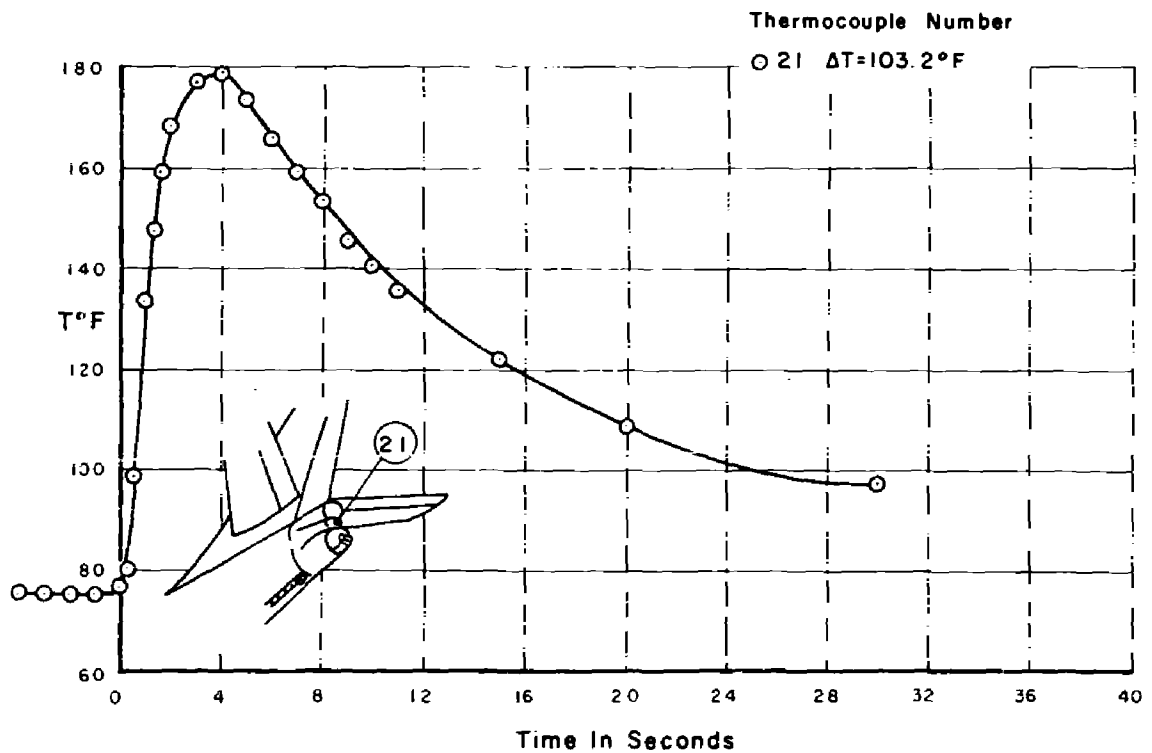


Figure D.50 Temperature time history of tail turret, gray paint, Shot Huron.

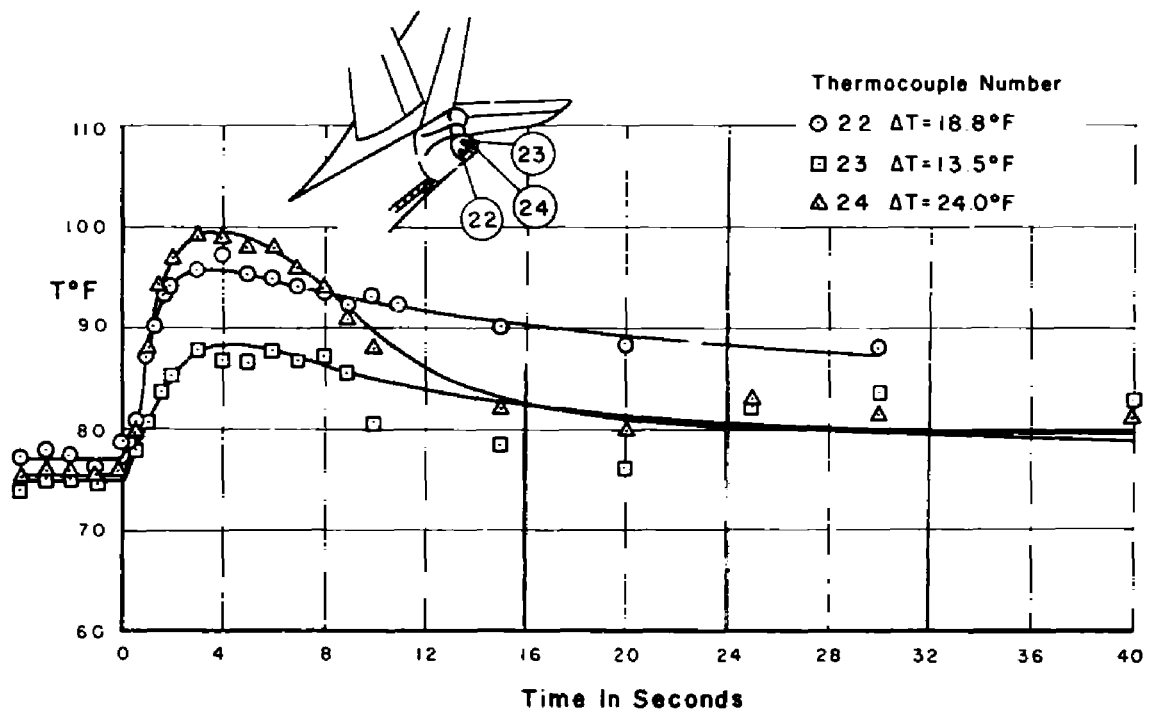


Figure D.51 Temperature time history of tail turret, white paint, Shot Huron.

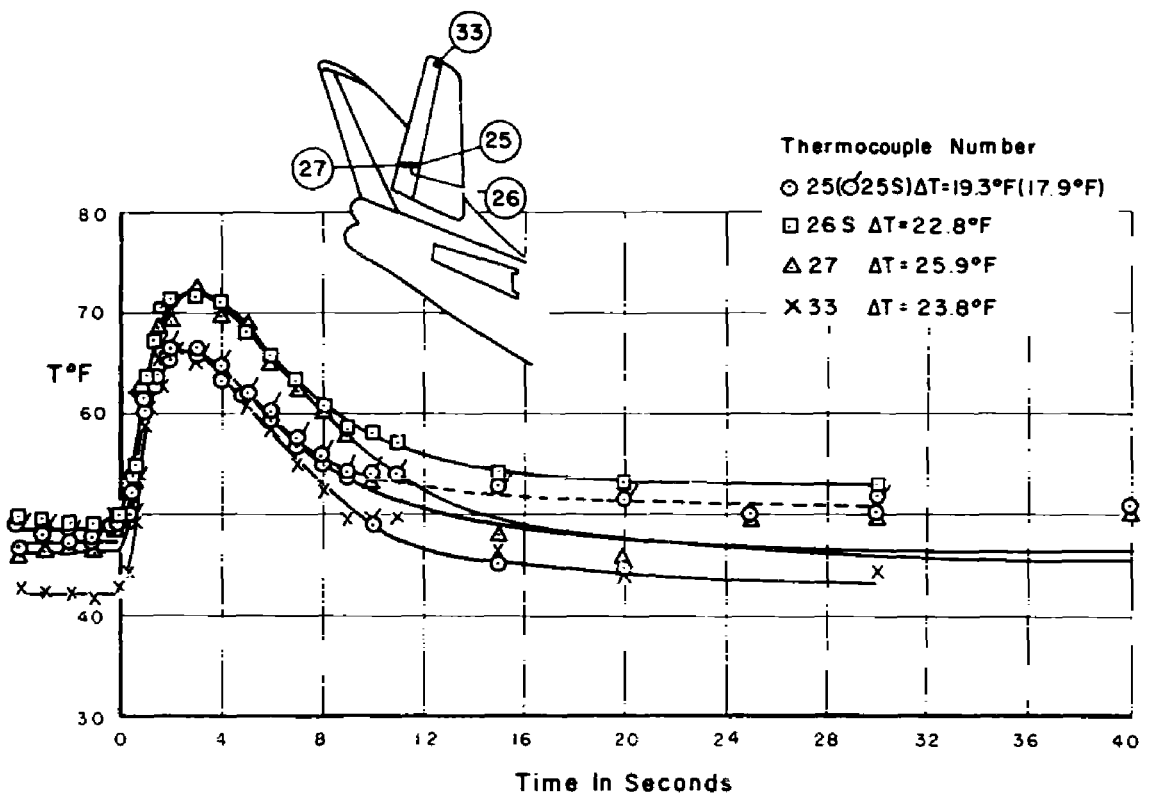


Figure D.52 Temperature time history of elevator skin, Shot Huron.

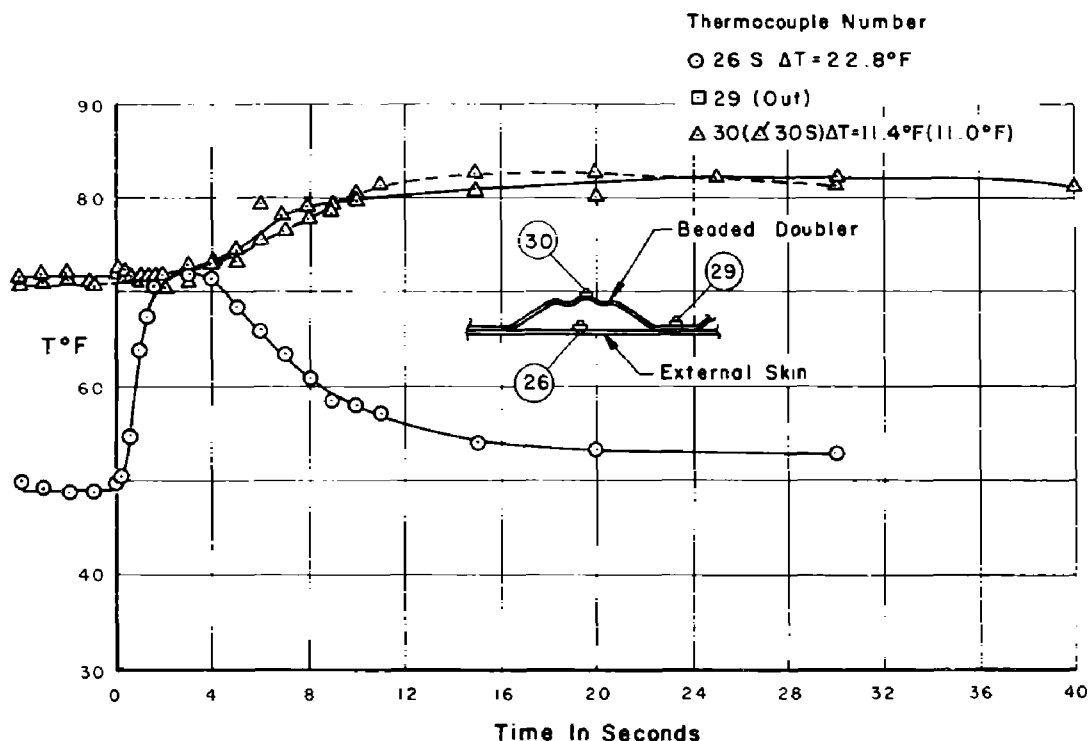


Figure D.53 Temperature time history comparing outer skin and internal beaded doubler, Shot Huron.

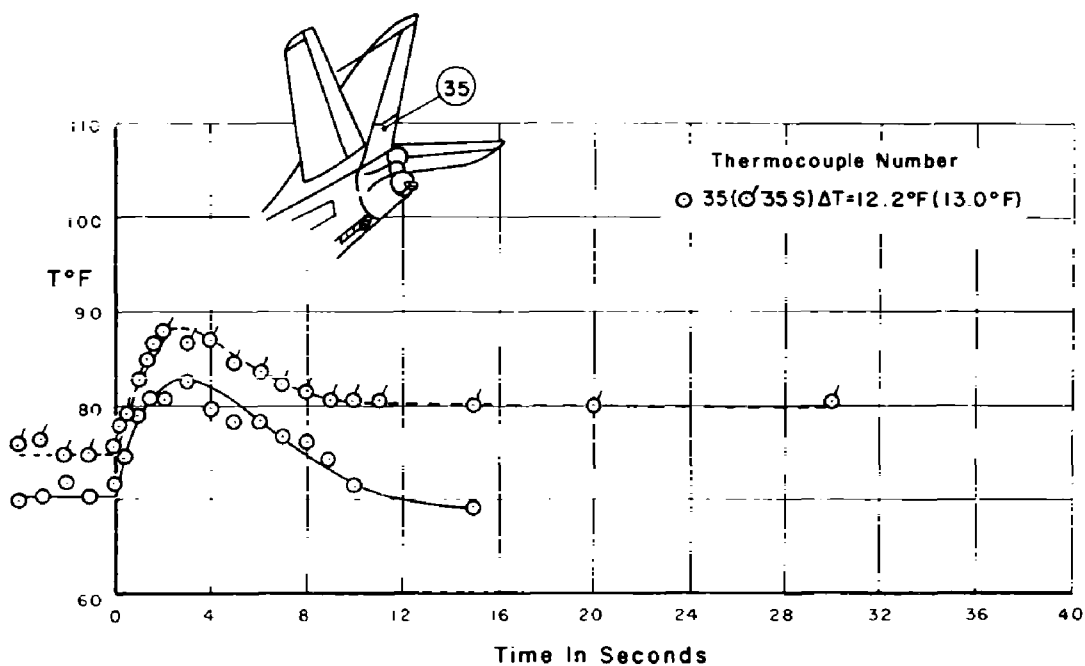


Figure D.54 Temperature time history of lower rudder, Shot Huron.

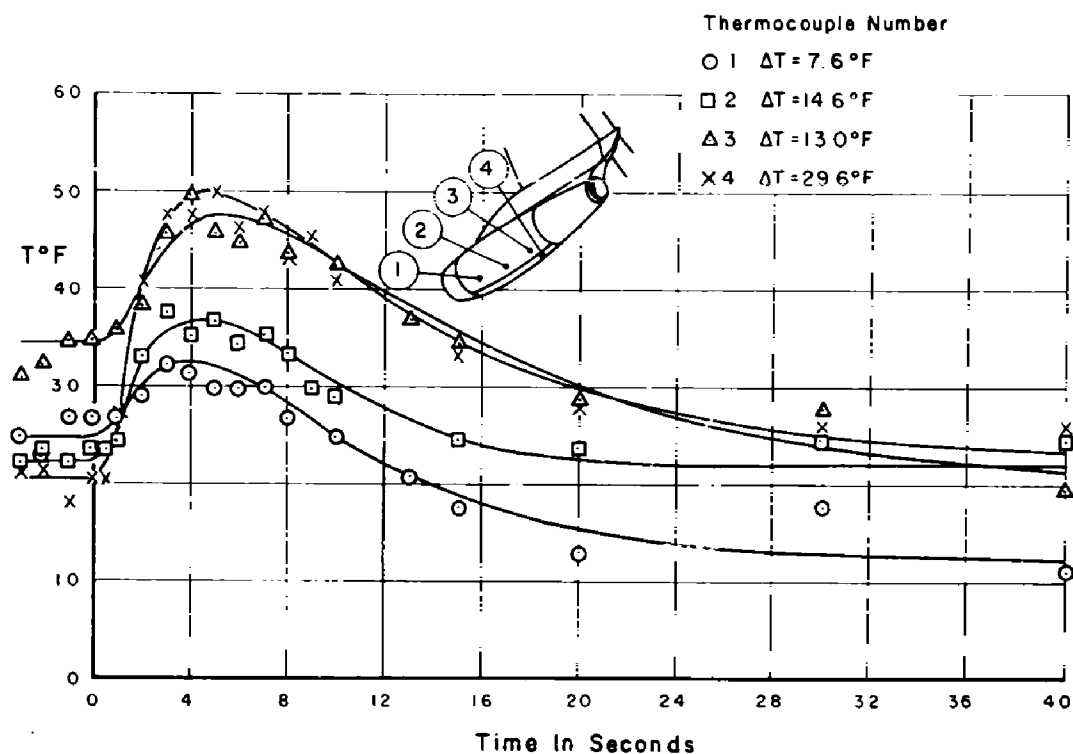


Figure D.55 Temperature time history of nacelle skin, Shot Cherokee.

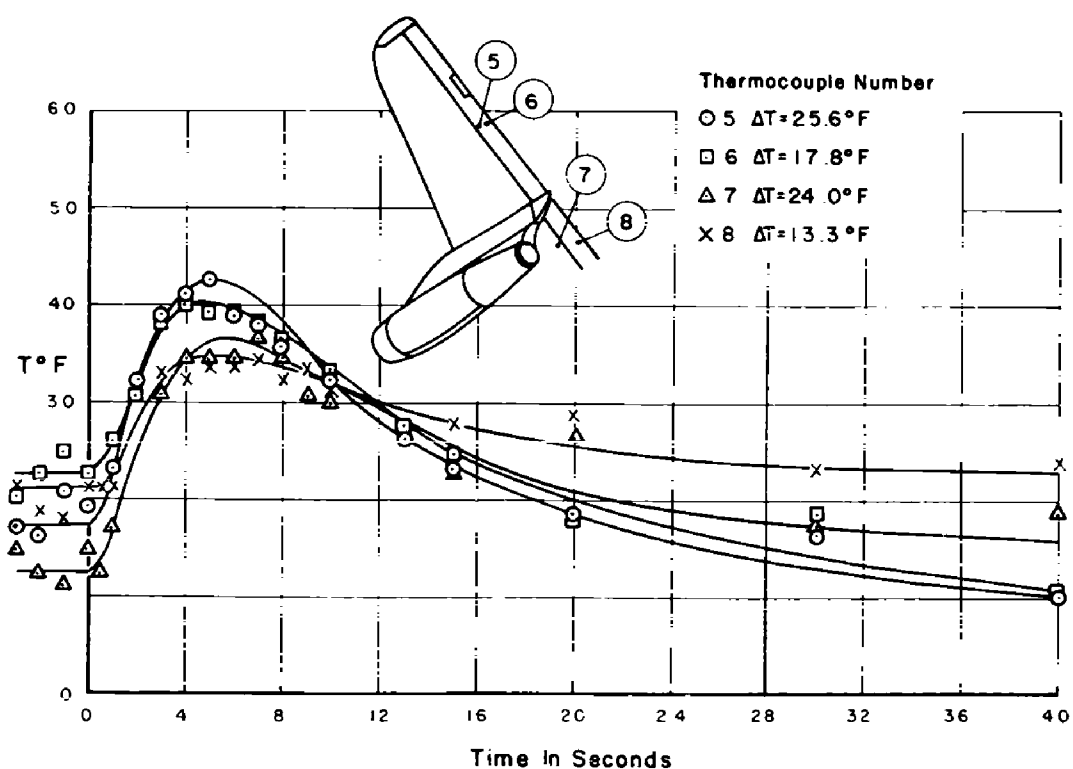


Figure D.56 Temperature time history of aileron and flap skin, Shot Cherokee.

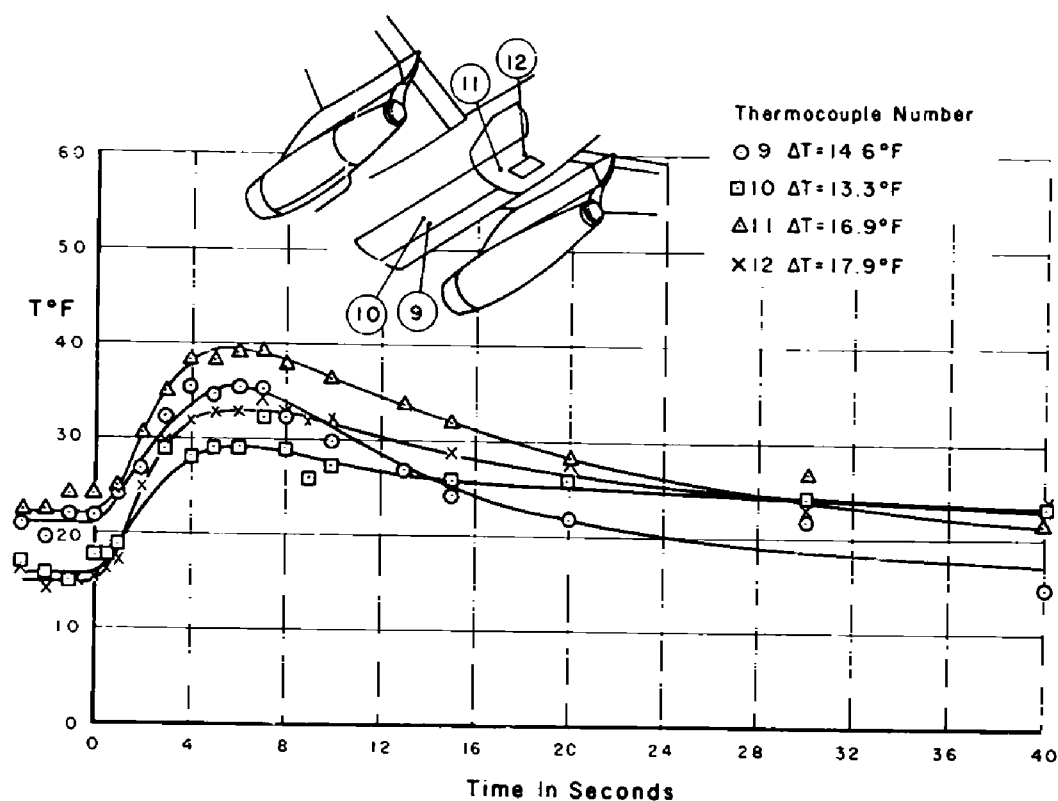


Figure D.57 Temperature time history of bomb bay door and lower fuselage, Shot Cherokee.

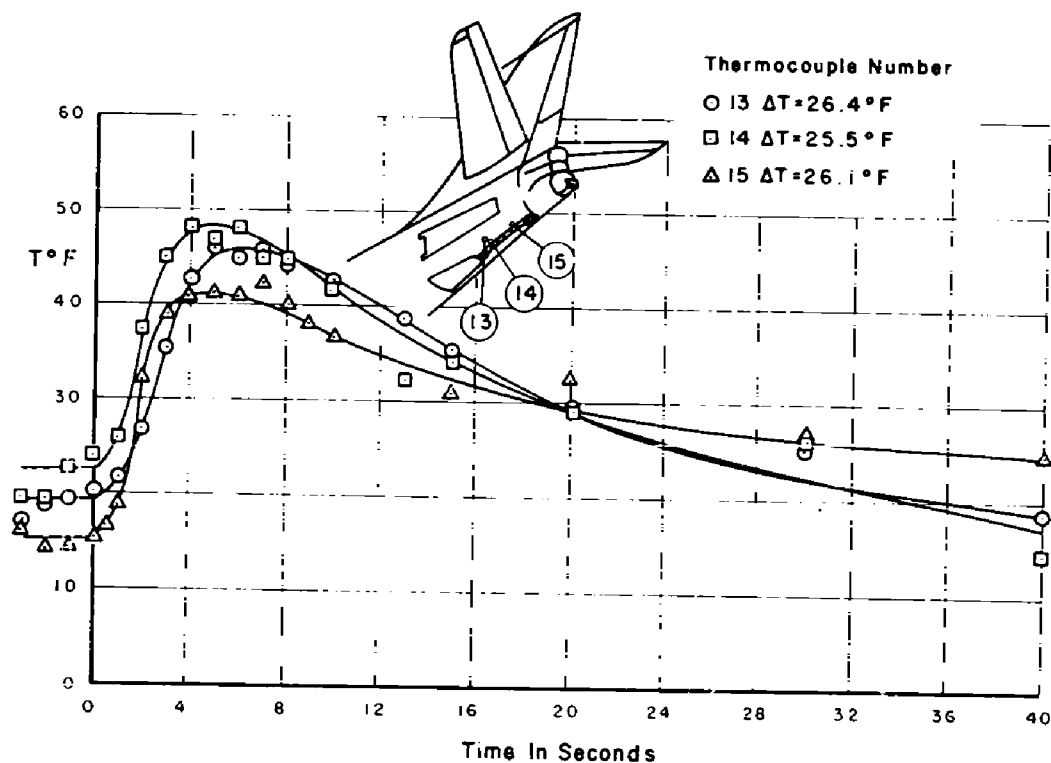


Figure D.58 Temperature time history of arresting hook area, Shot Cherokee.

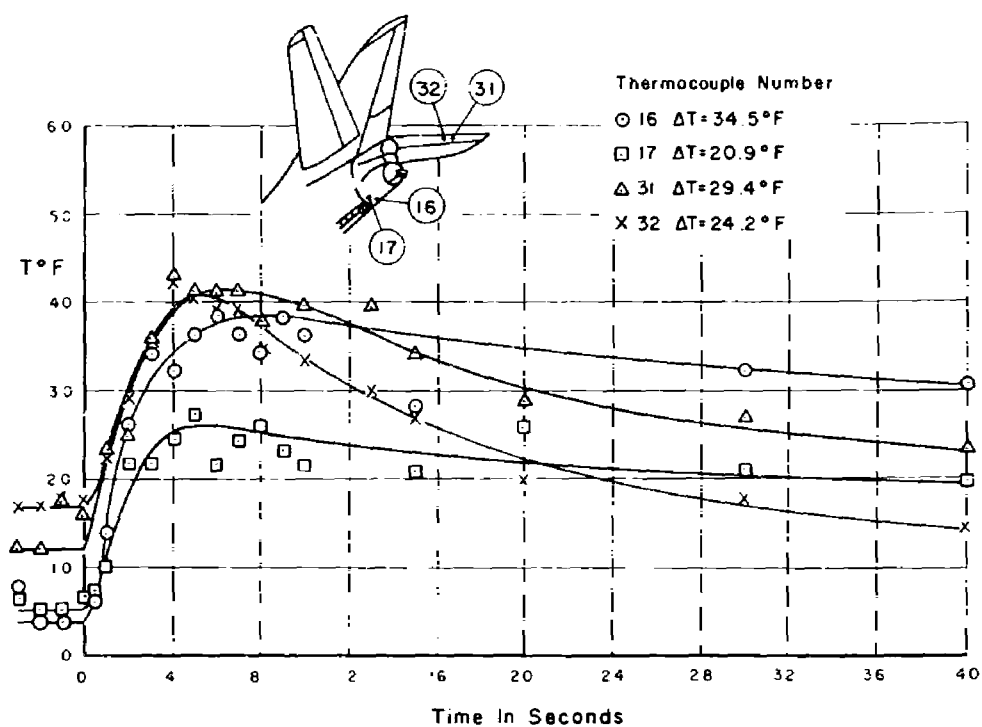


Figure D.59 Temperature time history of quartz covered thermocouple compared to adjacent uncovered thermocouple, Shot Cherokee.

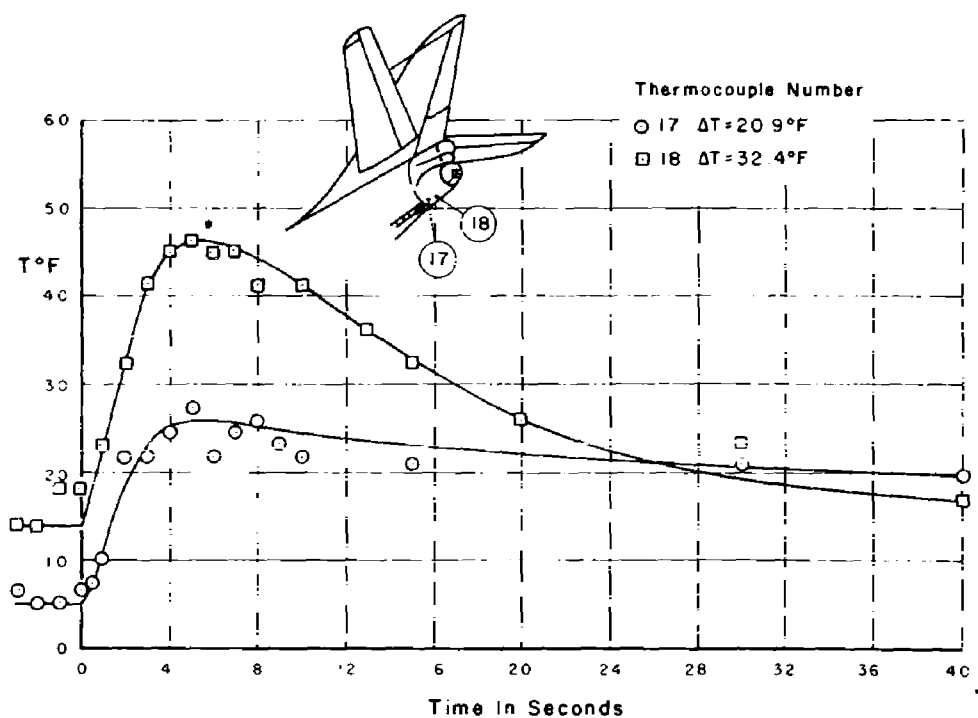


Figure D.60 Temperature time history of aft portion of lower fuselage, Shot Cherokee.

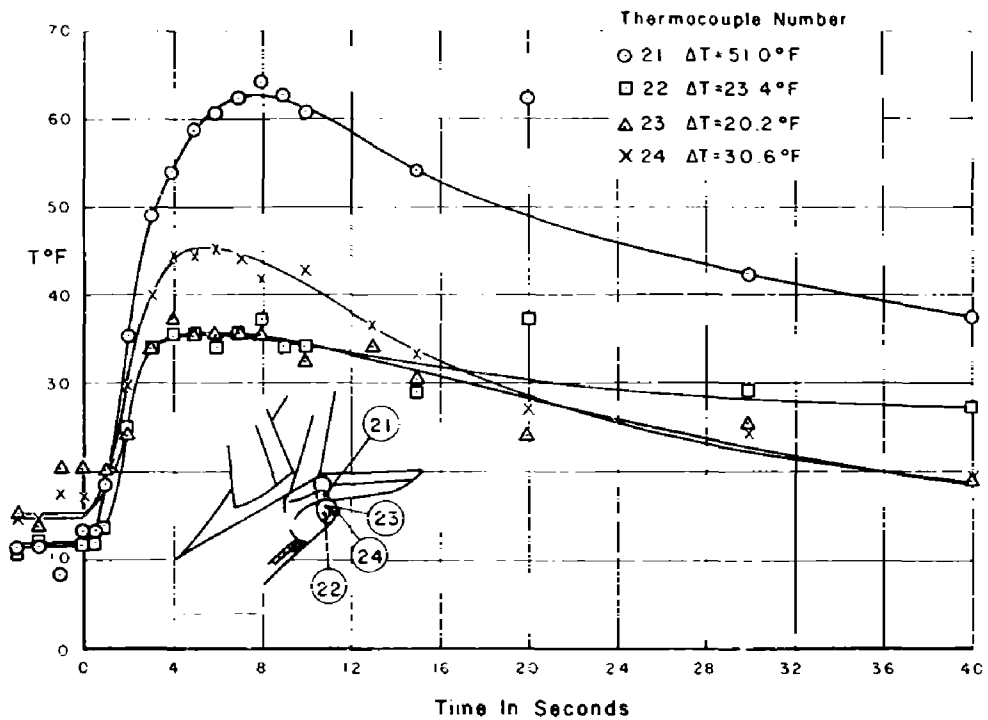


Figure D.81 Temperature time history of tail turret, Shot Cherokee.

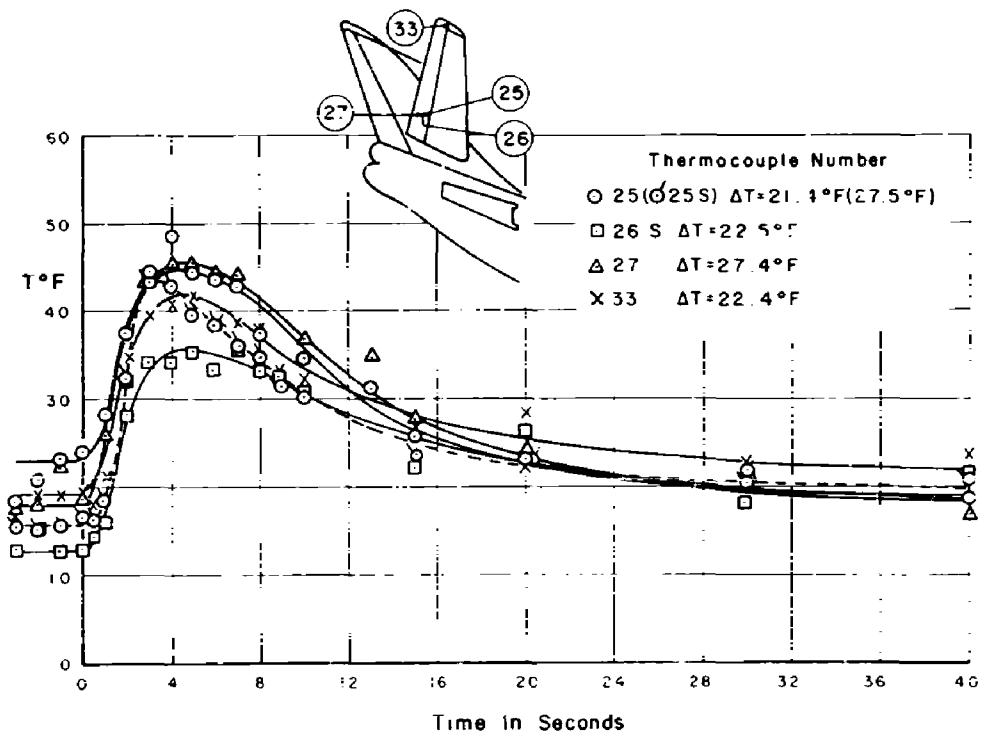


Figure D.62 Temperature time history of elevator skin, Shot Cherokee.

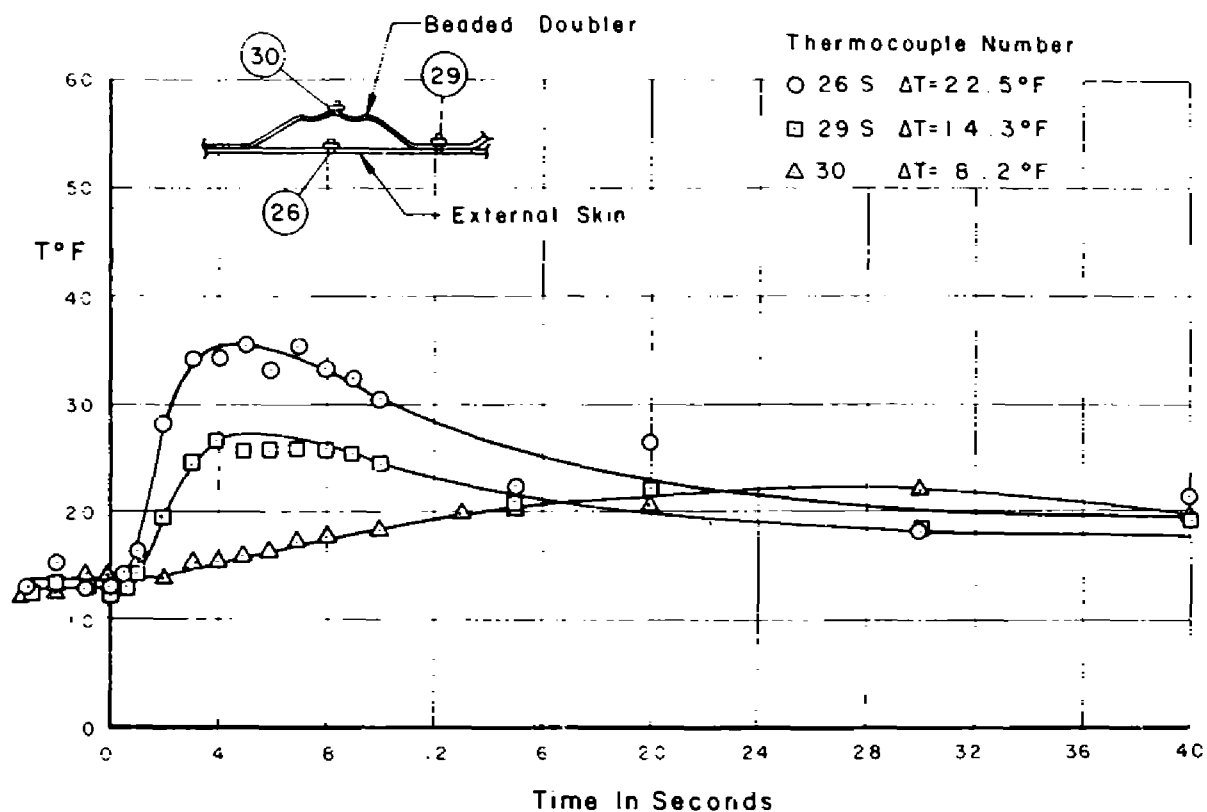


Figure D.63 Temperature time history comparing outer skin and internal beaded doubler. Shot Cherokee.

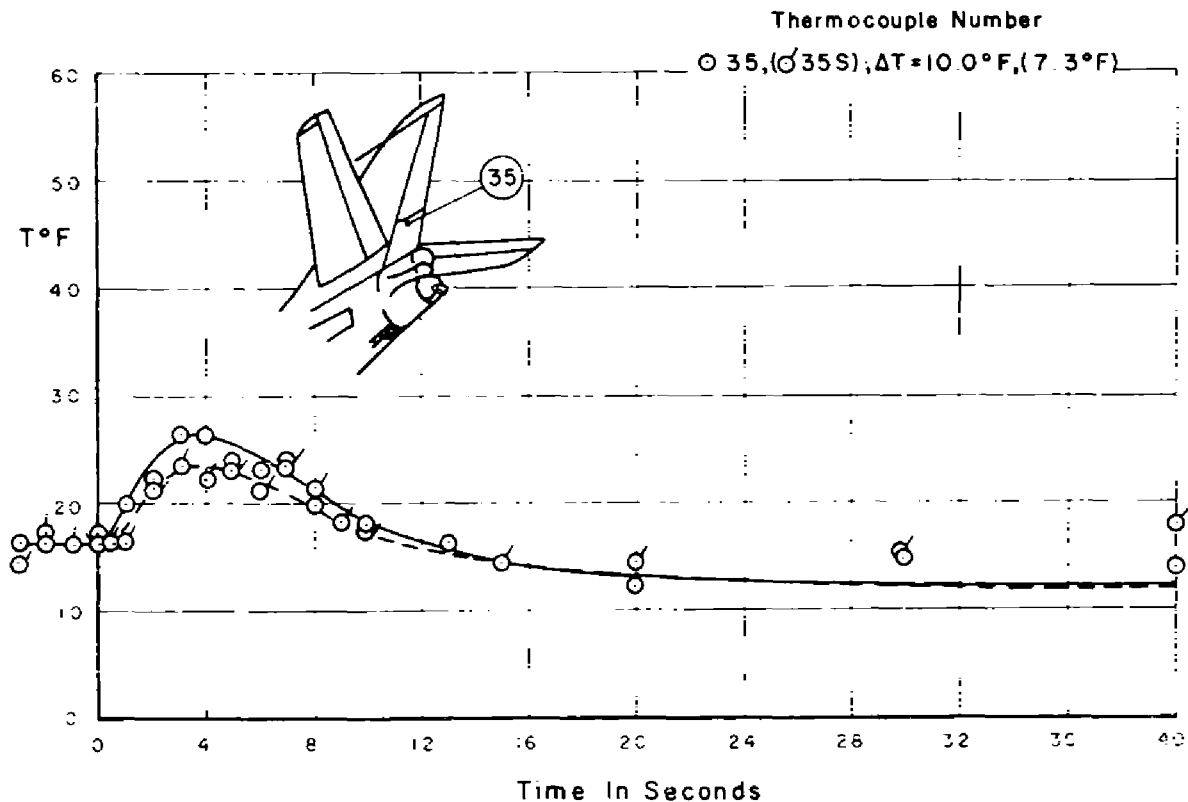


Figure D.64 Temperature time history of lower rudder, Shot Cherokee.

REFERENCES

1. "Atomic Weapon Effects on AD Type Aircraft in Flight"; Project 5.1, Operation Upshot-Knothole, WT-748, March 1954; Secret Restricted Data.
2. "Measurement of Direct and Ground Reflected Thermal Radiation at Altitude"; Project 8.1, Operation Teapot, WT-1143, Feb.-May 1955; Secret Restricted Data.
3. L. E. Bothell; "The Dependent Effects of Fly-away and Convective Cooling on the Expected Temperature Rise of Aircraft Delivering Nuclear Weapons"; SC-3846(TR), June 8, 1956; Sandia Corporation, Albuquerque, New Mexico; Secret Restricted Data.
4. L. M. Barker; "Diffuse Reflection of Radiation from Spherical and Hemispherical Sources to an Inclined Receiver"; SC-3827(TR), April 4, 1956; Sandia Corporation, Albuquerque, New Mexico; Secret Restricted Data.
5. Ralph Zirkind; "Reflection of Radiation from an Infinite Plane; DR-1434, Parts I-IV, 1953-1954; Research Division, Bureau of Aeronautics, Navy Department, Washington, D. C.; Unclassified.
6. J. S. Murphy, L. E. Sattler, and R. B. Smith; "The Radiation Field for a Source Located Above an Infinite Diffuse Plane"; ES 17782, March 22, 1956; El Segundo Division, Douglas Aircraft Company, Inc., El Segundo, California; Confidential.
7. R. M. Chapman and M. H. Seavey; "Preliminary Report on the Attenuation of Thermal Radiation from Atomic or Thermonuclear Weapons"; AFCRC Technical Report No. TN-54-25, November 1954; Air Forces Cambridge Research Center; Secret Restricted Data.
8. W. E. Schorr; "Outline for Obtaining Deliverable Yield"; SC 1283-2, Unpublished; Sandia Corporation, Albuquerque, New Mexico; Secret Restricted Data.
9. "Capabilities of Atomic Weapons"; OPNAV Instruction 003400.1A, June 1, 1955; Armed Forces Special Weapons Project, Washington, D. C.; Secret Restricted Data.
10. T. B. Cook, Jr. and C. D. Broyles; "Curves of Atomic Weapon Effects for Various Burst Altitudes (S. L. to 100,000 ft.)"; SC-3282(TR), March 9, 1954; Sandia Corporation, Albuquerque, New Mexico; Secret Restricted Data.
11. E. R. Fleming; "Gust Loads and Overpressure Effects Induced by Passage Through a Shock Front, A3D-1 Airplane"; ES 26155, January 23, 1956; El Segundo Division, Douglas Aircraft Company, Inc., El Segundo, California; Confidential.
12. L. D. Kovack; "Gust Loads and Overpressure Effects Induced by Passage Through a Shock Front by Analog Computer"; ES 26158, October 16, 1956; El Segundo Division, Douglas Aircraft Company, Inc., El Segundo, California; Confidential.
13. "Naval Air Special Weapons Facility Final Report on BuAer Project TED-NASWF-AD 2202"; Naval Air Special Weapons Facility, Albuquerque, New Mexico; Secret Restricted Data.
14. "Guide to the Effects of Atomic Weapons on Naval Aircraft"; NAVAER 00-25-536, July 1, 1954; Bureau of Aeronautics, Washington, D. C.; Secret Restricted Data.
15. L. E. Sattler and A. G. Taylor; "Model A3D-1 Airplane Special Weapons Delivery Capability"; ES 26246, April 13, 1956; El Segundo Division, Douglas Aircraft Company, Inc., El Segundo, California; Secret Restricted Data.
16. L. E. Sattler and A. G. Taylor; "Model A3D-1 Supplementary Study of Special Weapons Delivery Capability Including Fly-Over and Lay-Down Techniques"; ES 26415, September 10,

1956; El Segundo Division, Douglas Aircraft Company, Inc., El Segundo, California; Secret Restricted Data.

17. E. R. G. Eckert; "Introduction to the Transfer of Heat and Mass"; First Edition, 1950; McGraw-Hill Book Company, Inc., New York, New York; Unclassified.

18. G. M. Matthews; "Final Ground Vibration Tests Model A3D-1"; ES 18083, May 1954; El Segundo Division, Douglas Aircraft Company, Inc., El Segundo, California; Confidential.

19. G. M. Matthews and F. W. Melching; "Ground Vibration Tests, Model XA3D-1"; ES 15409, February 1953; El Segundo Division, Douglas Aircraft Company, Inc., El Segundo, California; Unclassified.

20. "Final Engineering Report on Services and Lease of a Raydist Aircraft Tracking and Positioning System"; Contract NOas 56-475/M, May 1957; Hastings-Raydist, Inc., Hampton, Virginia; Confidential.

DISTRIBUTION

Military Distribution Category 52

ARMY ACTIVITIES

- 1 Deputy Chief of Staff for Military Operations, D/A, Washington 25, D.C. ATTN: Dir. of SW&R
- 2 Chief of Research and Development, D/A, Washington 25, D.C. ATTN: Atomic Div.
- 3 Assistant Chief of Staff, Intelligence, D/A, Washington 25, D.C.
- 4 Chief of Engineers, D/A, Washington 25, D.C. ATTN: ENGTE
- 5- 6 Office, Chief of Ordnance, D/A, Washington 25, D.C. ATTN: CRDTN
- 7 Chief of Transportation, D/A, Office of Planning and Int., Washington 25, D.C.
- 8- 10 Commanding General, U.S. Continental Army Command, Ft. Monroe, Va.
- 11 Director of Special Weapons Development Office, Headquarters CONARC, Ft. Bliss, Tex. ATTN: Capt. Chester I. Peterson
- 12 President, U.S. Army Artillery Board, Ft. Sill, Okla.
- 13 President, U.S. Army Air Defense Board, Ft. Bliss, Tex.
- 14 President, U.S. Army Aviation Board, Ft. Rucker, Ala. ATTN: ATEG-DC
- 15 Commandant, U.S. Army Command & General Staff College, Ft. Leavenworth, Kansas. ATTN: ARCHIVES
- 16 Commandant, U.S. Army Air Defense School, Ft. Bliss, Tex. ATTN: Command & Staff Dept.
- 17 Commandant, U.S. Army Artillery and Missile School, Ft. Sill, Okla. ATTN: Combat Development Department
- 18 Commandant, U.S. Army Aviation School, Ft. Rucker, Ala.
- 19 Commandant, U.S. Army Ordnance School, Aberdeen Proving Ground, Md.
- 20 Commandant, U.S. Army Ordnance and Guided Missile School, Redstone Arsenal, Ala.
- 21 Commanding General, U.S. Army Chemical Corps, Research and Development Comd., Washington 25, D.C.
- 22- 23 Commanding Officer, Chemical Warfare Lab., Army Chemical Center, Md. ATTN: Tech. Library
- 24 Commanding Officer, Diamond Ord. Fuze Lab., Washington 25, D.C. ATTN: Chief, Nuclear Vulnerability Br. (230)
- 25- 26 Commanding General, Aberdeen Proving Grounds, Md. ATTN: Director, Ballistics Research Laboratory
- 27- 28 Commanding General, U.S. Army Ord. Missile Command, Redstone Arsenal, Ala.
- 29 Commander, Army Rocket and Guided Missile Agency, Redstone Arsenal, Ala. ATTN: Tech Library
- 30 Commanding General, White Sands Proving Ground, Las Cruces, N. Mex. ATTN: CRDBS-3M
- 31 Commander, Army Ballistic Missile Agency, Redstone Arsenal, Ala. ATTN: ORCAB-RT
- 32 Commanding General, Ordnance Ammunition Command, Joliet, Ill.
- 33 Commanding Officer, USA Transportation Research Command, Ft. Eustis, Va. ATTN: Chief, Tech. Info. Div.
- 34 Commanding Officer, USA Transportation Combat Development Group, Ft. Eustis, Va.
- 35 Director, Operations Research Office, Johns Hopkins University, 6935 Arlington Rd., Bethesda 14, Md.
- 36 Commander-in-Chief, U.S. Army Europe, APO 403, New York, N.Y. ATTN: Opct. Div., Weapons Br.

NAVY ACTIVITIES

- 37 Chief of Naval Operations, D/N, Washington 25, D.C. ATTN: OP-03BG

- 38 Chief of Naval Operations, D/N, Washington 25, D.C. ATTN: OP-75
- 39 Chief of Naval Operations, D/N, Washington 25, D.C. ATTN: OP-922G1
- 40- 41 Chief of Naval Research, D/N, Washington 25, D.C. ATTN: Code 811
- 42- 43 Chief, Bureau of Aeronautics, D/N, Washington 25, D.C.
- 44- 48 Chief, Bureau of Aeronautics, D/N, Washington 25, D.C. ATTN: ABB-AD-41/20
- 49 Chief, Bureau of Ordnance, D/N, Washington 25, D.C.
- 50 Chief, Bureau of Ordnance, D/N, Washington 25, D.C. ATTN: S.P.
- 51 Director, U.S. Naval Research Laboratory, Washington 25, D.C. ATTN: Mrs. Katherine H. Case
- 52- 53 Commander, U.S. Naval Ordnance Laboratory, White Oak, Silver Spring 19, Md.
- 54 Director, Material Lab. (Code 900), New York Naval Shipyard, Brooklyn 1, N.Y.
- 55 Commanding Officer, U.S. Naval Mine Defense Lab., Panama City, Fla.
- 56- 57 Commanding Officer, U.S. Naval Radiological Defense Laboratory, San Francisco, Calif. ATTN: Tech. Info. Div.
- 58 Commanding Officer, U.S. Naval Schools Command, U.S. Naval Station, Treasure Island, San Francisco, Calif.
- 59 Superintendent, U.S. Naval Postgraduate School, Monterey, Calif.
- 60 Commanding Officer, Nuclear Weapons Training Center, Atlantic, U.S. Naval Base, Norfolk 11, Va. ATTN: Nuclear Warfare Dept.
- 61 Commanding Officer, Nuclear Weapons Training Center, Pacific, Naval Station, San Diego, Calif.
- 62 Commanding Officer, U.S. Naval Damage Control Tug. Center, Naval Base, Philadelphia 12, Pa. ATTN: ABC Defense Course
- 63 Commanding Officer, Air Development Squadron 5, VI-5, China Lake, Calif.
- 64 Director, Naval Air Experiment Station, Air Material Center, U.S. Naval Base, Philadelphia, Pa.
- 65 Commander, Officer U.S. Naval Air Development Center, Johnsville, Pa. ATTN: NAS, Librarian
- 66 Commanding Officer, Naval Air Sp. Wpns. Facility, Kirtland AFB, Albuquerque, N. Mex.
- 67 Commander, U.S. Naval Ordnance Test Station, China Lake, Calif.
- 68 Commandant, U.S. Marine Corps, Washington 25, D.C. ATTN: Code AQ3H
- 69 Director, Marine Corps Landing Force, Development Center, MCS, Quantico, Va.
- 70 Commanding Officer, U.S. Naval CIC School, U.S. Naval Air Station, Glynnco, Brunswick, Ga.

AIR FORCE ACTIVITIES

- 71 Assistant for Atomic Energy, HQ, USAF, Washington 25, D.C. ATTN: DCS/O
- 72 HQ, USAF, ATTN: Operations Analysis Office, Office, Vice Chief of Staff, Washington 25, D.C.
- 73- 74 Air Force Intelligence Center, HQ, USAF, ACS/I (AFICR-3V1) Washington 25, D.C.
- 75 Director of Research and Development, DCS/D, HQ, USAF, Washington 25, D.C. ATTN: Guidance and Weapons Div.
- 76 The Surgeon General, HQ, USAF, Washington 25, D.C. ATTN: Bio.-Def. Pre. Med. Division
- 77 Commander, Tactical Air Command, Langley AFB, Va. ATTN: Doc. Security Branch

SECRET

- ANNALS OF THE ENTOMOLOGICAL SOCIETY OF AMERICA



Defense Threat Reduction Agency

45045 Aviation Drive
Dulles, VA 20166-7517

*Resel
11/3/2000*

CPWPT

October 11, 2000

MEMORANDUM TO THE DEFENSE TECHNICAL INFORMATION CENTER
ATTN: OCQ

SUBJECT: DOCUMENT UPDATES

The Defense Threat Reduction Agency Security Office has performed a classification review of the following two documents. The documents classification has been changed and the distribution statements added to read as stated below:

WT-1333, AD-361768, UNCLASSIFIED, STATEMENT A, Operational Redwing, Project 5.7, Thermal Flux and Albedo Measurements from Aircraft.

WT-1334, AD-339910, UNCLASSIFIED, STATEMENT A, Operation Redwing, Project 5.8, Evaluation of the A3D1 Aircraft for Special Weapons Delivery Capability.

If you have any questions, please call me at 703-325-1034.

Arldith Jarrett

ARDITH JARRETT
Chief, Technical Resource Center



DEFENSE THREAT REDUCTION AGENCY
Defense Threat Reduction Information Analysis Center (DTRIAC)
1680 TEXAS STREET SE
KIRTLAND AFB, NM 87117-5669

14 April 2004

BDQ (505) 846-0847

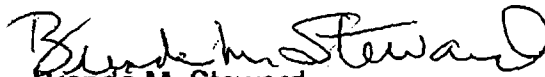
To: Larry Downing, DTIC

Subject: Re-Review of DNA reports

Here is the sixth increment of the results of the re-review project:

See Attached List

We will send more as they are reviewed.


Brenda M. Steward
COTR,
Defense Threat Reduction Information
Analysis Center (DTRIAC)

REPORT NO.	AD NO.	CLASS	DISTRIBUTION
DASA 1254	333113	Unc.	C, Software Documentation
DASA 1420 Chapter 7	C020626	Unc.	C, Admin - Operational
DASA 1420 Chapter 11	C020628	Unc.	C, Admin – Operational
DASA 1958	383870	Unc.	C, Test and Evaluation
DNA 2808	519841	Unc.	C, Test and Evaluation
DNA 3014F	524387	Unc.	C, Test and Evaluation
DNA 3070F	526432	Unc.	C, Test and Evaluation
DNA 3273F	529507	Unc.	C, Test and Evaluation
DNA 3315F	530559	Unc.	C, Test and Evaluation
POR 6723	531141	SFRD	
WT 1333	361768	Unc.	A
WT 1334	339910	Unc.	A